Tharwat F. Tadros

WILEY-VCH

Rheology of Dispersions

Principles and Applications

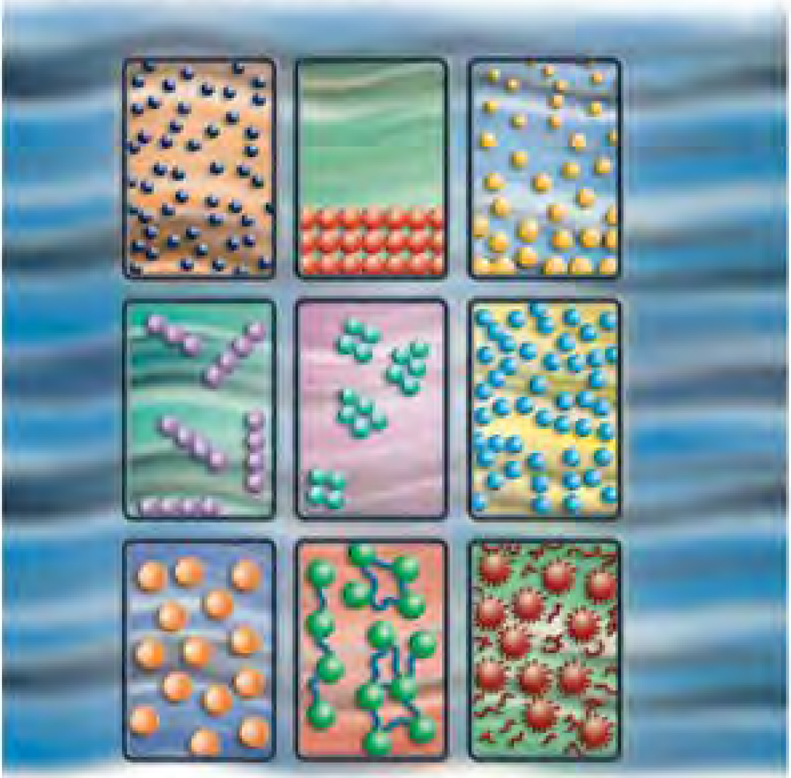

Tharwat F. Tadros

Rheology of Dispersions

Principles and Applications

WILEY-VCH Verlag GmbH & Co. KGaA

Tharwat F. Tadros

Rheology of Dispersions

Related Titles

Tadros, T. F. (ed.)

Colloids and Interface Science Series

6 Volume Set

2010
Hardcover
ISBN: 978-3-527-31461-4

Gomes, V. G., Immanuel, C. D.

Emulsion Polymerization Reactors

Operation and Control

2009
Hardcover
ISBN: 978-3-527-32033-2

Tadros, T. F. (ed.)

Topics in Colloid and Interface Science

Volume 1: Self-Organized Surfactant Structures

2010
Hardcover
ISBN: 978-3-527-31990-9

Wilkinson, K. J., Lead, J. R. (eds.)

Environmental Colloids and Particles

Behaviour, Separation and Characterisation

2007
Hardcover
ISBN: 978-0-470-02432-4

Platikanov, D., Exerowa, D. (eds.)

Highlights in Colloid Science

2009
Hardcover
ISBN: 978-3-527-32037-0

Tharwat F. Tadros

Rheology of Dispersions

Principles and Applications

WILEY-VCH Verlag GmbH & Co. KGaA

The Author

Prof. Dr. Tharwat F. Tadros
89 Nash Grove Lane
Wokingham, Berkshire RG40 4HE
United Kingdom

Library of Congress Card No.: applied for

British Library Cataloguing-in-Publication Data
A catalogue record for this book is available from the British Library.

Bibliographic information published by the Deutsche Nationalbibliothek
The Deutsche Nationalbibliothek lists this publication in the Deutsche Nationalbibliografie; detailed bibliographic data are available on the Internet at http://dnb.d-nb.de.

Cover Design Adam Design, Weinheim
Typesetting Toppan Best-set Premedia Limited, Hong Kong
Printing and Binding Fabulous Printers Pte Ltd, Singapore

Printed in Singapore
Printed on acid-free paper

ISBN: 978-3-527-32003-5

Dedicated to our Grand-Children

Nadia
Dominic
Theodore
Bruno
Viola

Rheology of Dispersions: Principles and Applications. Tharwat F. Tadros

ISBN: 978-3-527-32003-5

Contents

Rheology of Dispersions: Principles and Applications. Tharwat F. Tadros

ISBN: 978-3-527-32003-5

Preface

The rheology (flow characteristics) of dispersions of both solid/liquid (suspensions) and liquid/liquid (emulsions) types is applicable to many industrial situations, including paints, printing inks, paper coatings, ceramics, cosmetics, food systems, pharmaceutical and agrochemical formulations, and liquid detergents. In all of these complex multiphase systems it is necessary to control the rheology of a formulation during its preparation, to maintain its long-term physical stability, and during its application. The requirements for a good paint formulation illustrate these points very well: a paint may consist of polymer particles (latexes) and pigments that must be maintained in a colloidally stable state not only in the formulation but also on coating, to produce a uniform film. In storage, the paint formulation should not show any sedimentation of the pigments, there should be no separation (syneresis), and it should produce a weak gel that is thixotropic in nature. This means that, on application, the gel structure must be broken under shear so as to produce a uniform film, but recovered within a controlled time scale so as to prevent the paint from dripping. But, if the gel structure is recovered too quickly after application, the paint film will show brush marks! In order to achieve such behavior on both storage and application, rheology modifiers – which sometimes are referred to as “thickeners” or “gels” – must be incorporated into the formulation. Today’s research chemist, when formulating a chemical product, must understand the basic principles of rheology and how to control the various parameters of the system so as to achieve a desired effect. In addition, the formulation chemist must design accelerated tests to predict any changes that might occur in the system during storage. Rheological measurements represent the most powerful tools for such predictions, as the formulation can be investigated without dilution or disturbing its structure.

This book is targeted at research scientists, both in industry and in academic institutes. Following a brief introduction (Chapter 1) which highlights the scope of the book, Chapter 2 is dedicated to understanding the colloidal properties of dispersions, where the theories of colloid stability – both for electrostatically and sterically stabilized dispersions – are briefly summarized. This is followed by a description of the conditions required for the stability/instability of a dispersion, with particular attention being paid to the states of suspensions and emulsions on standing. The various breakdown processes are described and analyzed in terms

Rheology of Dispersions: Principles and Applications. Tharwat F. Tadros

ISBN: 978-3-527-32003-5

of the interaction forces between the particles or droplets. Chapters 3 and 4 describe the basic principles of rheology, and the experimental techniques that can be applied to investigate the rheological properties of a system. In this case, it was convenient to separate the basic principles into two chapters. First, the steady-state principles (high deformation measurements) are outlined in Chapter 3, whereby a constant and increasing shear rate is applied to a system (which may be placed in the gap between concentric cylinders, parallel plates, or cone and plate geometry), after which the stress and viscosity are obtained as a function of shear rate so as to distinguish between Newtonian and non-Newtonian systems. The flow curves of shear stress versus shear rate can be fitted to various models, and particular attention is given to the reversible time-dependence of viscosity (thixotropy and negative thixotropy). Chapter 4 provides details of viscoelastic behavior (low-deformation measurements), with descriptions of three methods (that are equivalent, but not identical) which can be applied: (i) strain relaxation after the sudden application of stress (constant-stress or creep measurements); (ii) stress relaxation after the sudden application of strain; and (iii) dynamic (oscillatory) techniques. The models that can be applied to describe each of these measurements are briefly outlined. In this way, various rheological parameters can be obtained, such as creep compliance, residual (zero) shear viscosity, relaxation time, storage (elastic) and loss (viscous) modulus. Each of these parameters is important for controlling the physical stability of the dispersion, as well as predicting its long-term stability. Chapter 5 describes the rheology of suspensions, with four basic systems being outlined. The first of these is hard-sphere dispersions, where both repulsion and attraction are screened (neutral stability). In this case, the rheological behavior is simple as it depends only on the balance between Brownian diffusion and hydrodynamic interaction. These hard-sphere dispersions form the basis of the development of theoretical treatments of the rheology of suspensions. The second system is that of "soft" (electrostatic) interaction, where rheology is determined by double-layer repulsion. For this, models are available to relate some of the rheological parameters such as the high-frequency modulus to the double-layer repulsion energy of interaction. The third category is that of sterically stabilized systems which contain adsorbed or grafted nonionic polymers. In this case, the rheology is determined by the steric repulsion of the adsorbed or grafted chains. It is also possible to relate the high-frequency modulus to the steric interaction energy. Finally, flocculated and coagulated systems, where the rheology is determined by the van der Waals attractions, can be used to distinguish between weak (reversible) and strong (irreversible) systems. The rheology of these flocculated systems is complicated, as they are under nonequilibrium, and only semi-empirical models are available for this purpose. The use of a fractal dimension concepts allows information to be obtained on the structure of flocculated systems. Chapter 6 deals with the rheology of emulsions. It starts with a discussion of interfacial rheology and how this can be correlated with emulsion stability. The bulk rheology of emulsions is described at a fundamental level with special reference to the analysis of the rheology of concentrated emulsions and the effect of droplet deformability. A section is devoted to the rheology of high internal phase emulsions (HIPE). Chapter 7 provides information on the rheology of modifiers, thickeners and gels, with various systems being described ranging from physical gels (obtained simply by an overlap of the polymer coils) to associative thickeners (hydrophobically modified polymers), crosslinked polymers, and particulate gels (including swellable clays and silica gels). One important rheology modifier that is used in many cosmetic creams and liquid detergents is based on surfactant liquid crystalline phases. In Chapter 8, the various rheological methods that can be applied to assess and predict the long-term physical stability of dispersions are described, with practical examples being given to illustrate the validity of these methods.

Although this book is by no means comprehensive, its aim is to provide both the fundamentals and applications of the rheology of dispersions. It should serve as a valuable text for those scientists in industry who deal regularly with the formulation of chemicals, and also as an introduction to those research workers investigating the rheology of dispersions.

February 2010 *Tharwat Tadros*

1
General Introduction

Several types of disperse system may be defined, depending on the nature of the disperse phase and medium; these are summarized in Table 1.1.

The present book deals with the rheology of three main disperse systems, namely solid in liquid (suspensions), liquid in liquid (emulsions), and liquid in solid (gels). It is essential to define the dimensions of the particles or droplets of the internal phase. Systems where such dimensions fall within 1 nm to 1000 nm (1 μm) are classified as "colloidal systems," whereas those which contain particles or droplets larger than 1 μm are outside the colloid range. However, in both cases, the property of the system is determined by the nature of the interface which separates the internal phase from the medium in which it is dispersed. Clearly, with colloidal systems the interfacial region presents a significant proportion of the whole system. The structure of the interfacial region determines the properties of the system, and in particular the tendency of the particles to form aggregate units or to remain as individual particles.

Two main types of interfacial structure may be distinguished. The first type occurs with charged interfaces, whereby a double layer develops as a result of the presence of a surface charge which is compensated near the interface by unequal distribution of counter-ions and co-ions. At the interface, there will be an excess of counter-ions and a deficiency of co-ions. This picture of the double layer has been introduced by Gouy and Chapman [1, 2], and is referred to as "the diffuse double layer." Later, Stern [3] introduced a modified picture whereby the first layer of the counter-ions is regarded to be fixed (due to specific adsorption) and the rest of the double is diffuse in nature. In this way, Stern defined a potential ψ_d at the center of the first fixed layer; this potential may be close to the measurable electrokinetic or zeta potential. A modification of the Stern picture was later introduced by Grahame [4, 5], who considered two planes: an inner Helmholtz plane (IHP) at the center of the counter-ions that lose their hydration shell (chemisorbed counter ions); and an outer Helmholtz plane (OHP) at the center of the physically adsorbed counter-ions with their hydration shell. As will be seen in Chapter 2, the extension of the double layer depends on the concentration of counter-ions and co-ions, as well as their valency. At low electrolyte concentrations ($<10^{-2}\,\mathrm{mol\,dm^{-3}}$ for 1:1 electrolyte and ($<10^{-3}\,\mathrm{mol\,dm^{-3}}$ for 2:2 electrolyte), the double layer is sufficiently extended.

Rheology of Dispersions: Principles and Applications. Tharwat F. Tadros

ISBN: 978-3-527-32003-5

Table 1.1 Types of disperse systems.

Disperse phase	Disperse medium	Type
Solid	Liquid	Suspension
Liquid	Liquid	Emulsion
Liquid	Solid	Gel
Liquid	Gas	Aerosol
Gas	Liquid	Foam
Solid	Solid	Composite

As will be discussed in detail in Chapter 2, when two particles or droplets with their extended double layers (at low electrolyte concentration) approach each other to a distance of separation at which the diffuse parts of the double layers begin to overlap, a strong repulsion occurs as the double layers can no longer develop unrestrictedly. This repulsion decreases exponentially with the decrease in the distance of separation h between the particles or droplets. The magnitude of the repulsive energy, G_{el}, at any separation distance h increases with a decrease in electrolyte concentration and a decrease in the valency of the electrolyte.

In addition to the repulsive energy described above, the particles or droplets in a dispersion have an attractive energy, sometimes referred to as van der Waals attraction, G_A, which is universal to all disperse systems. The main contribution to the van der Waals attraction is the *London dispersion energy*, and expressions have been derived by Hamaker [6] for G_A (as will be discussed in detail in Chapter 2).

The combination of G_{el} and G_A results in the well-known theory due to Derjaguin–Landau–Verwey–Overbeek (DLVO [7, 8]; this is discussed in detail in Chapter 2). The DLVO theory predicts the presence of an energy barrier at intermediate distances of separation between the particles that prevents flocculation of the dispersion. The height of the barrier depends on the surface or zeta potential, the electrolyte concentration, and the particle radius.

The second type of interfacial structure arises when surfactants and/or macromolecules are adsorbed at the particle surface. With surfactant molecules consisting of few units, adsorption simply occurs with one part of the molecule being preferentially attached to the particle surface. For example, with ionic surfactants adsorbed onto charged surfaces, an electrostatic attraction occurs between the charged head groups of the surfactant molecule and the charged sites on the surface. The surfactant molecules may adopt either horizontal or vertical orientations. With nonionic surfactants, such as alcohol or alkyl phenol ethoxylates, the alkyl or alkyl phenyl chain may become adsorbed onto a hydrophobic surface, leaving the poly(ethylene oxide) (PEO) chain dangling in solution.

With polymer molecules consisting of a large number of units, the adsorbed molecule adopts different configurations depending on the concentration, the molecular weight of the polymer, and its structure (e.g., flexibility, branching, etc). The most general configuration is that whereby a number of units become attached to the surface, in so-called "trains," with loops in between and tails at the ends of the chain. However, with block copolymers of the A–B or A–B–A type (where B represents the "anchor" chain that is strongly attached to the surface by small loops and A is the stabilizing chain), the polymer can adopt a configuration whereby the B chain becomes strongly attached to the surface, leaving one or two A chains (which are strongly solvated by the molecules of the medium) that provide a strong steric repulsion; in this way, a very stable dispersion is produced.

When two particles or droplets which have a radius R and contain adsorbed layers with thickness δ approach each other to a surface-to-surface distance h that is less than 2δ, a strong repulsion will occur as a result of two main effects [9]. When the layers begin to overlap, the segment density in the overlap region becomes larger than the rest of the layer, and this results in an increase in the osmotic pressure in this region. Provided that the stabilizing chains are in good solvent conditions, this increase in osmotic pressure resists any overlap of the layers (unfavorable mixing of the stabilizing chains) and results in a strong repulsion that is given by G_{mix} (which has a positive sign). As a result, solvent diffuses to the overlap region, thus separating the particles or droplets. The second repulsive energy arises from the loss of configurational entropy of the chains on significant overlap; this is referred to as elastic interaction, G_{el}. A combination of G_{mix} and G_{el} gives the total steric interaction free energy which, when added to the van der Waals attraction, causes the energy–distance curve to show a shallow minimum at separation distances comparable to 2δ; moreover, when $h < 2\delta$ a strong repulsion will occur with a further decrease of h.

As mentioned above, the structure of the interfacial region determines the interaction between particles in a disperse system. For example, with systems containing double layers or adsorbed layers of surfactants or polymers, an interaction will lead to a repulsion as soon as the double layers or the adsorbed layers begin to overlap. This repulsion leads to a colloidally stable system. On the other hand, if the repulsive energy is not sufficiently large, then the van der Waals attraction will dominate the interaction and an aggregated system will result. These interactions determine the flow characteristics (rheology) of the disperse systems.

The main objective of this book is to describe the rheology of dispersions in terms of the various forces between the particles or droplets. The rheology of a dispersion is determined by the balance of three main forces [10–12]: Brownian diffusion; hydrodynamic interaction; and surface forces (repulsive or attractive). For this reason, Chapter 2 will be dedicated to describing these interaction forces, and how these can be controlled in practice. As will be seen, four different types of interaction must be considered:

- Hard-sphere interaction, whereby both the repulsive and attractive forces are screened (this is sometimes referred to as "neutral stability"). In this case, the rheology of the dispersion is determined by the balance between Brownian diffusion and hydrodynamic interaction. This simplifies the analysis and, as will be seen in Chapter 3, theories are available to describe the variation of relative viscosity η_r with the volume fraction ϕ of the dispersion.

- Systems with “soft” (electrostatic) interaction with extended double layers. As will be seen in Chapter 3, the rheology of the dispersion will be determined by the double-layer repulsion.

- Systems with steric interaction – that is, containing adsorbed surfactant or polymer layers. In this case, the rheology of the dispersion is determined by the steric repulsion.

- Systems where the net interaction is attractive; in this case, it is possible to distinguish between weak and strong flocculation, depending on the magnitude of the attraction.

Particular attention will be given to concentrated systems and the formation of three-dimensional (3-D) structural units that determine the rheology of dispersions. These structural units are the result of the balance between the various interaction forces. In addition, the effect of gravity must be considered, since the presence of dense particles with diameters larger than the colloid range may result in the settling and formation of hard sediments. The latter must be prevented when dealing with suspensions.

Investigations of the rheology of dispersions are very important in many industrial applications such as:

Paints: The rheological characteristics of any paint formulation is important, both for its long-term stability as well as on application.

Printing inks: The flow behavior of inks (e.g., ink jets) is crucial for its application.

Paper coatings: These mostly consist of suspensions which need to be applied at high shear rates. Shear thickening (dilatancy) must be prevented under these conditions.

Ceramics: These are suspensions with a high volume fraction (approaching maximum packing), and control of their rheology for molding and casting is crucial.

Cosmetics: Most cosmetic formulations consist of emulsions or suspensions and their mixtures. The control of their rheology is crucial for long-term stability and application (skinfeel).

Food industry: Most products used in the food industries, such as mayonnaise, salad creams, and desserts require an accurate control of their rheology for good texture and mouthfeel.

Pharmaceutical formulations: These include emulsions, suspensions, creams, and gels. The control of rheology is crucial for long-term physical stability and application, especially for injectables and topical applications.

Agrochemical formulations: These consist mostly of concentrated suspensions and emulsions. To control the rheology of the formulation is important for the long-term physical stability, as well as applications in the spray tank.

Liquid detergents: These consist of concentrated surfactant solutions in which solids such as phosphates and silicates are dispersed. Rheology modifiers are required to prevent separation and facilitate dispersion on dilution.

At a fundamental level, it is important to relate the bulk rheology of dispersions to the interaction forces between the particles or droplets. Some progress has been made as a result of the possibility of directly measuring the interaction energies between macroscopic bodies, using for example the surface force apparatus and the technique of atomic force microscopy (AFM).

Within this book, the text is organized as follows. In Chapter 2, attention is focused on the colloidal aspects of dispersions, both of the solid–liquid (suspensions) and liquid–liquid type. The three main energies involved – namely, double-layer repulsion, steric interaction, and van der Waals attractions – will be considered. A combination of these energies provides energy–distance curves that can be used to describe the stability/flocculation of dispersions. The different states of suspensions and emulsions will also be described, highlighting the structure of the concentrated dispersions that are produced on standing. Particular attention will also be given to the sedimentation of suspensions and creaming of emulsions. The flocs that can be produced as the result of a lack of stability are described, and both strong and weak flocculation can be distinguished in these dispersions. Subsequently, Chapters 3 and 4 describe the basic principles of rheology in relation to both steady-state and viscoelastic behaviors, and also provide details of the experimental techniques that may be applied for their investigation. Rheology is well recognized as the study of the deformation and flow of matter. Typically, steady-state measurements are carried out using shear rate-controlled rheometers, where the shear is gradually increased while simultaneously measuring the stress produced, so as to produce flow curves of shear stress and viscosity versus shear rate. The curves obtained may then be analyzed by using different models, so as to produce the various rheological parameters such as yield value, viscosity, and shear thinning index. The viscoelastic measurements (which are referred to as "low-deformation measurements") are carried out using highly sensitive rheometers that are capable of applying low torques (stress) or oscillation at a variety of amplitudes and frequency. For this, three main types of investigation can be applied: (i) strain relaxation after the application of constant stress (referred to as "creep measurements"); (ii) stress relaxation after a sudden application of strain; and (iii) dynamic or oscillatory techniques. In the latter case, a sinusoidal strain (with amplitude γ_o) or stress (with amplitude σ_o) is applied at a frequency ω (rad s^{-1}), and the sign waves of strain and stress (or stress and strain) are compared so as to obtain the phase angle shift, δ. In this way, the various rheological parameters can be obtained as a function of amplitude and frequency, and the elastic and viscous components of the system thus obtained, with a variety of models being used to analyze the results. The basic laws that govern the rheology of a dispersion are also described, whilst avoiding – as much as possible – the use of complex mathematical analyses. The rheology of suspensions is discussed in Chapter 5, by describing the four main forces – hard-sphere, electrostatic, steric, and van der Waals attractions – where the rheological behavior of each system is described using the well-known theories of rheology of dispersions. The rheology of emulsions, which have some features in common with suspensions, is detailed in Chapter 6. Due to the fluid nature of the interface, it is also necessary to consider the interfacial rheology that results from surfactant and/or polymer adsorption. The deformability of the emulsion droplets must also be considered, particularly at the high volume fraction of the emulsion.

Finally, a section will be devoted to the rheology of highly concentrated emulsions (high internal-phase emulsions, HIPE), whereby the rheology of emulsions during flow and the break-up of drops will also be described. Consequently, Chapter 8 is devoted to rheology modifiers, thickeners, gels, and liquid crystalline structures, and considers the application of rheological measurements to assess and predict the long-term physical stability of dispersions, which is especially important in their industrial application.

References

1 Gouy, G. (1910) *J. Phys.*, **9**, 457; Gouy, G. (1917) *Ann. Phys.*, **7**, 129.

2 Chapman, D.L. (1913) *Philos. Mag.*, **25**, 475.

3 Stern, O. (1924) *Z. Electrochem.*, **30**, 508.

4 Grahame, D.C. (1947) *Chem. Rev.*, **41**, 44.

5 Tadros, T.F. (1987) *Solid/Liquid Dispersions*, Academic Press, London.

6 Hamaker, H.C. (1937) *Physica*, **4**, 1058.

7 Derjaguin, B.V., and Landau, L. (1941) *Acta Physicochem. USSR*, **14**, 633.

8 Verwey, E.J.W., and Overbeek, J.T.G. (1948) *Theory of Stability of Lyophobic Colloids*, Elsevier, Amsterdam.

9 Napper, D.H. (1983) *Polymeric Stabilization of Colloidal Dispersions*, Academic Press, London.

10 Barnes, H.A., Hutton, J.F., and Walters, K. (1989) *Introduction to Rheology*, Elsevier, Amsterdam.

11 Goodwin, J.W., and Hughes, R.W. (2000) *Rheology for Chemists*, Royal Society of Chemistry Publication, Cambridge.

12 Tadros, T. (2005) *Applied Surfactants*, Wiley-VCH Verlag GmbH, Germany.

2
Interparticle Interactions and Their Combination

In order to control the properties (rheology) of concentrated dispersions, it is first essential to control the interparticle interactions [1], four different types of which can be distinguished (see Figure 2.1). Details of these interactions are summarized as follows.

2.1
Hard-Sphere Interaction

The particles are considered to behave as "hard-spheres" with a radius R_{HS} that is slightly larger than the core radius R (Figure 2.1a). When the particles reach a center-to-center distance that is smaller than $2\,R_{HS}$, the interaction increases very sharply, approaching ∞. It is possible to define a maximum hard-sphere volume fraction above which the flow behavior suddenly changes, from "fluid-like" to "solid-like" (a viscous to elastic response).

2.2
"Soft" or Electrostatic Interaction

The particles in this case have a surface charge (either by ionization of surface groups as in the case of oxides) or in the presence of adsorbed ionic surfactants (Figure 2.1b). The surface charge σ_o is compensated by unequal distribution of counter-ions (opposite in charge to the surface) and co-ions (same sign as the surface) which extend to some distance from the surface [2]. This is shown schematically in Figure 2.2.

The potential decays exponentially with distance x. At low potentials,

$$\psi = \psi_o \exp - (\kappa x) \tag{2.1}$$

Note that when $x = 1/\kappa$, $\psi_x = \psi_o/e$; $1/\kappa$ is referred to as the "thickness" of the double layer.

The double-layer extension depends on electrolyte concentration and valency of the counter-ions,

Rheology of Dispersions: Principles and Applications. Tharwat F. Tadros

ISBN: 978-3-527-32003-5

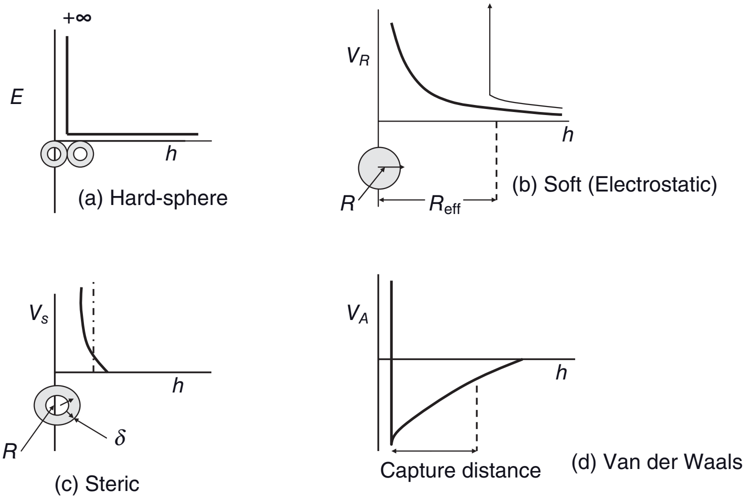

Figure 2.1 Types of interaction force.

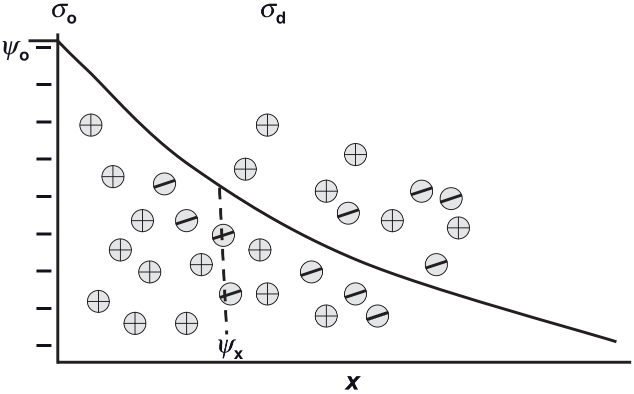

Figure 2.2 Schematic representation of the diffuse double layer according to Gouy and Chapman [2].

$$\left(\frac{1}{\kappa}\right)=\left(\frac{\varepsilon_r\varepsilon_o kT}{2n_o Z_i^2 e^2}\right)^{1/2} \tag{2.2}$$

where ε_r is the permittivity (dielectric constant; this is 78.6 for water at 25 °C), ε_o is the permittivity of the free space, k is the Boltzmann constant, T is the absolute temperature, n_o is the number of ions per unit volume of each type present in bulk solution, Z_i is the valency of the ions, and e is the electronic charge.

Values of $(1/\kappa)$ for 1 : 1 electrolyte (e.g., KCl) are given in Table 2.1.

Table 2.1 Values of $(1/\kappa)$ for a 1:1 electrolyte at 25 °C.

	C (mol dm^{-3})				
	10^{-5}	10^{-4}	10^{-3}	10^{-2}	10^{-1}
$(1/\kappa)$ (nm)	100	33	10	3.3	1

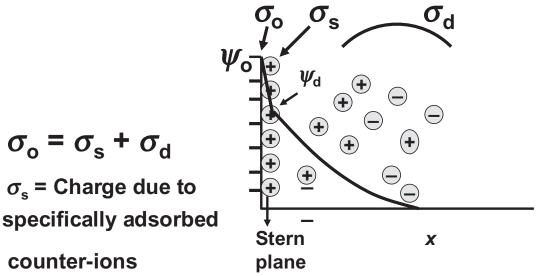

Figure 2.3 Schematic representation of the double layer according to Stern and Grahame [2].

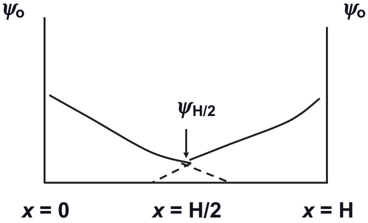

Figure 2.4 Schematic representation of double layer interaction for two flat plates.

The double-layer extension increases with a decrease in electrolyte concentration.

Stern [3] introduced the concept of the nondiffuse part of the double layer for specifically adsorbed ions, the rest being diffuse in nature. This is shown schematically in Figure 2.3. In this case, the potential drops linearly in the Stern region, and then exponentially. Grahame distinguished two types of ion in the Stern plane – physically adsorbed counter-ions (outer Helmholtz plane), and chemically adsorbed ions (that lose part of their hydration shell) (inner Helmholtz plane).

When charged colloidal particles in a dispersion approach each other such that the double layers begin to overlap (the particle separation becomes less than twice the double layer extension), then repulsion will occur. The individual double layers can then no longer develop unrestrictedly, as the limited space does not allow complete potential decay [3]. This is illustrated in Figure 2.4 for two flat plates.

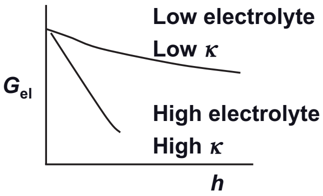

Figure 2.5 Variation of G_{el} with h at different electrolyte concentrations.

The potential $\psi_{H/2}$ half-way between the plates is no longer zero (as would be the case for isolated particles at $x \to \infty$).

For two spherical particles of radius R and surface potential ψ_o and condition $\kappa R < 3$, the expression for the electrical double-layer repulsive interaction is given by [4]:

$$G_{el} = \frac{4\pi\varepsilon_r\varepsilon_o R^2 \psi_o^2 \exp-(\kappa h)}{2R + h} \tag{2.3}$$

where h is the closest distance of separation between the surfaces.

The above expression shows the exponential decay of G_{el} with h. The higher the value of κ (i.e., the higher the electrolyte concentration), the steeper the decay, as shown schematically in Figure 2.5. This means that at any given distance h, the double-layer repulsion decreases with an increase of electrolyte concentration.

The importance of the double-layer extension can be illustrated as follows. First, consider a very small particle with a radius of 10 nm in 10^{-3} mol dm^{-3} NaCl. The core radius R is 10 nm, but the effective radius R_{eff} (the core radius plus the double-layer thickness) is now 110 nm. The core volume is $(4/3) \times \pi \times R^3 = (4/3) \times \pi \times (10)^3$ nm^{-3}, but the effective volume is now $(4/3) \times \pi \times (110)^3$, which is ~1000-fold higher than the core volume. The same applies to the volume fraction:

$$\phi_{eff} = \phi\left(\frac{110}{10}\right)^3 \approx 1000\phi \tag{2.4}$$

For a dispersion with equal-sized particles, the maximum possible volume fraction (for hexagonal packing) ϕ_p is 0.74. For the above case of 10 nm particles in 10^{-5} mol dm^{-3} NaCl, the maximum core volume fraction is ~7.4×10^{-4}, while at and above this volume fraction a strong repulsion occurs such that the system may now be considered as concentrated.

With an increase in electrolyte concentration, the double-layer thickness decreases and ϕ_{eff} decreases; thus, the core volume fraction must be increased in order to produce a "concentrated" system.

2.3
Steric Interaction

Steric interaction occurs when the particles contain adsorbed nonioinic surfactant or polymer layers of the A–B, A–B–A block or BA$_n$ graft types, where B is the

Interpenetration without compression

Compression without interpenetration

Figure 2.6 Schematic representation of the interaction between particles containing adsorbed polymer layers.

"anchor" chain that has a high affinity to the surface (strongly adsorbed) and A is the "stabilizing" chain that is highly soluble in the medium and strongly solvated by its molecules (see Figure 2.1c). It is possible to define an adsorbed layer thickness δ_h for the surfactant or polymer and hence an effective radius $R_{eff} = R + \delta_h$.

When two particles, each of radius R and containing an adsorbed polymer layer with a hydrodynamic thickness δ_h, approach each other to a surface–surface separation distance h that is smaller than 2 δ_h, the polymer layers interact with each other to result in two main situations [5]: (i) The polymer chains may overlap with each other; or (ii) the polymer layer may undergo some compression. In both cases, there will be an increase in the local segment density of the polymer chains in the interaction region, as shown schematically in Figure 2.6. However, the "real" situation is perhaps in between the above two cases – that is, the polymer chains may undergo some interpenetration and some compression.

Provided that the dangling chains (the A chains in A–B, A–B–A block or BA_n graft copolymers) are in a good solvent, this local increase in segment density in the interaction zone will result in a strong repulsion as a result of two main effects:

- An increase in the osmotic pressure in the overlap region as a result of the unfavorable mixing of the polymer chains, when these are in good solvent conditions; this is referred to as "osmotic repulsion" or "mixing interaction," and is described by a free energy of interaction G_{mix}.

- A reduction of the configurational entropy of the chains in the interaction zone; this entropy reduction results from a decrease in the volume available for the chains when these are either overlapped or compressed; this is referred to as "volume restriction interaction" or "entropic or elastic interaction," and is described by a free energy of interaction G_{el}.

A combination of G_{mix} and G_{el} is usually referred to as the steric interaction free energy, G_s; that is:

$$G_s = G_{mix} + G_{el} \tag{2.5}$$

The sign of G_{mix} depends on the solvency of the medium for the chains. If in a good solvent (i.e., the Flory–Huggins interaction parameter χ is <0.5), then G_{mix} is positive and the mixing interaction leads to repulsion (see below). In contrast, if $\chi > 0.5$ (i.e., the chains are in a poor solvent condition), then G_{mix} is negative

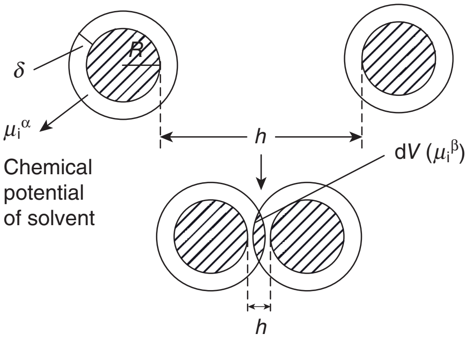

Figure 2.7 Schematic representation of polymer layer overlap.

and the mixing interaction becomes attractive. G_{el} is always positive such that, in some cases, it is possible to produce stable dispersions in a relatively poor solvent (enhanced steric stabilization).

As mentioned above, the mixing interaction results from the unfavorable mixing of the polymer chains, when these are in a good solvent conditions; this is shown schematically in Figure 2.7. In this case, consider two spherical particles with the same radius, each containing an adsorbed polymer layer with thickness δ. Before overlap, it is possible to define in each polymer layer a chemical potential for the solvent μ_i^α and a volume fraction for the polymer in the layer, ϕ_2.

In the overlap region (volume element dV), the chemical potential of the solvent is reduced to μ_i^β; this results from the increase in polymer segment concentration in the overlap region, where the chemical potential of the polymer chains is now higher than in the rest of the layer (with no overlap). This amounts to an increase in the osmotic pressure in the overlap region, which in turn causes solvent to diffuse from the bulk to the overlap region so as to separate the particles. The strong repulsive energy which arises from this effect can be calculated by considering the free energy of mixing of two polymer solutions, as for example treated by Flory and Krigbaum [6]. The free energy of mixing is given by two terms: (i) an entropy term that depends on the volume fraction of polymer and solvent; and (ii) an energy term that is determined by the Flory–Huggins interaction parameter, χ.

By using the above theory it is possible to derive an expression for the free energy of mixing of the two polymer layers (assuming a uniform segment density distribution in each layer) surrounding two spherical particles as a function of the separation distance h between the particles [4]. The expression for G_{mix} is,

$$\frac{G_{mix}}{kT} = \left(\frac{2V_2^2}{V_1}\right)\nu_2^2\left(\frac{1}{2}-\chi\right)\left(\delta-\frac{h}{2}\right)^2\left(3R+2\delta+\frac{h}{2}\right) \tag{2.6}$$

where k is the Boltzmann constant, T is the absolute temperature, V_2 is the molar volume of polymer, V_1 is the molar volume of solvent, and ν_2 is the number of polymer chains per unit area.

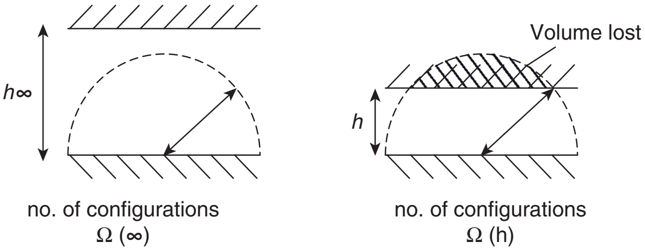

Figure 2.8 Schematic representation of configurational entropy loss on approach of a second particle.

The sign of G_{mix} depends on the value of the Flory–Huggins interaction parameter χ: if $\chi < 0.5$, G_{mix} is positive and the interaction is repulsive, but if $\chi > 0.5$, G_{mix} is negative and the interaction is attractive. If $\chi = 0.5$, $G_{\text{mix}} = 0$, and this defines the θ-condition.

The elastic interaction arises from the loss in configurational entropy of the chains on the approach of a second particle. As a result of this approach, the volume available for the chains becomes restricted, and this results in a loss of the number of configurations. This can be illustrated by considering a simple molecule, represented by a rod that rotates freely in a hemisphere across a surface (Figure 2.8). When the two surfaces are separated by an infinite distance, ∞, the number of configurations of the rod is $\Omega(\infty)$, which is proportional to the volume of the hemisphere. When a second particle approaches to a distance h, such that it cuts the hemisphere (thus losing some volume), the volume available to the chains is reduced and the number of configurations becomes $\Omega(h)$, which is less than $\Omega(\infty)$. For two flat plates, G_{el} is given by the following expression [5]:

$$\frac{G_{\text{el}}}{kT} = 2\nu_2 \ln\left[\frac{\Omega(h)}{\Omega(\infty)}\right] = 2\nu_2 R_{\text{el}}(h) \tag{2.7}$$

where $R_{\text{el}}(h)$ is a geometric function the form of which depends on the segment density distribution. It should be stressed that G_{el} is always positive, and could play a major role in steric stabilization; typically, it becomes very strong when the separation distance between the particles becomes comparable to the adsorbed layer thickness, δ.

It is also possible to define an effective volume fraction ϕ_{eff} that is determined by the ratio of the adsorbed layer thickness δ to the core radius:

$$\phi_{\text{eff}} = \phi\left[1 + \left(\frac{\delta}{R}\right)\right]^3 \tag{2.8}$$

If (δ/R) is small (say for a particle with radius 1000 nm and δ of 10 nm), $\phi_{\text{eff}} \sim \phi$ and the dispersion behaves as near "hard-sphere"; in this case, high ϕ-values can be reached before the system becomes "concentrated." However, if (δ/R) is appreciable (e.g., >0.2 for particles with a radius of 100 nm and δ of 20 nm), then $\phi_{\text{eff}} > \phi$

and the system will show a strong interaction at relatively low ϕ-values. For example, if $\delta = 0.5\phi$, $\phi_{\text{eff}} \sim 3.4\phi$ and the system may be considered concentrated at a core volume fraction of ~0.2.

2.4
van der Waals Attractions

It is well known that atoms or molecules always attract each other at short distances of separation, the attractive forces being of three different types: (i) dipole–dipole interaction (Keesom); (ii) dipole-induced dipole interaction (Debye); and (iii) the London dispersion force. Of these three, the London dispersion force is the most important, as it arises from fluctuations in electron density distribution and occurs for both polar and nonpolar molecules.

At small distances of separation r in vacuum, the attractive energy between two atoms or molecules is given by:

$$G_{\text{aa}} = -\frac{\beta_{11}}{r^6} \tag{2.9}$$

where β_{11} is the London dispersion constant.

For colloidal particles which are made from atom or molecular assemblies, the attractive energies may be added, and this results in the following expression for two spheres (at small h) [7]:

$$G_{\text{A}} = -\frac{A_{11(2)}R}{12\,h} \tag{2.10}$$

where $A_{11(2)}$ is the effective Hamaker constant of two identical particles with Hamaker constant A_{11} in a medium with Hamaker constant A_{22}. When the particles are dispersed in a liquid medium, the van der Waals attractions have to be modified to take into account the medium effect. For example, when two particles are brought from infinite distance to h in a medium, an equivalent amount of medium must be transported in the other direction. Hamaker forces in a medium are excess forces.

Consider two identical spheres 1 at a large distance apart in a medium 2, as illustrated in Figure 2.9a; in this case, the attractive energy is zero. Figure 2.9b shows the same situation, with the arrows indicating the exchange of 1 against 2. Figure 2.9c demonstrates the complete exchange, which now shows the attraction between the two particles 1 and 1 and equivalent volumes of the medium 2 and 2.

The effective Hamaker constant for two identical particles 1 and 1 in a medium 2 is given by:

$$A_{11(2)} = A_{11} + A_{22} - 2A_{12} = \left(A_{11}^{1/2} - A_{22}^{1/2}\right)^2 \tag{2.11}$$

Equation 2.8 shows that two particles of the same material attract each other unless their Hamaker constant exactly matches each other. The Hamaker constant of any material is given by:

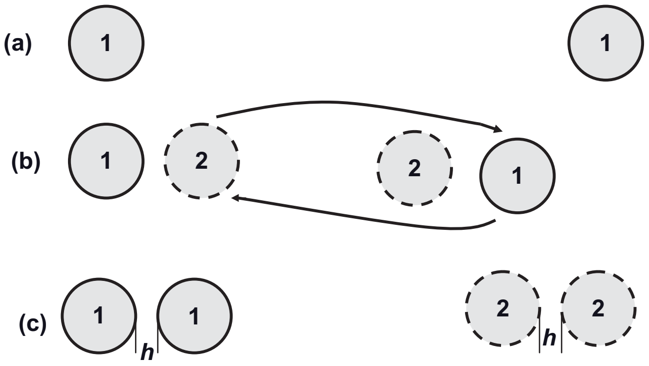

Figure 2.9 Schematic representation of the interaction of two particles in a medium.

Table 2.2 Hamaker constants of some liquids.

Liquid	$A_{22} \times 10^{20}$ J
Water	3.7
Ethanol	4.2
Decane	4.8
Hexadecane	5.2
Cyclohexane	5.2

Table 2.3 Effective Hamaker constant $A_{11(2)}$ of some particles in water.

System	$A_{11(2)} \times 10^{20}$ J
Fused quartz/water	0.83
Al_2O_3/water	5.32
Copper/water	30.00
Poly(methylmethacrylate)/water	1.05
Poly(vinylchloride)/water	1.03
Poly(tetrafluoroethylene)/water	0.33

$$A = \pi q^2 \beta_{11} \tag{2.12}$$

where q is number of atoms or molecules per unit volume.

In most cases, the Hamaker constant of the particles is higher than that of the medium. Examples of Hamaker constant for some liquids are given in Table 2.2, while values of the effective Hamaker constant for some particles in some liquids are listed in Table 2.3. Generally speaking, the effect of the liquid medium is to reduce the Hamaker constant of the particles below its value in vacuum (air).

As shown in Figure 2.1d, V_A increases very sharply with h at small h values. A capture distance can be defined at which all the particles become strongly attracted to each other (coagulation).

2.5
Combination of Interaction Forces

The combination of G_{el} and G_A results in the well-known theory of stability of colloids [the Derjaguin–Landau–Verwey–Overbeek (DLVO) theory] [8, 9]:

$$G_T = G_{el} + G_A \tag{2.13}$$

A plot of G_T versus h is shown in Figure 2.10, which represents the case at low electrolyte concentrations – that is, with a strong electrostatic repulsion between the particles. G_{el} decays exponentially with h; that is, $G_{el} \rightarrow 0$ as h becomes large, while G_A is ∞ $1/h$, so that G_A does not decay to 0 at large h.

At long distances of separation, $G_A > G_{el}$, which will result in a shallow minimum (secondary minimum); however, at very short distances, $G_A \gg G_{el}$, this will result in a deep primary minimum. At intermediate distances, $G_{el} > G_A$, the result will be an energy maximum, G_{max}, the height of which will depend on ψ_o (or ψ_d) and the electrolyte concentration and valency.

At low electrolyte concentrations ($<10^{-2}$ mol dm^{-3} for a 1 : 1 electrolyte), G_{max} is high ($>25\,kT$), and this prevents particle aggregation into the primary minimum. Thus, the higher the electrolyte concentration (and the higher the valency of the ions), the lower the energy maximum.

Under some conditions (depending on electrolyte concentration and particle size), flocculation into the secondary minimum may occur, although such flocculation will be weak and reversible. By increasing the electrolyte concentration, however, G_{max} will be decreased until, at a given concentration, it vanishes and

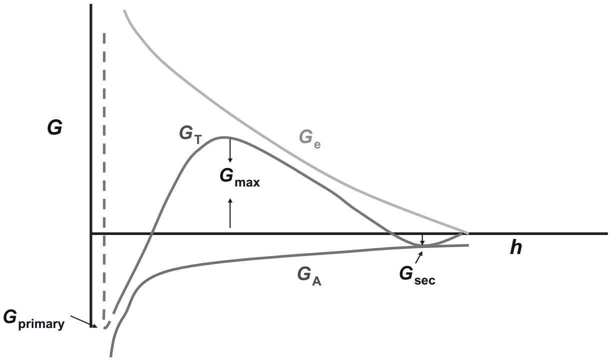

Figure 2.10 Schematic representation of the variation of G_T with h according to the Derjaguin–Landau–Verwey–Overbeek (DLVO) theory.

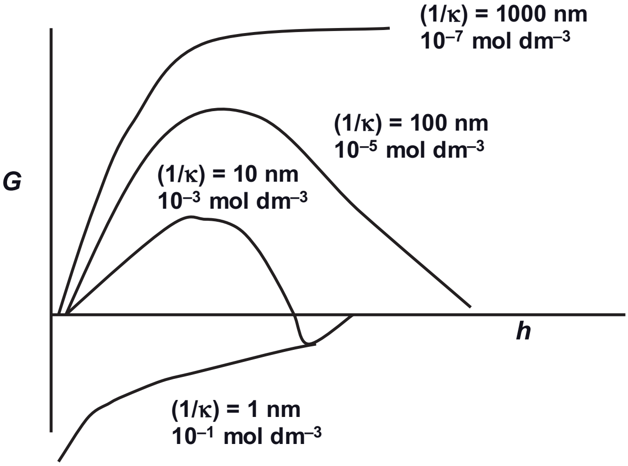

Figure 2.11 Variation of G with h at various electrolyte concentrations.

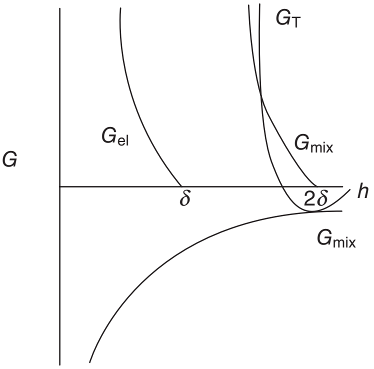

Figure 2.12 Energy–distance curves for sterically stabilized systems.

particle coagulation occurs. This situation is illustrated in Figure 2.11, which shows the variation of G_T with h at various electrolyte concentrations.

The combination of G_{mix} and G_{el} with G_A (the van der Waals attractive energy) gives the total free energy of interaction G_T (assuming that there is no contribution from any residual electrostatic interaction); that is:

$$G_T = G_{mix} + G_{el} + G_A \tag{2.14}$$

A schematic representation of the variation of G_{mix}, G_{el}, G_A and G_T with surface-surface separation distance h is shown in Figure 2.12. In this case, G_{mix} increases very sharply with a decrease in h, when $h < 2\delta$. Likewise, G_{el} increases very sharply with a decrease in h, when $h < \delta$, while G_T versus h shows a minimum, G_{min}, at separation distances comparable to 2δ. When $h < 2\delta$, G_T shows a rapid increase with any decrease in h.

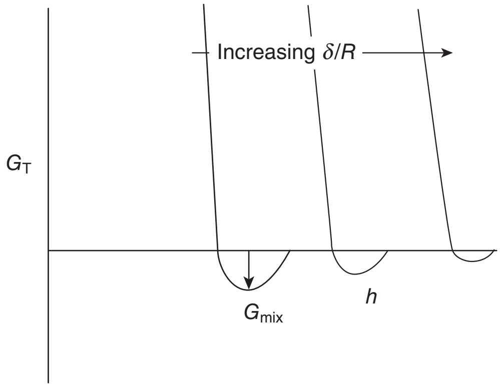

Figure 2.13 Variation of G_T with h at various δ/R values.

The depth of the minimum depends on the Hamaker constant A, the particle radius R, and the adsorbed layer thickness, δ. G_{min} increases with increase of A and R such that, at a given A and R, G_{min} will increase with a decrease in δ (i.e., with decrease of the molecular weight, M_w, of the stabilizer). This effect is illustrated graphically in Figure 2.13, which shows the energy–distance curves as a function of δ/R; typically, the larger the value of δ/R, the smaller the value of G_{min}. In this case, the system may approach thermodynamic stability, as is the case with nanodispersions.

The combination of electrostatic repulsion, steric repulsion and van der Waals attractions is referred to as "electrosteric stabilization," and this is the case when using a mixture of ionic and nonionic stabilizers, or when using polyelectrolytes. In this case, the energy–distance curve has two minima, one shallow maximum (corresponding to the DLVO type), and a rapid increase at small h corresponding to steric repulsion; this is illustrated in Figure 2.14.

2.6
Flocculation of Dispersions, and Its Prevention

Flocculation is the result of van der Waals attractions that is universal for all disperse systems. The van der Waals attractions, G_A, are inversely proportional to the particle–particle distance of separation h, and depends on the effective Hamaker constant A of the suspension. One way to overcome the van der Waals attractions is by electrostatic stabilization using ionic surfactants; this results in the formation of electrical double layers that introduce a repulsive energy which overcomes the attractive energy. Suspensions stabilized by electrostatic repulsion become flocculated at intermediate electrolyte concentrations (see below).

The second – and most effective – method of overcoming flocculation is by "steric stabilization," using nonionic surfactants or polymers. In this case, stability may

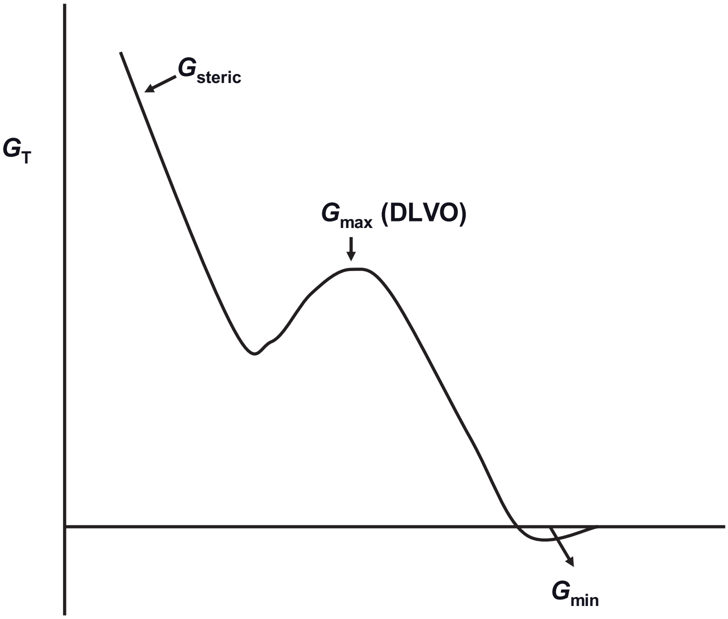

Figure 2.14 Energy–distance curve for electrosteric stabilization.

be maintained in electrolyte solutions (up to 1 mol dm^{-3}, depending on the nature of the electrolyte) and up to high temperatures (in excess of 50 °C), provided that the stabilizing chains [e.g., poly(ethylene oxide); PEO] are still in better than θ-conditions ($\chi < 0.5$).

2.6.1
Mechanism of Flocculation

Flocculation can occur if the energy barrier is small or absent (for electrostatically stabilized dispersions), or when the stabilizing chains reach poor solvency (for sterically stabilized dispersions, i.e., $\chi > 0.5$). At this point, for convenience, the flocculation of electrostatically and sterically stabilized suspensions will be discussed separately.

2.6.1.1 Flocculation of Electrostatically Stabilized Suspensions

As noted above, the condition for kinetic stability is $G_{max} > 25\,kT$, but when $G_{max} < 5\,kT$, flocculation occurs.

Two types of flocculation kinetics may be distinguished: (i) *fast flocculation* with no energy barrier; and (ii) *slow flocculation* when an energy barrier exists. The kinetics of fast flocculation was treated by Smoluchowski [10], who considered the process to be represented by second-order kinetics and the process simply to be diffusion-controlled.

Table 2.4 Half-life of dispersion flocculation.

R (µm)	**$\phi = 10^{-5}$**	**$\phi = 10^{-2}$**	**$\phi = 10^{-1}$**	**$\phi = 5 \times 10^{-1}$**
0.1	765 s	76 ms	7.6 ms	1.5 ms
1.0	21 h	76 s	7.6 s	1.5 s
10.0	4 months	21 h	2 h	25 min

The number of particles n at any time t may be related to the initial number (at $t = 0$) n_o :

$$n = \frac{n_o}{1 + kn_o t} \tag{2.15}$$

where k is the rate constant for fast flocculation that is related to the diffusion coefficient of the particles D; that is:

$$k = 8\pi DR \tag{2.16}$$

where D is given by the Stokes–Einstein equation:

$$D = \frac{kT}{6\pi\eta R} \tag{2.17}$$

By combining Equations 2.16 and 2.17,

$$k = \frac{4}{3}\frac{kT}{\eta} = 5.5 \times 10^{-18}\ \mathrm{m^3\,s^{-1}} \text{for water at } 25\,^{\circ}\mathrm{C} \tag{2.18}$$

The half life $t_{1/2}$ ($n = (1/2)\ n_o$) can be calculated at various n_o or volume fraction ϕ, as given in Table 2.4.

The slow flocculation kinetics was treated by Fuchs [11] , who related the rate constant k to the Smoluchowski rate by the stability ratio W:

$$W = \frac{k_o}{k} \tag{2.19}$$

where W is related to $G_{\max}$ by the following expression [12]:

$$W = \frac{1}{2}\exp\left(\frac{G_{\max}}{kT}\right) \tag{2.20}$$

Since $G_{\max}$ is determined by the salt concentration C and valency, it is possible to derive an expression relating W to C and Z:

$$\log W = -2.06 \times 10^9 \left(\frac{R\gamma^2}{Z^2}\right) \log C \tag{2.21}$$

where γ is a function that is determined by the surface potential ψ_o,

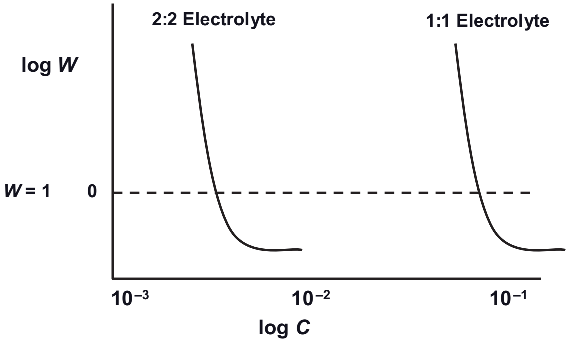

Figure 2.15 Log *W*–log *C* curves.

$$\gamma = \left[\frac{\exp(Ze\psi_{\mathrm{o}}/kT) - 1}{\exp(ZE\psi_{\mathrm{o}}/kT) + 1} \right] \tag{2.22}$$

Plots of log W versus log C are shown in Figure 2.15 for 1 : 1 and 2 : 2 electrolytes.

The condition log $W = 0$ ($W = 1$) is the onset of fast flocculation; the electrolyte concentration at this point defines the critical flocculation concentration (CFC). Above the CFC, $W < 1$ (due to the contribution of van der Waals attractions, which accelerate the rate above the Smoluchowski value). Below the CFC, $W > 1$, and this increases with a decrease in electrolyte concentration. It can also be seen from Figure 2.15 that the CFC decreases with an increase of valency, in accordance with the Schultze–Hardy rule.

Weak (Reversible) Flocculation Another mechanism of flocculation is that involving the secondary minimum (G_{min}) which is a few kT units. In this case, flocculation is weak and reversible, and hence both the rate of flocculation (forward rate k_{f}) and deflocculation (backward rate k_{b}) must be considered. The rate of decrease of particle number with time is given by the expression:

$$-\frac{dn}{dt} = -k_{\mathrm{f}} n^2 + k_{\mathrm{b}} n \tag{2.23}$$

The backward reaction (break-up of weak flocs) reduces the overall rate of flocculation.

Orthokinetic (Shear-Induced) Flocculation Another process of flocculation that occurs under shearing conditions is referred to as “orthokinetic” (to distinguish it from the diffusion-controlled perikinetic process). In this case, the rate of flocculation is related to the shear rate by the expression:

$$-\frac{dn}{dt} = \frac{16}{3} \alpha^2 \dot{\gamma} R^3 \tag{2.24}$$

where α is the collision frequency, that is, the fraction of collisions that result in permanent aggregates.

2.6.1.2 **Flocculation of Sterically Stabilized Dispersions**

Flocculation can be weak and reversible or strong and irreversible, depending on the magnitude of the attractive energy. Weak flocculation can occur when the thickness of the adsorbed layer becomes small, such that the attractive minimum (G_{min}) in the energy–distance curve reaches several kT units for weak flocculation to occur. Strong flocculation occurs when the solvency of the medium for the chains reaches the θ-point (i.e., the Flory–Huggins interaction parameter $\chi > 0.5$). This situation results in catastrophic flocculation, referred to as "incipient flocculation."

Weak Flocculation The G_T–h for systems that are sterically stabilized show only one minimum, G_{min}, followed by sharp increase in G_T with a decrease in h (when $h < 2\delta$). The depth of the minimum depends on the Hamaker constant A, the particle radius R, and adsorbed layer thickness δ, while G_{min} increases with increases of both A and R. At a given A and R, G_{min} will increase with a decrease in δ (i.e., with a decrease of the molecular weight, M_w, of the stabilizer. This was illustrated in Figure 2.13, which shows the energy–distance curves as a function of δ/R; in this case, the smaller the value of δ/R, the larger was the value of G_{min}. When G_{min} reached a critical value which depended on the volume fraction of the suspension, a weak flocculation occurred. However, such flocculation was reversible and, when the suspension was gently stirred, the particles became dispersed. On removal of the shear force, however, flocculation occurred.

Incipient Flocculation This occurs when the solvency of the medium for the chain becomes worse than a θ-solvent ($\chi > 0.5$). Under these conditions, G_{mix} becomes negative; that is, an attractive and a deep minimum is produced which results in catastrophic flocculation (this is referred to as "incipient flocculation"), as shown schematically in Figure 2.16.

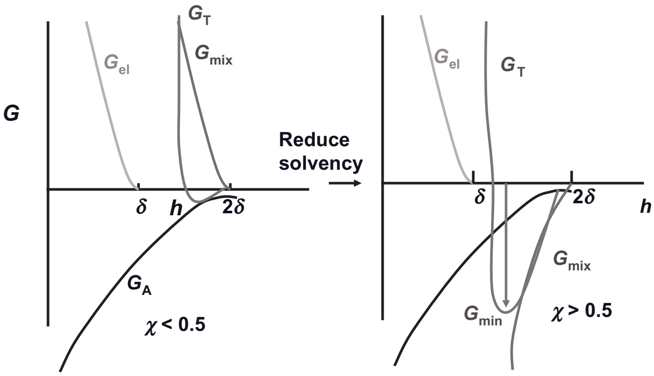

Figure 2.16 Schematic representation of the flocculation of sterically stabilized emulsions.

With many systems, a good correlation between the flocculation point and the θ point is obtained. For example, the suspension will flocculate at a temperature (referred to as the critical flocculation temperature, CFT) that is equal to the θ-temperature of the stabilizing chain. The suspension may flocculate at a critical volume fraction (CVF) of a nonsolvent, which is equal to the volume of nonsolvent that brings it to a θ-solvent.

2.6.1.3 Bridging or Charge Neutralization by Polymers

Bridging flocculation occurs under conditions of incomplete coverage of the particles by the polymer chains [13]. Segments of a polymer chain may adsorb onto different particles, causing them to link together. Such adsorption is an essential step, and requires certain favorable interactions between the polymer segments and the particle surface. Typical polymeric flocculants have molecular dimensions comparable to the size of colloidal particles (0.1–1 μm). Typically, the flocs produced by polymer bridging are considerably stronger than aggregates formed by the coagulation of dispersions by electrolytes.

With polyelectrolytes, however, the picture is more complicated as the dimensions of the polyelectrolyte chains depend on the ionic strength. At low ionic strength, screening of the charges on the chains is limited and the polyelectrolyte adopts an extended configuration, which makes bridging more likely. However, at a high ionic strength, screening of the charge produces a more compact configuration, thus reducing the chance of bridging. Yet, increasing the electrolyte concentration also results in a reduction in the range of interparticle repulsion, such that compact chains could still bridge the particles.

At a high electrolyte concentration, the adsorption of polyelectrolytes with the same charge sign on the particle surface is enhanced, and this also increases the likelihood of bridging.

Polyelectrolytes with a charge opposite to that of the particles are very effective in the flocculation of dispersions. With oppositely charged polyelectrolytes, it is likely that adsorption provides a rather flat configuration of the adsorbed chain, as a result of the strong electrostatic interaction between the ionic groups on the polyelectrolyte chain and charge sites on the surface; this most likely reduces the probability of bridging. The electrostatic-patch model can explain the flocculation by polyelectrolytes, since patches of excess positive charge, which correspond to the adsorbed polyelectrolyte chains (possibly in a flat configuration), are surrounded by areas of negative charge, representing the original particle surface. Those particles which have this patchy or mosaic-type surface may interact in such a way that positive and negative patches come in contact, providing a quite strong attachment (though not a strong as bridging flocculation).

2.6.2
General Rules for Reducing (Eliminating) Flocculation

The general rules for reducing (or even eliminating) flocculation include the following:

- **Charge-stabilized suspensions:** Examples include the use of ionic surfactants, where the most important criterion is to make $G_{\max}$ as high as possible. The condition for a high kinetic stability is $G_{\max} > 25\,kT$; this can be achieved by three main conditions: (i) a high surface or zeta potential; (ii) a low electrolyte concentration; and (iii) a low valency of ions.

- **Sterically stabilized suspensions:** In this case, four main criteria are necessary: (i) Complete coverage of the particles by the stabilizing chains; (ii) A firm attachment (strong anchoring) of the chains to the particles or droplets. This requires the chains to be insoluble in the medium and have a strong affinity to the surface. However, this is incompatible with stabilization, which requires a chain that is soluble in the medium and strongly solvated by its molecules. These conflicting requirements are overcome by the use of A–B, A–B–A block or BA_n graft copolymers (where B is the "anchor" chain and A is the stabilizing chain(s)). Examples of the B chains for hydrophobic particles include polystyrene, poly(methylmethacrylate) (PMMA), poly(propylene oxide) (PPO) and alkyl polypropylene oxide. For the A chain(s), poly(ethylene oxide) (PEO) or poly(vinyl alcohol) (PVA) are good examples; (c) Thick adsorbed layers, where the adsorbed layer thickness should be in the region of 5–10 nm. This means that the molecular weight of the stabilizing chains could be in the region of 1000–5000 Da; (iv) The stabilizing chain should be maintained in good solvent conditions ($\chi < 0.5$) under all conditions of temperature changes on storage.

2.7
Distinction between "Dilute," "Concentrated," and "Solid" Dispersions

A possible distinction between "dilute," "solid," and "concentrated" dispersion may be made by considering the balance between the thermal (or Brownian) motion and the hydrodynamic and interparticle interaction [14, 15]. If Brownian diffusion predominates over the effect of hydrodynamic interaction, then the dispersion may be considered "dilute." In this case, the distance between the particle surfaces is large compared to the range of the interaction forces (hydrodynamic or surface). For "dilute" dispersions, the particle interactions can be represented by two-body collisions when, provided that the gravitational force can be neglected (i.e., no settling occurs), the properties of such "dilute" dispersions are essentially time-independent. Any time-average quantity, such as light scattering, osmotic pressure and viscosity, may be extrapolated to infinite dilution so as to obtain the fundamental properties of the system, such as the particle or hydrodynamic radius.

As the particle number concentration in a dispersion is increased, the volume of space occupied by the particles relative to the total volume (i.e., the volume fraction, ϕ) is increased, such that a proportion of space is excluded in terms of its occupancy by any single particle. The probability of particle–particle interaction, both hydrodynamic and surface, is then increased. The hydrodynamic and surface forces play dominant roles in determining the properties of the system, such as its structure in space and its flow characteristics. With a gradual increase in particle number concentration, however, a situation is reached whereby the interparticle distances become relatively small compared to the particle radius; in this case, the system is referred to as a "solid" suspension. Any particle in the system can interact with many neighbors, and the repulsive interactions produce a specific order between the particles, to the extent that a highly developed structure is reached. However, when the spacing between the particles is very small, they can only undergo vibration with an amplitude smaller to the particle radius. This system will behave like a "solid," and show an elastic response but will not demonstrate any time-dependence of its properties. The above system is conveniently referred to as a "solid suspension" (e.g., the "green body" in ceramics).

Between the above two extremes of "dilute" and "solid" suspensions, it is possible to define a "concentrated" suspension [14, 15], where the volume fraction ϕ is sufficiently high for many-body interactions to occur. Both, hydrodynamic and surface interactions play a major role in determining the properties of the system. The interparticle distances are comparable to the particle size, and this allows the particles to diffuse (albeit slowly), while the properties of the system show time-dependence. The particle arrangements also show spatial correlations; that is, the position of one particle in space becomes determined by the position of the other particles in the neighborhood. The diffusion coefficient of the particles become a strong function of the volume fraction; that is, the system shows temporal correlations.

In order to understand the property of any dispersion, it is important to consider the arrangement of the particles in the system, whether a random arrangement with free diffusion, dilute or "vapor-like," loosely ordered with restricted diffusion, concentrated or "liquid-like," highly ordered, solid, or "crystal-like."

The microstructure of the dispersion may be investigated using either small-angle X-ray scattering (SAXS) or neutron scattering. When the microstructure of the system is understood, it is possible to recognize exactly how the interparticle interactions influence the macrostructure of the system, such as its osmotic pressure and rheology.

One convenient method to describe the structure of the suspension is to use the radial distribution function $g(r)$. If a system containing N_p particles in a volume V is considered, then the average macroscopic density, ρ_o, is expressed by:

$$\rho_\mathrm{o} = \frac{N_\mathrm{p}}{V} \tag{2.25}$$

If the container is examined more closely on a microscopic scale, it is possible to obtain the distribution of particles around any reference particle, as illustrated in Figure 2.17. In the immediate vicinity of the central particle, there is a space in which the particle density is zero. However, with an increasing distance r from the center of the chosen particle, the number of particles with their centers in any shell of thickness dr will vary.

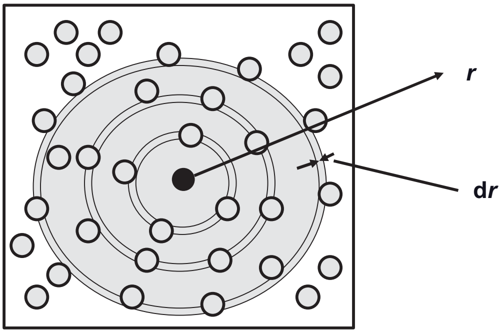

Figure 2.17 Microscopic view (schematic) of the distribution of particles around a central particle.

It is possible to define a number density $\rho(r)$ which varies with r and which describes the distribution of particles. This density function will have two limiting values:

$\rho(r) \to 0$ as $r \to 2R$ (where R is the particle radius); $\rho(r) \to \rho_o$ as $r \to \infty$.

The pair distribution function, $g(r)$ can be defined as:

$$g(r) = \frac{\rho(r)}{\rho_o} \tag{2.26}$$

which has the properties $g(r) \to 0$ as $r \to 2R$ and $g(r) \to 1$ as $r \to \infty$. $g(r)$ is directly related to the potential $\phi(r)$ of mean force acting between the particles,

$$g(r) = \exp-\left(\frac{\phi(r)}{kT}\right) \tag{2.27}$$

$$\phi(r) = V(r) + \psi(r) \tag{2.28}$$

where $V(r)$ is the simple pair potential and $\psi(r)$ is a perturbation term that takes into account the effect of many-body interactions.

For very dilute systems, with particles undergoing Brownian motion, the distribution will be random, and only occasional contacts will occur between the particles; that is, there will be only pairwise interaction ($\psi(r) = 0$). In this case, $g(r)$ will increase rapidly from the value of zero at $r = 2R$ to its maximum value of unity beyond the first shell (Figure 2.18a). With such dilute systems ("vapor-like"), no structure develops.

For "solid" suspensions, $g(r)$ shows distinct, sharp peaks similar to those observed with atomic and molecular crystals (Figure 2.18c). For "concentrated dispersions" ("liquid-like"), $g(r)$ shows the form represented in Figure 2.18b; this consists of a pronounced first peak, followed by a number of oscillatory peaks damping to unity beyond four or five particle diameters. On proceeding outwards from the first shell, the peaks become broader, while the dependence of $g(r)$ on r for colloidal dispersions can be determined by using scattering techniques.

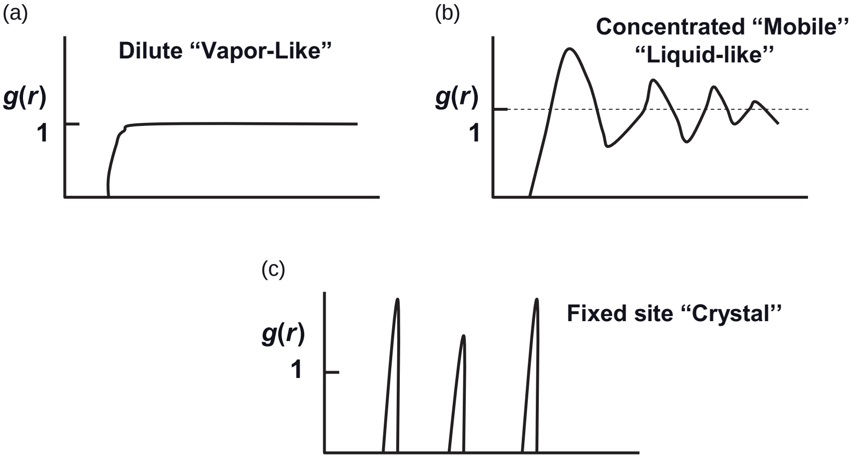

Figure 2.18 Radial distribution function for (a) "dilute," (b) "concentrated," and (c) "solid" suspensions.

2.8
States of Suspension on Standing

Several states can be identified (see Figure 2.19) which depend on:

- The magnitude and balance of the various interaction forces.
- The particle size distribution and density difference between the dispersed particles and the medium.
- The conditions and prehistory of the suspension, for example, agitation which determines the structure of the flocs formed (chain aggregates, compact clusters, etc.).
- The presence of additives in the formulation; for example, high-molecular-weight polymers may cause bridging or depletion flocculation.

All of the above factors can determine the flow characteristics or rheology of the system.

In Figure 2.19, states (a) to (c) represent the case for colloidally stable suspensions:

- *Small particles* (nanoparticles), whereby the Brownian diffusion overcomes the gravity force (Figure 2.19a).
- *Large uniform particles* (>1 μm) (Figure 2.19b) which settle individually under gravity to form a very compact sediment at the bottom of the container. These compact sediments (which are dilatant) are very difficult to redisperse, and must be prevented.

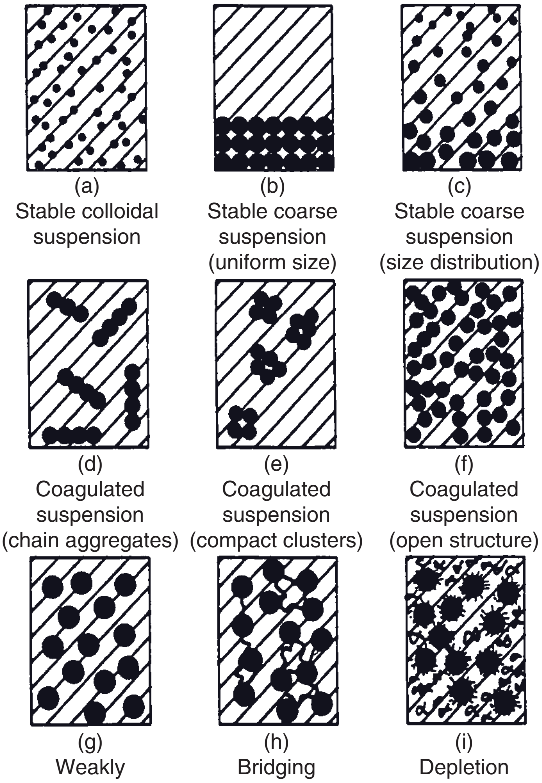

Figure 2.19 States of the suspension.

- *Large particles with size distribution* (Figure 2.19c); the larger particles may settle to form a hard sediment, leaving the smaller particles suspended in the top of the container.

In Figure 2.19d–f, the states represent the situation with very strong attraction (coagulation):

- *Chain aggregates* are produced under conditions of minimum agitation (Figure 2.19d). These aggregates may settle to form a sediment with an "open" structure.
- *Compact clusters* (Figure 2.19e) are produced for coagulated suspensions under conditions of agitation. The compact clusters may settle to form a "compact" sediment.
- A strong "*gel network*" may be formed at high particle volume fraction (Figure 2.19f). Here, the particles may aggregate in chains, while cross-chains may form a "one-floc" system which that undergo syneresis.

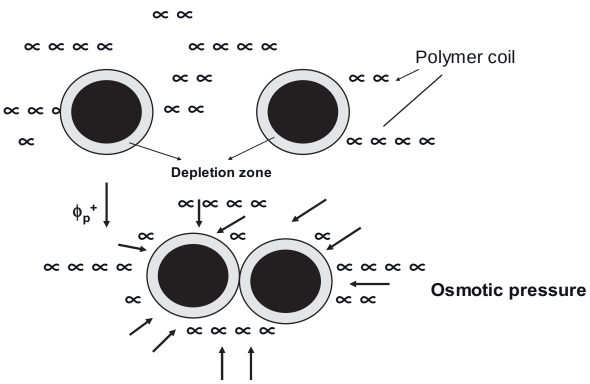

Figure 2.20 Schematic representation of depletion flocculation.

In Figure 2.19g–i, the states represent the case of relatively weak flocculation:

- The *weak flocculation* of particles can result in the formation of a "three-dimensional" (3-D) weak gel which could be fluidized by shaking. This weak gel can be applied to reduce sedimentation, and may also provide interesting rheological characteristics (e.g., thixotropy).
- *Bridging flocculation*; when using high-molecular-weight nonionic polymers, which are only weakly attached to the particles, bridging can produce a weak "gel-network" that may also be useful in some applications.
- *Depletion flocculation* [16, 17]; this results when using a "free" (nonadsorbing) polymer. When the concentration of the polymer exceeds a certain critical concentration (which depends on the molecular weight of the polymer), the chains are "squeezed out" from between the particles. As a consequence, the osmotic pressure outside the particle surfaces is higher than in between the particles, and this results in weak attraction. A schematic representation of depletion flocculation if given in Figure 2.20.

2.9
States of the Emulsion on Standing

Emulsions show similar characteristics to suspensions, including sedimentation (when the density of the disperse phase is higher than the medium), flocculation, and Ostwald ripening (disproportionation) [18, 19]. However, they differ from suspensions in three aspects, namely *creaming* (when the density of the disperse phase, e.g., oil, is lower than that of the medium), *coalescence*, and *phase inversion*. A schematic representation of emulsion states on storage is shown in Figure 2.21.

The physical phenomena involved in each breakdown process is not simple, and requires an analysis of the various surface forces involved. In addition, the

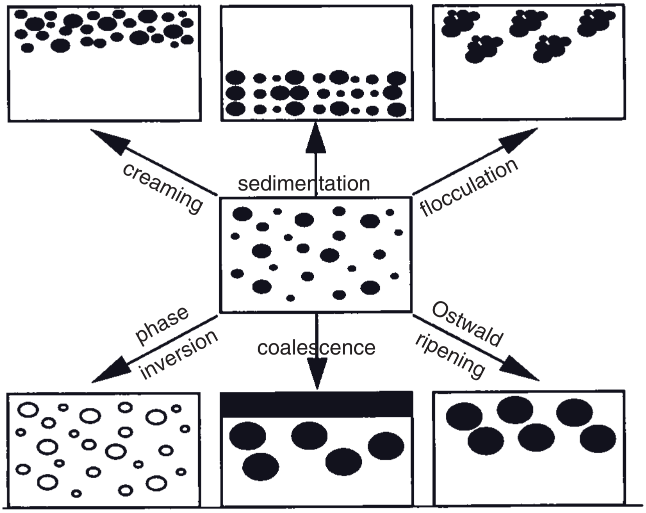

Figure 2.21 Schematic representation of emulsions on standing.

above-described processes may take place simultaneously rather than consecutively, which further complicates the analysis. Model emulsions, with monodisperse droplets cannot be easily produced, and hence any theoretical treatment must take into account the effect of droplet size distribution. Theories that take into account the polydispersity of the system are complex, and in many cases only numerical solutions are possible. In addition, measurements of surfactant and polymer adsorption in an emulsion are not easily made, and it is necessary to extract such information from measurements at a planar interface.

A summary of each of the above breakdown processes is provided in the following sections.

2.9.1
Creaming and Sedimentation

This process results from external forces which, usually, are either gravitational or centrifugal. When such forces exceed the thermal motion of the droplets (Brownian motion), a concentration gradient builds up in the system such that the larger droplets move more rapidly either to the top of the container (if their density is less than that of the medium) or to the container bottom (if their density is greater than that of the medium). In the limiting cases, the droplets may form a close-packed (random or ordered) array at the top or bottom of the system, with the remainder of the volume occupied by the continuous liquid phase:

$$C(h) = C_o \exp\left(-\frac{mgh}{kT}\right) \tag{2.29}$$

where $C(h)$ is the concentration (or volume fraction ϕ) of droplets at height h, whereas C_o is the concentration at zero time, which is the same at all heights.

Several methods may be applied to prevent creaming or sedimentation of emulsions:

- *Matching density of oil and aqueous phases*: Clearly, if $\Delta\rho = 0$, the rate of sedimentation $v = 0$. However, this method is seldom practical. Density matching, if possible, occurs only at one temperature.
- *Reduction of droplet size*: As the gravity force is proportional to R^3, then if R is reduced by a factor of 10, the gravity force is reduced by 1000. Below a certain droplet size (which also depends on the density difference between oil and water), the Brownian diffusion may exceed gravity, and creaming or sedimentation will be prevented. This principle is employed in the formulation of nanoemulsions (with size range 20–200 nm), which may show very little or no creaming or sedimentation. The same applies to microemulsions (size range 5–50 nm).
- *The use of "thickeners"*: these are high-molecular-weight polymers, both natural and/or synthetic, such as xanthan gum, hydroxyethyl cellulose, alginates, and carrageenans.

In order to understand the role of these "thickeners", it is important to consider the gravitational stresses exerted during creaming or sedimentation:

$$\text{stress} = \text{mass of drop} \times \text{acceleration due to gravity} = \frac{4}{3}\pi R^3 \Delta\rho g \tag{2.30}$$

In order to overcome such stress, a restoring force is required:

$$\text{Restoring force} = \text{area of drop} \times \text{stress of drop} = 4\pi R^2 \sigma_p \tag{2.31}$$

Thus, the stress exerted by the droplet σ_p is given by:

$$\sigma_p = \frac{\Delta\rho R g}{3} \tag{2.32}$$

A simple calculation shows that σ_p is in the range 10^{-3} to 10^{-1} Pa; this implies that, in order to predict creaming or sedimentation, it is necessary to measure the viscosity at such low stresses. This can be achieved by using constant stress or creep measurements (these are discussed in Chapter 4).

2.9.2
Flocculation

Flocculation is the result of van der Waals attractions that is universal for all disperse systems. As described previously, the van der Waals attractions, G_A (see Figure 2.1c) are inversely proportional to the droplet–droplet distance of separation h, and depend on the effective Hamaker constant A of the emulsion system. One way of overcoming the van der Waals attractions is by electrostatic stabilization using ionic surfactants; this results in the formation of electrical double layers that introduce a repulsive energy that overcomes the attractive energy. Emulsions stabilized by electrostatic repulsion then become flocculated at intermediate electrolyte concentrations. The second and most effective method of overcoming flocculation is by "steric stabilization," using nonionic surfactants or polymers. In this case, stability may be maintained in electrolyte solutions (as high as $1\,\mathrm{mol\,dm^{-3}}$, depending on the nature of the electrolyte) and up to high temperatures (in excess of 50 °C), provided that the stabilizing chains (e.g., PEO) are still in better than θ-conditions ($\chi < 0.5$).

2.9.3
Ostwald Ripening (Disproportionation)

The driving force for Ostwald ripening is the difference in solubility between the small and large droplets (the smaller droplets have a higher Laplace pressure and a higher solubility than their larger counterparts). This is illustrated in Figure 2.22, where r_1 decreases and r_2 increases as a result of diffusion of molecules from the smaller to the larger droplets.

The difference in chemical potential between the different-sized droplets was given by Kelvin [20]:

$$S(r) = S(\infty)\exp\left(\frac{2\gamma V_\mathrm{m}}{rRT}\right) \tag{2.33}$$

where $S(r)$ is the solubility surrounding a particle of radius r, $S(\infty)$ is the bulk solubility, V_m is the molar volume of the dispersed phase, R is the gas constant, and T is the absolute temperature. The quantity $(2\gamma V_\mathrm{m}/RT)$, termed the "characteristic length," has an order of ~1 nm or less, indicating that the difference in solubility of a 1 μm droplet is of the order of 0.1%, or less. Although, in theory, Ostwald ripening should lead to the condensation of all droplets into a single drop,

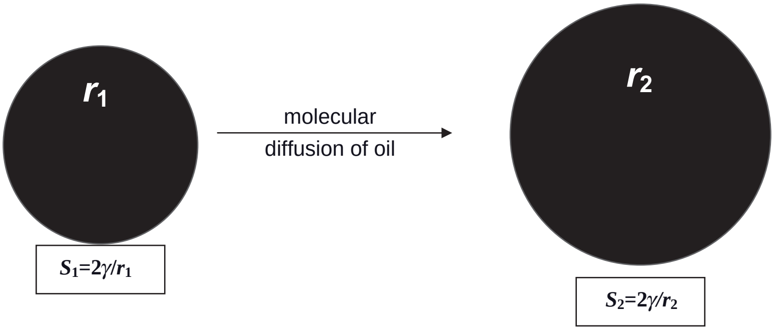

Figure 2.22 Schematic representation of Ostwald ripening.

this does not occur in practice as the rate of growth decreases with an increase of droplet size.

Typically, for two droplets with radii r_1 and r_2 ($r_1 < r_2$),

$$\frac{RT}{V_m}\ln\left[\frac{S(r_1)}{S(r_2)}\right]=2\gamma\left[\frac{1}{r_1}-\frac{1}{r_2}\right] \tag{2.34}$$

Equation 2.34 shows that the larger the difference between r_1 and r_2, the higher the rate of Ostwald ripening.

Ostwald ripening can be quantitatively assessed from plots of the cube of the radius versus time t [21, 22],

$$r^3=\frac{8}{9}\left[\frac{S(\infty)\gamma V_m D}{\rho RT}\right]t \tag{2.35}$$

where D is the diffusion coefficient of the disperse phase in the continuous phase, and ρ is the density of the disperse phase.

Several methods may be applied to reduce Ostwald ripening [23, 24]:

- The addition of a second disperse phase component which is insoluble in the continuous medium (e.g., squalane). In this case, partitioning between different droplet sizes occurs, with the component having a low solubility expected to be concentrated in the smaller droplets. During Ostwald ripening in a two-component system, equilibrium is established when the difference in chemical potential between different-sized droplets (which results from curvature effects) is balanced by the difference in chemical potential resulting from partitioning of the two components. This effect reduces further the growth of droplets.

- Modification of the interfacial film at the oil/water interface. According to Equation 2.35, a reduction in γ will result in a reduction of the Ostwald ripening rate. By using surfactants that are strongly adsorbed at the oil/water interface (i.e., polymeric surfactants), and which are not desorbed during ripening (by selecting a molecule that is insoluble in the continuous phase), the rate could be significantly reduced. An increase in the surface dilational modulus ε ($=d\gamma/d\ln A$) and a decrease in γ would be observed for the shrinking drop, and this would tend to reduce further growth.

A–B–A block copolymers such as poly(hydroxystearic acid) (PHS)–PEO–PHS (which is soluble in the oil droplets but insoluble in water) can be used to achieve the above effect. Similar effects can also be obtained using a graft copolymer of hydrophobically modified inulin, namely INUTEC®SP1 (ORAFTI, Belgium). This polymeric surfactant adsorbs with several alkyl chains (which may dissolve in the oil phase), leaving loops and tails of strongly hydrated inulin (polyfructose) chains. The molecule has limited solubility in water, and hence resides at the oil/water interface. These polymeric emulsifiers enhance the Gibbs elasticity, and thus significantly reduce the Ostwald ripening rate.

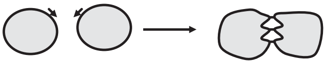

Figure 2.23 Schematic representation of surface fluctuations.

2.9.4
Emulsion Coalescence

When two emulsion droplets come into close contact in a floc or creamed layer, or during Brownian diffusion, then thinning and disruption of the liquid film may occur, resulting in eventual rupture. On close approach of the droplets, film thickness fluctuations may occur or, alternatively, the liquid surfaces may undergo fluctuations to form surface waves (as illustrated in Figure 2.23). The surface waves may grow in amplitude, and the apices may join as a result of the strong van der Waals attractions (at the apex, the film thickness is the smallest). The same applies if the film is thinned to a small value (the critical thickness for coalescence).

A very useful concept was introduced by Derjaguin [25], who suggested that a “disjoining pressure” $\pi(h)$ is produced in the film which balances the excess normal pressure:

$$\pi(h) = P(h) - P_o \tag{2.36}$$

where $P(h)$ is the pressure of a film with thickness h, and P_o is the pressure of a sufficiently thick film such that the net interaction free energy is zero. In this case, $\pi(h)$ may be equated to the net force (or energy) per unit area acting across the film:

$$\pi(h) = -\frac{dG_T}{dh} \tag{2.37}$$

where G_T is the total interaction energy in the film.

Here, $\pi(h)$ is made of three contributions due to electrostatic repulsion (π_E), steric repulsion (π_s), and van der Waals attractions (π_A):

$$\pi(h) = \pi_E + \pi_s + \pi_A \tag{2.38}$$

In order to produce a stable film, $\pi_E + \pi_s > \pi_A$, and this is the driving force for the prevention of coalescence, which can be achieved by two mechanisms and their combination: (i) an increased repulsion, both electrostatic and steric; and (ii) a dampening of the fluctuation by enhancing the Gibbs elasticity. In general, smaller droplets are less susceptible to surface fluctuations, and hence coalescence is reduced. This explains the high stability of nanoemulsions.

Several methods may be applied to achieve the above effects:

- The use of mixed surfactant films (such as anionic and nonionic or long chain alcohols) can, in many cases, reduce coalescence as a result of several effects: a high Gibbs elasticity; a high surface viscosity; and hindered diffusion of the surfactant molecules from the film.

- The formation of lamellar liquid crystalline phases at the oil/water interface. This mechanism was proposed by Friberg and coworkers [26], who suggested that a surfactant or a mixed surfactant film could produce several bilayers that would "wrap" the droplets. As a result of these multilayer structures, the potential drop would be shifted to longer distances, thus reducing the van der Waals attractions. For coalescence to occur, these multilayers would have to be removed "two-by-two," and this would form an energy barrier preventing coalescence.

Just as film drainage and rupture is a kinetic process, so too is coalescence. For example, when measuring the number of particles n (whether flocculated, or not) at time t,

$$n = n_t + n_v m \tag{2.39}$$

where n_t is the number of primary particles remaining, and n_v is the number of aggregates consisting of m separate particles.

When studying emulsion coalescence, it is important to consider the rate constant of flocculation and coalescence. If coalescence is the dominant factor, then the rate K will follow a first-order kinetics,

$$n = \frac{n_o}{Kt}[1 + \exp(-Kt)] \tag{2.40}$$

which shows that a plot of log n versus t should produce a straight line from which K can be calculated.

2.9.5
Phase Inversion

The phase inversion of emulsions may be one of two types: (i) *transitional inversion*, which is induced by changing factors that affect the hydrophilic–lipophilic balance (HLB) of the system, such as the temperature and/or electrolyte concentration; and (ii) *catastrophic inversion*, which is induced by increasing the volume fraction of the disperse phase. Inversion occurs at a critical ϕ, which may be identified with the maximum packing fraction. At ϕ_{cr}, η will suddenly be decreased, as the inverted water-in-oil emulsion will have a much lower volume fraction. The conductivity, κ, also decreases sharply at the inversion point as the continuous phase is now oil.

Earlier theories of phase inversion were based on packing parameters. When φ exceeds the maximum packing (~0.64 for random packing, and ~0.74 for hexagonal packing of monodisperse spheres; for polydisperse systems, the maximum packing exceeds 0.74), then inversion will occur. However, these theories are not adequate, as many emulsions invert at φ-values well below the maximum packing as a result of the change in surfactant characteristics with any variation of conditions. For example, when using a nonionic surfactant based on PEO, the latter chain changes its solvation by an increase of temperature and/or the addition of electrolyte. Many emulsions demonstrate phase inversion at a critical temperature (the phase inversion temperature) which depends on the HLB number of the surfactant, as well as the presence of electrolytes. By increasing the temperature and/or the addition of electrolyte, the PEO chains become dehydrated and finally become more soluble in the oil phase, although under these conditions the oil-in-water emulsion will invert to a water-in-oil emulsion. The above dehydration effect amounts to a decrease in the HLB number such that, when the latter reaches a value that is more suitable for a water-in-oil emulsion, then inversion will occur. At present, however, there is no quantitative theory that accounts for the phase inversion of emulsions.

References

1 Tadros, T.F. (1996) *Adv. Colloids Interface Sci.*, **68**, 97.

2 Gouy, G. (1910) *J. Phys.*, **9** (**4**), 457; Gouy, G. (1917) *Ann. Phys.*, **7** (**9**), 129; Chapman, D.L. (1913) *Phil. Mag.*, **25** (**6**), 475.

3 Stern, O. (1924) *Z. Elektrochem.*, **30**, 508.

4 Bijsterbosch, B.H. (1987) *Solid/Liquid Dispersions* (ed. T.F. Tadros), Academic Press, London, pp. 91–109.

5 Napper, D.H. (1983) *Polymeric Stabilisation of Colloidal Dispersions*, Academic Press, London.

6 Flory, P.J. and Krigbaum, W.R. (1950) *J. Chem. Phys.*, **18**, 1086.

7 Hamaker, H.C. (1937) *Physica*, **4**, 1058.

8 Derjaguin, B.V. and Landau, L. (1941) *Acta Physicochem. USSR*, **14**, 633.

9 Verwey, E.J.W. and Overbeek, J.T.G. (1948) *Theory of Stability of Lyophobic Colloids*, Elsevier, Amsterdam.

10 Smoluchowski, M.V. (1927) *Z. Phys. Chem.*, **92**, 129.

11 Fuchs, N. (1936) *Z. Physik*, **89**, 736.

12 Reerink, H. and Overbeek, J.T.G. (1954) *Disc. Faraday Soc.*, **18**, 74.

13 Gregory, G. (1987) *Solid/Liquid Dispersions* (ed. T.F. Tadros), Academic Press, London, pp. 163–181.

14 Ottewill, R.H. (1985) *Ber. Bunsenges. Phys. Chem.*, **89**, 517.

15 Ottewill, R.H. (1987) *Solid/Liquid Dispersions* (ed. T.F. Tadros), Academic Press, pp. 183–198.

16 Asakura, S. and Osawa, F. (1954) *J. Phys. Chem.*, **22**, 1255.

17 Asakura, S. and Osawa, F. (1958) *J. Polym. Sci.*, **33**, 183.

18 Tadros, T.F. and Vincent, B. (1983) *Encyclopedia of Emulsion Technology* (eds P. Becher), Marcel Dekker, New York.

19 Binks, B.P. (1998) *Modern Aspects of Emulsion Science*, The Royal Society of Chemistry Publication.

20 Thompson, W. (Lord Kelvin) (1871) *Phil. Mag.*, **42**, 448.

21 Lifshitz, I.M. and Slesov, V.V. (1959) *Sov. Phys. JETP*, **35**, 331.

22 Wagner, C. (1961) *Z. Electrochem.*, **35**, 581.

23 Kabalanov, A.S. and Shchukin, E.D. (1992) *Adv. Colloid Interface Sci.*, **38**, 69.

24 Kabalanov, A.S. (1994) *Langmuir*, **10**, 680.

25 Derjaguin, B.V. and Scherbaker, R.L. (1961) *Kolloid Zh.*, **23**, 33.

26 Friberg, S., Jansson, P.O., and Cederberg, E. (1976) *J. Colloid Interface Sci.*, **55**, 614.

3
Principles of Steady-State Measurements

In this chapter, the principles of measurements under steady state will be described. In this case, the dispersion which is placed in the gap between concentric cylinders, cone and plate or parallel plates will be subjected to a constant shear rate until a steady state is reached whereby the stress remains constant. The measurement allows the stress and viscosity to be obtained as a function of the shear rate. Before describing these principles, it is useful to define the stress, strain, strain (shear) rate, and viscosity. The laws of elasticity (Hooke's law) and viscosity (Newton's law) are briefly described, and the reversible time effects of viscosity (thixotropy and dilatancy) are also discussed.

Stress (σ): The deformation produced by a force acting on a material depends on the magnitude of the force per unit area (stress). The units of σ are $\mathrm{Nm^{-2}}$ or Pa (SI units, $\mathrm{kg\,m^{-1}\,s^{-1}}$); σ may also be expressed in $\mathrm{dyne\,cm^{-2}}$ (c.g.s. units). The dimension of the Pa is $\mathrm{kg^{-1}\,s^{-2}}$, and that of the $\mathrm{dyne\,cm^{-2}}$ is $\mathrm{g\,cm^{-1}\,s^{-2}}$; hence, $1\,\mathrm{Pa} = 10\,\mathrm{dyne\,cm^{-2}}$.

Strain (γ): A stress, when applied to a material, results in its deformation. This is illustrated in Figure 3.1, which shows a schematic representation of the deformation of a material represented by ABC when a stress σ is applied. The material acquires a new shape, A′B′C′. Note that AB ≠ A′B′; AC ≠ A′C′; ABC ≠ A′B′C′.

In simple shear strain, the successive layers of a material move in their own planes, relative to a reference layer. The displacement of a layer is proportional to its distance from the reference layer (similar to a deck of cards that can only be deformed sideways). This is shown schematically in Figure 3.2 for two layers (represented by a rectangle).

$$\text{Strain} = \frac{\delta\ell}{\ell} \tag{3.1}$$

Dimensionless

$$\tan\gamma = \frac{\delta\ell}{\ell} \tag{3.2}$$

When γ is very small, $\tan\gamma \sim \gamma$.

Rheology of Dispersions: Principles and Applications. Tharwat F. Tadros

ISBN: 978-3-527-32003-5

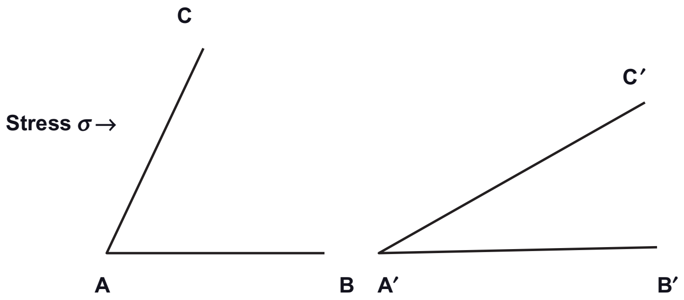

Figure 3.1 Schematic representation of deformation on the application of stress.

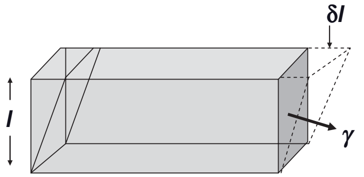

Figure 3.2 Deformation of a rectangular element in simple shear.

The shear strain is simply the angle of shear (in radians).

3.1
Strain Rate or Shear Rate

The shear rate is simply given by the change of strain with time, and has the unit s^{-1}.

$$\dot{\gamma} = \frac{\dot{\delta}\gamma}{\delta t} \tag{3.3}$$

When the flow is linear, a layer at a distance l from the reference layer moving with a velocity v will travel a distance $\delta l = v\delta t$, so that:

$$\dot{\gamma} = \frac{\dot{\delta}}{\delta t}\left(\frac{\delta \ell}{\ell}\right) = \frac{v}{\ell} = \frac{\mathrm{ms}^{-1}}{\mathrm{m}} = \mathrm{s}^{-1} \tag{3.4}$$

3.2
Types of Rheological Behavior in Simple Shear

Consider a layer of material placed between two large parallel plates (edge effects neglected) to which it adheres, such that a shear stress σ is applied via the plates. If the stress is removed, the strain may or may not return to zero, and this allows

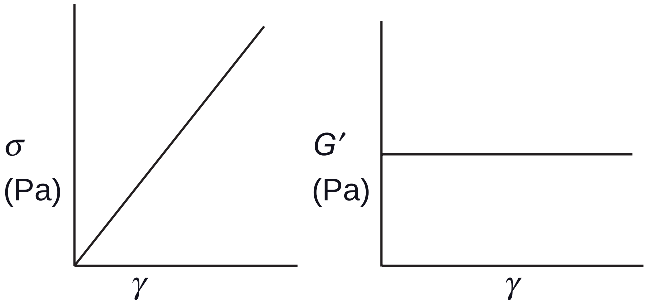

Figure 3.3 Hooke's law of elasticity.

the flow behavior to be distinguished. The strain does not return to zero; rather, flow has occurred and the material is considered as a liquid. Moreover, if flow occurs even for a vanishingly small stress, the material is still considered as a liquid. Types of rheological behavior can be considered as:

- *Inelastic solids:* no strain recovery occurs.
- *Elastic liquids:* a partial recovery occurs (e.g., adhesives).
- *Ideally elastic:* deformation followed by an instantaneous recovery.
- *Slow recovery:* viscoelastic (e.g., polymer solutions, suspensions and emulsions).

3.2.1
Models for Flow Behavior

3.2.1.1 Law of Elasticity (Hooke's Model)

The stress (force per unit area) is proportional to the relative deformation (strain). A plot of stress σ versus strain γ gives a straight line (at small applied strains), with a slope equal to the shear modulus G':

$$\sigma = G'\gamma \tag{3.5}$$

Figure 3.3 shows the relationship for an elastic solid. A material that obeys Hooke's law is described as a "Hookean solid". in this case, G′ is independent of the applied stress.

3.2.1.2 Newton's Law of Viscosity

The resistance which arises from the lack of slipperiness of parts of a liquid (all other things being equal) is proportional to the velocity with which the parts of the liquid are separated one from another. The strain rate $\dot{\gamma}$ is a single valued function of the stress σ:

$$\dot{\gamma} = f(\sigma) \tag{3.6}$$

In other words, the stress σ versus shear rate $\dot{\gamma}$ is linear, and the slope is equal to the viscosity η (Pa·s):

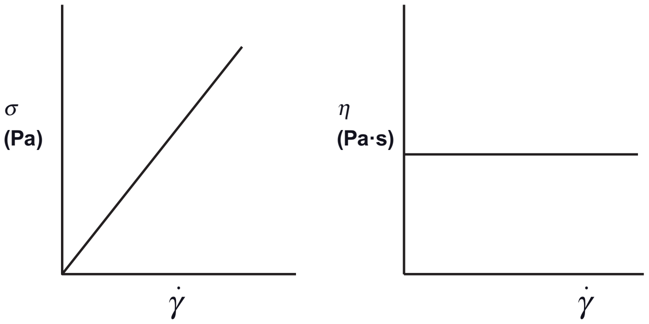

Figure 3.4 Newton's law.

$$\sigma = \eta\dot{\gamma} \tag{3.7}$$

Plots for σ and η versus shear rate are given in Figure 3.4. A material that obeys Newton's law is described as "Newtonian."

The viscosity η is given by the ratio of shear stress over shear rate:

$$\eta = \frac{\sigma}{\dot{\gamma}} = \frac{\mathrm{Nm}^{-2}}{\mathrm{s}^{-1}} = \mathrm{Nm}^{-2}\mathrm{s} = \mathrm{Pa}\cdot\mathrm{s} \tag{3.8}$$

$$\eta = \text{dyne cm}^{-2}\text{s} = \text{Poise} \tag{3.9}$$

Note that 1 Pa·s = 10 Poise (P). The viscosity of water at ~20 °C is 10^{-3} Pa·s or 1 mPa·s (as this is also 10^{-2} Poise or 1 cP, 1 mPa·s = 1 cP).

3.2.1.3 **The Kinematic Viscosity** ν

When Newtonian liquids are tested by means of capillary viscometers (see below), the kinematic viscosity ν is often used. In this case, the force of gravity acts as the force driving the liquid sample through the capillary. The density of the liquid is one additional parameter, and the kinematic viscosity is simply the ratio of the dynamic viscosity to the density of the fluid. The unit of kinematic viscosity is the Stoke (St) or centi-Stoke (cSt), where 1 St = 100 cSt (1 cSt is equal to 1 $\mathrm{mm^2\,s^{-1}}$). In SI units, the kinematic viscosity is given by the ratio of viscosity (in $\mathrm{Nm^{-2}\,s}$) to the density (in $\mathrm{kg\,m^{-3}}$), so that $\nu = \mathrm{m^2\,s^{-1}}$.

3.2.1.4 **Non-Newtonian Flow**

Most dispersions–and particularly those with a high volume fraction and/or containing rheology modifiers–do not obey Newton's law. This can be clearly shown from plots of shear stress σ versus shear rate, as illustrated in Figure 3.5. In this figure, five different flow curves can be identified: (a) Newtonian; (b) Bingham plastic; (c) Pseudoplastic (shear thinning); (d) Dilatant (shear thickening); and (e) Yield stress and shear thinning. The variation of viscosity with shear rate for the above five systems is shown in Figure 3.6. Apart from the Newtonian flow (curve a), all other systems show a change of viscosity with applied shear rate.

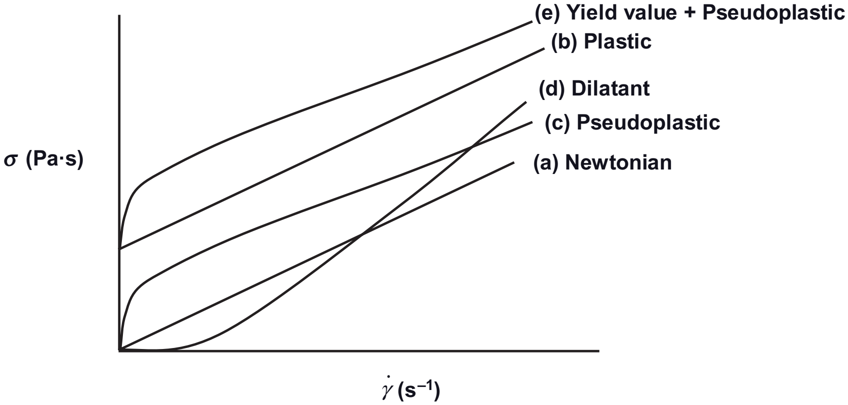

Figure 3.5 Flow curves for various systems.

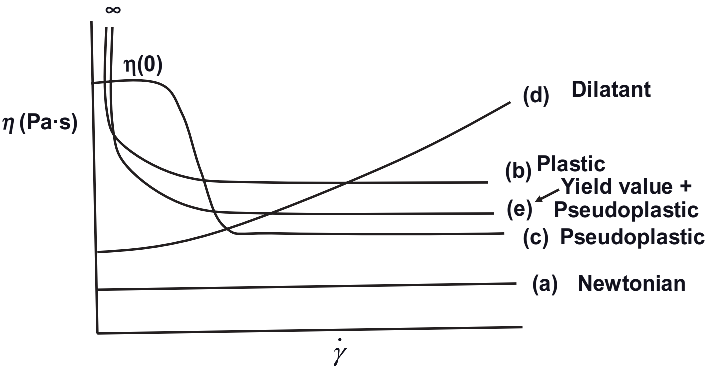

Figure 3.6 Viscosity–shear rate relationship.

3.2.2
Rheological Models for the Analysis of Flow Curves

3.2.2.1 Newtonian Systems

In this case:

$$\sigma = \eta\dot{\gamma} \tag{3.10}$$

where η is independent of the applied shear rate, for example, in simple liquids and very dilute dispersions.

3.2.2.2 Bingham Plastic Systems [4]

In this case:

$$\sigma = \sigma_\beta + \eta_{pl}\dot{\gamma} \tag{3.11}$$

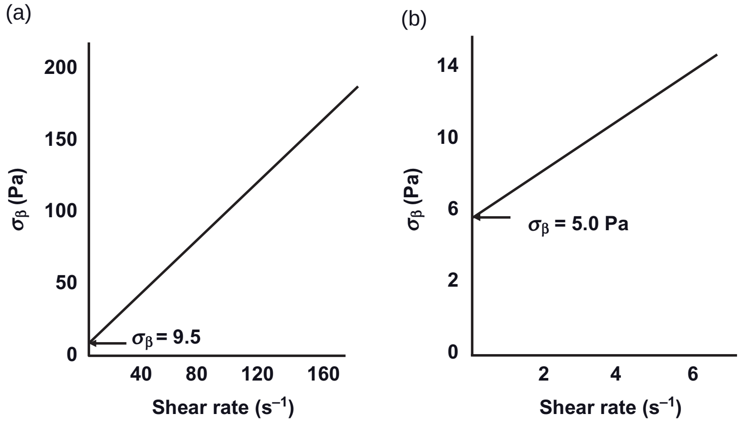

Figure 3.7 Bingham plots for a latex dispersion, using two ranges of shear rate.

The system shows a (dynamic) yield stress σ_β that can be obtained by extrapolation to zero shear rate. Clearly, at and below σ_β the viscosity $\eta \rightarrow \infty$, while the slope of the linear curve gives the plastic viscosity η_{pl}. Some systems, such as clay suspensions, may show a yield stress above a certain clay concentration.

The *Bingham equation* describes the shear stress/shear rate behavior of many shear thinning materials at low shear rates, although unfortunately, the value of σ_β obtained depends on the shear rate ranges used for the extrapolation procedure. This is illustrated in Figure 3.7 for a latex dispersion, whereby the extrapolation was made using the shear rate range 20 to 160 s^{-1} (Figure 3.7a) where a σ_β value of 9.5 Pa is obtained; in contrast, when the extrapolation was made in the shear rate range 1 to 6 s^{-1}, a σ_β value of 5.0 Pa is obtained.

3.2.2.3 **Pseudoplastic (Shear Thinning) System**

In this case, the system does not show a yield value, but rather shows a limiting viscosity $\eta(0)$ at low shear rates (this is referred to as "residual" or "zero shear" viscosity). The flow curve can be fitted to a power law fluid model (Ostwald de Waele):

$$\sigma = k\dot{\gamma}^n \tag{3.12}$$

where k is the consistency index and n is the shear thinning index $(n < 1)$.

By fitting the experimental data to Equation 3.12, it is possible to obtain values of both k and n. The viscosity at a given shear rate can be calculated:

$$\eta = \frac{\sigma}{\dot{\gamma}} = \frac{k\dot{\gamma}^n}{\dot{\gamma}} = k\dot{\gamma}^{n-1} \tag{3.13}$$

The power law model (Equation 3.12) fits the experimental results for many non-Newtonian systems over two or three decades of shear rate. Thus, this model is more versatile than the Bingham model, although care should be taken when applying this model outside the range of the data used to define it. In addition,

Table 3.1 Typical power-law parameters of some non-Newtonian systems for a particular range of shear rates.

Material	k (Pa·s^n)	n	Shear rate range (s^{-1})
Ball-point pen ink	10	0.85	10^0–10^3
Fabric conditioner	10	0.6	10^0–10^2
Polymer melt	10 000	0.6	10^2–10^4
Molten chocolate	50	0.5	10^{-1}–10
Synovial fluid	0.5	0.4	10^{-1}–10^2
Toothpaste	300	0.3	10^0–10^3
Skin cream	250	0.1	10^0–10^2
Lubricating grease	1 000	0.1	10^{-1}–10^2

the power law fluid model fails at high shear rates, whereby the viscosity must ultimately reach a constant value; that is, the value of n should approach unity. This problem can be rectified by using other models such as the Sisko model [5] (see below). Some typical values for the power law parameters for some non-Newtonian systems are listed in Table 3.1 [2].

3.2.2.4 **Dilatant (Shear Thickening) System**

In some cases, the very act of deforming a material can cause a rearrangement of its microstructure such that the resistance to flow increases with any increase in shear rate. In other words, the viscosity increases with applied shear rate and the flow curve can be fitted with the power law (Equation 3.13), although in this case $n > 1$. A typical example is shown in Figure 3.8 for a deflocculated clay suspension [6], whereby the viscosity is plotted as a function of shear rate at various clay concentrations.

The shear thickening regime extends over only about a decade of shear rate. In almost all cases of shear thickening, there is a region of shear thinning at low shear rates.

Several other systems can show shear thickening, such as wet sand, corn starch dispersed in milk, and some polyvinyl chloride sols. Shear thickening can be illustrated when a person walks on wet sand, such that some water is "squeezed out" and the sand appears dry. In this case, the deformation applied by the foot has caused a rearrangement of the close-packed structure produced by the water motion. The process is accompanied by a volume increase (hence the term "dilatancy") as a result of the "sucking in" of water. Overall, the process amounts to a rapid increase in viscosity.

3.2.2.5 **The Herschel–Bulkley General Model** [7]

Many systems show a dynamic yield value followed by a shear thinning behavior. The flow curve can be analyzed using the Herschel–Bulkley equation:

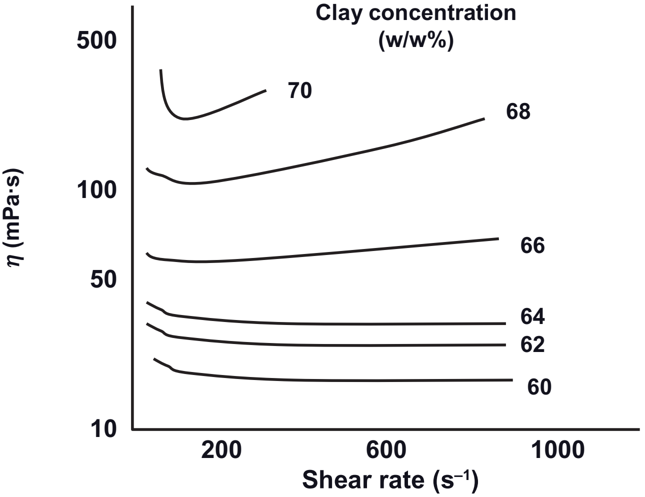

Figure 3.8 Viscosity–shear rate relationship for clay suspensions at various concentrations.

$$\sigma = \sigma_\beta + k\dot{\gamma}^n \tag{3.14}$$

When $\sigma_\beta = 0$, Equation 3.14 reduces to the power fluid model, whereas when $n = 1$, Equation 3.14 reduces to the Bingham model. When $\sigma_\beta = 0$ and $n = 1$, Equation 3.15 becomes the Newtonian equation.

Although, the Herschel–Bulkley equation fits most flow curves with a good correlation coefficient, and hence is the most widely used model, several other models have been suggested of which the following is worthy of mention.

3.2.2.6 **The Casson Model** [8]

This is a semi-empirical linear parameter model that has been applied to fit the flow curves of many paints and printing ink formulations:

$$\sigma^{1/2} = \sigma_C^{1/2} + \eta_C^{1/2}\dot{\gamma}^{1/2} \tag{3.15}$$

Thus, a plot of $\sigma^{1/2}$ versus $\dot{\gamma}^{1/2}$ should give a straight line from which σ_C and η_C can be calculated from the intercept and slope of the line.

Care should be taken when using the Casson equation, however, as straight lines are only obtained from the results above a certain shear rate.

3.2.2.7 **The Cross Equation** [9]

This can be used to analyze the flow curve of shear thinning systems that show a limiting viscosity $\eta(0)$ in the low shear rate regime, and another limiting viscosity $\eta(\infty)$ in the high shear rate regime. These two regimes are separated by a shear thinning behavior, as shown schematically in Figure 3.9.

$$\frac{\eta - \eta(\infty)}{\eta(0) - \eta(\infty)} = \frac{1}{1 + K\dot{\gamma}^m} \tag{3.16}$$

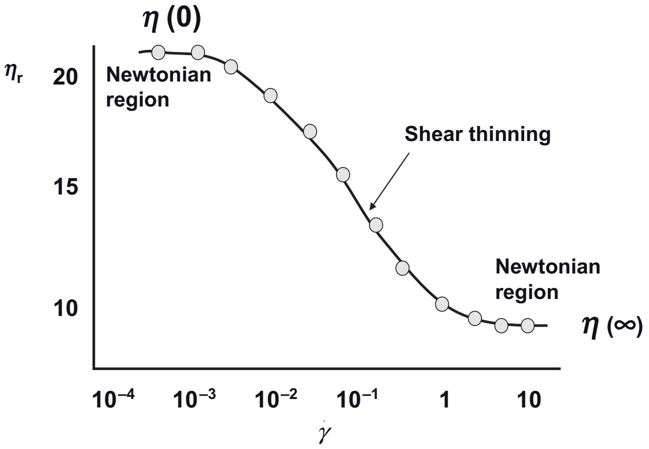

Figure 3.9 Viscosity versus shear rate for a shear thinning system.

where K is a constant parameter with dimension of time, and m is a dimensionless constant.

An equivalent equation to (3.16) is:

$$\frac{\eta_o - \eta}{\eta - \eta_\infty} = (K\dot{\gamma}^m) \tag{3.17}$$

An alternative model was given by Carreau [10]:

$$\frac{\eta - \eta_\infty}{\eta_o - \eta_\infty} = \frac{1}{\left(1 + (K_1\dot{\gamma})^2\right)^{m_1/2}} \tag{3.18}$$

where K_1 and m_1 have a similar significance to the Cross model.

The Cross model can provide several approximations; for example, when $\eta \ll \eta_o$ and $\eta \gg \eta_\infty$, the Cross equation reduces to:

$$\eta = \frac{\eta_o}{(K\dot{\gamma})^m} \tag{3.19}$$

Equation 3.19 reduces to the power law model,

$$\eta = K_2\dot{\gamma}^{n-1} \tag{3.20}$$

such that K_2 is now the consistency, with units of Pa·s.

Further, if $\eta \ll \eta_o$,

$$\eta = \eta_\infty + \frac{\eta_o}{(K\dot{\gamma})^m} \tag{3.21}$$

which can be written as:

$$\eta = \eta_\infty + K_2\dot{\gamma}^{n-1} \tag{3.22}$$

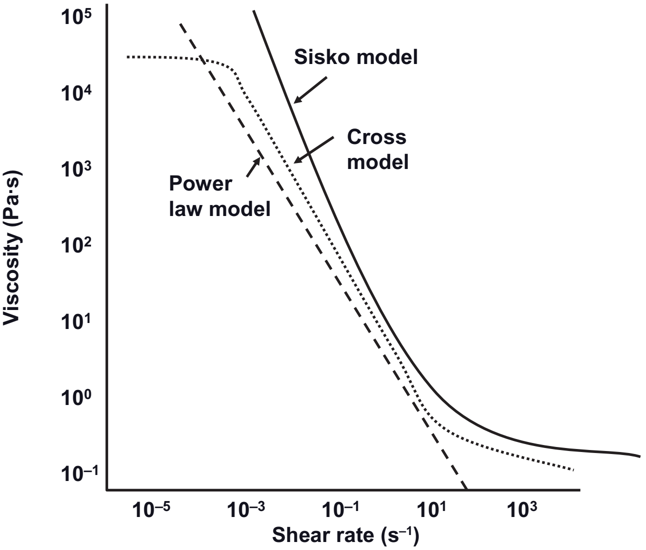

Figure 3.10 Schematic representation of the variation of viscosity with shear rate according to the power law, and the Sisko and Cross models.

Equation 3.22 is referred to as the Sisko model.

If $n = 0$,

$$\eta = \eta_\infty + \frac{K_2}{\dot{\gamma}} \tag{3.23}$$

which, with a simple redefinition of parameters can be written as,

$$\sigma = \sigma_y + \eta_{\text{pl}}\dot{\gamma} \tag{3.24}$$

which is the Bingham equation.

A schematic representation of the variation of viscosity with shear rate according to the power law, the Sisko, and Cross models is shown in Figure 3.10.

3.3
Time Effects During Flow: Thixotropy and Negative (or Anti-) Thixotropy

When a shear rate is applied to a non-Newtonian system, the resulting stress may not be achieved simultaneously because: (i) the molecules or particles will undergo a spatial rearrangement to follow the applied flow field; and/or (ii) the structure of the system may change. The latter may include the breaking of weak bonds, the alignment of irregularly shaped particles, and the collision of particles to form aggregates.

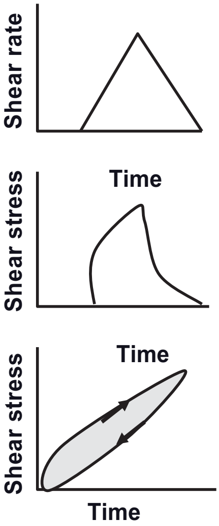

Figure 3.11 The loop test for studying thixotropy.

The above changes are accompanied by a decrease or an increase of viscosity with time at any given shear rate. These changes are referred to as "thixotropy" if the viscosity *decreases* with time, or "negative thixotropy" or "anti-thixotropy" if the viscosity *increases* with time.

Thixotropy: This refers to the reversible time-dependent decease of viscosity. When the system is sheared for some time, the viscosity decreases; however, when the shear is stopped (when the system is left to rest) the viscosity of the system is restored. Practical examples for systems that show thixotropy include paint formulations (these sometimes are referred to as thixotropic paints), tomato ketchup, and some hand creams and lotions.

Negative thixotropy or anti-thixotropy: When the system is sheared for some time the viscosity increases; however, when the shear is stopped (the system is left to rest), the viscosity decreases. A practical example of the above phenomenon is corn starch suspended in milk.

Generally speaking, two methods can be applied to study thixotropy in a paint formulation. The first – and most commonly used – procedure is the "loop test," whereby the shear rate is increased continuously and linearly in time from zero to a maximum value, and then decreased to zero in the same way. This is illustrated schematically in Figure 3.11.

The main problem with the above procedure is the difficulty in interpreting the results. The nonlinear approach used is not ideal for developing loops because, by decoupling the relaxation process from the strain, the material may not be allowed

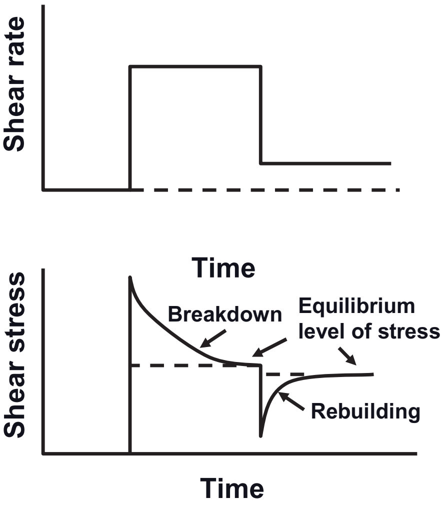

Figure 3.12 The step change test for studying thixotropy.

to recover. Nonetheless, the loop test does provide a qualitative behavior of paint thixotropy.

An alternative method for studying thixotropy is to apply a “step change test,” whereby the paint is suddenly subjected to a constant high shear rate, after which the stress is followed as a function of time whereby the structure breaks down and an equilibrium value is reached. The stress is further followed as a function of time to evaluate the rebuilding of the structure. A schematic representation of the step change test is shown in Figure 3.12.

Application of the above tests for a highly elastic dispersion is not straightforward, as there are contributions to the stress growth and decay from viscoelasticity. The occurrence of thixotropy implies that the flow must be taken into account when making predictions of flow behavior.

The above analysis may not be straightforward, however, as many systems may also show an “elastic overshoot,” as indicated in Figure 3.13. Simple nonlinear relaxation behavior may show a complex behavior of the stress with time. This is illustrated in Figure 3.14, which shows the change of stress with time at a shear strain $\gamma = 1$; here, the peak observed is referred to as the “elastic overshoot.” For the accurate investigation of thixotropy, it is preferable to use viscoelastic measurements (this will be discussed in Chapter 4).

3.4
Rheopexy

Rheopexy is the increase in thixotropy recovery rate when a gentle oscillation is applied to the system. Rheopexy is sometimes described qualitatively as an

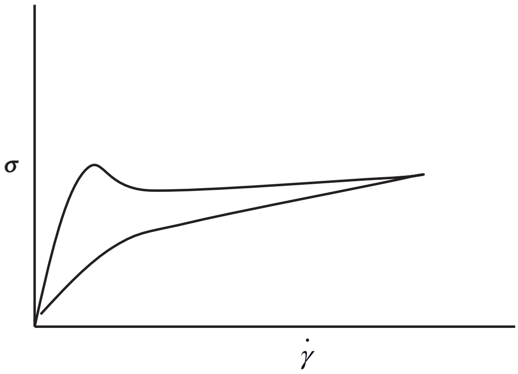

Figure 3.13 Elastic overshoot.

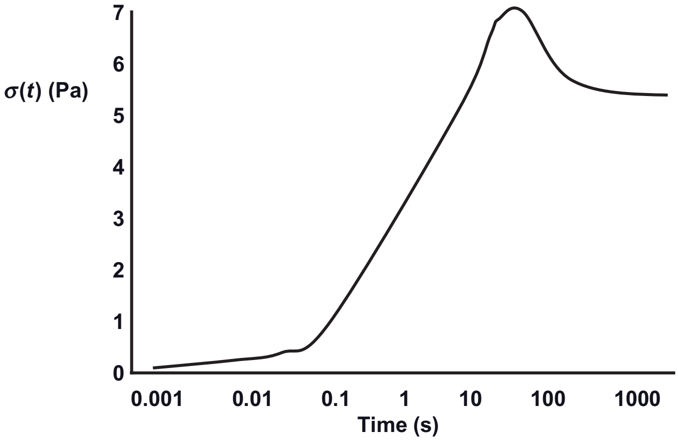

Figure 3.14 Variation of stress with time at a strain $\gamma = 1$.

"increase in viscosity by touch," and should not be confused with anti-thixotropy, which is used to describe time-dependent shear thickening.

Some thixotropic dispersions (such as vanadium oxide suspensions) can be solidified by orienting the particles when a gentle shear action is applied [11]. In contrast to dilatancy, no immediate liquefaction occurs when the shear is removed. Thus, a rheopectic dispersion may be defined as either thixotropic or plastic material that will solidify when subjected to a certain shear, and will not regain its more fluid structure immediately after shear removal. Rheopexy will most likely occur in suspensions consisting of anismetric particles (such as vanadium oxide, as mentioned above). Due to this anisometry, the orientation of the particles can cause solidification that may remain at least for a period of time before reaching its initial liquid state.

The best way to investigate rheopexy is to follow the modulus G as a function of time t on application of strains with increasing amplitudes (see Chapter 4). With a rheopectic system, G increases more rapidly with time at higher amplitudes when compared to lower amplitudes. Care must be taken when characterizing the thixotropic recovery in order to avoid any enhancement of the rate.

3.5
Turbulent Flow

In all of the above analyses, the flow was assumed to be laminar (streamline flow), so that distinct layers of material would pass each other. However, in turbulent flow no distinct layers are observed, and all layers mix with one another by forming eddy currents, swirls, and vortices. Turbulent flow occurs when the shear rate exceeds a certain critical value. The onset of turbulent flow occurs at a critical (dimensionless) Reynolds number, R_e, which for Newtonian materials is given by: [12],

$$R_e = \frac{vx\rho}{\eta} \tag{3.25}$$

where v is the mean velocity (ms^{-1}), x is an instrument length parameter (m), ρ is the density (kg m^{-3}), and η is the viscosity ($\text{Pa}\cdot\text{s}$, $\text{N m}^{-2}\,\text{s}^{-1}$, or $\text{kg m}^{-1}\,\text{s}^{-1}$).

Turbulent flow in pipes can occur if R_e exceeds 2000, whereas below this critical value the flow is laminar. In turbulent flow, the viscosity shows an apparent increase with increase of shear rate, in a manner that is similar to dilatant flow. However, this does not mean that the viscosity of the material increases with an increase of the shear rate; rather, it indicates that, with increasing shear stress, the degree of turbulence increases so that part of the stress is used to increase the number of eddy currents rather than to increase the flow of the bulk of material.

Empirical equations have been established for the turbulent flow of materials in pipes and capillaries, where x in Equation 3.25 is replaced by the pipe or capillary diameter D. For smooth pipes [13],

$$\frac{1}{\varphi^{1/2}} = 2\log\left(\frac{R_e}{\varphi^{1/2}}\right) - 0.8 \tag{3.26}$$

whereas for rough pipes:

$$\frac{1}{\varphi^{1/2}} = 2\log\left(\frac{D}{2k}\right) + 1.7 \tag{3.27}$$

where k is the grain diameter that indicates surface roughness and φ is the friction factor that is given by:

$$\varphi = \frac{2DP}{\rho L v^2} = \frac{64}{R_e} \tag{3.28}$$

where P is pressure in the pipe or capillary, and L is the length.

Thus, for turbulent flow in smooth pipes the flow velocity depends on the Reynolds number and hence on the viscosity, whereas in rough pipes the flow velocity is independent of the viscosity.

In a well-dimensioned concentric cylinder rotational viscometer, turbulent flow is infrequent. However, it can occur and the flow curve must be rejected. Turbulent flow sets in at higher shear rates in viscometers, where the outside cylinder rotates, than in those where the inner cylinder is the rotor.

The pressure required to pump a material through a pipeline system at a given flow rate depends on the pressure loss in the total pipeline system. Pressure losses are incurred by the viscous resistance of the material in the straight pipeline, and in the pipeline transitions such as bends, valves, elbows, pipe expansions, and contractions. However, the viscous losses in the straight pipelines are frequently large compared to the pipe transitions, so that the latter can sometimes be neglected.

The pressure loss for an entire pipeline system is given by:

$$\Delta P = \rho \frac{v^2}{2}\left[\frac{L}{D}\varphi + C_\mathrm{L}\right] \tag{3.29}$$

where C_L is the sum of all pressure loss coefficients obtained from all pipeline transitions in the pipeline system.

The flow of Newtonian materials in pipelines under laminar flow is well understood, and is given by the Poiseuille equation:

$$\eta = \frac{\pi R^4 P}{8QL} \tag{3.30}$$

where Q is the volumetric flow (in $\mathrm{m^3\,s^{-1}}$) and R is the pipe radius.

In turbulent flow, the flow for Newtonian systems is given by Equations 3.26 and 3.27.

Although, the flow of non-Newtonian materials (as is the case with paints) in pipelines is less well understood, Buckingham [14] derived the following equation for evaluating the plastic viscosity of a Bingham plastic system from the flow curve in a capillary viscometer (assuming that end effects, kinetic energy effects and slippage flow are absent):

$$\eta_\mathrm{pl} = \frac{\pi P R^4}{8QL}\left[1 - \frac{8L\sigma_\beta}{3RP} + \frac{1}{3}\left(\frac{2L\sigma_\beta}{RP}\right)^4\right] \tag{3.31}$$

Equation 3.31 can be used to determine the laminar flow of plastic materials in pipelines, with R being the pipe radius. For pseudoplastic and dilatant materials, the power law equation can be used:

$$\eta = k\dot{\gamma}^{n-1} \tag{3.32}$$

where k is the consistency index and n is the shear thinning index ($n < 1$ for pseudoplastic materials).

For a Bingham plastic in laminar flow, the friction factor φ is given by:

$$\varphi = \frac{64}{R_e}\frac{Pl}{8s} \tag{3.33}$$

where Pl is the "plasticity number" that is given by,

$$Pl = \frac{\sigma_\beta D}{Uv} \tag{3.34}$$

where U is the coefficient of plastic viscosity and v is the velocity.

In Equation 3.33, s is the ratio of yield value to the shear stress at the wall. Since s is a function of Pl, the friction factor for Bingham plastics is fully determined from R_e and Pl.

For pseudoplastic materials in laminar flow, the friction factor is given by:

$$\varphi = \frac{64}{R_e}\left(\frac{3+N}{4}\right) \tag{3.35}$$

where $N = 1/n$. Thus, the friction factor for pseudoplastic materials is fully determined from R_e and N.

The shear rate in the pipeline for the flow of pseudoplastic materials is given by:

$$\dot{\gamma} = \frac{2v(N+3)}{D} \tag{3.36}$$

The apparent viscosity that is to be used in the Reynolds number must be measured in the viscometer at the pipeline shear rate. This can be obtained by fitting the flow curve to the power law relationship given by Equation 3.32.

In turbulent non-Newtonian flow, the friction factor is a unique function of the Reynold's number. For Bingham plastic systems, R_e is calculated by using the plastic viscosity, since this remains constant with increasing shear rates. For pseudoplastic flow, R_e is calculated by using an estimated apparent viscosity that is obtained by extrapolation to infinite shear rate.

3.6
Effect of Temperature

Newtonian liquids normally show an exponential decrease of viscosity with increase of temperature t, as is illustrated by the following empirical equation:

$$\eta = A\exp(-Bt) \tag{3.37}$$

where A and B are constants of the liquid.

Alternatively, an Arrhenius-type equation can be used:

$$\eta = A\exp(E/RT) \tag{3.38}$$

where E is a constant that may be related to the activation energy of viscous flow (as suggested by Eyring's theory) and T is the absolute temperature. Equation 3.38 shows that a plot of log η versus $(1/T)$ should give a straight line with a slope equal to (E/R). For water, η decreases by 3% per °C.

With non-Newtonian disperse systems the variation of viscosity with temperature shows a variety of trends. In its simplest case, the change in viscosity with temperature for a disperse system may simply reflect the change in the viscosity of the continuous phase. However, this trend is not observed with most non-Newtonian systems, whereby the interparticle interaction changes with increase in temperature. For example, if the dispersion shows flocculation above a critical temperature, the viscosity may show an initial decrease with increase of temperature, followed by an increase above the critical flocculation temperature. With many disperse systems that contain surfactant liquid crystalline structures, the viscosity may a show a more rapid decrease with increase of temperature above the melting temperature of the liquid crystalline structures.

3.7
Measurement of Viscosity as a Function of Shear Rate: The Steady-State Regime

The measurement of viscosity as a function of shear rate is achieved when a steady state is reached. It is important to consider the shear rates involved in various industrial processes; these are summarized in Table 3.2, while Figure 3.15 provides a summary of the viscosities of various materials given on a log scale to cover the whole range.

Steady-state measurements can be applied to measure the viscosity as a function of shear rate in the range $10^{-1}$to $10^{3}\,s^{-1}$. Measurement at very low shear rates (the range that is important for prediction of creaming or sedimentation) can only be

Table 3.2 Shear rates of various processes.

Process	**(s^{-1})**	**Application**
Sedimentation	10^{-6}–10^{-4}	Paints, agrochemicals
Leveling	$10^{-2^{\cdot\gamma}} - 10^{-1}$	Paints, printing inks
Extrusion	10^{0}–10^{2}	Polymer processing
Stirring, mixing	10^{1}–10^{2}	Manufacturing
Pipeline flow	10^{0}–10^{3}	Pumping
Ball-milling	10^{3}–10^{5}	Paints, inks
Brushing, spraying	10^{3}–10^{4}	Coatings
Topical rubbing	10^{4}–10^{5}	Cosmetics
High-speed coating	10^{3}–10^{7}	Paper coating

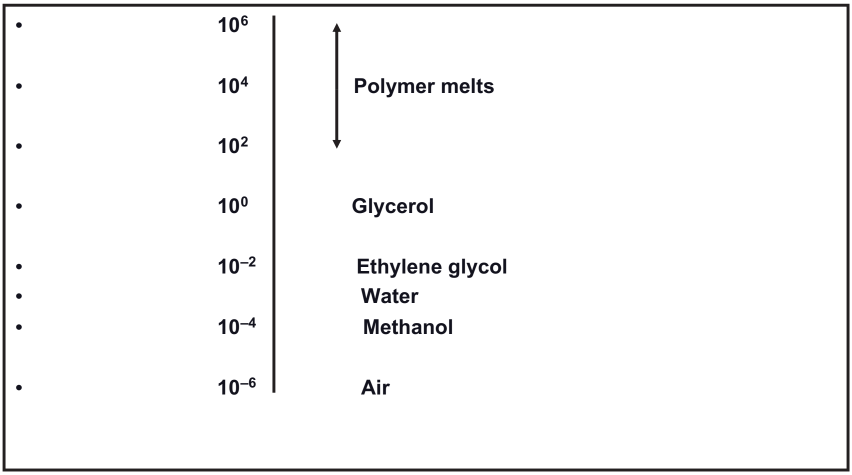

Figure 3.15 The viscosities of some typical materials (values in Pa·s).

achieved using constant stress (creep) measurements. Shear rates above $10^3\,s^{-1}$ require special instruments, for example, using capillary viscometry.

3.7.1
Capillary Viscometers

These are essential for calibration purposes (using standard liquids), for measuring Newtonian systems such as dilute polymer solutions, dilute suspensions and emulsions. The most widely used capillary viscometer is the Ostwald type, which is shown schematically in Figure 3.16. A variant of the Ostwald viscometer, the Cannon–Fenske type, is more convenient to use (Figure 3.16). In capillary viscometry, the volumetric flow Q ($m^3\,s^{-1}$) is measured, after which the viscosity η is calculated using the Poiseuille equation:

$$\eta = \frac{\pi R^4 p}{8QL} \tag{3.39}$$

where R is the tube radius with length L, p is the pressure drop (= $h\rho g$, where h is the liquid height with density ρ and g is the acceleration due to gravity).

Usually, the viscosity of the liquid in question, η_2, is compares with that of a liquid with known viscosity, η_1. In this way, it is possible to measure the flow rates of the two liquids using the same viscometer with a bulb of volume V (the flow rate is simply given as V divided by the time taken for the liquid to flow between the two marks on the viscometer t_1 and t_2 for the two liquids).

The use of Equation 3.39 leads to:

$$\frac{\eta_1}{\eta_2} = \frac{t_1 \rho_1}{t_2 \rho_2} \tag{3.40}$$

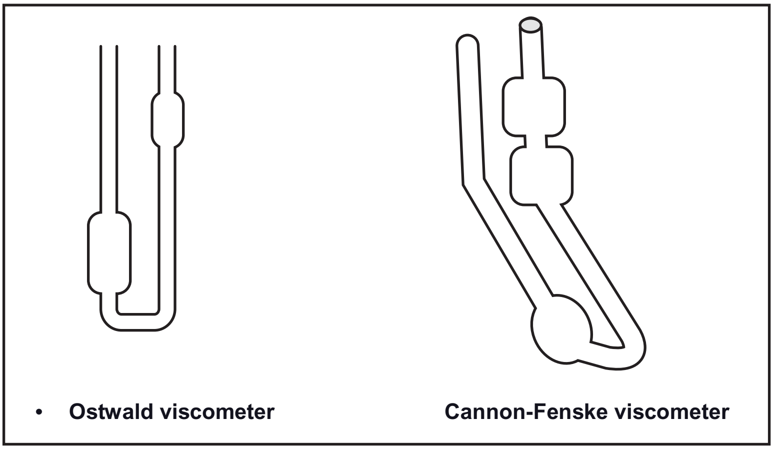

Figure 3.16 Schematic diagrams of the Ostwald and Cannon–Fenske viscometers.

where t_1 and t_2 are simply measured using a stop watch (for automatic viscometers, two fiber optics are used). In these measurements, an accurate temperature control is necessary (±0.01 °C), while the flow time t must be measured with an accuracy of ±0.01 s.

3.7.2
Measurement of Intrinsic Viscosity of Polymers

Capillary viscometers are useful for measurement of the intrinsic viscosity $[\eta]$ of polymers; this term can be used to obtain the molecular weight and solvation of the polymer chains. In this case, the relative viscosity η_r is measured as a function of the polymer concentration C (over the range of 0.01 to 0.1%):

$$\eta_r = \frac{\eta_s}{\eta_0} \tag{3.41}$$

where η_s is the viscosity of the polymer solution and η_o is that of the solvent.

From η_r, it is possible to obtain the specific viscosity η_{sp}:

$$\eta_{sp} = (\eta_r - 1) \tag{3.42}$$

while from η_{sp} it is possible to obtain the reduced viscosity η_{red}:

$$\eta_{red} = \frac{\eta_{sp}}{C} \tag{3.43}$$

A plot of η_{red} versus C gives a straight line that can be extrapolated to $C = 0$ to obtain the intrinsic viscosity $[\eta]$. This is illustrated in Figure 3.17.

From $[\eta]$, it is possible to obtain the molecular weight M using the Mark–Houwink equation:

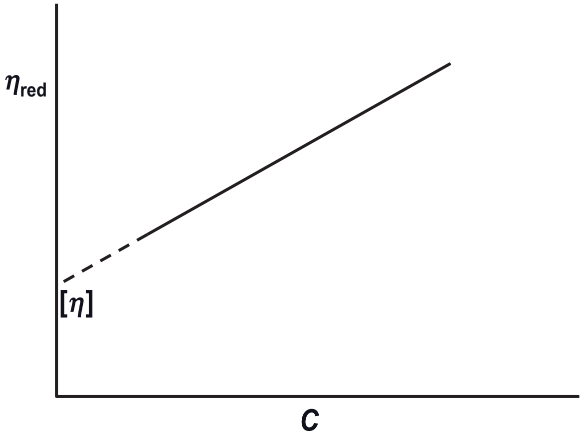

Figure 3.17 Measurement of the intrinsic viscosity of polymers.

$$[\eta] = KM^{\alpha} \tag{3.44}$$

where K and α are constants for a particular polymer and solvent (values for many polymer–solvent systems are tabulated in the *Polymer Handbook*). In this case, α is related to the solvency of the medium for the polymer chain. In a good solvent, $\alpha > 0.5$, and has values in the range 0.5–0.8. In general, the higher the value of α, the better the solvent for the chain.

3.7.3
Capillary Rheometry for Non-Newtonians

Capillary rheometers can be used for non-Newtonian systems, particularly when high shear rates need to be applied. The flow rate Q is measured as a function of pressure drop p, while the stress at the wall σ_W can be calculated as:

$$\sigma_W = \frac{Rp}{2L} \tag{3.45}$$

The apparent viscosity η_a is then calculated at each pressure drop using the Poiseuille equation (Equation 3.17), and graphs are then established between log η_a versus log σ_W. The slope m is then calculated at each datum point:

$$m = \frac{\delta \log \eta_a}{\delta \log \sigma_W} \tag{3.46}$$

The viscosity at the wall $\eta(\sigma_W)$ is then calculated using the Weissenberg equation:

$$\eta(\sigma_W) = \frac{\eta_a}{1 - \frac{m}{4}} \tag{3.47}$$

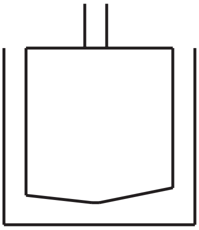

Figure 3.18 Schematic diagram of a concentric cylinder viscometer.

The shear rate at the wall can also be calculated:

$$\dot{\gamma}(\sigma_W) = \frac{\sigma_W}{\eta(\sigma_W)} = \frac{\sigma_W}{\eta_a}\left(1 - \frac{m}{4}\right) \tag{3.48}$$

3.7.4
Rotational Viscometers [1, 3]

Rotational viscometers have two main advantages over tube viscometers, in that: (i) the sample can be sheared for any length of time; and (ii) there is an approximately constant shear rate (particularly with the cone and plate).

For rotational viscometers, three main geometries are commonly used, namely the concentric cylinder (Couette), the cone and plate, and the parallel plate. The concentric cylinder geometry is the most convenient due to its high sensitivity (high surface area) and minimum sample evaporation, although the shear rate is not uniform in the gap. The cone and plate geometry is the most accurate (uniform shear rate in the gap), while the parallel plate has the advantage that the gap width may be changed (although the shear rate will not be uniform).

3.7.4.1 **Concentric Cylinder Viscometer**

This consists of an inner (bob) and outer (cup) concentric cylinders (as shown schematically in Figure 3.18. The bob may contain a concave base that is designed to entrap air in order to reduce the drag contribution from the base.

Consider first a Newtonian liquid that is placed in the gap between the two cylinders with radii R_1 (inner) and R_2 (outer) and length L. The stress σ is simply the force F per unit area A, while the force is the ratio of the torque M to the radius R. The area is $2\pi RL$:

$$\sigma = \frac{F}{A} = \frac{(M/R)}{2\pi RL} = \frac{M}{2\pi R^2 L} \tag{3.49}$$

Stresses can be defined at the inner cylinder σ_1 and at the outer cylinder σ_2:

$$\sigma_1 = \frac{M}{2\pi R_1^2 L} \tag{3.50}$$

$$\sigma_2 = \frac{M}{2\pi R_2^2 L} \tag{3.51}$$

The shear rate can be calculated by assuming that the fluid elements move in circles about the common axis if the cylinders with an angular velocity ω, which is a function of radius r from the center to the position in the gap (where the stress is σ):

$$\dot{\gamma} = r\frac{\delta\omega}{\delta r} \tag{3.52}$$

$$\delta\omega = \frac{\dot{\gamma}}{r}\delta r = \frac{M\delta r}{2\pi r^3 L\eta} \tag{3.53}$$

To calculate the angular velocity Ω of the outer cylinder, it is necessary to sum all of the contributions from the inner to the outer cylinder:

$$\Omega = \int_{R_1}^{R_2} \delta\omega = \frac{M}{2\pi L\eta}\int_{R_1}^{R_2}\frac{\delta r}{r^3} = \frac{M}{4\pi L\eta}\left(\frac{1}{R_1^2} - \frac{1}{R_2^2}\right) \tag{3.54}$$

Equation 3.54, which is referred to as the Margules equation, shows that a plot of Ω versus M should give a straight line that passes through the origin, and from the slope of which η can be obtained.

3.8
Non-Newtonians

3.8.1
Shear Thinning or Pseudoplastic

This could follow a power law:

$$\sigma = k\dot{\gamma}^n \tag{3.55}$$

In this case, a plot of Ω versus M is not linear; however, a log-log plot would be linear, such that the slope would give $N = 1/n$.

The stress σ_1 at the inner cylinder is calculated for each datum point:

$$\sigma_1 = \frac{M}{2\pi R_1^2 L} \tag{3.56}$$

and the shear rate at the inner cylinder is calculated as

$$\dot{\gamma}_1 = \frac{2N\Omega}{1 - s^{-2N}} \tag{3.57}$$

where $s = R_2/R_1$.

3.8.2
Bingham Plastic

In this case:

$$\sigma = \sigma_{\beta} + \eta_{\text{pl}}\dot{\gamma} \tag{3.58}$$

a plot of Ω versus M would be linear, with an intercept that gives the yield value and a slope that gives the plastic viscosity:

$$\Omega = \frac{M}{4\pi\eta_{\text{pl}}}\left(\frac{1}{R_1^2} = \frac{1}{R_2^2}\right) - \frac{\sigma_{\beta}}{\eta_{\text{pl}}}\ln\frac{R_2}{R_1} \tag{3.59}$$

It is assumed that all the material is flowing–that is, the shear stress at the outer cylinder is higher than the yield value:

$$\frac{M}{2\pi R_2^2 L} \geq \sigma_{\beta} \tag{3.60}$$

3.9
Major Precautions with Concentric Cylinder Viscometers

3.9.1
Shear Rate Calculations

The shear rate in the gap is not uniform, and varies according to the position r in the gap. Using the Margules Equation 3.32, it is possible to calculate the shear at any distance r in the gap. The stress σ at r is given by:

$$\sigma = \frac{F}{A} = \frac{M/r}{2\pi r L} = \frac{M}{2\pi r^2 L} \tag{3.61}$$

By combining Equations 3.40 and 3.32, the shear rate at r is given by:

$$\dot{\gamma} = \frac{\sigma}{\eta} = \frac{2\Omega}{r^2}\left[\frac{1}{R_1^2} - \frac{1}{R_2^2}\right]^{-1} \tag{3.62}$$

The shear rate at the inner and outer cylinders can be calculated as shown below.

At $r = R_1$

$$\dot{\gamma}_1 = 2\Omega\frac{R_2^2}{R_2^2 - R_1^2} \tag{3.63}$$

At $r = R_2$

$$\dot{\gamma}_2 = 2\Omega\frac{R_1^2}{R_2^2 - R_1^2} \tag{3.64}$$

Mean value:

$$\langle\dot{\gamma}\rangle = \Omega\frac{R_2^2+R_1^2}{R_2^2-R_1^2} \tag{3.65}$$

Simple calculations show that if the gap is 5% of the outer cylinder radius, then the shear rate will vary by 5% across the gap. If ($R_2 - R_1$) is made sufficiently small (i.e., much smaller than R_1), an average shear stress and shear rate can be calculated:

$$\sigma_{\mathrm{av}} = \frac{M}{2\pi R_{\mathrm{a}}^2} \tag{3.66}$$

$$\dot{\gamma}_{\mathrm{av}} = \frac{\Omega R_2}{R_2 - R_1} \tag{3.67}$$

The above equations are only valid if ($R_2 - R_1$) ~ 1% R_1, but this is not possible for two reasons: (i) it is difficult to machine cylinders with such high tolerances; and (ii) the gap width must be much larger (>>10×) the largest particle or droplet size (which may exceed 10 μm). Gap widths in the range 500–1000 μm are usually used, and it is possible to refer to the shear rate at the outer or inner cylinder or the mean value. If a constant shear rate in the gap is required, a cone and plate geometry should be used (as discussed below).

3.9.2
Wall Slip and Sample Evaporation During Measurement

Many suspensions and emulsions that are concentrated and/or "structured" or "weakly flocculated" (to avoid separation) may cause wall slip. The depletion of particles close to the wall may lead to an erroneously low viscosity and a low yield value. Whilst the slip can be prevented by roughening the inside surfaces of the cylinders, care must be taken when using rough surfaces that may cause fluctuations in the shear rate. Alternatively, different gap widths may be used and the results extrapolated to a large gap width (assuming that the slip layer is independent of the gap width). A better approach to avoid wall slip would be to use a vane rheometer (see below), which is particularly useful for highly concentrated systems such as ceramic pastes. Any sample evaporation that occurs during measurement can be significantly reduced by using a solvent trap.

3.9.2.1 The Vane Rheometer

The vane method uses a vane spindle which is attached to a constant-stress rheometer. The spindle has four or eight blades fixed to a cylindrical shaft, and the depth of the suspension and diameter of the vessel should be at least twice the length and diameter of the vane, so as to minimize any slip effects at the boundary with the walls of the vessel. Either a constant shear rate can be applied and the torque measured, or a constant torque can be applied to the vane spindle and the strain observed for a period of time at successively high stresses; any movement of the spindle is observed. When the applied stress exceeds the yield stress, the vane spindle will begin to rotate. The vane method has the advantage of minimum disturbance of the structure when introducing the vane when compared to rotational cylinders.

3.9.2.2 Cone and Plate Rheometer

This consists of a flat plate and a low angle cone θ ($1° \leq \theta \leq 4°$) that rotates against the flat plate (see Figure 3.19a). The shear rate does not vary from the axis of rotation, because both the linear velocity and the gap between the cone and plate increases with any increase of distance from the rotational axis.

If θ is small, $\sin\theta \sim \theta$, and the shear rate will be uniform across the gap:

$$\dot{\gamma} = \frac{r\Omega}{r\theta} = \frac{\Omega}{\theta} \tag{3.68}$$

Experimentally, the moment of the force MT (the torque) on the cone is measured at a given shear rate. This is the sum of the forces on each element δr wide, multiplied by the distance from the center R (the sum can be replaced by an integral from 0 to R):

$$M_{\mathrm{T}} = \int_0^R \sigma 2\pi r^2 \delta r = \frac{2\pi R^3}{3}\sigma \tag{3.69}$$

Three problems are encountered with the cone and plate geometry: (i) in terms of alignment, the tip of the cone must be at the plate center; (ii) the cone apex may be damaged; and (iii) the particles or droplets may be "ground" at the small gap of the center.

However, the above problems can be reduced by using a truncated cone (as shown in Figure 3.19b;) where $R_1 \sim 0.2\,R$. In this case, the cone will be aligned such that the "apex" (which is now cut) is still at the same position as the original cone, without truncation. The torque is now given by:

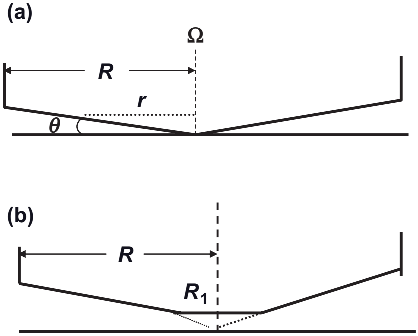

Figure 3.19 Schematic diagram of the cone and plate.

$$M_{\mathrm{T}} = \frac{2\pi(R^3 - R_1^3)}{3}\sigma \tag{3.70}$$

If $R_1 \sim 0.2\,R$, then the torque will be reduced by less than 1%.

3.9.2.3 **Parallel Plates (Discs)**

The parallel plate viscometer consists of two disks with an adjustable gap that allows the sample to be held between the disks. The main advantage of this approach is that the variable gap can be adjusted so as to accommodate dispersions with large particles; this in turn allows calculation of the actual shear rate from the shear rates measured at different gap widths.

The torque generated on the upper disk is measured as a function of the angular velocity Ω of the lower disk. The maximum shear rate at the disk edge is given by:

$$\dot{\gamma}_{\mathrm{m}} = \frac{\Omega R}{\ell} \tag{3.71}$$

where R is the radius of the disk and l is the gap width.

The torque can be obtained by using the same principle as for cone and plate (i.e., Equation 3.69) and substituting for the stress by $\eta\ \gamma$. By using Equation 3.50 for the shear rate, the following equation is obtained for a Newtonian:

$$M = \frac{2\pi\Omega\eta}{L}\int_0^R r^3 dr = \frac{\pi\Omega R^4\eta}{2L} \tag{3.72}$$

For a non-Newtonian, an apparent viscosity η_{a} and the maximum shear rate given by Equation 3.51 are obtained. A correction must be made to obtain the viscosity at each shear rate:

$$\eta(\dot{\gamma}_{\mathrm{m}}) = \eta_{\mathrm{a}}\left(1 + \frac{m}{4}\right) \tag{3.73}$$

where

$$m = \frac{\delta \log \eta_{\mathrm{a}}}{\delta \log \dot{\gamma}_{\mathrm{m}}} \tag{3.74}$$

3.9.2.4 **The Brookfield Viscometer**

This is the most commonly used viscometer, due to the ease with which a viscosity can be measured (particularly for quality control). Several spindles are available to cover a wide range of viscosities, and the results are usually quoted as viscosity at a given rpm-value, using a specific spindle. In order to calculate the shear rate, it is necessary to use the long-cylinder spindle (as shown in Figure 3.20). This geometry approximates that of an infinitely long cylinder in an infinite sea of fluid.

For a "long" cylinder $(L/R) > 10$, where L is the length of the cylinder and R is its radius. For an "infinite" medium, (R_1/R_2) is very small, and (R_1/R_2) is denoted by s.

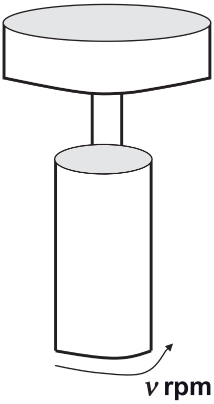

Figure 3.20 Schematic diagram of the Brookfield viscometer (cylinder).

Within the instrument, the apparent viscosity η_a is measured as a function of rotation in rpm (denoted as ν):

$$\nu = \frac{30}{\pi}\Omega \tag{3.75}$$

The stress σ_1 at the cylinder is given by:

$$\sigma_1 = \frac{M}{2\pi R_1^2 L} \tag{3.76}$$

and the apparent viscosity η_a is given by

$$\eta_a = \frac{1}{4\pi R_1^2}\frac{M}{\Omega} = \frac{\sigma_1}{2\Omega} \tag{3.77}$$

Ω is given by Equation 3.54, and σ_1 is then given by:

$$\sigma_1 = \frac{\pi \nu \eta_a}{15} \tag{3.78}$$

Let $N = \frac{\delta \log \eta_a}{\delta \log \sigma_1} = \frac{1}{1+m}$ where $m = \frac{\delta \log \eta_a}{\delta \log \nu}$

$$\dot{\gamma}(\sigma_1) = \frac{2N\Omega}{1-s^{-2N}} = 2N\Omega = \frac{\pi\nu}{15(1+m)} \tag{3.79}$$

$$\eta(\sigma_1) = \frac{\sigma_1}{\dot{\gamma}(\sigma_1)} = \eta_a(1+m) \tag{3.80}$$

A plot of log η_a versus log ν is shown in Figure 3.21, where the shear rate and viscosity can be obtained at each point by using Equations 3.58 and 3.59. Further details of the analysis are provided by Pierce [15].

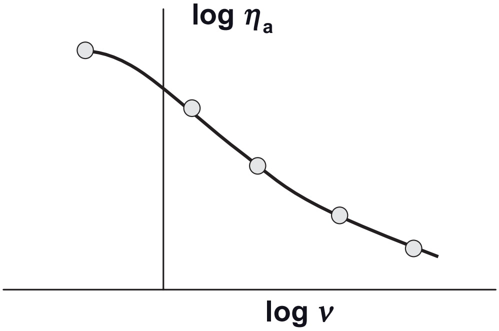

Figure 3.21 Plot of log η_a versus log v for the Brookfield viscometer.

References

1 van Wazer, J.R., Lyons, J.W., Kim, K.Y., and Cowell, R.E. (1983) *Viscosity and Flow Measurements*, Interscience Publishers, New York.

2 Whorlow, R.W. (1980) *Rheological Techniques*, John Wiley & Sons, Inc., New York.

3 Goodwin, J.W. and Hughes, R.W. (2000) *Rheology for Chemists*, Royal Society of Chemistry Publications, Cambridge.

4 Bingham, E.C. (1922) *Fluidity and Plasticity*, McGraw-Hill, New York.

5 Sisko, A.W. (1958) The flow of lubricating greases. *Ind. Eng. Chem.*, **50**, 1789.

6 Bezely, K.M. (1980) Industrial aqueous suspensions, in *Rheometry: Industrial Applications* (ed. K. Walters), John Wiley & Sons, Inc., New York.

7 Herschel, W.H. and Bulkley, R. (1926) *Proc. Am. Soc. Test. Materials*, **26**, 621; Herschel, W.H. and Bulkley, R. (1926) *Kolloid Z.*, **39**, 291.

8 Casson, N. (1959) *Rheology of Disperse Systems* (ed. C.C. Mill), Pergamon Press, New York, pp. 84–104.

9 Cross, M.M. (1965) *J. Colloid Interface Sci.*, **20**, 417.

10 Carreau, P.J. (1972) *Trans. Soc. Rheol.*, **16**, 99.

11 Freundlich, H. and Juliusberger, F. (1935) *Trans. Faraday Soc.*, **31**, 920.

12 Reynolds, O. (1883) *Philos. Trans. R. Soc. London*, **A174**, 935.

13 Weltman, R.N. (1960) *Rheology, Theory and Applications* (ed. F.R. Eirich), Academic Press, New York, pp. 189–247.

14 Buckingham, E. (1921) *Proc. Am. Soc. Test. Materials*, **21**, 1154.

15 Pierce, P.E. (1971) *J. Paint Technol.*, **43**, 35.

4
Principles of Viscoelastic Behavior

4.1
Introduction

Elasticity deals with the mechanical properties of elastic solids which obey Hooke's law, where:

$$\text{Stress } \sigma \propto \text{ Strain } \gamma \text{ (in small deformations)}$$

or:

$$\sigma = G'\gamma \tag{4.1}$$

where G' is the shear modulus (in Pa), and is independent of the applied strain (at low values).

Viscosity deals with the properties of liquids in the classical theory of hydrodynamics according to Newton's law, where:

$$\text{Stress } \sigma \propto \text{ shear rate } \dot{\gamma} \text{ (at small shear rates)}$$

or:

$$\sigma = \eta\dot{\gamma} \tag{4.2}$$

where η is the viscosity (in Pa·s), and is independent of the applied shear rate (at low values).

Whether a material behaves as an elastic solid or as a viscous liquid depends on the length of time over which the relevant experiments are carried out. One convenient way to describe a material is to compare its relaxation time with that of the experimental observation time, as will be discussed below in terms of the dimensionless *Deborah number* [1].

4.2
The Deborah Number [1]

Viscous flow is a manifestation of the decay of elastically stored energy (the Maxwell concept). If a dispersion is considered in which all particles or droplets

Rheology of Dispersions: Principles and Applications. Tharwat F. Tadros

ISBN: 978-3-527-32003-5

have time to diffuse to a low-energy state, then if the system is strained (deformed), the structure will be perturbed such that the particles or droplets will be in a higher energy state. Subsequently, if the system is held in this new shape, then the particles or droplets will diffuse until the original low-energy state is achieved, although the original shape will have been; that is, *viscous flow* has occurred. The characteristic time taken for this process to occur is termed the stress relaxation time, τ, of the dispersion, which can be related to the experimental time t by the dimensionless Deborah number, D_e:

$$D_e = \frac{\tau}{t} \tag{4.3}$$

As most rheological time-scale experiments are conducted in the range of 10^{-3} s (1 ms) to 10^{+3} s (1 ks), a rough distinction can be made between an elastic response (with high relaxation times), a viscous response (with very low relaxation times), and a viscoelastic response (where the relaxation times are comparable with the experimental time of measurement).

De >> 1	De ~ 1	De << 1
Elastic	Viscoelastic	Viscous

Viscoelasticity can be investigated using three different types of experiment [2–8]:

- Strain relaxation after the sudden application of stress (creep).
- Stress relaxation after the sudden application of strain.
- Dynamic (oscillatory) technique.

The basic principles involved in each of the above methods are described in detail below; in addition, detail will be provided of the experimental methods that can be applied in each case.

4.3
Strain Relaxation after the Sudden Application of Stress (Creep)

In this process, a constant stress σ is first applied to the system (which may be placed in the gap between two concentric cylinders, or in a cone and plate geometry), and the strain (relative deformation) γ or compliance J ($= \gamma/\sigma$, Pa^{-1}) is then followed as a function of time for a period of t. At $t = t$, the stress is removed and the strain γ or compliance J is followed for another period t.

The above procedure is referred to as "creep measurement," and from the variation of J with t when the stress is applied, and the change of J with t when the stress is removed (in this case, J changes sign), it is possible to distinguish between viscous, elastic, and viscoelastic response (as illustrated in Figure 4.1):

- **Viscous response:** In this case, the compliance J shows a linear increase with increase of time, reaching a certain value after time t. When the stress is removed after time t, J remains the same; hence, in this case no creep recovery will occur.

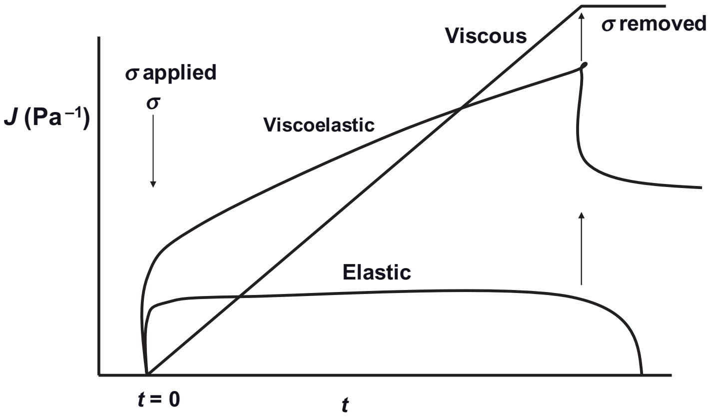

σ

Figure 4.1 Creep curves for viscous, elastic and viscoelastic responses.

- **Elastic response:** In this case, the compliance J shows a small increase at $t = 0$, and remains almost constant for the whole period t. When the stress is removed, J changes sign and reaches 0 after some time t; hence, complete creep recovery will occur in this case.
- **Viscoelastic response:** at $t = 0$, J shows a sudden increase, and this is followed by slower increase for the time applied. When the stress is removed, J changes sign and shows an exponential decrease with an increase of time (creep recovery); however, it does not reach 0, as in the case of an elastic response.

4.4
Analysis of Creep Curves

4.4.1
Viscous Fluid

The linear curve of J versus t gives a slope that is equal to the reciprocal viscosity:

$$J(t) = \frac{\gamma}{\sigma} = \frac{\dot{\gamma}t}{\sigma} = \frac{t}{\eta(0)} \tag{4.4}$$

This system can be represented by a mechanical analog of a "dash-pot" (Newtonian behavior), as shown schematically in Figure 4.2.

4.4.2
Elastic Solid

With an increase of compliance at $t = 0$ (rapid elastic response), $J(t)$ becomes equal to the reciprocal of the instantaneous modulus $G(0)$:

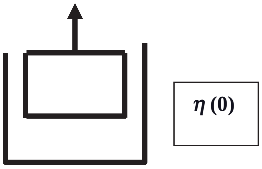

Figure 4.2 Schematic representation of a "dash-pot."

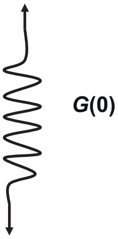

Figure 4.3 Schematic representation of an elastic element.

$$J(t) = \frac{1}{G(0)} \tag{4.5}$$

The system can be represented by a mechanical analog of a spring with a constant $G(0)$; this is shown schematically in Figure 4.3.

4.4.3
Viscoelastic Response

4.4.3.1 **Viscoelastic Liquid**

Figure 4.4 shows the case for a viscoelastic liquid whereby the compliance $J(t)$ is given by two components – an elastic component J_e that is given by the reciprocal of the instantaneous modulus, and a viscous component J_v that is given by $t/\eta(0)$.

$$J(t) = \frac{1}{G(0)} + \frac{t}{\eta(0)} \tag{4.6}$$

Figure 4.4 also shows the recovery curve which gives $\sigma_o J_e^o$; when this is subtracted from the total compliance, it gives $\sigma_o t/\eta(0)$.

The mechanical analog for a viscoelastic liquid is a spring and dash-pot in series (Maxwell element), as illustrated in Figure 4.5. The driving force for relaxation is the spring, while the viscosity controls the rate.

The Maxwell relaxation time, τ_M, is given by:

$$\tau_M = \frac{\eta(0)}{G(0)} \tag{4.7}$$

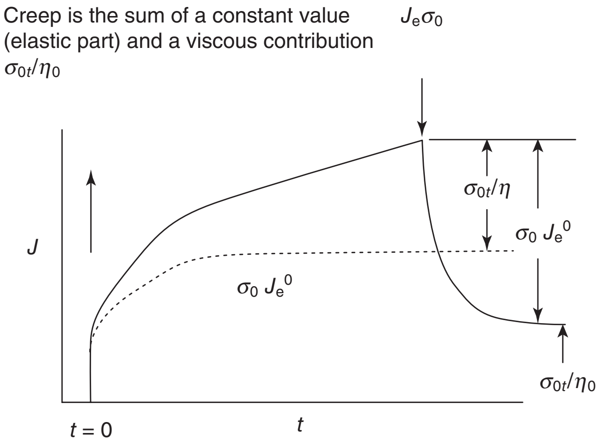

Figure 4.4 Creep curve for a viscoelastic liquid.

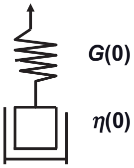

Figure 4.5 Mechanical analog of a viscoelastic liquid.

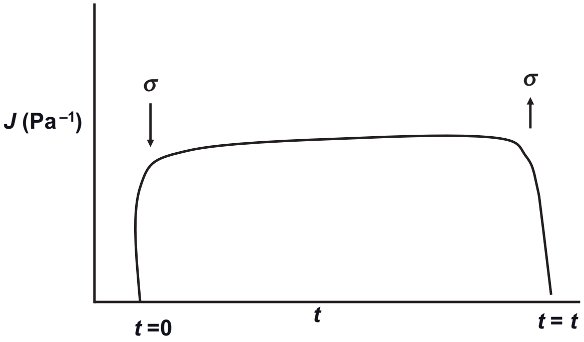

Figure 4.6 Creep curve for a viscoelastic solid.

4.4.3.2 **Viscoelastic Solid**

In this case, complete recovery occurs as illustrated in Figure 4.6; the mechanical analog is represented by a spring and dash-pot in parallel, as illustrated in Figure 4.7.

The dash-pot simply retards the motion of the spring (similar to the shock absorber in the suspension unit of a motor car), and the system is characterized by a Kelvin retardation time τ_k that is also given by the ratio of $\eta(0)/G(0)$.

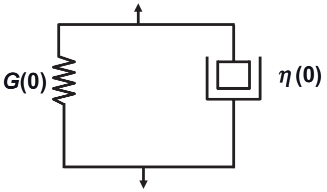

Figure 4.7 Mechanical analog of a viscoelastic solid.

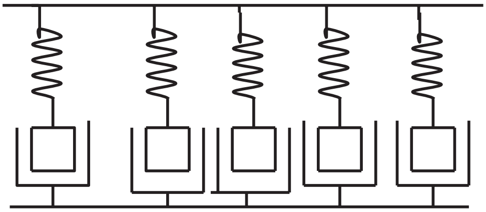

Figure 4.8 Generalized Maxwell model.

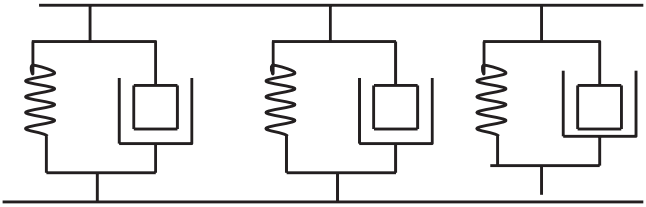

Figure 4.9 Generalized Kelvin model.

4.5
The Berger Model (Maxwell + Kelvin)

This model which represents most practical dispersions, and consists of a Maxwell element and a Kelvin element. The modulus of the spring in the Maxwell element is G_1, and the viscosity in the dash-pot is η_1; thus, the Maxwell relaxation time is η_1/G_1. The modulus of the spring in the Kelvin element is G_2 and the viscosity in the dash-pot is η_2; thus, the Kelvin retardation time is η_2/G_2. The Berger model provides an instantaneous elastic response from G_1 and a continuous viscous response from η_1.

More complex models can be introduced, including a generalized Maxwell model whereby several elements with different relaxation times are introduced (Figure 4.8). The generalized Kelvin model also consists of several Kelvin elements with different retardation times (Figure 4.9).

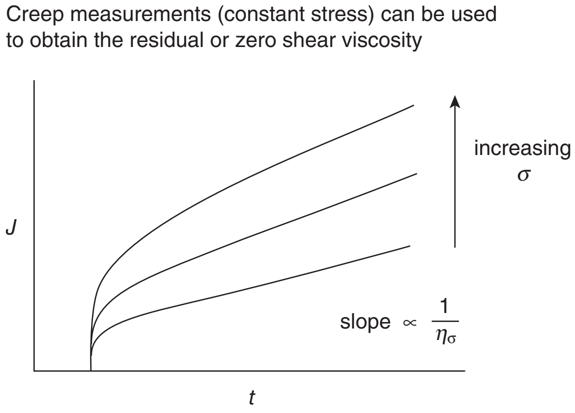

Figure 4.10 Creep curves at increasing applied stress.

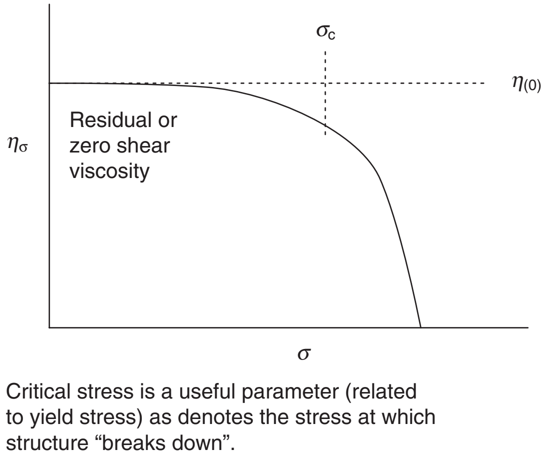

Figure 4.11 Variation of viscosity with applied stress.

4.6
Creep Procedure

Creep experiments begin with a low applied stress (below the critical stress σ_{cr}; see below) at which the system behaves as a viscoelastic solid with complete recovery (as illustrated in Figure 4.6). The stress is gradually increased such that several creep curves are obtained. Above σ_{cr}, the system behaves as a viscoelastic liquid, and shows only a partial recovery (see Figure 4.4). A schematic representation of the variation of compliance J with time t at increasing σ (above σ_{cr}) is shown in Figure 4.10.

From the slopes of these lines, it is possible to obtain the viscosity η_σ at each applied stress. The plot of η_σ versus σ shown in Figure 4.11 demonstrates a limiting viscosity $\eta(0)$ below σ_{cr}, while above σ_{cr} the viscosity shows a sharp decrease with a further increase in σ.

$\eta(0)$, which is referred to as the "residual" or "zero-shear" viscosity, is an important parameter for predicting sedimentation. σ_{cr} is the critical stress above which the structure "breaks down," and is sometimes referred to as the "true" yield stress.

4.7
Stress Relaxation after Sudden Application of Strain

In this case, a small strain is rapidly applied within a very short period of time (which must be less than the relaxation time of the system) and is kept at a constant value. The shear rate remains constant within this period (as illustrated in Figure 4.12).

The stress will follow the strain, and increases to a maximum value $\sigma(0)$. For a perfectly elastic material, $\sigma(0)$ will remain constant over time t, but for a viscoelastic liquid the stress will decrease exponentially with time, reaching 0 at infinite time. The stress required to maintain a constant strain decreases with time due to viscous flow (this is illustrated in Figure 4.13). For a viscoelastic solid, the stress

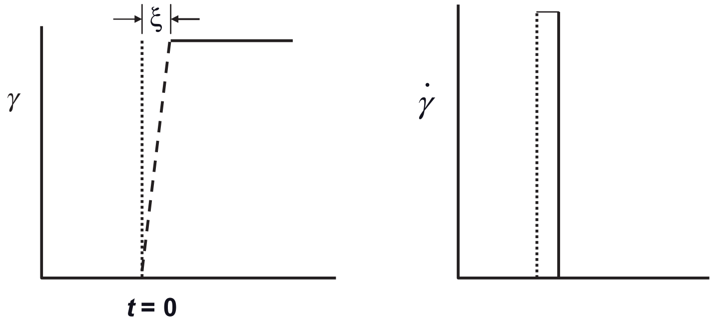

Figure 4.12 Schematic representation of a strain experiment.

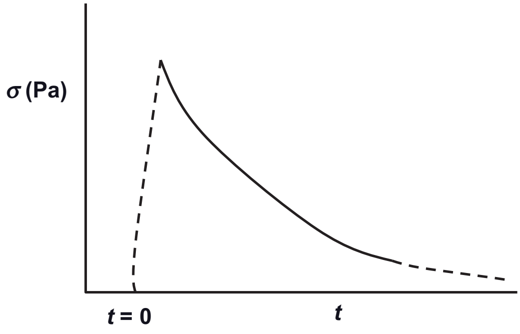

Figure 4.13 Stress relaxation after sudden application of strain.

reaches a limiting value at infinite time. The variation of stress with time is similar to a kinetic process represented by first-order equations.

The stress $\sigma(t)$ is related to the initial maximum stress $\sigma(0)$ by:

$$\sigma(t) = \sigma(0)\exp\left(-\frac{t}{\tau_{\mathrm{m}}}\right) \tag{4.8}$$

where τ_{m} is the Maxwell relaxation time that is given by the ratio of the viscosity η to the modulus G:

$$\tau_{\mathrm{m}} = \frac{\eta}{G} \tag{4.9}$$

If the shear stress in Equation 4.8 is divided by the applied strain γ, the shear modulus $G(t)$ is obtained:

$$G(t) = \frac{\sigma(t)}{\gamma} = \frac{\sigma(0)}{\gamma}\exp\left(-\frac{t}{\tau_{\mathrm{m}}}\right) = G(0)\exp\left(-\frac{t}{\tau_{\mathrm{m}}}\right) \tag{4.10}$$

Figure 4.14 shows the variation of the modulus G with time for a viscoelastic liquid, whereas Figure 4.15 shows the trend for a viscoelastic solid.

For a viscoelastic solid, the modulus reaches a limiting value G_{e} after a long time (this sometimes is referred to as the "equilibrium modulus"), and in this case Equation 4.10 must be modified to account for G_{e}:

$$G(t) = G(0)\exp\left(-\frac{t}{\tau_{\mathrm{m}}}\right) + G_{\mathrm{e}} \tag{4.11}$$

It should be noted that, according to Equations 4.8 and 4.10, $t = \tau_{\mathrm{m}}$ when $\sigma(t) = \sigma(0)/e$ or when $G(t) = G(0)/e$. This shows that stress relaxation can be used to obtain the relaxation time for a viscoelastic liquid.

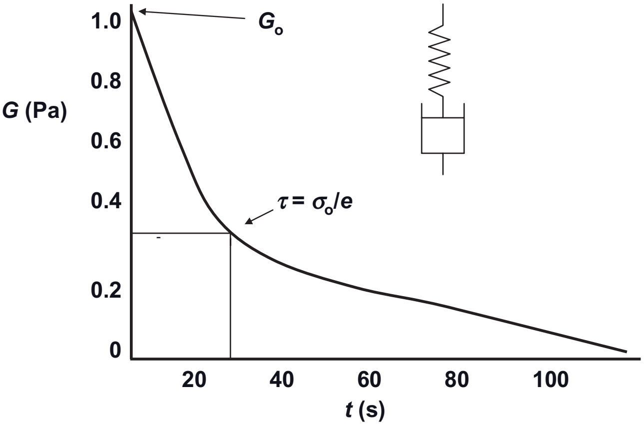

Figure 4.14 Variation of modulus with time for a viscoelastic liquid.

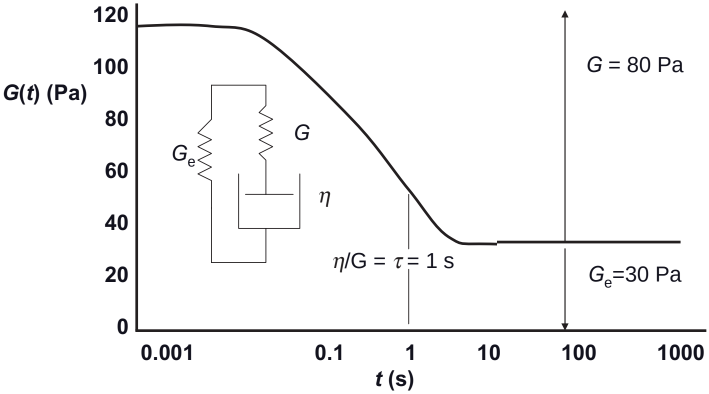

Figure 4.15 Variation of $G(t)$ with t for a viscoelastic solid.

4.8
Dynamic (Oscillatory) Techniques

This is the response of the material to an oscillating stress or strain. When a sample is constrained in, for example, a cone and plate or concentric cylinder assembly, an oscillating strain at a given frequency ω (rad s^{-1}) ($\omega = 2\nu\pi$, where ν is the frequency in cycles s^{-1} or Hz) can be applied to the sample. After an initial start-up period, a stress develops in response of the applied strain – that is, it oscillates with the same frequency. The change of the sine waves of the stress and strain with time can be analyzed to distinguish between elastic, viscous, and viscoelastic responses. An analysis of the resultant sine waves can be used to obtain the various viscoelastic parameters, as discussed below.

Three cases can be considered:

- **Elastic response:** This occurs when the maximum of the stress amplitude is at the same position as the maximum of the strain amplitude (no energy dissipation). In this case, there is no time shift between the stress and strain sine waves.
- **Viscous response:** This occurs when the maximum of the stress is at the point of maximum shear rate (i.e., the inflection point), where there is maximum energy dissipation. In this case, the strain and stress sine waves are shifted by $\omega t = \pi/2$ (this is referred to as the phase angle shift δ which, in this case, is 90°)
- **Viscoelastic response:** In this case, the phase angle shift δ is greater than 0° but less than 90°.

A schematic representation of the above three cases is shown in Figure 4.16.

4.8.1
Analysis of Oscillatory Response for a Viscoelastic System

For the case of a viscoelastic system, the sine waves of strain and stress are shown in Figure 4.17, where the frequency ω is in rad s^{-1} and the time shift between strain

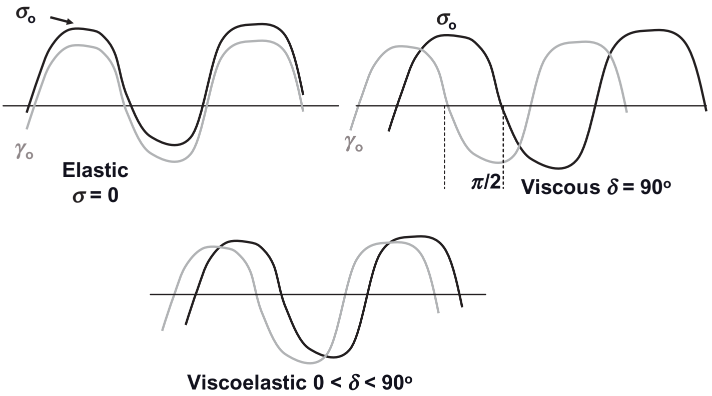

Figure 4.16 Schematic representation of response to an oscillatory strain or stress for elastic, viscous, and viscoelastic systems.

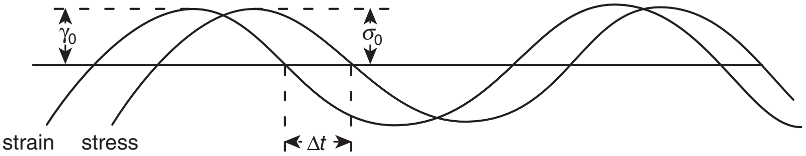

Δt = time shift for sine waves of stress and strain
$\Delta t\ \omega = \delta$ phase angle shift
ω = frequency in radian s^{-1}
$\omega = 2\pi\upsilon$

Perfectly elastic solid	$\delta = 0$
Perfectly viscous liquid	$\delta = 90^\circ$
Viscoelastic system	$0 < \delta < 90^\circ$

Figure 4.17 Strain and stress sine waves for a viscoelastic system.

and stress sine waves is Δt. The phase angle shift δ is given by (in dimensionless units of radians):

$$\delta = \omega \Delta t \tag{4.12}$$

As discussed before:

Perfectly elastic solid $\delta = 0$
Perfectly viscous liquid $\delta = 90^\circ$
Viscoelastic system $0 < \delta < 90^\circ$

The ratio of the maximum stress σ_o to the maximum strain γ_o gives the complex modulus $|G^*|$

$$|G^*| = \frac{\sigma_o}{\gamma_o} \tag{4.13}$$

In this case, $|G^*|$ can be resolved into two components: (i) the storage (elastic) modulus G′, the real component of the complex modulus; and (ii) the loss (viscous) modulus G'', the imaginary component of the complex modulus:

$$|G^*| = G' + iG'' \tag{4.14}$$

where i is the imaginary number that is equal to $(-1)^{1/2}$.

The complex modulus can be resolved into G' and G'' by using vector analysis and the phase angle shift δ, as shown below.

4.8.1.1 Vector Analysis of the Complex Modulus

$$G' = |G^*|\cos\delta \tag{4.15}$$

$$G'' = |G^*|\sin\delta \tag{4.16}$$

$$\tan\delta = \frac{G''}{G'} \tag{4.17}$$

Dynamic viscosity

$$\eta' = \frac{G''}{\omega} \tag{4.18}$$

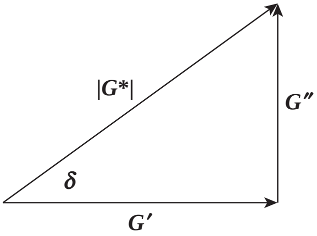

Note that $\eta \rightarrow \eta(0)$ as $\omega \rightarrow 0$.

Both, G' and G'' can be expressed in terms of frequency ω and Maxwell relaxation time τ_m by:

$$G'(\omega) = G\frac{(\omega\tau_m)^2}{1+(\omega\tau_m)^2} \tag{4.19}$$

$$G''(\omega) = G\frac{\omega\tau_m}{1+(\omega\tau_m)^2} \tag{4.20}$$

In oscillatory techniques, it is necessary to perform two types of experiment:

Strain sweep: In this case, the frequency ω is kept constant and G^*, G' and G'' are measured as a function of strain amplitude.

Frequency sweep: Here, the strain is kept constant (in the linear viscoelastic region), and G^*, G' and G'' are measured as a function of frequency.

Strain Sweep The frequency is fixed say at 1 Hz (or 6.28 rad s^{-1}) and G^*, G' and G'' are measured as a function of the strain amplitude, γ_o, as illustrated in

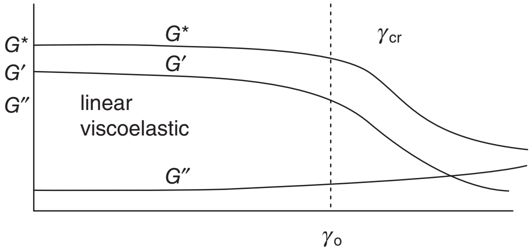

Fixed frequency (0.1 or 1 Hz) and follow G^*, G' and G'' with strain amplitude γ_o

linear viscoelastic region
G^*, G' and G'' are independent of strain amplitude

γ_{cr} is the critical strain above which system shows non-linear response (break down of structure)

Figure 4.18 Schematic representation of strain sweep.

Figure 4.18. G^*, G' and G'' remain constant up to a critical strain γ_{cr}; this is the linear viscoelastic region where the moduli are independent of the applied strain. Above γ_{cr}, G^* and G' begin to decrease, whereas G'' begins to increase with further increase in γ_o; this is the nonlinear region.

γ_{cr} may be identified with the critical strain above which the structure starts to "break down." It can also be shown that, above another critical strain, G'' becomes higher than G'; this is sometimes referred to as the "melting strain" at which the system becomes more viscous than elastic.

Oscillatory Sweep The strain γ_o is fixed in the linear region (taking a mid point, i.e., not a too-low strain, where the results may show some "noise" and far from γ_{cr}). Then, G^*, G' and G'' are measured as a function of frequency (a range of 10^{-3} to 10^2 rad s^{-1} may be chosen, depending on the instrument and operator patience). Figure 4.19 shows a schematic representation of the variation of G^*, G' and G'' with frequency ω (rad s^{-1}) for a viscoelastic system that can be represented by a Maxwell model. It is possible to identify a characteristic frequency ω^* at which $G' = G''$ (the "crossover point") which can be used to obtain the Maxwell relaxation time τ_m:

$$\tau_m = \frac{1}{\omega^*} \tag{4.21}$$

In the low-frequency regime (i.e., when $\omega < \omega^*$), it is found that $G'' > G'$; this corresponds to a long-term experiment (time is reciprocal of frequency), and hence the system can dissipate energy as viscous flow.

In the high-frequency regime (i.e., when $\omega > \omega^*$), it is found that $G' > G''$; this corresponds to a short-term experiment where the energy dissipation is reduced.

At a sufficiently high frequency, $G' \gg G''$, and in this case $G'' \rightarrow 0$ and $G' \sim G^*$. The high-frequency modulus $G'(\infty)$ is sometimes referred to as the "rigidity modulus," where the response is mainly elastic.

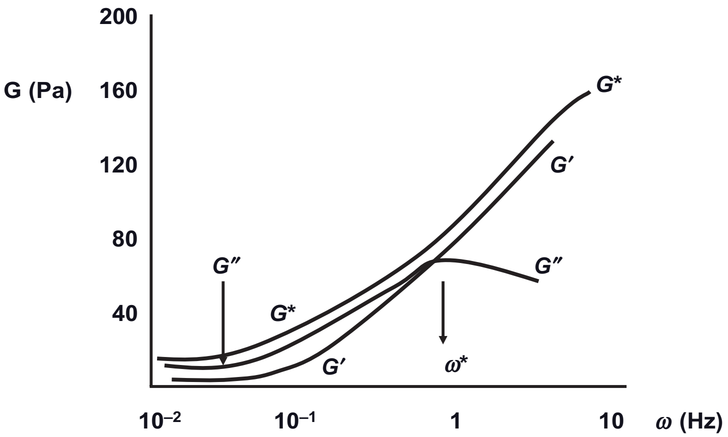

Figure 4.19 Schematic representation of oscillatory measurements for a viscoelastic liquid.

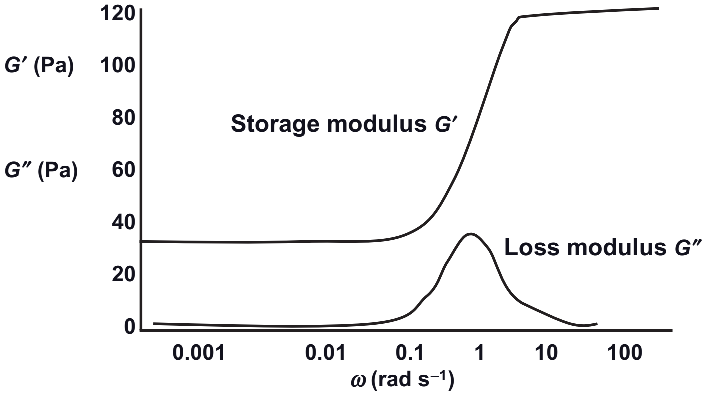

Figure 4.20 Schematic representation for oscillatory measurements for a viscoelastic solid.

For a viscoelastic solid, G' does not become zero at low frequency, but G'' still shows a maximum at intermediate frequency (as illustrated in Figure 4.20).

4.8.1.2 The Cohesive Energy Density E_c

The cohesive energy density, E_c, which is an important parameter for identification of the "strength" of the structure in a dispersion, can be obtained from the change of G' with γ_o (see Figure 4.18).

$$E_c = \int_0^{\dot{\gamma}_{cr}} \sigma \delta \gamma \tag{4.22}$$

where σ is the stress in the sample that is given by:

$$\sigma = G'\gamma \tag{4.23}$$

$$E_c = \int_0^{\gamma_{cr}} G' \gamma_{cr} \delta\gamma = \frac{1}{2} \gamma_{cr}^2 G' \tag{4.24}$$

Note here that the units of E_c are J m^{-3}.

4.8.1.3 The Weissenberg Effect and Normal Forces

An interesting phenomenon was observed many years ago by Weissenberg, who noted that, when a viscoelastic liquid is stirred in a pot, the liquid is drawn up the rotor shaft against the force of gravity. This was in contrast to a Newtonian liquid where, as a result of the centrifugal force, the liquid would be thrown outwards and upwards against the wall of the pot. The Weissenberg effect is clearly observed when stirring a dough, a polymer solution with a high molecular weight (e.g., polyacrylamide), or melt adhesives. With a viscoelastic liquid, the continuously rotating rotor creates concentric layers of the liquid with decreasing rotational speeds towards inwards–outwards. Within these layers, the molecules become disentangled and oriented in the direction of their particular layer and, in being viscoelastic, it can be assumed that those molecules on the outer layers would be stretched more than those nearer to the rotor. A higher degree of stretching also means a higher state of energy from which the molecules would tend to escape; indeed, the only possibility of escape for these stretched molecules is to move towards the rotor axis. However, if all of the molecules move inwards the region will become "crowded," such that the only escape route is upwards.

Hence, rotation causes not only a shear stress along the concentric layers, but also an additional stress – to be denoted "normal" stress – that acts perpendicular to the shear stress. The normal stress forces the viscoelastic liquid to move up the rotating shafts, so as to create a normal force that will try to separate the cone from the plate in a cone–plate geometry. This results in the liquid being sucked out of the gap and up onto the outer rim of the cone when the rotational speed is increased. The normal stress difference, N_1, can be determined by measurement of the normal force F_n, which tries to separate the cone from the lower plate when testing viscoelastic liquids. N_1 shows a linear increase with an increase of the shear rate. For a full analysis of normal stress, the reader is referred to the description provided by Barnes *et al.* [9]

4.8.2
Viscoelastic Measurements

Viscoelastic measurements (low deformation) require the use of sensitive rheometers that operate using an air bearing (drag-cup motor) in order to minimize friction (very low torques need to be applied). Consequently, three types of measurement can be performed (these are equivalent but not identical), all of which are complementary in their application [10]:

- Constant stress (creep) measurements
- Constant strain (stress relaxation) measurements
- Dynamic (oscillatory) measurements.

Currently, several rheometers are available commercially to perform the above measurements. The suppliers include: Bohlin Instruments (Malvern UK); Carrimed and Rheometric Instruments (TA, UK); Physica (Paar Physica, Germany); and Haake (Germany).

4.8.2.1 Constant Stress (Creep) Measurements

In these measurements, a constant stress σ is applied to the sample (usually electrically, via a motor attached to the drag-cup), and the strain $\gamma(t)$ or compliance $J(t)$ (= $\gamma(t)/\sigma$ in Pa^{-1}) is measured using a position sensor below the drag-cup motor). Both the controlled stress and controlled strain set-ups are shown schematically in Figure 4.21.

In this case, a controllable known torque is applied to the cone, and the resultant rate of rotation of the plate is measured. The temperature of the sample is usually controlled using a Peltier device, while a solvent trap for the cone and plate (which is most commonly used) is placed in position to cover the whole geometry.

Main Requirements for Constant Stress Measurements The main requirements for constant stress measurements are that:

- The applied torque should cover a reasonable range so as to allow the stress to be increased until flow occurs.
- There should be a low bearing fraction (i.e., the frictional torque should be two to three orders of magnitude lower than the applied torque).
- The instrument should be fully computer-controlled (with user-friendly software).
- The output of the $J(t)$ versus t curves should be automatically recorded until a steady state is reached (linear increase of $J(t)$ with t).
- The software should automatically calculate the viscosity η_σ at every σ applied, and plots of η_σ versus σ should be automatically displayed to obtain the limiting (residual or zero shear) viscosity $\eta(0)$ and critical stress ("true" yield value) σ_{cr}.

Procedure for Constant Stress Measurements For a given sample, it is not necessary to know *a priori* the critical stress σ_{cr} below which the material would show a near-elastic response (where the compliance shows a very slow increase with time after

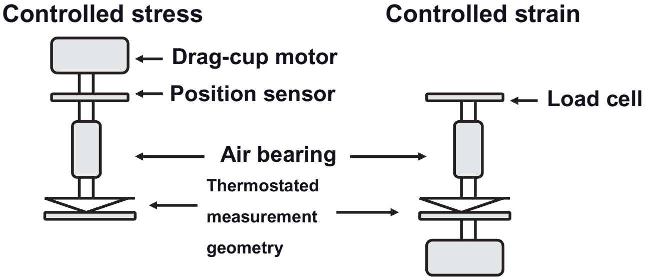

Figure 4.21 Controlled stress and controlled strain set-up.

the instantaneous increase and complete recovery after release of the stress). The slopes of $J(t)$ versus t below σ_{cr} are very small and equal; this gives $\eta(0)$ that is the reciprocal of this small slope (high viscosity values are obtained below σ_{cr}).

Initially, a sample should be used so as to roughly obtain σ_{cr} by applying large increments of σ (a log scale can be used). When σ_{cr} has been obtained, measurements are then carried on a new sample whereby reasonable σ-values are applied below and above σ_{cr}. In this way, several creep curves can be measured (about 10 curves are usually sufficient at σ-values below and above σ_{cr}). A schematic representation of the creep curves is shown in Figure 4.22.

Stress Relaxation (after Application of Constant Strain) In this case, the material is kept under constant deformation (constant shear rate) and the resulting stress is measured as a function of time. The main problem here is the speed with which a sudden strain is applied; typically, such application should be completed within a much shorter time than the relaxation time of the sample. Currently, very few strain-controlled instruments are produced commercially, with the "Fluid" rheometer of Rheometric Instruments possibly being the only instrument available (previously, Bohlin produced a strain-controlled instrument – the Bohlin VOR – but this is no longer available).

One of the earliest strain-controlled instruments to be produced was the Weissenberg Rheogoniometer, with a cone and plate attachment; this is currently produced by TA instruments.

One of the main problems associated with stress-relaxation experiments is the possibility of fluctuations in stress at short times, in particular for elastic samples. However, the above behavior can be explored by using "Stress Growth" experiments, where the application of a linearly ramped strain can provide information on both the sample viscosity and elasticity. As the stress will grow in proportion to the applied strain, the ratio of the strain over the applied time provides the shear rate. The variation of viscosity $\eta(t)$ versus time for a system represented by a Maxwell model with a relaxation time τ_r, is shown in Figure 4.23. The results can be analyzed to obtain the modulus $G(\infty)$ and the zero-shear viscosity $\eta(0)$.

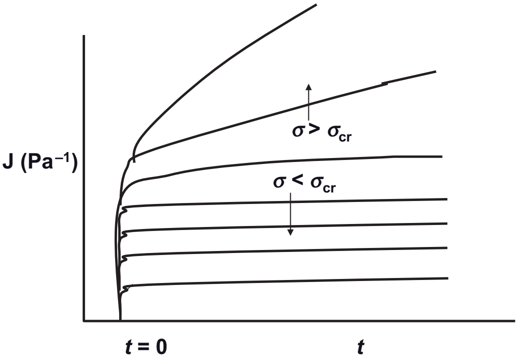

Figure 4.22 Schematic representation of creep curves.

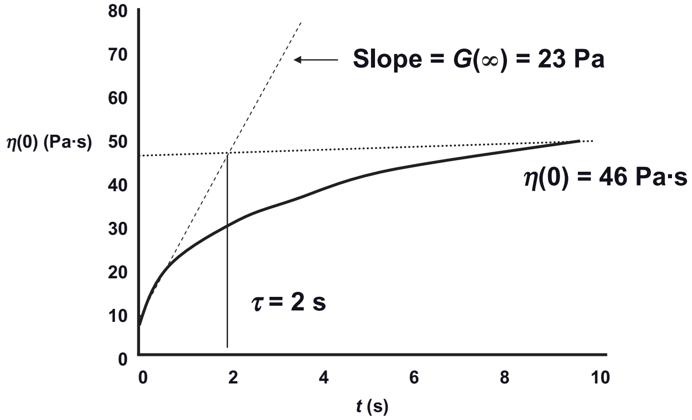

Figure 4.23 Stress growth function for a Maxwell model.

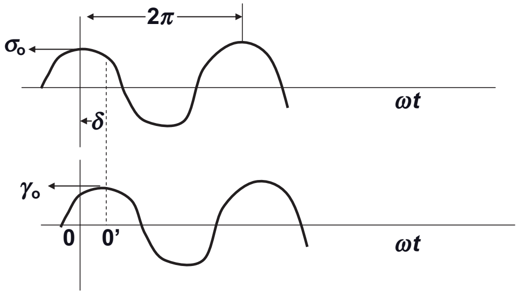

Figure 4.24 Stress and strain waveforms.

4.8.2.2 **Dynamic (Oscillatory) Measurements**

These refer to experiments in which both stress and strain vary harmonically. If a harmonic unique shear stress of amplitude σ_o is applied to the upper face of a thin block of material, the stress σ will produce a strain γ_o that is shifted by an angle δ (the phase angle shift) according to:

$$\sigma = \sigma_o \cos \omega t \tag{4.25}$$

$$\gamma = \gamma_o (\cos \omega t - \delta) \tag{4.26}$$

The above stress and strain waveforms are shown schematically in Figure 4.24 where, from σ_o, γ_o and δ, it is possible to calculate the storage modulus G' (the elastic component) and the loss modulus G'' (the viscous component):

$$G' = \frac{\sigma_o}{\gamma_o} \cos \delta \tag{4.27}$$

$$G'' = \frac{\sigma_o}{\gamma_o} \sin \delta \tag{4.28}$$

In dynamic measurements, the stress is proportional to the force F applied to the test material. The strain is proportional to the relative displacement of the bounding surfaces, while the shear rate is proportional to the relative velocity, v.

If the force and displacement vary harmonically:

$$F = bG^* x = b\eta^* v = \frac{bG^*}{i\omega} v \tag{4.29}$$

where F, x and v represent complex amplitudes, and b is a shape factor for the test material. The material can be confined between cone and plate, parallel plate or cylinders. In this case, one of the boundary surfaces is first oscillated, after which the motion of the other surface can be measured.

In the Bohlin VOR, for example, when using a concentric cylinder, the inner cylinder (the suspended member) is connected to interchangeable torque bars (to measure the stress). A sinusoidal strain is then applied to the cup by moving it back and forth in a sinusoidal manner, with the displacement being measured using a transducer.

If θ_2 and θ_1 are the angular positions of the driven and suspended elements, respectively, then the torque in the material M is:

$$M = bG^*(\theta_2 - \theta_1) \tag{4.30}$$

$$G' = \frac{1}{b}\frac{|M|}{\theta_2}\cos\phi \tag{4.31}$$

$$G'' = \frac{1}{b}\frac{|M|}{\theta_2}\sin\phi \tag{4.32}$$

where ϕ is the phase shift of the torque element relative to θ_2. Normally, the ratio $[\theta_1/\theta_2]$ is measured, together with the phase shift ϕ of the suspended element, to obtain both G' and G''. These computations are carried out using the computer's software.

As mentioned above, two types of measurement are carried out:

- **Strain sweep measurement:** In this case, the frequency is fixed at 1 Hz (or 6.28 rad s^{-1}), and the strain amplitude is then gradually increased from the lowest possible value to a critical value γ_{cr} (that depends on the system), above which the system shows a nonlinear response.
- **Oscillatory sweep measurements:** In this case, the strain is fixed below γ_{cr} (i.e., in the linear viscoelastic region, where the moduli are independent of the applied strain), and measurement is then carried out as a function of frequency. The range used depends on the system and the instrument; however, the majority of measurements are carried out in the range 10^{-2} to 1 Hz.

4.8.2.3 Shear Modulus (Rigidity) Measurement

The shear (rigidity) modulus can be measured by initiating a shear wave in the dispersion, and then measuring the damping of the wave [11, 12]. A simple instrument that can be used for this purpose is the Rank Brothers pulse shearometer (Bottisham,

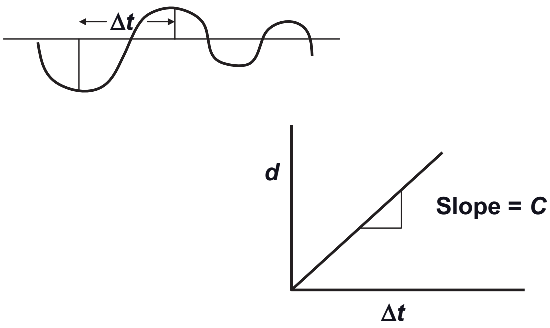

Figure 4.25 Schematic representation of a shear wave and variation of *d* with Δ*t*.

Cambridge, UK), where two disks (Perspex or steel) are placed in the dispersion and the inter-disk gap is changed using a micrometer. Each disk is connected to a transducer (A and B) constructed from piezoelectric crystals of LiCl. B is connected to a pulse generator that provides a small amplitude ($<10^{-4}$ rad) deformation with a high frequency (~200 Hz). The output from A is displayed (using a computer) to observe the shear wave; this is shown schematically in Figure 4.25.

A plot of *d* (the gap width between the plates) versus Δ*t* is linear, and the slope *C* of the graph gives the velocity of the shear wave. The rigidity (high-frequency) modulus $G(\infty)$ is simply given by the expression:

$$G(\infty) = \rho C^2 \tag{4.33}$$

where ρ is the density of suspension.

References

1 Reiner, M. (1968) *Phys. Today*, **17**, 62.
2 Ferry, J.D. (1980) *Viscoelastic Properties of Polymers*, John Wiley & Sons, Inc., New York.
3 Gross, B. (1968) *Mathematical Structures of the Theories of Viscoelasticity*, Hermann, Paris.
4 Mackosko, C.W. (1994) *Rheology: Principles, Measurement and Applications*, Wiley-VCH, New York.
5 Goodwin, J.W. (1984) The Microstructure and Rheology of Surfactants and Related Systems, in *Surfactants* (ed. T.F. Tadros), Academic Press, London, pp. 133–151.
6 Goodwin, J.W. and Hughes, R.W. (1992) *Adv. Colloid Interface Sci.*, **42**, 303.
7 Tadros, T.F. (1996) *Adv. Colloid Interface Sci.*, **68**, 97.
8 Goodwin, J.W. and Hughes, R.W. (2000) *Rheology for Chemists*, Royal Society of Chemistry Publication, Cambridge.
9 Barnes, H.A., Hutton, J.F., and Walters, K. (1996) *An Introduction to Rheology*, Elsevier, Amsterdam.
10 Wohrlow, R.W. (1980) *Rheological Techniques*, John Wiley & Sons, Inc., New York.
11 van Olphen, H. (1956) *Clays Clay Minerals*, **4**, 204.
12 Goodwin, J.W. and Khider, A.M. (1976) *Colloid and Interface Science*, vol. **IV** (ed. M. Kerker), Academic Press, New York, p. 529.

5
Rheology of Suspensions

5.1
Introduction

Rheological measurements are useful tools for probing the microstructure of suspensions, and this is particularly the case if measurements are carried out at low stresses or strains, as discussed in Chapter 4. In this situation, the spatial arrangement of particles is only slightly perturbed by the measurement; in other words, the convective motion due to the applied deformation is less than the Brownian diffusion. The ratio of the stress applied (σ) to the "thermal stress" (that is equal to $kT/6\pi a^3$, where k is the Boltzmann constant, T is the absolute temperature and a is the particle radius) is defined in terms of a dimensionless Peclet number P_e:

$$P_e = \frac{6\pi a^3 \sigma}{kT} \tag{5.1}$$

For a colloidal particle with radius of 100 nm, σ should be less than 0.2 Pa to ensure that the microstructure is relatively undisturbed; in this case, $P_e < 1$.

In order to remain in the linear viscoelastic region, the structural relaxation by diffusion must occur on a time scale comparable to the experimental time. As mentioned in Chapter 4, the ratio of the structural relaxation time to the experimental measurement time is given by the dimensionless Deborah number, D_e, which is ~1 and the suspension appears viscoelastic.

The rheology of suspensions depends on the balance between three main forces: Brownian diffusion; hydrodynamic interaction; and interparticle forces (the latter was discussed in detail in Chapter 2).

The above forces are determined by three main parameters: (i) the volume fraction ϕ (total volume of the particles divided by the volume of the dispersion); (ii) the particle size and shape distribution; and (iii) the net energy of interaction G_T; that is, the balance between repulsive and attractive forces.

The earliest theory for prediction of the relationship between the relative viscosity η_r and ϕ was described by Einstein, which is applicable to $\phi \leq 0.01$.

Rheology of Dispersions: Principles and Applications. Tharwat F. Tadros

ISBN: 978-3-527-32003-5

5.2
The Einstein Equation

Einstein [1] assumed that the particles behave as hard-spheres (with no net interaction). Thus, the flow field must dilate because the liquid must move around the flowing particles. At $\phi \leq 0.01$, the disturbance around one particle does not interact with the disturbance around another particle.

η_r is related to ϕ by the following Equation 5.2:

$$\eta_r = 1 + [\eta]\phi = 1 + 2.5\phi \tag{5.2}$$

where $[\eta]$ is referred to as the intrinsic viscosity and has the value 2.5.

For the above hard-sphere, very dilute dispersions, the flow is Newtonian – that is, the viscosity is independent of the shear rate. However, at higher ϕ-values ($0.2 > \phi > 0.1$) it is necessary to consider the hydrodynamic interaction (as suggested by Bachelor [2]) that is still valid for hard-spheres.

5.3
The Bachelor Equation

When $\phi > 0.01$, hydrodynamic interaction between the particles become important. Typically, when the particles come close to each other, the nearby stream lines and the disturbance of the fluid around one particle interacts with that around a moving particle.

By using the above picture, Bachelor [2] derived the following expression for the relative viscosity:

$$\eta_r = 1 + 2.5\phi + 6.2\phi^2 + O\phi^3 \tag{5.3}$$

The third term in Equation 5.3 (i.e., $6.2\,\phi^2$) is the hydrodynamic term, whereas the fourth term is due to higher-order interactions.

5.4
Rheology of Concentrated Suspensions

When $\phi > 0.2$, η_r becomes a complex function of ϕ. At such high volume fractions, the system mostly shows non-Newtonian flow ranging from viscous to viscoelastic to elastic response, depending on the Deborah number D_e. In this respect, three responses can be considered: (i) a viscous response, when $D_e < 1$; (ii) an elastic response, when $D_e > 1$; and (iii) a viscoelastic response, when $D_e \sim 1$.

Clearly, the above responses for any suspension depend on the time or frequency of the applied stress or strain (see Chapter 4).

Four different types of system (with increasing complexity) can be considered, as described below.

- **Hard-sphere suspensions:** These are systems where both repulsive and attractive forces are screened.
- **Systems with "soft" interaction:** These systems contain electrical double layers with a long-range repulsion. The rheology of the suspension is determined mainly by the double-layer repulsion.
- **Sterically stabilized suspensions:** Here, the rheology is determined by the steric repulsion produced by adsorbed nonionic surfactant or polymer layers. The interaction can be either "hard" or "soft," depending on the ratio of the adsorbed layer thickness to particle radius (δ/R).
- **Flocculated systems:** These are systems where the net interaction is attractive. A distinction can be made between weak (reversible) and strong (irreversible) flocculation, depending on the magnitude of the attraction.

5.5
Rheology of Hard-Sphere Suspensions

Hard-sphere suspensions (neutral stability) were developed by Krieger and coworkers [3, 4] by using polystyrene latex suspensions, whereby the double-layer repulsion was screened using NaCl or KCl at a concentration of 10^{-3} mol dm^{-3}, or by replacing water with a less-polar medium such as benzyl alcohol.

The relative viscosity η_r (= η/η_o) is plotted as a function of reduced shear rate (shear rate × time for a Brownian diffusion, t_r):

$$\dot{\gamma}_{\text{red}} = \dot{\gamma} t_r = \frac{6\pi\dot{\gamma}a^3}{kT} \tag{5.4}$$

where a is the particle radius, η_o is the viscosity of the medium, k is the Boltzmann constant, and T is the absolute temperature.

A plot of (η/η_o) versus ($\eta_o a^3/kT$) is shown in Figure 5.1 at $\phi = 0.4$ for particles with different sizes. In this case, at a constant ϕ all points fall on the same curve; however, the curves are shifted to higher values for larger ϕ, and to lower values for smaller ϕ.

The curve in Figure 5.1 shows two limiting (Newtonian) viscosities at low and high shear rates that are separated by a shear thinning region. In the low shear rate regime, the Brownian diffusion predominates over hydrodynamic interaction, and the system shows a "disordered" three-dimensional (3-D) structure with a high relative viscosity. However, as the shear rate is increased, these disordered structures start to form layers that are coincident with the plane of shear, and this results in the shear thinning region. In the high-shear rate regime, the layers can "slide" freely, and hence a Newtonian region (with a much lower viscosity) is obtained. In this region the hydrodynamic interaction predominates over the Brownian diffusion.

If the relative viscosity in the first or second Newtonian region is plotted versus the volume fraction, then the curve shown in Figure 5.2 is obtained. This curve

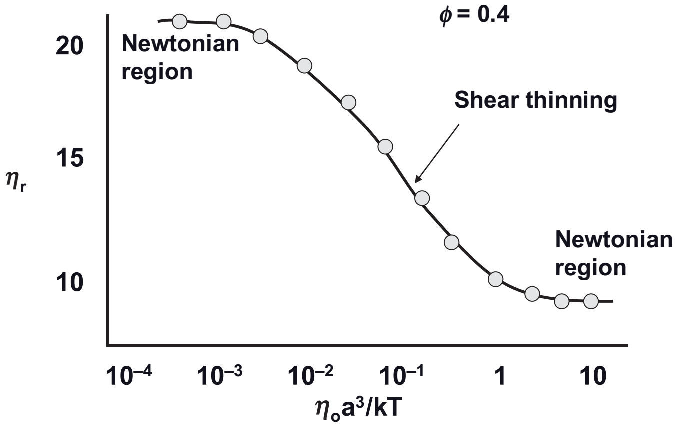

Figure 5.1 Reduced viscosity versus reduced shear rate for hard-sphere suspensions.

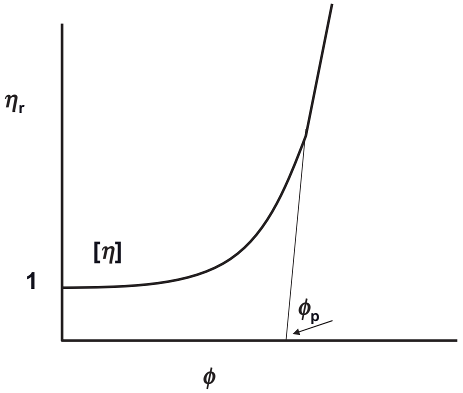

Figure 5.2 Relative viscosity versus volume fraction for hard-sphere suspensions.

has two asymptotes: (i) The slope of the linear portion at low ϕ-values (the Einstein region) that gives the intrinsic viscosity [η] that is equal to 2.5; and (ii) the asymptote that occurs at a critical volume fraction ϕ_p at which the viscosity shows a sharp increase with increase in ϕ.

Here, ϕ_p is referred to as the maximum packing fraction for hard-spheres; for the hexagonal packing of equal-sized spheres, $\phi_p = 0.74$, whereas for random packing of equal-sized spheres, $\phi_p = 0.64$

For polydisperse systems, ϕ_p reaches higher values, as illustrated in Figure 5.3 for one-size, two-size, three-size, and four-size suspensions.

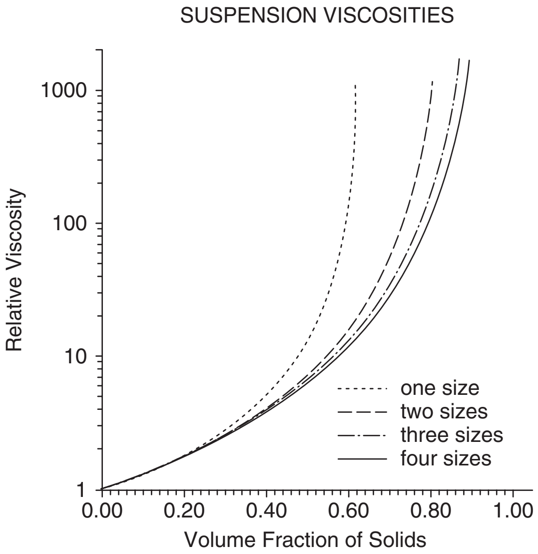

Figure 5.3 Viscosity–volume fraction curves for polydisperse suspensions.

5.5.1
Analysis of the Viscosity–Volume Fraction Curve

The best analysis of the $\eta_r - \phi$ curve is due to Krieger and Dougherty [3], who used a mean field approximation by calculating the increase in viscosity as small increments of the suspension were consecutively added. Each added increment corresponded to replacement of the medium by more particles. As a result, Krieger and Dougherty arrived at the following simple semi-empirical equation that could fit the viscosity data over the whole volume fraction range:

$$\eta_r = \left(1 - \frac{\phi}{\phi_p}\right)^{-[\eta]\phi_p} \tag{5.5}$$

Equation 5.5, which is referred to as the Dougherty–Krieger equation, is commonly used for the analysis of viscosity data.

5.6
Rheology of Systems with "Soft" or Electrostatic Interaction

In this case, the rheology is determined by the double-layer repulsion, particularly with small particles and extended double layers [5]. In the low-shear rate regime, the viscosity is determined by the Brownian diffusion, where the particles approach

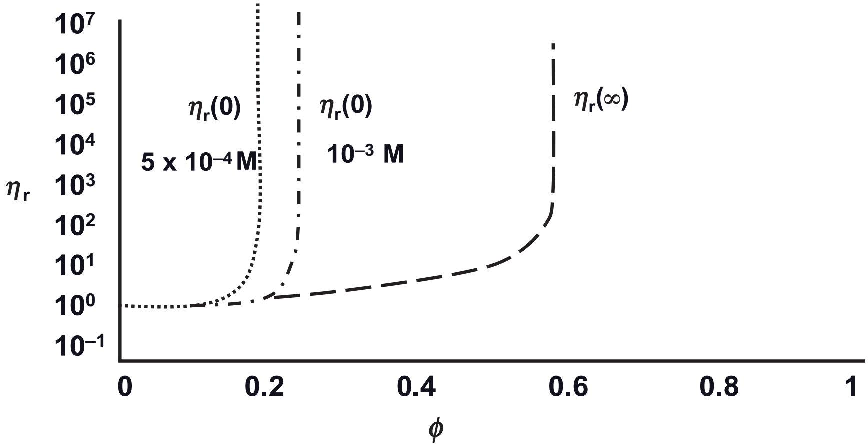

Figure 5.4 Variation of η_r with ϕ for polystyrene latex dispersions at two NaCl concentrations.

each other to a distance of the order of ~4.5 κ^{-1} (where κ^{-1} is the "double-layer thickness" that is determined by electrolyte concentration and valency). This means that the effective radius of the particles R_{eff} is much higher than the core radius R. For example, in the case of 100 nm particles with a zeta-potential (ζ) of 50 mV dispersed in a medium of 10^{-5} mol dm^{-3} NaCl (κ^{-1} = 100 nm), the R_{eff} will be approximately 325 nm.

The effective volume fraction ϕ_{eff} is also much higher than the core volume fraction, and this results in rapid increase in the viscosity at low core volume fraction [5]. This is illustrated in Figure 5.4, which shows the variation of η_r with ϕ at 5×10^{-4} and 10^{-3} mol dm^{-3} NaCl (R = 85 nm and ζ = 78 mV).

The low shear viscosity $\eta_r(0)$ shows a rapid increase at $\phi \sim 0.2$ (the increase occurs at a higher volume fraction at the higher electrolyte concentration), whereas at $\phi > 0.2$ the system shows "solid-like" behavior, with $\eta_r(0)$ reaching very high values (>107). At such high ϕ-values the system will show a near-plastic flow.

In the high-shear rate regime, the increase in η_r occurs at much higher ϕ-values; this is illustrated from the plot of the high-shear relative viscosity $\eta_r(\infty)$ versus ϕ. At such high shear rates, hydrodynamic interactions will predominate over the Brownian diffusion, and the system will show a low viscosity, denoted by $\eta_r(\infty)$. However, when ϕ reaches a critical value, pseudoplastic flow will be observed.

5.6.1
Viscoelastic Behavior of Electrostatically Stabilized Suspensions

One of the most powerful techniques used to study the interaction in electrostatically stabilized suspensions is that of dynamic (oscillatory) measurements [6, 7]. This process is illustrated in Figure 5.5, which shows the variation of the complex modulus G^*, storage (elastic) modulus G', and loss (viscous) modulus G'' versus

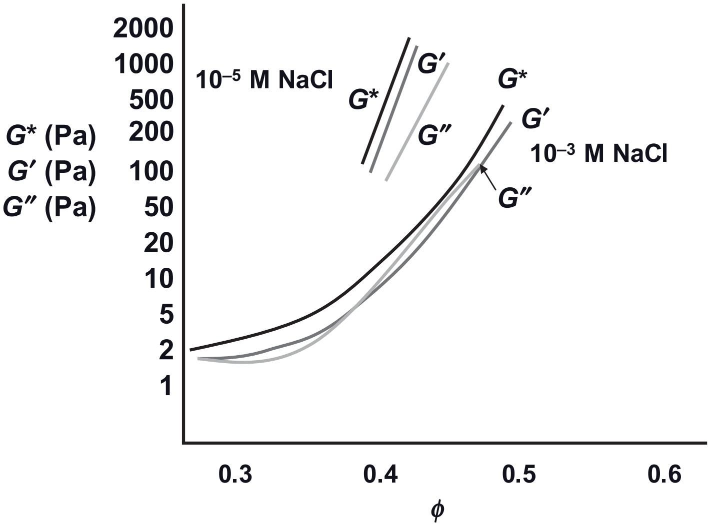

Figure 5.5 Variation of G^*, G' and G'' with ϕ for electrostatically stabilized latex dispersions.

core latex (with radius of 700 nm) volume fraction ϕ. The moduli were measured at low strain (in the linear region) and high frequency (1 Hz).

The trends obtained were seen to depend on the NaCl concentration. For example, at a concentration of 10^{-5} mol dm^{-3} the moduli values increased very rapidly at $\phi > 0.46$ and $G' \gg G''$. However, at 10^{-3} mol dm^{-3} the moduli values showed a rapid increase at $\phi > 0.57$, and G'' was either lower than or equal to G'.

The above trend reflect the larger ϕ_{eff} values at low NaCl (with more extended double layer) when compared to the higher NaCl concentration (with a smaller extension). Such trends can be explained by considering the presence of the double layer around the particles. At a first approximation, the double-layer thickness $(1/\kappa)$ should be added to the particle radius a so as to obtain the effective radius, a_{eff}. At any given particle size, a_{eff} will depend on the electrolyte concentration C (and valency Z), as the double-layer thickness is determined by both C and Z. At a concentration of 10^{-5} mol dm^{-3} NaCl, $(1/\kappa) = 100$ nm and $a_{\text{eff}} = 700 + 100 = 800$ nm, whereas at 10^{-3} mol dm^{-3}, $(1/\kappa) = 10$ nm and $a_{\text{eff}} = 710$ nm.

The effective volume fraction of the dispersion, ϕ_{eff}, is related to ϕ by the expression:

$$\phi_{\text{eff}} = \phi\left[1 + \frac{(1/\kappa)}{a}\right]^3 \tag{5.6}$$

At a NaCl concentration of 10^{-5} mol dm^{-3}, $\phi_{\text{eff}} = 1.5\,\phi$, whilst at the lowest ϕ-value studied (i.e., 0.46 , $\phi_{\text{eff}} = 0.7$, which is above the maximum packing fraction (0.64 for random packing). In this case, the double layer interaction is strong and some overlap of the double layers may occur, and the response in this situation is predominantly elastic. At the highest volume fraction studied (i.e., 0.524 , $\phi_{\text{eff}} = 0.79$

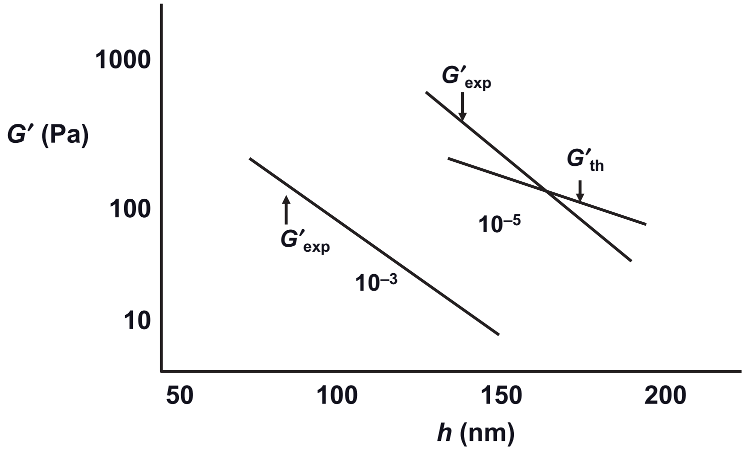

Figure 5.6 Plots of G'_{th} and G'_{exp} at 10^{-5} and 10^{-3} mol dm^{-3} NaCl.

and the dispersion behaves as a near-elastic solid; in this case, $G' \sim G^*$. In 10^{-3} mol dm^{-3} NaCl, $\phi_{eff} = 1.05\,\phi$ and up to the maximum volume fraction studied (namely 0.566), ϕ_{eff} is well below the maximum packing fraction. In this case, there is little overlap of the double layers and the dispersions show a more viscous than an elastic response. In order to achieve a predominantly elastic response, the volume fraction must be increased above 0.6.

5.6.1.1 Elastic Modulus (*G′*)–Distance (*h*) Relation

The above results may be presented in another form by plotting G' versus h, the surface-to-surface separation between the particles in the dispersion [8, 9]:

$$h = 2a\left[\left(\frac{\phi_p}{\phi}\right)^{1/3} - 1\right] \tag{5.7}$$

A value of $\phi_p = 0.68$ was used in the above calculation of the surface-to-surface separation distance. Figure 5.6 shows plots of G' versus h for 10^{-5} and 10^{-3} mol dm^{-3} NaCl. At the lower NaCl concentration (10^{-5} mol dm^{-3}), G' increased very rapidly when h was decreased to less than 200 nm (twice the double-layer thickness), but reached very high values (>1000 Pa) when h was less than 100 nm. However, at a NaCl concentration of 10^{-3} mol dm^{-3}, high values of G' were achieved only when h was <50 nm.

It is clear from Figure 5.6 that, at any given value of h, G' in 10^{-5} mol dm^{-3} NaCl is several orders of magnitude higher than the corresponding value in 10^{-3} mol dm^{-3} NaCl. This trend is a direct consequence of the double-layer repulsion which, at any given distance of separation, is much stronger at the lower electrolyte concentration.

It is possible to relate the high-frequency modulus, G_o, to the total energy of interaction between the particles, G_T:

$$G_o = \left(\frac{a}{d}\right)\left(\frac{\partial^2 G_T}{\partial d^2}\right) \tag{5.8}$$

$$\alpha = \left(\frac{3}{32}\right)\phi_p n \tag{5.9}$$

where n is the coordination number and d is the distance of separation between the centers of the particles ($d = 2a + h$).

The total energy of interaction (mainly the double layer repulsion) is given by the expression:

$$G_T = \frac{4\pi\varepsilon\varepsilon_o\psi_d^2}{d}\exp[-\kappa(d-2a)] \tag{5.10}$$

where ε is the permittivity of the medium, ε_o is the permittivity of free space, and ψ_d is the Stern potential.

By differentiating Equation 5.10 twice, it is possible to obtain the theoretical shear modulus, G'_{th}:

$$G'_{th} = 4\pi\varepsilon\varepsilon_o a^2\psi_d^2\left(\frac{\kappa^2 d^2 + 2\kappa d + 2}{d^4}\right)\exp[-(\kappa(d-2a))] \tag{5.11}$$

Values of G'_{th} were calculated for dispersions in 10^{-5} mol dm^{-3} NaCl ($\kappa a < 10$), as these were highly elastic and the modulus showed little dependence on frequency; a value of $\alpha = 0.833$ was used in these calculations, the results of which are shown in Figure 5.6. The theoretical G'-values were seen to increase less rapidly with a decrease of h when compared to the experimental results. The calculation of G'_{th}, using Equation 5.11, is based on a number of assumptions (which may not be completely valid), and the latex dispersions used were relatively large (700 nm). The strains used may not be sufficiently small to ensure that the measurements were made in the linear viscoelastic region.

5.6.1.2 **Scaling Laws for Dependence of G′ on ϕ**

Another useful way to describe the interaction in concentrated dispersions is to apply scaling laws for the dependence of G′ on ϕ (Equation 5.10):

$$G' = k\phi^n \tag{5.12}$$

In other words, the storage modulus scales with ϕ with an exponent n which depends on the interparticle interaction. The power n can be obtained from log–log plots of G' versus ϕ; in 10^{-5} mol dm^{-3} NaCl, $n = 20$, whereas in 10^{-3} mol dm^{-3} NaCl, $n = 30$, with the lower power at the lower electrolyte concentration reflecting the softness of the interaction as a result of the extended double layers. At the higher electrolyte concentration, the double layer is significantly compressed and the dispersions behave as near-hard-spheres.

5.6.2
Control of Rheology of Electrostatically Stabilized Suspensions

Notably, three main parameters control the rheology of electrostatically stabilized suspensions: (i) the volume fraction of the dispersion ϕ; (ii) the particle size (a) and shape distribution; and (iii) the electrolyte concentration (C) and valency.

In order to produce dispersions with high ϕ-values with minimal elasticity in the system, it is necessary to increase a and to add small amounts of electrolyte (well below the flocculation value). In this case, the double-layer thickness will be small compared to the particle radius, and $\phi_{\mathrm{eff}} \sim \varphi$. In contrast, to produce dispersions with a high elasticity (and order) at low volume fractions, the particle radius (a) should be kept as small as possible, and the electrolyte concentration (C) as low as possible.

The above principles are applied in practice to many industrial dispersions, for example, charged lattices. These principles can also be applied to the formulation of many chemical products, including paints, personal care products, agrochemicals, and pharmaceuticals. In all of these cases, it is essential to realize the various physico-chemical parameters in the system, in order to control the rheology.

5.7
Rheology of Sterically Stabilized Dispersions

These are dispersions where the particle repulsion results from the interaction between adsorbed or grafted layers of nonionic surfactants or polymers [10]. The flow is determined by the balance of viscous and steric forces. Steric interaction is repulsive as long as the Floury–Huggins interaction parameter $\chi < ½$ (see Chapter 2). With short chains, the interaction may be represented by a hard-sphere-type with $a_{\mathrm{eff}} = a + \delta$. This is particularly the case with nonaqueous dispersions with an adsorbed layer of thickness that is smaller compared to the particle radius (any electrostatic repulsion is negligible in this case). With most sterically stabilized dispersions, the adsorbed or grafted layer has an appreciable thickness (compared to the particle radius); hence, the interaction is "soft" in nature as a result of the longer range of interaction.

Results for aqueous sterically stabilized dispersions were produced using polystyrene (PS) latex with grafted poly(ethylene oxide) (PEO) layers [11]. As an illustration, Figure 5.7 shows the variation of η_r with ϕ for latex dispersions with three particle radii (77.5, 306, and 502 nm). For comparison, the $\eta_r - \phi$ curve calculated using the Dougherty–Krieger equation is shown on the same figure. The $\eta_r - \phi$ curves are shifted to the left as a result of the presence of the grafted PEO layers.

The experimental relative viscosity data may be used to obtain the grafted polymer layer thickness at various volume fractions of the dispersions. By using the Dougherty–Krieger equation, it is possible to obtain the effective volume fraction of the dispersion; then from a knowledge of the core volume fraction, the grafted layer thickness can be calculated at each dispersion volume fraction.

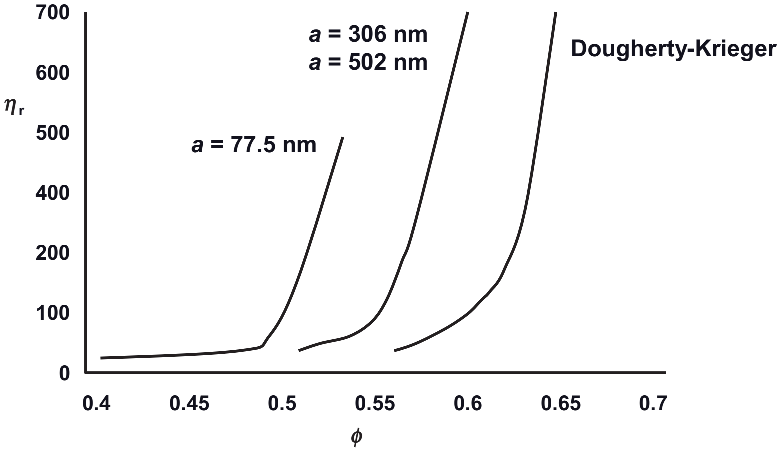

Figure 5.7 $\eta_r - \phi$ curves for polystyrene latex dispersions containing grafted PEO chains.

To apply the Dougherty–Krieger equation, it is necessary to know the maximum packing fraction, ϕ_p. This can be obtained from a plot of $1/(\eta_r)^{1/2}$ versus ϕ and extrapolation to $1/(\eta_r)^{1/2}$, using the following empirical equation:

$$\frac{K}{\eta_r^{1/2}} = \phi_p - \phi \tag{5.13}$$

The value of ϕ_p using Equation 5.13 was found to be in the range 0.6 to 0.64, while the intrinsic viscosity $[\eta]$ was assigned a value of 2.5.

Using the above calculations, the grafted PEO layer thickness δ was calculated as a function of ϕ for the three latex dispersions. For the dispersions with $a = 77.5$ nm, δ was found to be 8.1 nm at $\phi = 0.42$, decreasing to 5.0 nm when ϕ was increased to 0.543. For the dispersions with $a = 306$ nm, δ was 12.0 nm at $\phi = 0.51$, decreasing to 10.1 when ϕ was increased to 0.60. For the dispersions with $a = 502$ nm, δ was 21.0 nm at $\phi = 0.54$, decreasing to 14.7 as ϕ was increased to 0.61.

5.7.1
Viscoelastic Properties of Sterically Stabilized Suspensions

The rheology of sterically stabilized dispersions is determined by the steric repulsion, particularly for small particles with "thick" adsorbed layers. This is illustrated in Figure 5.8, which shows the variation of G^*, G' and G'' with frequency ω (Hz) for polystyrene latex dispersions of 175 nm radius containing grafted PEO with a molecular weight of 2000 Da (giving a hydrodynamic thickness $\delta \sim 20$ nm) [12]. The results clearly show the transition from a predominantly viscous response when $\phi \leq 0.465$ to a predominantly elastic response when $\phi \geq 0.5$. This behavior reflects the steric interaction between the PEO layers. When the surface-to-surface

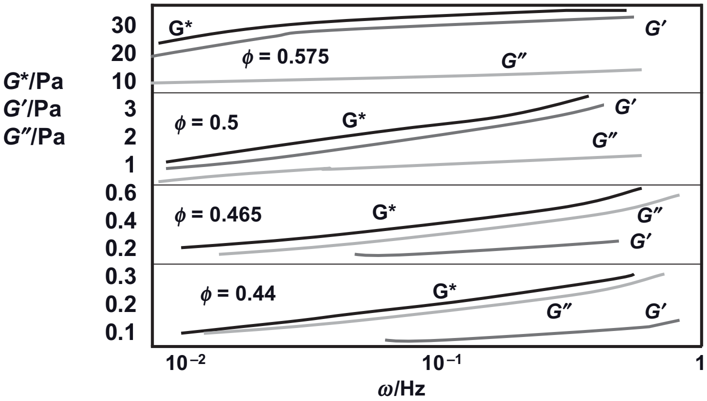

Figure 5.8 Variation of G^*, G' and G'' with frequency for sterically stabilized dispersions.

distance (h) between the particles becomes $<2\delta$, an elastic interaction will occur and $G' > G''$.

The exact volume fraction at which a dispersion changes from a predominantly viscous to a predominantly elastic response may be obtained from plots of G^*, G' and G'' (at fixed strain in the linear viscoelastic region and fixed frequency) versus the volume fraction of the dispersion. This is illustrated in Figure 5.9, which shows the results for the above latex dispersions. At $\phi = 0.482$, $G' = G''$ (sometimes referred to as the "crossover point"), which corresponds to $\phi_{\text{eff}} = 0.62$ (close to maximum random packing). At $\phi > 0.482$, G' becomes progressively larger than G'', and ultimately the value of G' approaches G^* and G'' becomes relatively much smaller than G'. At $\phi = 0.585$, $G' \sim G^* = 4.8 \times 10^3$ Pa, and at $\phi = 0.62$, $G' \sim G^* = 1.6 \times 10^5$ Pa. Such high elastic moduli values indicate that the dispersions behave as near-elastic solids ("gels") as a result of interpenetration and/or compression of the grafted PEO chains.

5.7.2
Correlation of the Viscoelastic Properties of Sterically Stabilized Suspensions with Their Interparticle Interactions

For this purpose, the energy $E(D)$–distance D curve is determined for two mica cross-cylinders containing an adsorbed graft copolymer consisting of a poly(methylmethacrylate) (PMMA) backbone with PEO chains (with a similar molecular weight as that used in latex) [13–16].

The force between mica surfaces bearing the copolymer is converted to interaction energy between flat surfaces using the Derjaguin approximation:

$$E(D) = \frac{F(D)}{2\pi a} \tag{5.14}$$

where D is the surface separation and a is the cylinder radius.

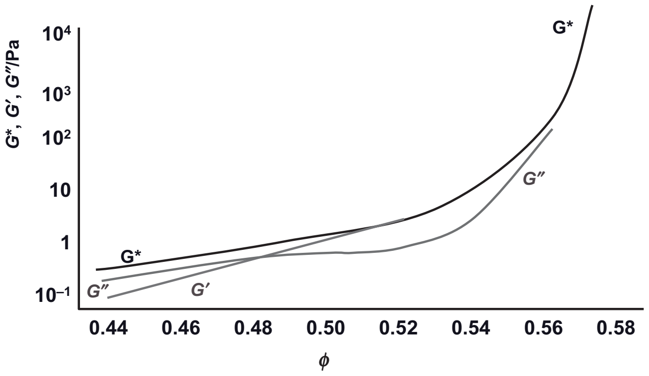

Figure 5.9 Variation of G^*, G' and G'' (at $\omega = 1$ Hz) with ϕ for latex dispersions (a = 175 nm) containing grafted PEO chains.

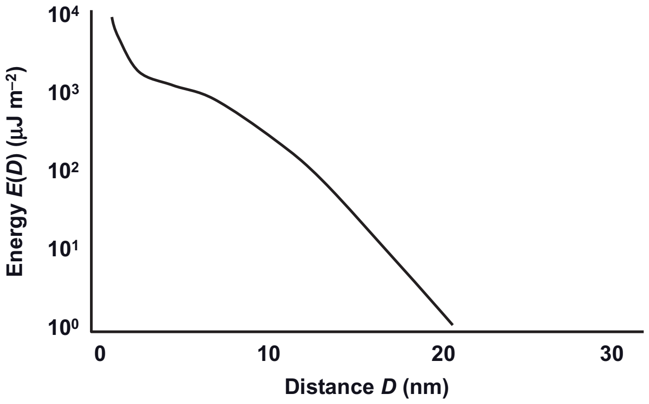

Figure 5.10 Interaction energy $E(D)$ versus separation distance D.

Figure 5.10 shows the energy–distance curve for mica sheets covered with the graft copolymer, where the PEO side chain has molecular weight of 750 Da. The figure demonstrates a monotonic exponential decrease of $E(D)$ with increasing surface separation. Steric interaction starts at $D \sim 25$ nm, which corresponds to an adsorbed layer thickness of ~12.5 nm. The same copolymer was used as a steric stabilizer for latex dispersions (with a particle radius of 165 nm) for subsequent rheological measurements.

By using the de Gennes scaling theory [17], it is possible to calculate $E(D)$ as a function of D:

$$E(D) = \frac{\beta kT}{s^3}\left[\frac{(2L)^{2.25}}{1.25(D)^{1.25}} + \frac{D^{1.75}}{1.75(2L)^{0.75}}\right] - \left[\frac{2L}{1.25} + \frac{2L}{1.75}\right] \tag{5.15}$$

where L is the stabilizer thickness on each layer, s is the distance between the side chain attachment points, k is the Boltzmann constant, T is the absolute temperature, and β is a numerical prefactor. When L was taken to be 12.5 nm, this gave a good agreement between theory and experiment.

The high-frequency modulus G_∞ was calculated using the following equation:

$$G_\infty = NkT + \frac{\phi_m n}{5\pi R^2}\left[4\frac{dV(R)}{dR} + R\frac{d^2V(R)}{dR^2}\right] \tag{5.16}$$

where $V(R)$ is the potential of mean force, n is the coordination number, and ϕ_m is the maximum packing fraction.

5.7.3
The High-Frequency Modulus–Volume Fraction Results

The results of Figure 5.10 are given as interaction energy between flat plates, but can be converted to the force between spheres by using the Derjaguin approximation:

$$G_\infty = NkT - \frac{\phi n a}{5R^2}\left[4E(D) + R\frac{dE(D)}{dD}\right] \tag{5.17}$$

By using Equation 5.15 for $E(D)$, it is possible to calculate G'_∞ as a function of the core volume fraction ϕ. The results of these calculations are shown in Figure 5.11, together with the experimental data. Although Figure 5.11 shows the expected trend of variation of G'_∞ with ϕ, the calculated values are about two orders of

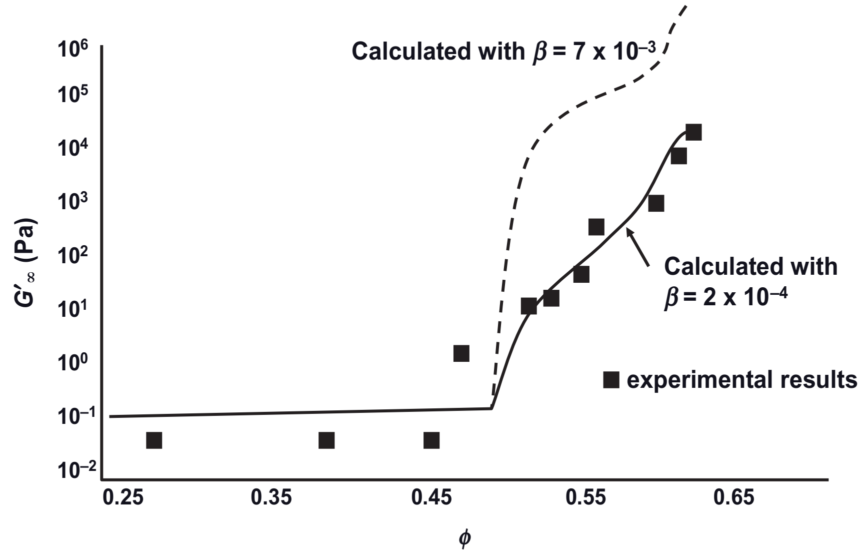

Figure 5.11 G'_∞ versus ϕ.

magnitude higher than the experimental results. Yet, by adjusting the numerical prefactor it is possible to obtain a good agreement between theory and experiment, as indicated by the solid line in Figure 5.11.

5.8
Rheology of Flocculated Suspensions

The rheology of unstable systems poses problems both from the experimental and theoretical points of view. This is due to the nonequilibrium nature of the structure, resulting from the weak Brownian motion [18]. For this reason, advances in the rheology of suspensions, where the net energy is attractive, have been slow and of only a qualitative nature. On the practical side, controlling the rheology of flocculated and coagulated suspensions is difficult, as the rheology depends not only on the magnitude of the attractive energies but also how the flocculated or coagulated structures in question are arrived at. As mentioned in Chapter 2, a variety of structures can be formed, including compact flocs, weak and metastable structures, and chain aggregates. At a high volume fraction of the suspension, a "3-D" network of the particles is formed throughout the sample; however, under shear this network is broken into smaller units of flocculated spheres which can withstand the shear forces [19]. The size of the units that survive is determined by the balance of shear forces which tend to break the units down, and the energy of attraction that holds the spheres together [20–22]. The appropriate dimensionless group characterizing this process (a balance of viscous and van der Waals forces) is $\eta_{\mathrm{o}} a^{4\dot{\gamma}}/A$ (where η_{o} is the viscosity of the medium, a is the particle radius, $\dot{\gamma}$ is the shear rate, and A is the effective Hamaker constant).

Each flocculated unit is expected to rotate in the shear field, and it is likely that these units will tend to form layers as individual spheres do. As the shear stress increases, each rotating unit will ultimately behave as an individual sphere and, therefore, a flocculated suspension will show pseudoplastic flow with the relative viscosity approaching a constant value at high shear rates. The viscosity–shear rate curve will also show a pseudo-Newtonian region at low and high shear rates (similar to the case with stable systems, as described above). However, the values of the low- and high-shear rate viscosities η_{o} and η_{∞}) will, of course, depend on the extent of flocculation and the volume fraction of the suspension. It is also clear that such systems will show an apparent yield stress (Bingham yield value, σ_{β}) which normally is obtained by an extrapolation of the linear portion of the $\sigma^{-\dot{\gamma}}$ curve to $\dot{\gamma} = 0$. Moreover, as the structural units of a weakly flocculated system change with change in shear rate, most flocculated suspensions will show thixotropy (as discussed in Chapter 3). Once shear has been initiated, a finite time is required to break the network of agglomerated flocs into smaller units which persist under the shear forces applied. As smaller units are formed, some of the liquid entrapped in the flocs will be liberated, thereby reducing the effective volume fraction, ϕ_{eff}, of the suspension. This reduction in ϕ_{eff} is accompanied by a reduction in η_{eff}, and this plays a major role in generating thixotropy.

It is convenient to distinguish between two types of unstable system, depending on the magnitude of the net attractive energy:

- **Weakly flocculated suspensions:** The attraction in this case is weak (energy of few kT units) and reversible, for example, in the secondary minimum of the DLVO curve or the shallow minimum obtained with sterically stabilized systems. A particular case of weak flocculation is that obtained on the addition of a "free" (nonadsorbing) polymer, referred to as "depletion flocculation."
- **Strongly flocculated (coagulated) suspensions:** The attraction in this case is strong (involving energies of several hundreds of kT units) and irreversible. This is the case of flocculation in the primary minimum (see Chapter 2), or of those flocculated by a reduction in the solvency of the medium (for sterically stabilized suspensions) to worse than a θ-solvent (see Chapter 2).

Studies of the rheology of flocculated suspensions are difficult, as the structure of the flocs is at nonequilibrium. Theories for flocculated suspensions are also qualitative, and based on a number of assumptions.

5.8.1
Weakly Flocculated Suspensions

As mentioned in Chapter 2, weak flocculation may be obtained by the addition of a "free" (nonadsorbing) polymer to a sterically stabilized dispersion [10]. Several rheological investigations of such systems have been carried out by Tadros and collaborators [23–27], and this is exemplified by a latex dispersion containing grafted PEO chains of M = 2000 to which "free" PEO is added at various concentrations. The grafted PEO chains were made sufficiently dense to ensure the absence of any adsorption of the added free polymer. Three PEOs of different molecular weights were used, namely 20 000 Da, 35 000 Da, and 90 000 Da. For illustrative purposes, Figures 5.12–5.14 show the variation in the Bingham yield value σ_β with the volume

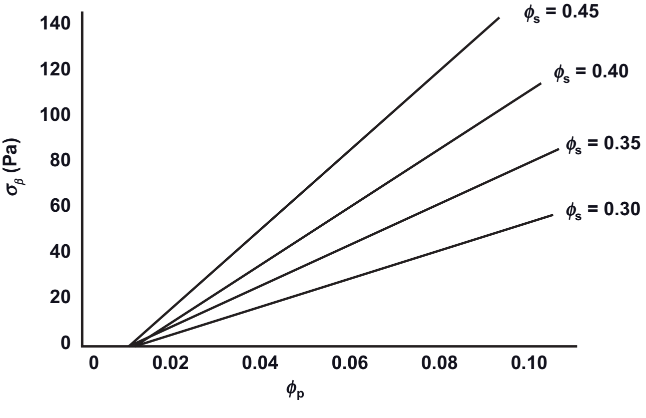

Figure 5.12 Variation of yield value σ_β with volume fraction ϕ_p of "free polymer" (PEO; M = 20 000) at various latex volume fractions ϕ_s.

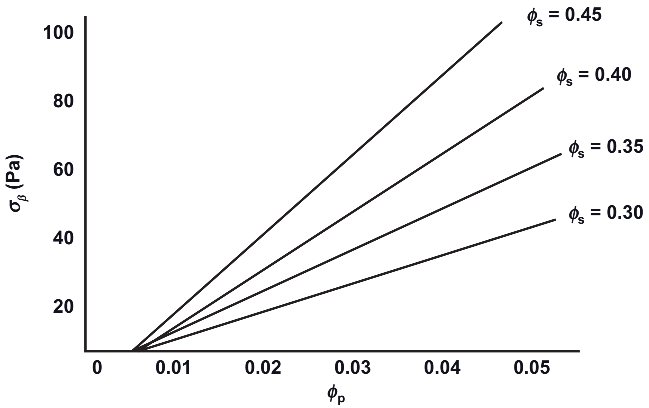

Figure 5.13 Variation of yield value σ_β with volume fraction ϕ_p of "free polymer" (PEO; $M = 35\,000$) at various latex volume fractions ϕ_s.

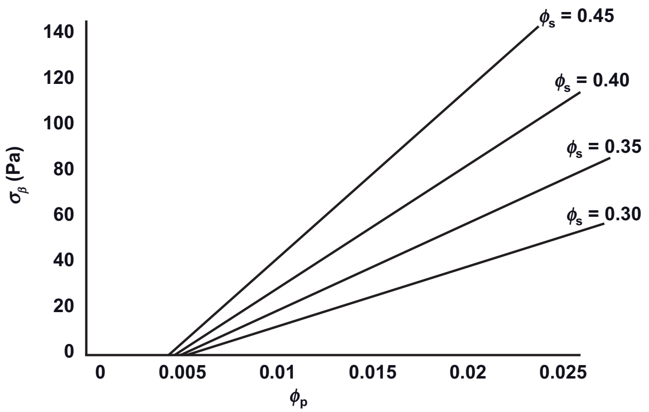

Figure 5.14 Variation of yield value σ_β with volume fraction ϕ_p of "free polymer" (PEO; $M = 100\,000$) at various latex volume fractions ϕ_s.

fraction of "free" polymer ϕ_p at the three PEO molecular weights studied, and at various latex volume fractions ϕ_s. The latex radius a in this case was 73.5 nm.

The results of Figures 5.12–5.14 show a rapid and linear increase in σ_β with increase in ϕ_p when the latter exceeds a critical value, ϕ_p^+. The latter value, which is the critical free polymer volume fraction for depletion flocculation, decreases with an increase of the molecular weight M of the free polymer, as might be expected. There does not appear to be any dependence of ϕ_p^+ on the volume fraction of the latex, ϕ_s.

Whilst a similar trend was obtained using larger latex particles (with radii 217.5 and 457.5 nm), but there was a definite trend towards an effect of the particle size; that is, the larger the particle size, the smaller the value of ϕ_p^+. A summary of

Table 5.1 Volume fraction of free polymer, ϕ_p^+, at which flocculation starts.

Particle radius (nm)	*M* (PEO)	ϕ_p^+
73.5	20 000	0.0150
73.5	35 000	0.0060
73.5	10 000	0.0055
73.5	20 000	0.0150
217.5	20 000	0.0055
457.5	20 000	0.0050

ϕ_p^+-values for the various molecular weights and particle sizes is provided in Table 5.1. These data show a significant reduction in ϕ_p^+ when the molecular weight of PEO was increased from 20 000 to 35 000 Da, whereas when M was increased from 35 000 to 100 000 the reduction in ϕ_p^+ was relatively smaller. Similarly, there was a significant reduction in ϕ_p^+ when the particle radius was increased from 73.5 to 217.5 nm, and a relatively smaller decrease when a was further increased to 457.5 nm.

The straight-line relationship between the extrapolated yield value and the volume fraction of free polymer can be described by the following scaling law:

$$\sigma_\beta = K\phi_s^m(\phi_p - \phi_p^+) \tag{5.18}$$

where K is a constant and m is the power exponent in ϕ_s, which may be related to the flocculation process. The values of m used to fit the data of σ_β versus ϕ_s are listed in Table 5.2, from which it can be seen that m is nearly constant, and is independent of both the particle size and the free polymer concentration. An age-related value for m of 2.8 may be assigned to such weakly flocculated system. This value was close to the exponent predicted for diffusion-controlled aggregation (3.5 ± 0.2) as predicted by Ball and Brown (personal communication) [28]; these authors developed a computer simulation method in which the flocs were treated as fractals that were closely packed throughout the sample.

The near-independence of ϕ_p^+ from ϕ_s can be explained on the basis of the statistical mechanical approach of Gast *et al.* [29], which demonstrated such independence when the osmotic pressure of the free polymer solution was relatively low, and/or the ratio of the particle diameter to the polymer coil diameter was relatively large (>8–9). The latter situation is certainly the case for the latex suspensions with diameters of 435 and 915 nm, at all PEO molecular weights. The only situation where this condition is not satisfied is with the smallest latex and the highest molecular weight PEO.

The dependence of ϕ_p^+ on particle size can be explained from a consideration of the dependence of free energy of depletion and van der Waals attractions on particle radius, as will be discussed below. Since both attractions increase with an

Table 5.2 Power law plot for σ_β versus ϕ_s for various PEO molecular weights and latex radii.

Latex a = 73.5 nm					
PEO 20 000		**PEO 35 000**		**PEO 100 000**	
ϕ_p	m	ϕ_p	m	ϕ_p	m
0.040	3.0	0.022	2.9	0.015	2.7
0.060	2.7	0.030	3.0	0.020	2.7
0.080	2.8	0.040	2.8	0.025	2.8
0.100	2.8	0.050	2.9	–	–

Latex a = 217.5		**Latex a = 457.5**	
ϕ_p	m	ϕ_p	m
0.020	3.0	0.020	2.7
0.040	2.9	0.030	2.7
0.060	2.8	0.040	2.8
0.080	2.8	0.050	2.7

increase of the particle radius, the larger particles would require a lower free polymer concentration at the onset of flocculation.

It is possible, in principle, to relate the extrapolated Bingham yield value, σ_β, to the energy required to separate the flocs into single units, E_{sep} [23, 24]:

$$\sigma_\beta = \frac{3\phi_s n E_{sep}}{8\pi a^3} \tag{5.19}$$

where n is the average number of contacts per particle (the coordination number). The maximum value of n is 12, which corresponds to hexagonal packing of the particles in a floc. Although, for random packing of particles in the floc, $n = 8$, it is highly unlikely that n-values of 12 or 8 will be reached in a weakly flocculated system, and a more realistic value for n is probably 4 (a relatively open structure in the floc).

In order to calculate E_{sep} from σ_β , it must be assumed that all particle–particle contacts are broken by shear. Indeed, this is highly likely as the high shear viscosity of the weakly flocculated latex was close to that of the latex before addition of the free polymer. Values of E_{sep} obtained using Equation 5.19 with $n = 4$ are listed in Table 5.3, at the three PEO molecular weights for the latex with the radius of 73.5 nm. It can be seen that E_{sep}, at any given ϕ_p increases with an increase of the volume fraction ϕ_s of the latex.

A comparison between E_{sep} and the free energy of depletion flocculation, G_{dep}, can be made using the theories of Asakura and Oosawa (AO) [30, 31] and Fleer,

Table 5.3 Results of E_{sep}, G_{dep} calculated on the basis of AO and FSV models.

ϕ_p	ϕ_s	σ_β (Ps)	E_{sep} (kT)	G_{dep} (kT) AO model	G_{dep} (kT) FSV model
(a) M (PEO) = 20 000					
0.04	0.30	12.5	8.4	18.2	78.4
	0.35	21.0	12.1	18.2	78.4
	0.40	30.5	15.4	18.2	78.4
	0.45	40.0	18.0	18.2	78.4
(b) M (PEO) = 35 000					
0.03	0.30	17.5	11.8	15.7	78.6
	0.35	25.7	14.8	15.7	78.6
	0.40	37.3	18.9	15.7	78.6
	0.45	56.8	25.5	15.7	78.6
(c) M (PEO) = 10 000					
0.02	0.30	10.0	6.7	9.4	70.8
	0.35	15.0	8.7	9.4	70.8
	0.40	22.0	11.1	9.4	70.8
	0.45	32.5	14.6	9.4	70.8

Vincent and Scheutjens (FVS) [32]. Asakura and Oosawa [31, 32] derived the following expression for G_{dep}, which is valid for the case where the particle radius is much larger the polymer coil radius:

$$\frac{G_{\text{dep}}}{kT} = -\frac{3}{2}\phi_2 \beta x^2;\ 0 < x < 1 \tag{5.20}$$

where k is the Boltzmann constant, T is the absolute temperature, and ϕ_2 is the volume concentration of free polymer that is given by:

$$\phi_2 = \frac{4\pi\Delta^3 N_2}{3v} \tag{5.21}$$

Here, Δ is the depletion layer thickness that is equal to the radius of gyration of free polymer (R_g), and N_2 is the total number of polymer molecules in a volume v of the solution:

$$\beta = \frac{a}{\Delta} \tag{5.22}$$

$$x = \frac{[\Delta - (h/2)]}{\Delta} \tag{5.23}$$

where h is the distance of separation between the outer surfaces of the particles. Clearly when $h = 0$, at the point where the polymer coils are "squeezed out" from the region between the particles, $x = 1$.

The FSV model [31] allowed the development of a general approach to the interaction of hard-spheres in the presence of a free polymer. The model takes into account the dependence of the range of interaction on free polymer concentration, and also any contribution from the non-ideal mixing of polymer solutions. This theory gives the following expression for G_{dep}:

$$G_{\text{dep}} = 2\pi a\left(\frac{\mu_1 - \mu_1^o}{v_1^o}\right)\Delta^2\left(1+\frac{2\Delta}{3a}\right) \tag{5.24}$$

where μ_1 is the chemical potential at bulk polymer concentration ϕ_p, μ_1^o is the corresponding value in the absence of free polymer, and v_1^o is the molecular volume of the solvent.

The difference in chemical potential $\mu_1 - \mu_1^o$ can be calculated from the volume fraction of the free polymer ϕ_p and the polymer–solvent (Flory–Huggins) interaction parameter $\chi()$:

$$\frac{\mu_1 - \mu_1^o}{kT} = -\left[\frac{\phi_p}{n_2} + \left(\frac{1}{2} - \chi\right)\phi_p^2\right] \tag{5.25}$$

where n_2 is the number of polymer segments per chain.

A summary of the values of E_{sep} and G_{dep}, calculated on the basis of AO and FSV models, is provided in Table 5.3 at three molecular weights for PEO and for a latex with $a = 77.5$ nm.

The data in Table 5.3 show clearly that E_{sep}, at any given ϕ_p, increases with an increase of the volume fraction ϕ_s of the latex. In contrast, the value of G_{dep} does not depend on the value of ϕ_s. The theories on depletion flocculation only show a dependence of G_{dep} on ϕ_p and a, such that no direct comparison can be made between E_{sep} and G_{dep}. The close agreement between E_{sep} and G_{dep} using the AO theory [30, 31] and assuming a value of $n = 4$ should only be considered fortuitous.

By using Equations 5.18 and 5.19, a general scaling law may be used to show the variation of E_{sep} with the various parameters of the system:

$$E_{\text{sep}} = \frac{8\pi a^3}{3\phi_s n}K_1\phi_s^{2.8}(\phi_p - \phi_p^+) = \frac{8\pi K_1}{3n}a^3\phi_s^{1.8}(\phi_p - \phi_p^+) \tag{5.26}$$

Equation 5.26 shows the four parameters that determine E_{sep}, namely the particle radius a, the volume fraction of the suspension ϕ_s, the concentration of free polymer ϕ_p, and the molecular weight of the free polymer which, together with a, determines ϕ_p^+.

Further insight into the structure of the flocculated latex dispersions was obtained using viscoelastic measurements (Equation 5.26). As an illustration, Figure 5.15 shows the variation of the storage modulus G' with ϕ_p ($M = 20\,000$) at various latex ($a = 77.5$) volume fractions ϕ_s. Similar trends were obtained for the other PEO molecular weights. All results showed the same trend, namely an increase in G' with an increase in ϕ_p, so at to reach a plateau value at high ϕ_p-values. These results were different from those obtained using steady-state

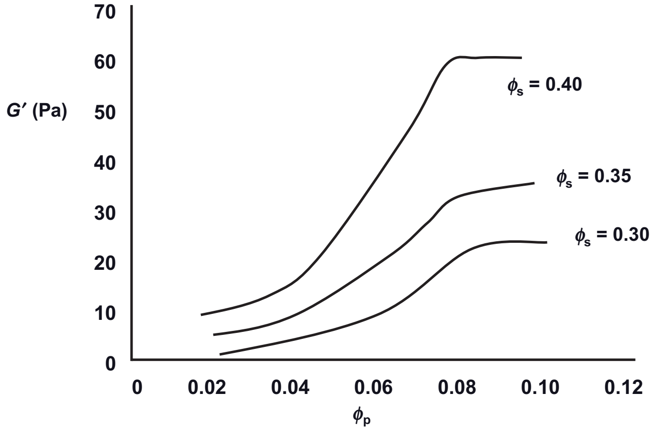

Figure 5.15 Variation of storage modulus G' with volume fraction ϕ_p of free polymer (PEO; $M = 20\,000$) for latex dispersions ($a = 77.5$ nm).

measurements, which showed a rapid and linear increase of the yield value σ_β. This difference reflected the behavior when using oscillatory (low deformation) measurements, which cause minimal perturbation of the structure when using low-amplitude and high-frequency measurements. Above ϕ_p^+, flocculation occurs and G' increases in magnitude with further increases in ϕ_p, until a 3-D network structure is reached and G' reaches a limiting value. Although any further increase in the free polymer concentration may cause a change in the floc structure, this may not cause a significant increase in the number of bonds between the units formed (which determine the magnitude of G').

5.8.2
Strongly Flocculated (Coagulated) Suspensions

Steady-state shear stress–shear rate curves show a pseudoplastic flow curve, as illustrated in Figure 5.16. The flow curve is characterized by three main parameters:

- The shear rate above which the flow curve shows a linear behavior. Above this shear rate, collisions occur between the flocs, and this may cause interchange between the flocculi (the smaller floc units that aggregate to form a floc). In this linear region, the ratio of the floc volume to the particle volume (ϕ_F/ϕ_p) – that is, the floc density – remains constant.
- σ_β the residual stress (yield stress) that arises from the residual effect of interparticle potential.
- η_{pl}: the slope of the linear portion of the flow curve that arises from purely hydrodynamic effects.

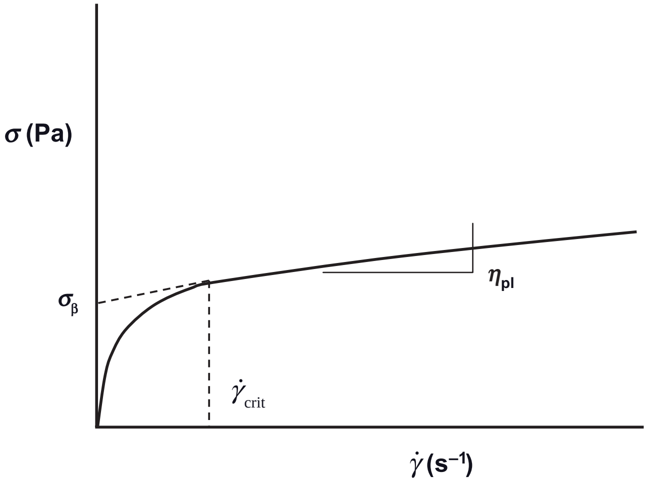

Figure 5.16 Pseudoplastic flow curve for a flocculated suspension.

5.8.2.1 Analysis of the Flow Curve

Impulse Theory: Goodeve and Gillespie [33, 34] The interparticle interaction effects (given by σ_β) and hydrodynamic effects (given by η_{pl}) are assumed to be additive:

$$\sigma = \sigma_\beta + \eta_{pl}\dot{\gamma} \tag{5.27}$$

In order to calculate σ_β, Goodeve proposed that when shearing occurs, the links between particles in a flocculated structure would be stretched, broken, and reformed; consequently, an impulse would be transferred from a fast-moving layer to a slow-moving layer. Non-Newtonian effects are due to effect of shear on the number of links, the life time of a link, and any change in the size of the floc.

According to Goodeve theory the yield value is given by:

$$\sigma_\beta = \left(\frac{3\phi^2}{2\pi a^3}\right)E_A \tag{5.28}$$

where ϕ is the volume fraction of the dispersed phase, a is the particle radius, and E_A is the total binding energy:

$$E_A = n_L \varepsilon_L \tag{5.29}$$

where n_L is the number of links with a binding energy ε_L per link.

According to Equation 5.6, $\sigma_\beta \propto \phi^2$; $\propto (1/a^3)$; $\propto E_A$ (the energy of attraction).

Elastic Floc Model: Hunter and Coworkers [35, 36] The floc is assumed to consist of an open network of "girders," as shown schematically in Figure 5.17. The floc undergoes extension and compression during rotation in a shear flow, such that

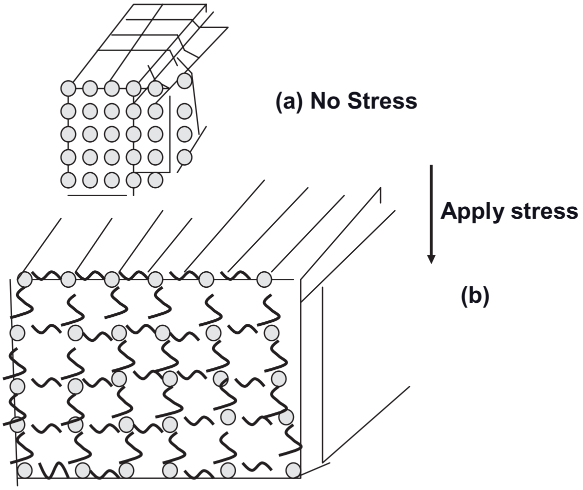

Figure 5.17 Schematic representation of the elastic floc.

the bonds are stretched by a small amount Δ (this may be as small as 1% of the particle radius).

To calculate σ_β, Hunter considered the energy dissipation during rupture of the flocs (assumed to consist of doublets). Thus, the yield value σ_β would be given by the expression:

$$\sigma_\beta = \alpha_o \beta \lambda \eta \dot{\gamma} \left(\frac{a_{\text{floc}}^2}{a^3} \right) \phi_s^2 \Delta C_{\text{FP}} \tag{5.30}$$

where α_o is the collision frequency, β is a constant (=(27/5), λ is a correction factor (~1), and C_{FP} is the floc density (= ϕ_F/ϕ_s).

5.8.2.2 Fractal Concept for Flocculation

The floc structure can be treated as fractals, whereby an isolated floc with radius a_F can be assumed to have uniform packing throughout that floc [37, 38].

In the above case, the number of particles in a floc is given by:

$$n_f = \phi_{\text{mf}} \left(\frac{a_F}{a} \right)^3 \tag{5.31}$$

where ϕ_{mf} is the packing fraction of the floc.

If the floc does not have constant packing throughout its structure, but is dendritic in form, the packing density of the floc begins to reduce when passing from the center to the edge. If this reduction is with a constant power law D, then

$$n_F = \left(\frac{a_F}{a} \right)^D \tag{5.32}$$

where $0 < D \leq 3$.

In this case, D is termed the “packing index,” and represents the packing change with distance from the center. Two cases may be considered:

- **Rapid aggregation** (diffusion-limited aggregation, DLA): When particles touch, they stick so that particle–particle aggregation gives $D = 2.5$, while aggregate–aggregate aggregation gives $D = 1.8$. The lower the value of D, the more open is the floc structure.
- **Slow aggregation** (rate-limited aggregation, RLA): The particles have a lower sticking probability; some are able to rearrange and densify the floc, such that $D \approx 2.0–2.2$.

The lower the value of D, the more open is the floc structure; consequently, by determining D it is possible to obtain information on the flocculation behavior. If the flocculation of a suspension occurs by changing the conditions (e.g., increasing temperature), then sites can be visualized for the nucleation of flocs occurring randomly throughout the whole volume of the suspension.

The total number of primary particles does not change and the volume fraction of the floc is given by:

$$\phi_{\mathrm{F}} = \phi\left(\frac{a_{\mathrm{F}}}{F}\right)^{3-D} \tag{5.33}$$

As the yield stress σ_β and elastic modulus G' depend on the volume fraction, a power law can be used in the form:

$$\sigma_\beta = K\phi^m \tag{5.34}$$

$$G' = K\phi^m \tag{5.35}$$

where the exponent m reflects the fractal dimension.

Thus, by plotting log σ_β or log G' versus log ϕ, it is possible to obtain m from the slope, and this can be used to characterize the floc nature and structure ($m = 2/(3\text{-}D)$.

5.8.2.3 Examples of Strongly Flocculated (Coagulated) Suspensions

Coagulation of Electrostatically Stabilized Suspensions by Addition of Electrolyte As mentioned in Chapter 2, electrostatically stabilized suspensions become coagulated when the electrolyte concentration is increased above the critical coagulation concentration (CCC). This is illustrated by using a latex dispersion (prepared using surfactant-free emulsion polymerization) to which 0.2 mol dm^{-3} NaCl has been added (well above the CCC, which is 0.1 mol dm^{-3} NaCl).

Figure 5.18 shows the strain sweep results for latex dispersions at various volume fractions ϕ, in the presence of 0.2 mol dm^{-3} NaCl. It can be seen from the figure that G^* and G' (which are very close to each other) remain independent of the applied strain (the linear viscoelastic region). However, above a critical strain, γ_{cr}, G^* and G' each show a rapid reduction with a further increase in strain (the nonlinear region). In contrast, G'' (which is much less than G') remains constant,

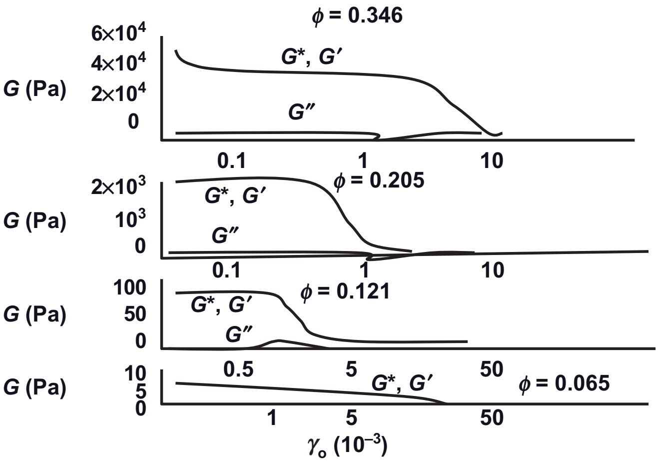

Figure 5.18 Strain sweep results for latex dispersions at various volume fractions ϕ in the presence of 0.2 mol dm^{-3} NaCl.

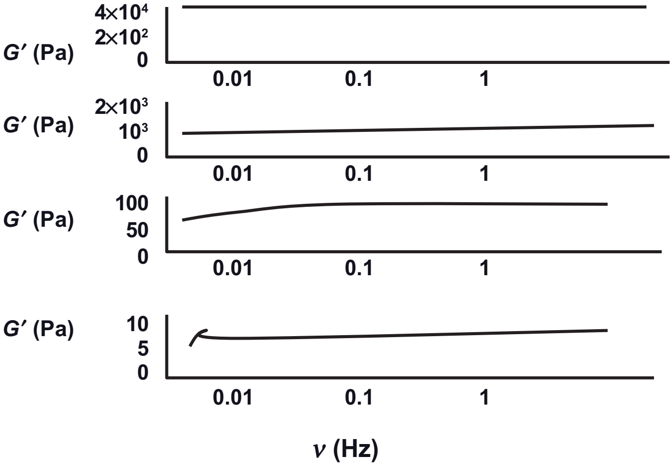

Figure 5.19 Variation of G' with frequency at various latex volume fractions.

showing an ill-defined maximum at intermediate strains. Above γ_{cr}, the flocculated structure becomes broken down with applied shear.

Figure 5.19 shows the variation of G' (measured at strains in the linear viscoelastic region) with frequency ν (in Hz) at various latex volume fractions. As noted above, G' is almost equal to G^* since G'' is very low.

In all cases, $G' >> G''$, and shows little dependence on frequency. This behavior is typical of a highly elastic (coagulated) structure, whereby a "continuous gel" network structure is produced at such high volume fractions (see Chapter 2). Scaling laws can be applied for the variation of G' with the volume fraction of the

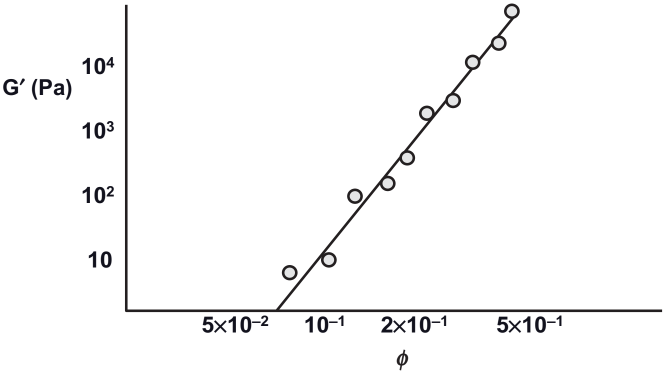

Figure 5.20 Log–log plots of G' versus ϕ for coagulated polystyrene latex suspensions.

latex ϕ. A log–log plot of G' versus ϕ is shown in Figure 5.20; this plot is linear, and can be represented by the following scaling equation:

$$G' = 1.98 \times 10^7 \phi^{6.0} \tag{5.36}$$

The high power in ϕ is indicative of a relatively compact coagulated structure. This power give a fractal dimension of 2.67 that confirms the compact structure.

It is also possible to obtain the cohesive energy of the flocculated structure E_c from a knowledge of G' (in the linear viscoelastic region) and γ_{cr}. E_c is related to the stress σ in the coagulated structure by the following equation:

$$E_c = \int_0^{\gamma_{cr}} \sigma d\gamma \tag{5.37}$$

Since $\sigma = G'\gamma_o$, then,

$$E_c = \int_0^{\gamma_{cr}} \gamma_o G' d\gamma = \frac{1}{2}\gamma_{cr}^2 G' \tag{5.38}$$

A log–log plot of E_c versus ϕ is shown in Figure 5.21 for such coagulated latex suspensions.

The E_c versus ϕ curve can be represented by the following scaling relationship:

$$E_c = 1.02 \times 10^3 \phi^{9.1} \tag{5.39}$$

The high power in ϕ is indicative of the compact structure of these coagulated suspensions.

5.8.2.4 Strongly Flocculated, Sterically Stabilized Systems

Influence of Addition of Electrolyte As mentioned in Chapter 2, sterically stabilized suspensions show strong flocculation (sometimes referred to as incipient

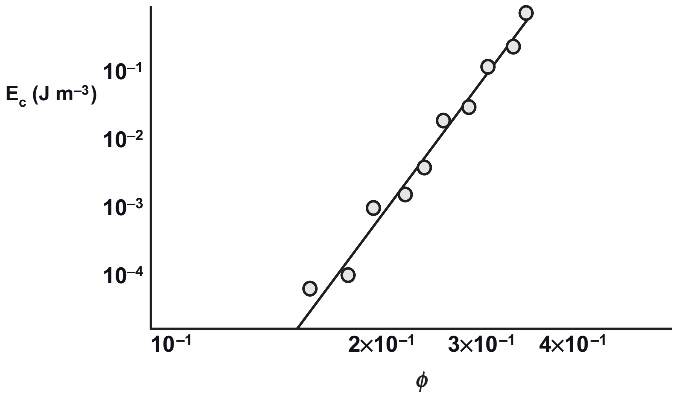

Figure 5.21 Log–log plots of E_c versus ϕ for coagulated polystyrene latex suspensions.

flocculation) when the medium for the stabilizing chain becomes worse than a θ-solvent (the Flory–Huggins interaction parameter $\chi > 0.5$). The reduction of solvency for a PEO stabilizing chain can be reduced by the addition of a nonsolvent for the chains, or by the addition of an electrolyte such as Na_2SO_4. Above a critical Na_2SO_4 concentration (referred to here as the critical flocculation concentration, CFC), the χ parameter exceeds 0.5 and this results in incipient flocculation. This process of flocculation can be investigated using rheological measurements, without diluting the latex; however, dilution may result in a change in the floc structure. Hence, investigations conducted without any dilution will ensure an absence of change of the floc structure, in particular when using low-deformation (oscillatory) techniques [39].

Figure 5.22 shows the variation of extrapolated yield value, σ_β, as a function of Na_2SO_4 concentration at various latex volume fractions ϕ_s at 25 °C. The latex had a z-average particle diameter of 435 nm, and contained grafted PEO with $M = 2000$. It was clear that, when $\phi_s < 0.52$, σ_β was virtually equal to zero up to 0.3 mol dm^{-3} Na_2SO_4, but above this concentration there was a rapid increase in σ_β with a further increase in Na_2SO_4 concentration. When $\phi_s > 0.52$, a small yield value was obtained below 0.3 mol dm^{-3} Na_2SO_4, though this may have been attributed to the possible elastic interaction between the grafted PEO chains when the particle–particle separation was less than 2δ (where δ is the grafted PEO layer thickness). Above 0.3 mol dm^{-3} Na_2SO_4, there was a rapid increase in σ_β. Thus, the CFC of all concentrated latex dispersions was around 0.3 mol dm^{-3} Na_2SO_4. It should be mentioned that, when the Na_2SO_4 concentration was below the CFC, σ_β showed a measurable decrease with any increase in Na_2SO_4 concentration. This was due to a reduction in the effective radius of the latex particles as a result of the reduction in the solvency of the medium for the chains. This, in turn, accounted for a reduction in the effective volume fraction of the dispersion, which was accompanied by a reduction in σ_β.

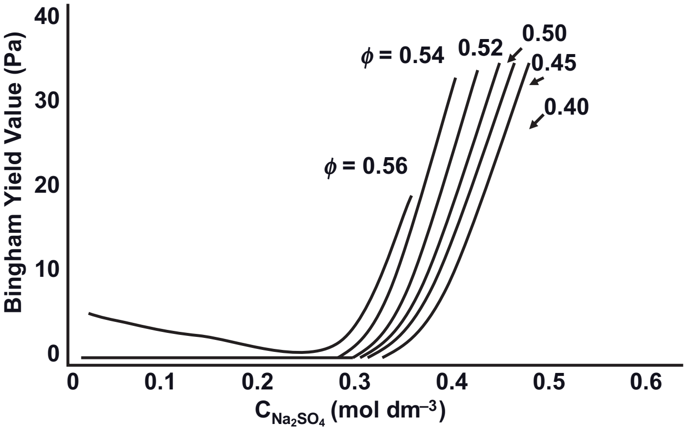

Figure 5.22 Variation of Bingham yield value with Na_2SO_4 concentration at various volume fractions ϕ of latex.

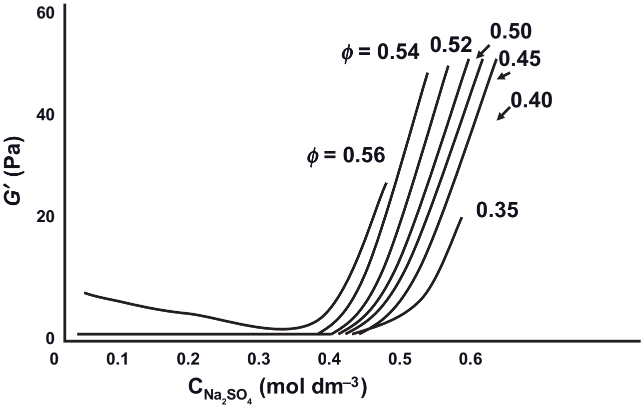

Figure 5.23 Variation of storage modulus G' with Na_2SO_4 concentration at various volume fractions ϕ of latex.

Figure 5.23 shows the results for the variation of the storage modulus G' with Na_2SO_4 concentration. These results showed the same trend as those in Figure 5.22 – that is, an initial reduction in G' due to a reduction in the effective volume fraction was followed by a sharp increase above the CFC (which was 0.3 mol dm^{-3} Na_2SO_4).

Log–log plots of σ_β and G' versus ϕ_s at various Na_2SO_4 concentrations are shown in Figures 5.24 and 5.25. All of these data are described by the following scaling equations:

$$\sigma_\beta = k\phi_s^m \tag{5.40}$$

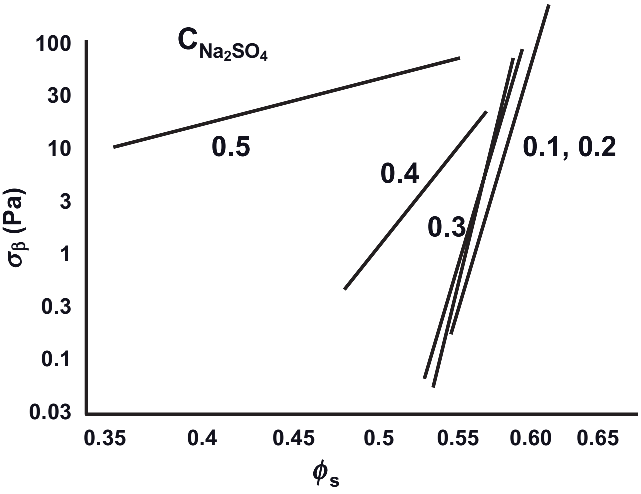

Figure 5.24 Log–log plots of σ_β versus ϕ_s.

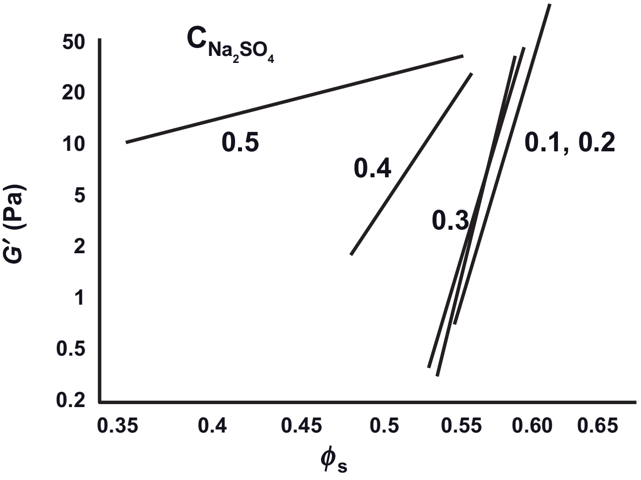

Figure 5.25 Log–log plots of G' versus ϕ_s.

$$G' = k'\phi_s^n \tag{5.41}$$

where $0.35 < \phi_s < 0.53$.

The values of m and n were very high at Na_2SO_4 concentrations below the CFC, reaching values in the range of 30–50 that indicated a strong steric repulsion between the latex particles. When the Na_2SO_4 concentration exceeded the CFC, both m and n decreased very sharply to reach values of $m = 9.4$ and $n = 12$ when

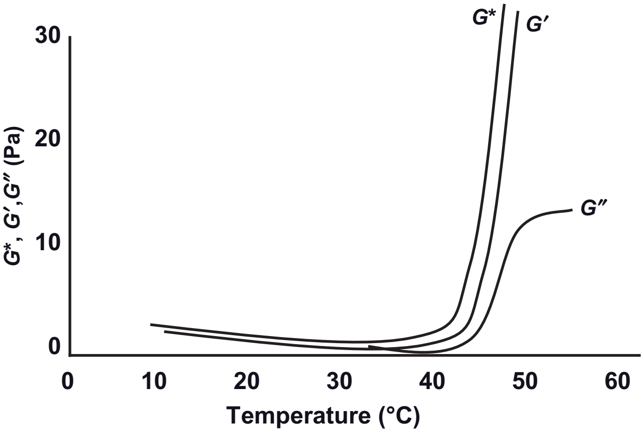

Figure 5.26 Variation of G^*, G' and G'' with temperature for latex dispersions ($\phi_s = 0.55$) in 0.2 mol dm^{-3} Na_2SO_4.

the Na_2SO_4 concentration increased to 0.4 mol dm^{-3}, and values of $m = 2.8$ and $n = 2.2$ at 0.5 mol dm^{-3} Na_2SO_4. These slopes could be used to calculate the fractal dimensions (see above), giving a value of $D = 2.70$–2.75 at 0.4 mol dm^{-3} Na_2SO_4, and $D = 1.6$–1.9 at 0.5 mol dm^{-3} Na_2SO_4.

The above results of fractal dimensions indicated a different floc structure when compared to results obtained using an electrolyte to induce coagulation. In the latter case, $D = 2.67$ indicated a compact structure similar to that obtained at 0.4 mol dm^{-3} Na_2SO_4. However, when the Na_2SO_4 concentration exceeded the CFC value (0.5 mol dm^{-3} Na_2SO_4), a much more open floc structure with a D-value less than 2 was obtained.

Influence of an Increase in Temperature Sterically stabilized dispersions with PEO chains as stabilizers undergo flocculation on increasing the temperature. At a critical temperature, termed the critical flocculation temperature (CFT), the Flory–Huggins interaction parameter becomes higher than 0.5, and results in incipient flocculation. This is illustrated graphically in Figure 5.26, which shows the variation of the storage modulus G' and loss modulus G'' with increasing temperature for a latex dispersion with a volume fraction $\phi = 0.55$ and at a Na_2SO_4 concentration of 0.2 mol dm^{-3}. At this electrolyte concentration, the latex was stable in the temperature range 10 to 40 °C, but above this temperature (CFT) it was strongly flocculated.

The data shown in Figure 5.26 demonstrate an initial systematic reduction in the moduli values when increasing the temperature to 40 °C. This was the result of a reduction in solvency of the chains with increasing temperature. The latter increase caused a breakdown in the hydrogen bonds between the PEO chains and water molecules, which in turn resulted in a reduction in the thickness of the grafted PEO chains and hence a reduction in the effective volume fraction of the dispersion. The latter effect caused a decrease in the moduli values. However, at 40 °C there was a rapid increase in the moduli values with a further increase of temperature; this indicated the onset of flocculation (the CFT). Similar results were obtained at 0.3 and 0.4 mol dm^{-3} Na_2SO_4, but in these cases the CFT was 35 °C and 15 °C, respectively.

5.9
Models for the Interpretation of Rheological Results

5.9.1
Doublet Floc Structure Model

Neville and Hunter [40] introduced a doublet floc model to deal with sterically stabilized dispersions which have undergone flocculation. These authors assumed that the major contribution to the excess energy dissipation in such pseudoplastic systems was derived from the shear field which provides energy to separate contacting particles in a floc. The extrapolated yield value can be expressed as:

$$\sigma_\beta = \frac{3\phi_H^2}{2\pi^2(a+\delta)^2} E_{sep} \tag{5.42}$$

where ϕ_H is the hydrodynamic volume fraction of the particles that is equal to the effective volume fraction:

$$\phi_H = \phi_s \left[1 + \frac{\delta}{a}\right]^3 \tag{5.43}$$

Here, $(a + \delta)$ is the interaction radius of the particle, and E_{sep} is the energy needed to separate a doublet, which is the sum of the van der Waals and steric attractions:

$$E_{sep} = \frac{Aa}{12H_o} + G_s \tag{5.44}$$

At a particle separation of ~12 nm (twice the grafted polymer layer thickness), the van der Waals attractions are very small (1.66 kT, where k is the Boltzmann constant and T is the absolute temperature), and the contribution of G_s to the attraction is significantly larger than the van der Waals attractions. Therefore, E_{sep} may be approximated to G_s.

From Equation 5.42, it is possible to estimate E_{sep} from σ_β. The results, as shown in Table 5.4, demonstrate an increase in E_{sep} with an increase in ϕ_s. Unfortunately, the values of E_{sep} listed in Table 5.4 are unrealistically high, and hence the assumptions made for the calculation of E_{sep} are not fully justified. Consequently, the data in Table 5.4 must be considered only as qualitative in nature.

Table 5.4 Results of E_{sep} calculated from σ_β for a flocculated sterically stabilized latex dispersions at various latex volume fractions.

0.4 mol dm^{-3} Na$_2$SO$_4$			**0.4 mol dm^{-3} Na$_2$SO$_4$**		
ϕ_s	σ_β (Pa)	E_{sep} (kT)	ϕ_s	σ_β (Pa)	E_{sep} (kT)
0.43	1.3	97	0.25	3.5	804
0.45	2.4	165	0.29	5.4	910
0.51	3.3	179	0.33	7.4	961
0.54	5.3	262	0.37	11.4	1170
0.55	7.3	336	0.41	14.1	1190
0.57	9.1	397	0.44	17.0	1240
0.58	17.4	736	0.47	21.1	1380
			0.49	23.1	1390
			0.52	28.3	1510

5.9.2
Elastic Floc Model

This model [41–43], which was described previously, is based on the assumption that the structural units are small flocs of particles (termed “flocculi”) that are characterized by the extent to which the structure is able to entrap the dispersion medium. A floc is made from an aggregate of several flocculi. The latter may range from a loose open structure (if the attractive forces between the particles are strong) to a very close-packed structure with little entrapped liquid (if the attractive forces are weak). In the system of flocculated sterically stabilized dispersions, the structure of the flocculi depends on the volume fraction of the solid, and how far the system is from the CFC. Just above the CFC, the flocculi are probably close-packed (with relatively small floc volume), whereas far above the CFC a more open structure is found which entraps a considerable amount of liquid. Both types of flocculi persist at high shear rates, although those flocculi with a weak attraction may become more compact by maximizing the number of interactions within the flocculus.

As discussed above, the Bingham yield value is given by Equation 5.30, which allows the floc radius a_{floc} to be obtained, provided that the floc volume ratio C_{FP} (ϕ_F/ϕ_s) can be calculated and that a value for Δ (the distance through which bonds are stretched inside the floc by the shearing force) can be assumed.

At high volume fractions, ϕ_F – and hence C_{FP} – can be calculated using the Krieger equation [3]:

$$\eta_{pl} = \eta_o \left(1 - \frac{\phi_F}{\phi_s^m}\right)^{-[\eta]\phi_s^m} \tag{5.45}$$

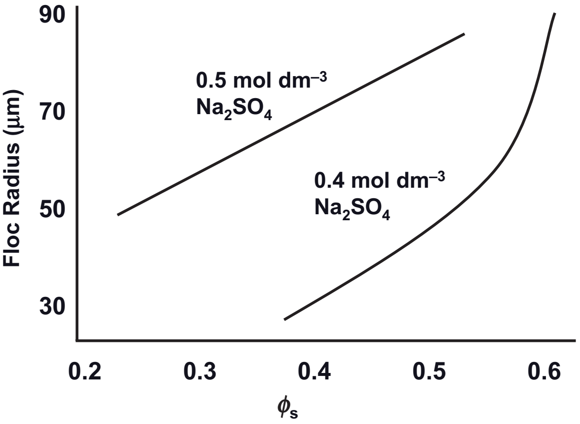

Figure 5.27 Floc radius (a_{floc}) as a function of latex volume fraction at 0.4 and 0.5 mol dm^{-3} Na_2SO_4 (above the CFC).

where η_o is the viscosity of the medium, ϕ_s^m is the maximum packing fraction which may be taken as 0.74, and $[\eta]$ is the intrinsic viscosity, taken as 2.5.

Assuming a value for Δ of 0.5 nm, the floc radius a_{floc} was calculated using Equation 5.30. Figure 5.27 shows the variation of a_{floc} with latex volume fraction at the two Na_2SO_4 concentrations studied. At any given electrolyte concentration, the floc radius increases with increase of the latex volume fraction, as expected. This can be understood by assuming that the larger flocs are formed by a fusion of two flocs, and the smaller flocs by a “splitting” of the larger ones. From simple statistical arguments, it can be predicted that a_{floc} will increase with increase in ϕ_s, because in this case the larger flocs are favored over smaller ones. In addition, at any given volume fraction of latex, the floc radius increases with an increase in electrolyte concentration. This is consistent with the scaling results, as discussed above.

The above results show clearly the correlation of viscoelasticity of flocculated dispersions with their interparticle attraction. These measurements allow the CFC and CFT of concentrated flocculated dispersions to be obtained with reasonable accuracy. In addition, the results obtained can be analyzed using various models so as to obtain some characteristics of the flocculated structure, such as the “openness” of the network, the liquid entrapped in the floc structure, and the floc radius. Although, clearly, several assumptions must be made, the trends obtained are consistent with expectation from theory.

References

1 Einstein, A. (1906) *Ann. Physik.*, **19**, 289; Einstein, A. (1911) *Ann. Physik.*, **34**, 591.
2 Bachelor, G.K. (1977) *J. Fluid Mech.*, **83**, 97.
3 Krieger, I.M. and Dougherty, T.J. (1959) *Trans. Soc. Rheol.*, **3**, 137.
4 Krieger, I.M. (1972) *Adv. Colloid Interface Sci.*, **3**, 111.

5 Goodwin, J.W. and Hughes, R.W. (2000) *Rheology for Chemists*, Royal Society of Chemistry Publication, Cambridge.

6 Tadros, T.F. (1989) Rheology of concentrated stable and flocculated suspension, in *Flocculation and Dewatering* (eds B.M. Mougdil and B.J. Scheiter), Engineering Foundation Publishers, pp. 43–87.

7 Tadros, T.F. (1996) *Adv. Colloid Interface Sci.*, **68**, 97.

8 Tadros, T.F. (1990) *Langmuir*, **6**, 28.

9 Tadros, T.F. and Hopkinson, A. (1990) *Faraday Disc. Chem. Soc.*, **90**, 41.

10 Napper, D.H. (1983) *Polymeric Stabilization of Colloidal Dispersions*, Academic Press, London.

11 Liang, W., Tadros, T.F., and Luckham, P.F. (1992) *J. Colloid Interface Sci.*, **153**, 131.

12 Prestidge, C. and Tadros, T.F. (1988) *J. Colloid Interface Sci.*, **124**, 660.

13 de Costello, B.A.L., Luckham, P.F., and Tadros, T.F. (1988/1989) *Colloids Surf.*, **34**, 301.

14 Luckham, P.F., Ansarifar, M.A., de Costello, B.A.L., and Tadros, T.F. (1991) *Powder Technol.*, **65**, 371.

15 Tadros, T.F., Liang, W., de Costello, B.A.L., and Luckham, P.F. (1993) *Colloids Surf.*, **79**, 105.

16 Luckham, P.F. (1989) *Powder Technol.*, **58**, 75.

17 de Gennes, P.G. (1987) *Adv. Colloid Interface Sci.*, **27**, 189.

18 Russel, W.B. (1980) *J. Rheol.*, **24**, 287.

19 Hoffman, R.L. (1983) *Science and Technology of Polymer Colloids*, vol. **II** (eds G.W. Poehlein, R.H. Ottewill, and J.W. Goodwin), Martinus Nijhoff Publishers, Boston, The Hague, p. 570.

20 Firth, B.A. and Hunter, R.J. (1976) *J. Colloid Interface Sci.*, **57**, 248.

21 van de Ven, T.G.M. and Hunter, R.J. (1976) *Rheol. Acta*, **16**, 534.

22 Hunter, R.J. and Frayane, J. (1980) *J. Colloid Interface Sci.*, **76**, 107.

23 Heath, D. and Tadros, T.F. (1983) *Faraday Disc. Chem. Soc.*, **76**, 203.

24 Prestidge, C. and Tadros, T.F. (1988) *Colloids Surf.*, **31**, 325.

25 Tadros, T.F. and Zsednai, A. (1990) *Colloids Surf.*, **49**, 103.

26 Liang, W., Tadros, Th.F., and Luckham, P.F. (1993) *J. Colloid Interface Sci.*, **155**, 156.

27 Liang, W., Tadros, Th.F., and Luckham, P.F. (1993) *J. Colloid Interface Sci.*, **160**, 183.

28 Buscall, R. and Mill, P.D.A. (1988) *J. Chem. Soc., Faraday Trans. I*, **84**, 4249.

29 Gast, A.P., Hall, C.K., and Russel, W.B. (1983) *J. Colloid Interface Sci.*, **96**, 251.

30 Asakura, S. and Oosawa, F. (1954) *J. Chem. Phys.*, **22**, 1255.

31 Asakura, S. and Oosawa, F. (1958) *J. Polym. Sci.*, **33**, 183.

32 Fleer, G.J., Schueutjens, J.H.M.H., and Vincent, B. (1984) *ACS Symp. Ser.*, **240**, 245.

33 Goodeve, C.V. (1939) *Trans. Faraday Soc.*, **35**, 342.

34 Gillespie, T. (1960) *J. Colloid Sci.*, **15**, 219.

35 Hunter, R.J. and Nicol, S.K. (1968) *J. Colloid Interface Sci.*, **28**, 200.

36 Firth, B.A. and Hunter, R.J. (1976) *J. Colloid Interface Sci*, **57**, 248, 257, 266.

37 Mills, P.D.A., Goodwin, J.W., and Grover, B. (1991) *Colloid Polym. Sci.*, **269**, 949.

38 Goodwin, J.W. and Hughes, R.W. (1992) *Adv. Colloid Interface Sci.*, **42**, 303.

39 Liang, W., Tadros, T.F., and Luckham, P.F. (1983) *Langmuir*, **9**, 2077.

40 Firth, B.A., Neville, P.C., and Hunter, R.J. (1974) *J. Colloid Interface Sci.*, **49**, 214.

41 van de Ven, T.G.M. and Hunter, R.J. (1974) *J. Colloid Interface Sci.*, **68**, 135.

42 Hunter, R.J. (1982) *Adv. Colloid Interface Sci.*, **17**, 197.

43 Friend, J.P. and Hunter, R.J. (1971) *J. Colloid Interface Sci.*, **37**, 548.

6
Rheology of Emulsions

6.1
Introduction

Although the rheology of emulsions has many similar features to that of suspensions, emulsions differ in three main aspects:

- The mobile liquid–liquid interface that contains surfactant or polymer layers introduces a response to deformation, such that the interfacial rheology must be considered.
- The dispersed phase viscosity relative to that of the medium has an effect on the rheology of the emulsion.
- The deformable nature of the disperse phase droplets, particularly for large droplets, has an effect on the emulsion rheology at high phase volume fraction ϕ.

When the above factors are taken into consideration, the bulk rheology of emulsions can be treated in a similar manner as for suspensions, and the same techniques can be applied.

6.2
Interfacial Rheology

6.2.1
Interfacial Tension and Surface Pressure

A fluid interface in equilibrium exhibits an intrinsic state of tension that is characterized by its interfacial tension γ; this is expressed as the change in free energy with area of the interface, at constant composition n_i and temperature T:

$$\gamma = \left(\frac{\partial G}{\partial A}\right)_{n_i,T} \tag{6.1}$$

The unit for γ is energy per unit area (mJ m^{-1}) or force per unit length (mN m^{-1}), which are dimensionally equivalent.

Rheology of Dispersions: Principles and Applications. Tharwat F. Tadros

ISBN: 978-3-527-32003-5

The adsorption of surfactants or polymers lowers the interfacial tension, and this produces a two-dimensional (2-D) surface pressure π that is given by:

$$\pi = \gamma_o - \gamma \tag{6.2}$$

where γ_o is the interfacial tension of the "clean" interface (before adsorption), and γ is the tension after adsorption.

6.2.2
Interfacial Shear Viscosity

The interface is considered to be a macroscopically planar, dynamic fluid interface. Thus, the interface is regarded as a 2-D entity, independent of the surrounding three-dimensional (3-D) fluid. The interface is considered to correspond to a highly viscous insoluble monolayer, while the interfacial stress σ_s acting within such a monolayer is sufficiently large compared to the bulk-fluid stress acting across the interface. In this way, it becomes possible to define an interfacial shear viscosity η_s:

$$\sigma_s = \eta_s \dot{\gamma} \tag{6.3}$$

where $\dot{\gamma}$ is the shear rate. Here, η_s is expressed as surface Pa · s (N m^{-1} s) or surface poise (dyne cm^{-1} s).

It should be mentioned that the surface viscosity of a surfactant-free interface is negligible, and can reach high values for adsorbed rigid molecules such as proteins.

6.2.2.1 Measurement of Interfacial Viscosity

Many surface viscometers utilize torsional stress measurements upon a rotating a ring, disk or knife edge (shown schematically in Figure 6.1), within or near to the liquid–liquid interface [1]. This type of viscometer is moderately sensitive; for a disk viscometer the interfacial shear viscosity can be measured in the range $\eta_s \geq 10^{-2}$ surface Pa · s.

The disk is rotated within the plane of the interface with angular velocity ω. A torque is then exerted on the disk of radius R by both the surfactant film with

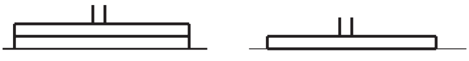

Ring viscometer Disk viscometer

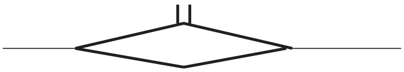

Knife-edge viscometer

Figure 6.1 Schematic representation of surface viscometers.

surface viscosity η_s and the viscous liquid (with bulk viscosity η) that is given by the expression:

$$M = (8/3)R^3\eta\omega + 4\pi R^2\eta_s\omega \tag{6.4}$$

6.2.3
Interfacial Dilational Elasticity

The interfacial dilational (Gibbs) elasticity ε, which is an important parameter in determining emulsion stability (reduction of coalescence during formation), is given by the following equation:

$$\varepsilon = \frac{\delta\gamma}{\delta \ln A} \tag{6.5}$$

where $\delta\gamma$ is the change in interfacial tension during expansion of the interface by an amount δA (referred to as interfacial tension gradient resulting from nonuniform surfactant adsorption on expansion of the interface).

One of the most convenient methods for measurement of ε is to use a Langmuir trough with two moving barriers for expansion and compression of the interface. Another method for measurement of ε is to use the oscillating bubble technique, for which instruments are commercially available.

One useful means of measuring ε is via the "pulsed drop" method [2]., in which a rapid expansion of a droplet at the end of a capillary, from radius r_1 to r_2, is obtained by the application of pressure. The pressure drop within the droplet is measured as a function of time, using a sensitive pressure transducer; subsequently, from the pressure drop it is possible to obtain the interfacial tension as a function of time. The Gibbs dilational elasticity is determined from values of the time-dependent interfacial tension, with measurements being made as a function of frequency, as illustrated in Figure 6.2 for stearic acid at the decane–water interface at pH 2.5.

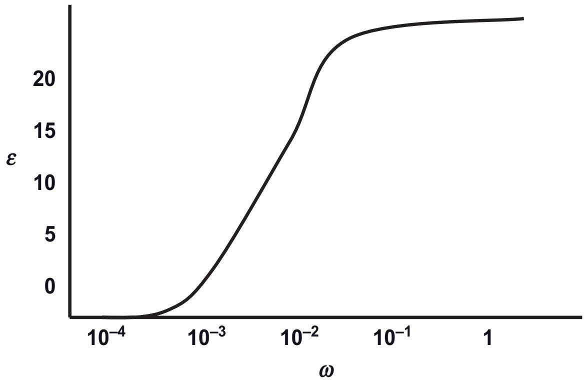

Figure 6.2 Gibbs dilational elasticity versus frequency.

6.2.4
Interfacial Dilational Viscosity

Measurement of the dilational viscosity is more difficult than measurement of the interfacial shear viscosity, this being due to the coupling between dilational viscous and elastic components. The most convenient method for measuring dilational viscosity is the "maximum bubble pressure technique," although this can only be applied at the air–water interface. According to this technique, the pressure drop across the bubble surface at the instant when the bubble possesses a hemispherical shape (corresponding to the maximum pressure) is due to a combination of bulk viscous, surface tension, and surface dilational viscosity effects which, together, allows the interfacial dilational viscosity to be obtained.

6.2.5
Non-Newtonian Effects

Most adsorbed surfactant and polymer coils at the oil–water (O/W) interface show non-Newtonian rheological behavior. The surface shear viscosity η_s depends on the applied shear rate, showing shear thinning at high shear rates. Some films also show Bingham plastic behavior with a measurable yield stress.

Many adsorbed polymers and proteins show viscoelastic behavior and, indeed, it is possible to measure viscous and elastic components by using sinusoidally oscillating surface dilation. For example, the complex dilational modulus ε^* obtained can be split into "in-phase" (the elastic component, ε') and "out-of-phase" (the viscous component, ε'') components. Both, creep and stress relaxation methods can be applied to the study of viscoelasticity.

6.2.6
Correlation of Emulsion Stability with Interfacial Rheology

6.2.6.1 Mixed-Surfactant Films

Prins *et al*. [3] found that a mixture of sodium dodecyl sulfate (SDS) and dodecyl alcohol produces a more stable O/W emulsion when compared to emulsions prepared using SDS alone. This enhanced stability is due to the higher interfacial dilational elasticity ε for the mixture when compared to that of SDS alone. Interfacial dilational viscosity does not play a major role here, as the emulsions are stable at high temperature whereby the interfacial viscosity becomes lower. The above correlation is not general for all surfactant films, since other factors such as thinning of the film between emulsion droplets (which depends on other factors such as repulsive forces) can also play a major role.

6.2.6.2 Protein Films

Biswas and Haydon [4] found some correlation between the viscoelastic properties of protein (albumin or arabinic acid) films at the O/W interface, and the stability of emulsion drops against coalescence. Viscoelastic measurements were carried

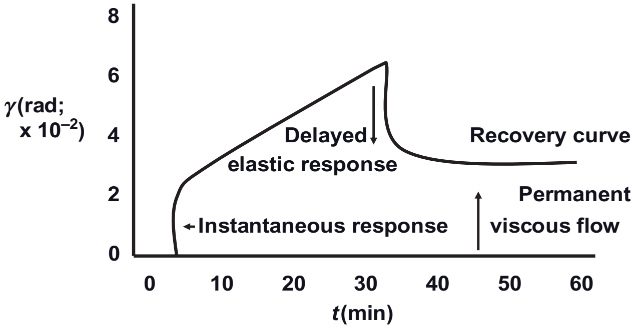

Figure 6.3 Creep curve for protein film at the oil–water (O/W) interface.

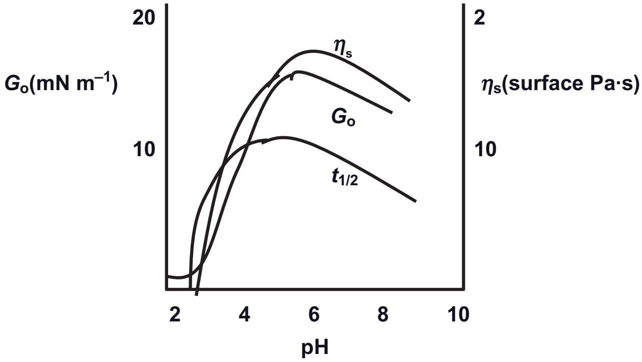

Figure 6.4 Variation of $t_{1/2}$ and G_o and η_s with pH.

out using creep and stress relaxation measurements (using a specially designed interfacial rheometer). For this, a constant torque or stress σ (mN m^{-1}) was applied and the deformation γ measured as a function of time for 30 min. After this period, the torque was removed and γ (which changes sign) was measured as a function of time to obtain the recovery curve. The results are illustrated in Figure 6.3.

From the creep curves, it is possible to obtain the instantaneous modulus G_o (σ/γ_{int}.) and the surface viscosity η_s from the slope of the straight line (which gives the shear rate) and the applied stress; G_o and η_s are then plotted versus pH, as shown in Figure 6.4. Both showed an increase with increase in pH, reaching a maximum at ~pH 6 (the isoelectric point of the protein), when the protein molecules showed maximum rigidity at the interface.

The stability of the emulsion was assessed by measuring the residence time t of several oil droplets at a planar O/W interface containing the adsorbed protein. Figure 6.4 shows the variation of $t_{1/2}$ (the time taken for half the number of oil droplets to coalesce with the oil at the O/W interface) with pH. Typically, a good correlation between $t_{1/2}$ and G_o and η_s is obtained.

Subsequently, Biswas and Haydon [4] derived a relationship between the coalescence time τ and surface viscosity η_s, the instantaneous modulus G_o and the adsorbed film thickness h:

$$\tau = \eta_s\left[3C'\frac{h^2}{A} - \frac{1}{G_o} - \phi(t)\right] \tag{6.6}$$

where $3C'$ is a critical deformation factor, A is the Hamaker constant, and $\phi(t)$ is the elastic deformation per unit stress.

Equation 6.6 shows that τ increases with an increase of η_s but, most importantly, it is directly proportional to h^2. These results show that viscoelasticity is necessary – but not sufficient – to ensure stability against coalescence. Rather, in order to ensure the stability of an emulsion it must be ensured that h is sufficiently large and that any film drainage is prevented.

6.3
Bulk Rheology of Emulsions

For rigid (highly viscous) oil droplets dispersed in a medium of low viscosity, such as water, the relative viscosity η_r of a dilute (volume fraction $\phi \leq 0.01$) O/W emulsion of noninteracting droplets behaves as "hard-spheres" (similar to suspensions).

In the above case, η_r is given by the Einstein equation:

$$\eta_r = 1 + [\eta]\phi \tag{6.7}$$

where $[\eta]$ is the intrinsic viscosity that is equal to 2.5 for hard-spheres.

For droplets with low viscosity (comparable to that of the medium), the transmission of tangential stress across the O/W interface, from the continuous phase to the dispersed phase, causes a liquid circulation in the droplets. Energy dissipation is less than that for hard-spheres, and the relative viscosity is lower than that predicted by the Einstein equation.

For an emulsion with viscosity η_i for the disperse phase and η_o for the continuous phase [5],

$$[\eta] = 2.5\left(\frac{\eta_i + 0.4\eta_o}{\eta_i + \eta_o}\right) \tag{6.8}$$

Clearly when $\eta_i \gg \eta_o$, the droplets behave as rigid spheres and $[\eta]$ approaches the Einstein limit of 2.5. In contrast, if $\eta_i \ll \eta_o$ (as is the case for foams), then $[\eta] = 1$.

In the presence of viscous interfacial layers, Equation 6.8 is modified to take into account the surface shear viscosity η_s and surface dilational viscosity μ_s:

$$[\eta] = 2.5\left(\frac{\eta_i + 0.4\eta_o + \xi}{\eta_i + \eta_o + \xi}\right) \tag{6.9}$$

$$\xi = \frac{(2\eta_s + 3\mu_s)}{R} \tag{6.10}$$

where R is the droplet radius.

When the volume fraction of droplets exceed the Einstein limit (i.e., $\phi > 0.01$), it is necessary to take into account the effect of Brownian motion and interparticles interactions. The smaller the emulsion droplets, the more important the contribution of Brownian motion and colloidal interactions. Brownian diffusion tends to randomize the position of colloidal particles, leading to the formation of temporary doublets, triplets, and so on. The hydrodynamic interactions are of longer range than the colloidal interactions, and they come into play at relatively low volume fractions ($\phi > 0.01$); this results in an ordering of the particles into layers and tends to destroy the temporary aggregates caused by the Brownian diffusion. This also explains the shear thinning behavior of emulsions at high shear rates.

For the volume fraction range $0.01 < \phi < 0.2$, Bachelor [6] derived the following expression for a dispersion of hydrodynamically interacting hard-spheres:

$$\eta_r = 1 + 2.5\phi + 6.2\phi^2 + \vartheta\phi^3 \tag{6.11}$$

The second term in Equation 6.11 is the Einstein limit, the third term accounts for hydrodynamic (two-body) interaction, while the fourth term relates to multibody interaction.

At higher volume fractions ($\phi > 0.2$), η_r is a complex function of ϕ, and the $\eta_r - \phi$ curve is shown schematically in Figure 6.5. This curve is characterized by two asymptotes: $[\eta]$ the intrinsic viscosity, and ϕ_p the maximum packing fraction.

A good semi-empirical equation that fits the curve is given by Dougherty and Krieger [7, 8]:

$$\eta_r = \left(1 - \frac{\phi}{\phi_p}\right)^{-[\eta]\phi_p} \tag{6.12}$$

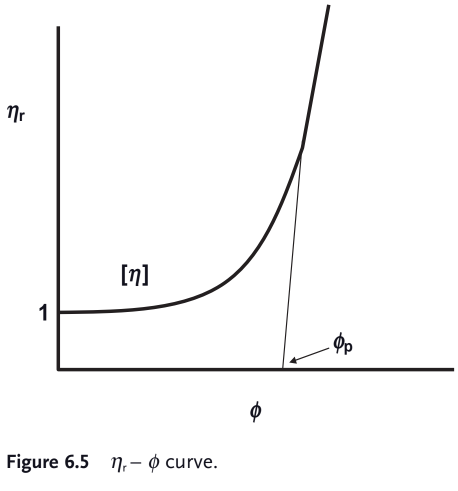

Figure 6.5 $\eta_r - \phi$ curve.

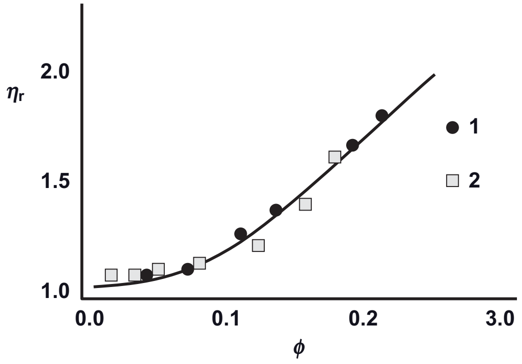

Figure 6.6 Comparison of experimental data of the concentration dependence of different emulsions with some theoretical predictions.

6.3.1
Analysis of the Rheological Behavior of Concentrated Emulsions

When considering the rheology of concentrated emulsions (without deformation of the emulsion drops), an attempt should be made to identify an expression for the fourth term in ϕ^3 of Equation 6.11. Unfortunately, however, there is no theoretical rigorous treatment of this term, and only semi-empirical equations are available [9, 10] for the case of intermediate-volume fractions.

Two models were proposed by Pal [11] that are described by the following expressions:

$$\eta_r\left[\frac{2\eta_r+5\lambda}{2+5\lambda}\right]^{1/2}=\exp\left[\frac{2.5\phi}{1-(\phi/\phi^*)}\right] \tag{6.13}$$

$$\eta_r\left[\frac{2\eta_r+5\lambda}{2+5\lambda}\right]^{1/2}=[1-(\phi/\phi^*)]^{-25\phi^*} \tag{6.14}$$

where λ is the ratio of viscosities of disperse drops and continuous medium, and ϕ^* is the limit of closest packing of drops in free space (as in suspensions), although it was used as a free-fitting factor.

The above models describe rather well the experimental data for various real emulsions over a wide concentration range, as illustrated in Figure 6.6.

The increase of the concentration of drops in emulsions results not only in an increase in viscosity at low shear rates (the limiting residual Newtonian viscosity $\eta(0)$), but also in the appearance of strong non-Newtonian effects – that is, a shear rate dependence of the apparent viscosity. This is illustrated in Figure 6.7, which shows the variation of viscosity with applied stress [9]. This figure shows the remarkable transition from an almost Newtonian behavior at low stresses to an anomalous flow with pronounced non-Newtonian effects.

Another example of the changes in the character of rheological properties just close to the upper boundary of the concentration domain – that is, when

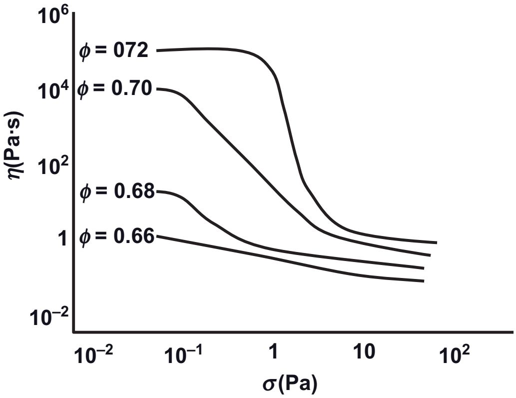

Figure 6.7 Flow curves of a model "oil-in-water" emulsion (average drop size of 4.6 μm) at various volume fractions [12].

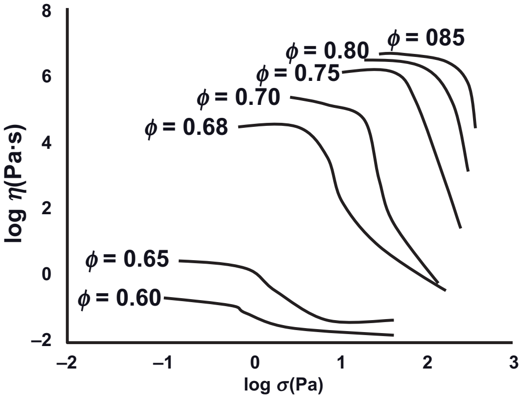

Figure 6.8 Flow curves of "water-in-oil" emulsions when approaching the concentration limit corresponding to the closest packing of spherical drops.

approaching the state of closest packing of spherical drops – is shown in Figure 6.8 for a water-in-oil emulsion [13].

As can be seen from Figures 6.7 and 6.8, the approach to the limit of high concentration and transition beyond the closest packing of nondeformable spherical drops leads to principal changes in the rheological properties. Typically, the Newtonian viscous flow is replaced by a viscoplastic behavior, with a jump-like decrease (by several orders of magnitude) in the apparent viscosity over a narrow range of applied stresses. The jump in the apparent viscosity at a certain shear stress reflects the rupture of the structure, and this stress may be treated as a yield stress.

At high volume fractions ($\phi > 0.6$) there is a significant effect of the average droplet diameter (volume to surface ratio d_{32}). The drop size influences the volume-to-surface ratio, and this leads to a more pronounced effect of the flow inside the drops. This phenomenon becomes more significant when approaching the upper boundary of intermediate concentrations. This is illustrated in Figures 6.9 and 6.10, which show the variation of viscosity with volume fraction for emulsions with different droplet diameters [9]. In the low-volume fraction regime (Figure 6.9) – that is, at $\phi < 0.6$ – there is hardly any effect of the droplet diameter on the viscosity of the emulsion. However, in the high-volume fraction regime ($\phi > 0.6$), a reduction in the droplet diameter results in a significant increase of the viscosity.

Another rheological behavior of concentrated emulsions is the presence of *thixotropy*. The interfacial layers in the closely arranged drops can produce a certain type of structure which is destroyed by deformation but restored at rest.

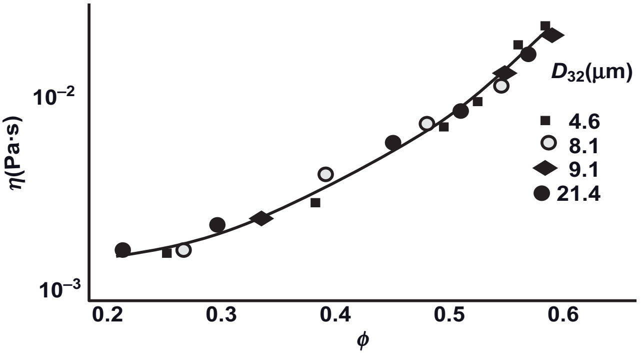

Figure 6.9 Viscosity–volume fraction curves for emulsions with different droplet diameters and at low volume fractions ($\phi < 0.6$).

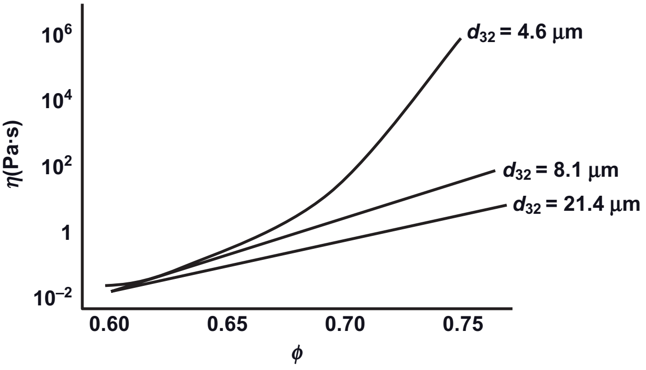

Figure 6.10 Viscosity–volume fraction curves for emulsions with different droplet diameters and at high volume fractions ($\phi > 0.6$).

The interaction between the drops and the evolution of their shape in flow can also result in viscoelastic effects, as will be discussed below.

6.3.1.1 Experimental $\eta_r - \phi$ Curves

Experimental results of $\eta_r - \phi$ curves were obtained for paraffin O/W emulsions [9] stabilized with an A–B–C surfactant consisting of nonyl phenol (B), 13 moles of propylene oxide (C) and polyethylene oxide (PEO), with 27, 48, 80 and 174 moles of ethylene oxide (EO). To illustrate this point, Figure 6.11 shows the results for an emulsion stabilized with the surfactant containing 27 EO (the volume medium diameter of the droplets was 3.5 μm). Calculations based on the Dougherty–Krieger equation are also shown in the same figure, where $[\eta] = 2.5$ and ϕ_p was obtained from a plot of $\eta^{-1/2}$ versus ϕ and extrapolation of the straight line to $\eta^{-1/2} = 0$. The value of ϕ_p was 0.73 (which was higher than the maximum random packing of 0.64, as a result of the polydispersity of the emulsion). Results using the other three surfactants showed the same trend; the experimental $\eta_r - \phi$ curves were close to those calculated using the Dougherty–Krieger equation, which indicated that these emulsions had behaved as hard-spheres.

6.3.1.2 Influence of Droplet Deformability

The influence of droplet deformability on emulsion rheology was investigated by Saiki *et al.* [14] by comparing the $\eta_r - \phi$ curves of hard-spheres of silica with two poly(dimethylsiloxane) (PDMS) emulsions with low (PDMS 0.3) and high deformability (PDMS 0.45) (by controlling the proportion of crosslinking agent for the droplets; 0.3 = low and 0.45 = high crosslinking agent). The $\eta_r - \phi$ curves for the three systems are shown in Figure 6.12. The $\eta_r - \phi$ curve for silica can be fitted by the Dougherty–Krieger equation over the whole volume fraction range, indicating a typical hard-sphere behavior. The $\eta_r - \phi$ curve for the less-deformable PDMS was seen to deviate from the hard-sphere curve at $\phi = 0.58$, while the $\eta_r - \phi$ curve for the more-deformable PDMS deviated from the hard-sphere curve at $\phi = 0.4$. This showed clearly that the deformation of "soft" droplets occurred at a relatively low volume fraction.

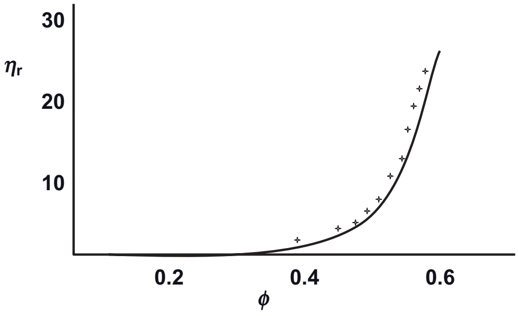

Figure 6.11 Experimental and theoretical $\eta_r - \phi$ curves.

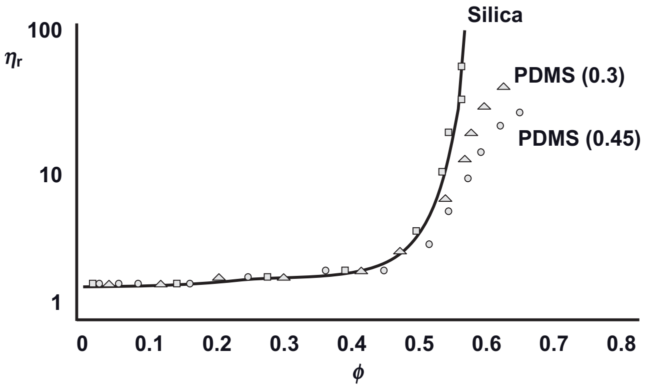

Figure 6.12 $\eta_r - \phi$ curves for silica and two poly(dimethylsiloxane) (PDMS) emulsions.

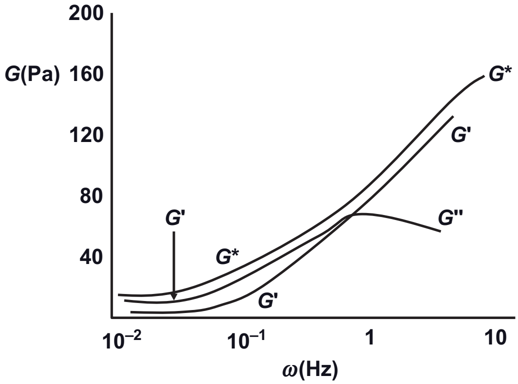

Figure 6.13 Variation of G^*, G' and G'' with frequency ω (Hz).

6.3.2
Viscoelastic Properties of Concentrated Emulsions

The viscoelastic properties of emulsions can be investigated using dynamic (oscillatory) measurements. For this, a sinusoidal strain with amplitude γ_o is applied to the system at a frequency ω (rad s^{-1}), and the stress σ (with amplitude σ_o) is measured simultaneously. From the time shift Δt between the sine waves of strain and stress, it is possible to measure the phase angle shift δ ($\delta = \Delta t\omega$).

From σ_o, γ_o and δ, the complex modulus G^*, the storage modulus G' (the elastic component) and the loss modulus G'' (the viscous component) can be obtained. In this case, G^*, G' and G'' are measured as a function of strain amplitude to obtain the linear viscoelastic region, and then as a function of frequency (keeping γ_o in the linear region). As an illustration, Figure 6.13 shows the results for an O/W emulsion at $\phi = 0.6$ (the emulsion was prepared using an A–B–A block

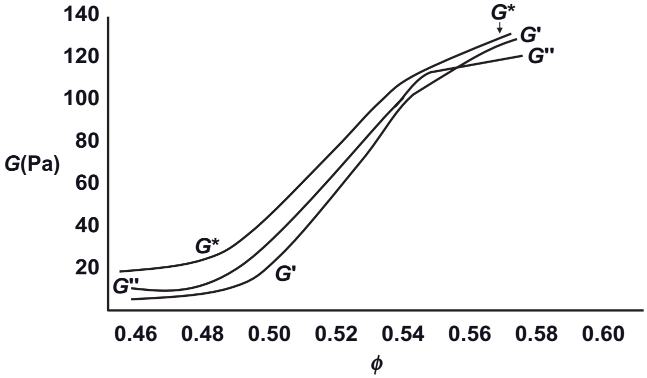

Figure 6.14 Variation of G^*, G' and G'' with ϕ.

copolymer of polyethylene oxide (PEO; A) and polypropylene oxide (PPO; B) with an average of 47 propylene oxide (PO) units and 42 EO units [15, 16].

The results shown in Figure 6.13 are typical for a viscoelastic liquid where, in the low-frequency regime (<1 Hz), $G'' > G'$. However, as the frequency ω increases, so too does G' increase such that, at a characteristic frequency ω^* (the crossover point), G' becomes higher than G'', whereas at a high frequency it becomes closer to G^*. Subsequently, G'' increases with an increase in frequency to reach a maximum at ω^*, after which it decreases with a further increase in frequency.

From ω^*, it is possible to calculate the relaxation time t^*:

$$t^* = \frac{1}{2\pi\omega^*} \tag{6.15}$$

For the above value of ϕ (= 0.6), $t^* = 0.12\,\text{s}$. Subsequently, t^* increases with an increase of ϕ, which reflects the stronger interaction with an increase of ϕ.

To obtain the onset of strong elastic interaction in emulsions, G^*, G' and G'' (obtained in the linear viscoelastic region and high frequency, e.g., 1 Hz) are plotted versus the volume fraction of the emulsion ϕ. At this point, care should be taken to ensure that the droplet size distribution in all emulsions is the same. The most convenient way to achieve this is to prepare an emulsion at the highest possible ϕ (e.g., 0.6), which can then be diluted to obtain various ϕ-values. A droplet size analysis should be conducted for each emulsion to ensure that the size distribution is the same.

Figure 6.14 shows the plots for G^*, G' and G'' versus ϕ. At $\phi < 0.56$, $G'' > G'$, whereas at $\phi > 0.56$, $G' > G''$. In addition, $\phi = 0.56$ is the onset of a predominantly elastic interaction, and reflects the small distance of separation between the droplets.

6.3.2.1 High-Internal Phase Emulsions (HIPES)

The maximum packing fraction ϕ^* of nondeformable droplets in an emulsion is in the region of 0.71–0.75, depending on the droplet size distribution and the arrangement of the drops in space. However, some emulsion systems can exceed this maximum – that is, with $\phi > \phi^*$ – and these are referred to as high-internal phase emulsions (HIPES). In order to achieve this, the deformation of spherical droplets must take place via compression of a dispersion, and this will result in a transformation of the spherical droplets into tightly packed, polygon-shaped particles that occupy the space. These systems have a wide application in cosmetics, foodstuffs, and emulsion explosives.

The general thermodynamic approach to understanding the nature and properties of HIPES was proposed by Princen [17]. According to this approach, HIPES are created by the application of an outer pressure that compresses the drops and transforms them from spheres to polygons. This outer pressure is equivalent to the osmotic pressure Π acting inside the thermodynamic system. The work produced by this pressure when creating a HIPE is equal to the energy stored by the increase in droplet surface area S due to changes in shape. This equality is given by the following expression:

$$-\Pi \delta V = \sigma \delta S \tag{6.16}$$

where σ is the interfacial tension.

Equation 6.13 shows that the osmotic pressure for decreasing the volume ΠdV is equal to the work needed for creating additional new surface δS. Substitution of the expression for concentration gives the equation for the osmotic pressure as a function of the volume fraction ϕ and change in surface area S (reduced by the volume V):

$$\Pi = \sigma \phi^2 \frac{\delta(S/V)}{\delta \phi} \tag{6.17}$$

The stored surface energy serves as a source of elasticity of the HIPES which is observed in shear deformation [18–21]. The experimental evidence of this concept is seen in the close correlation between the concentration dependence of the shear elastic modulus G and osmotic pressure Π, as shown in Figure 6.15. The experimental data of Figure 6.15 are reduced by the Laplace pressure (σ/R).

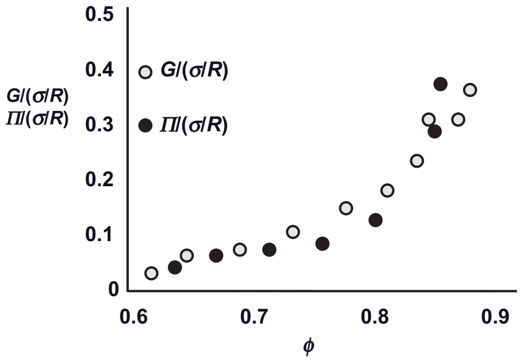

Figure 6.15 Correlation between the elastic modulus (○) and osmotic pressure (●) for HIPES.

Using a reduction factor (σ/R) reflects the proposed conception of elasticity of HIPES as a consequence of the increase of surface energy upon compression of a drop [17, 19]. This approach presumes that both G and Π are inversely proportional to the droplet size. The concentration-dependence of elasticity should be the product $\phi^{1/3}$ ($\phi - \phi^*$) or ϕ ($\phi - \phi^*$), as discussed by Princen [22]. The solid-like properties of HIPES can be observed when $\phi > \phi^*$. The elasticity of HIPES can be illustrated from measurements of the modulus as a function of frequency; this is shown in Figure 6.16 for a model emulsion of monodisperse droplets ($R = 500\,\text{nm}$) of PDMS in water at a volume fraction ϕ of 0.98 [20].

The elastic modulus G' show little dependency on frequency up to $10^2\,\text{s}^{-1}$, indicating that the HIPES behave as a linear elastic material. However, G' increases at very high frequencies, and this effect is attributed to a mechanical glass transition of the emulsion as a viscoelastic material [20].

Further rheological measurements [23] have indicated that HIPES show both nonlinear viscoelastic and viscous behaviors. This is illustrated in Figure 6.17, which shows the variation of the complex modulus with stress for highly concentrated emulsions at various volume fractions. It can be seen that the modulus remains virtually constant with increase of stress, but at a critical stress it shows a rapid decrease, indicating a "softening" of the structure at high stress values. Such behavior is typical of "structured" colloidal dispersions which undergo destruction of this structure when the stress exceeds a critical value.

It is important to compare the amplitude dependence of the elastic (storage) modulus G′ and the viscous (loss) modulus G″ under conditions of large deformation. Although, as mentioned above, HIPES behave as elastic systems with $G' > G''$, at high amplitudes a solid-like to liquid-like behavior is observed. Indeed, at a critical strain γ^* (which is referred to as the melting strain) $G' = G''$, and this can be considered as a measure of the point of rupture of the material structure [15]. Notably, above γ^*, $G'' > G'$.

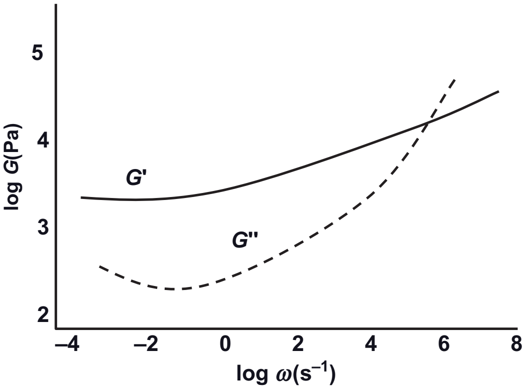

Figure 6.16 Variation of the storage modulus G' and loss modulus G'' with frequency for poly(dimethylsiloxane) emulsion ($r = 500\,\text{nm}$) at $\phi = 0.98$.

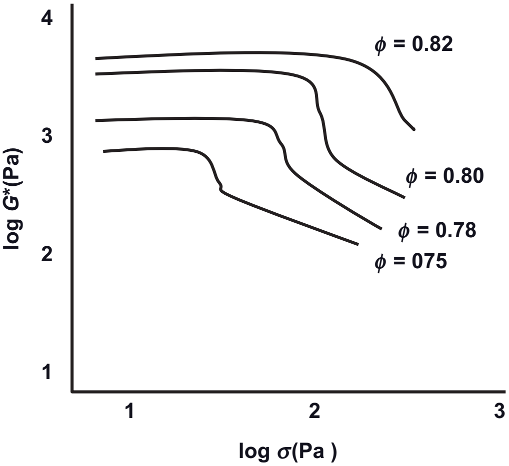

Figure 6.17 Variation of complex modulus with applied stress for highly concentrated (cosmotic grade) water-in-oil emulsions.

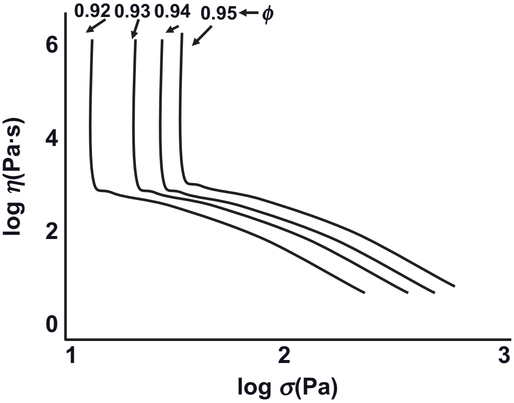

Figure 6.18 Flow curves for highly concentrated water-in-oil emulsions (liquid explosives).

Some authors [24] have observed a structure formation with increasing strain amplitude–a phenomenon which is analogous to negative (anti-) thixotropy discussed in Chapter 3.

The non-Newtonian behavior of HIPES can also be demonstrated from flow curves [25], as illustrated in Figure 6.18 for a water-in-oil emulsion (a liquid emulsion explosive) at various volume fractions of HIPES. The data in Figure 6.18 indicate that the yield values show a large increase with only a small increase in the volume fraction of the emulsions.

A schematic representation of the evolution of rheological properties of emulsions from dilute ($\phi \ll 1$) to highly concentrated emulsions ($\phi > \phi^*$) is shown in

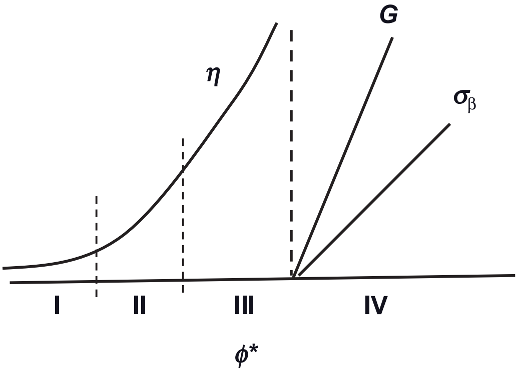

Figure 6.19 General trends for rheological properties of emulsions in the whole volume fraction range.

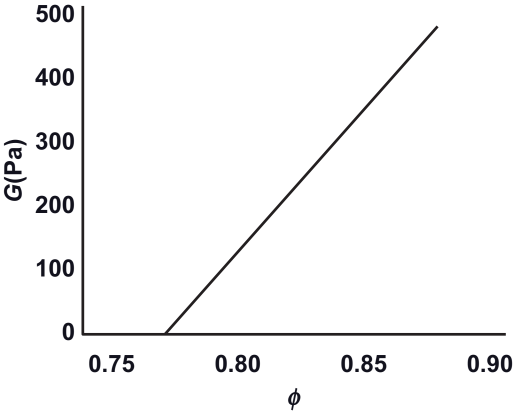

Figure 6.20 Variation of elastic modulus *G* with volume fraction ϕ.

Figure 6.19 [13]. Here, the transition into the domain of highly concentrated emulsions is accompanied by change in the volume fraction dependence, the rheological properties, and the influence of droplet size. This is illustrated in Figures 6.20 and 6.21, which show the variation of elastic modulus G and yield value σ_β with volume fraction ϕ at values above ϕ^*. The linear dependence of G and σ_β on ϕ is consistent with the proposals of Princen and Kiss [22], as discussed above.

The influence of droplet size on the viscosity of concentrated emulsions was investigated by Pal [26], who showed the viscosity of smaller droplets to be higher than that of larger droplets at the same volume fraction. This is illustrated in Figure 6.22, which shows the flow curves for an emulsion with $\phi = 0.76$ at two droplet sizes of 12 and 30 μm. In addition to the higher viscosity of the emulsion

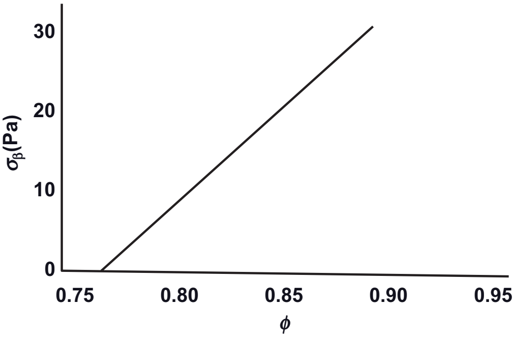

Figure 6.21 Variation of yield stress σ_β with volume fraction ϕ.

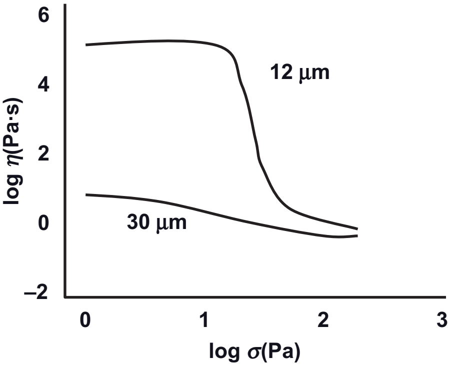

Figure 6.22 Flow curves for concentrated emulsions ($\phi = 075$) with two different droplet sizes.

with the smaller size, the latter shows a more pronounced non-Newtonian effect when compared to the emulsion with the larger size.

The dependence of elastic modulus on droplet diameter can be approximated by the following equation:

$$G = ad_{32}^{-2} \tag{6.18}$$

which shows that a plot of G versus $(1/d^2)$ should give a straight line, as illustrated in Figure 6.23.

It is worth mentioning that, according to the generally accepted Princen–Mason theory [17, 20], the dependence of G on d was always considered as reciprocal linear (but not squared), as it follows from the basic concept of elasticity of HIPES discussed above.

6.3.2.2 Deformation and Break-Up of Droplets in Emulsions During Flow

During flow, the emulsion drops undergo deformation (from spherical to ellipsoidal shape), which is then followed by a break-up to smaller drops. The driving

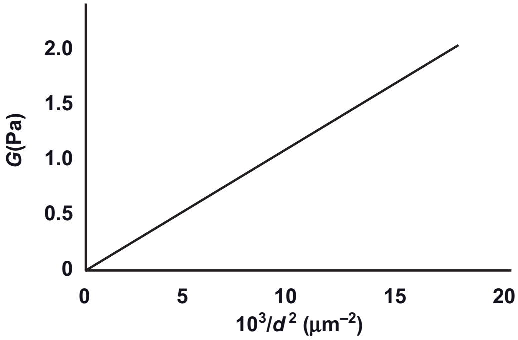

Figure 6.23 Dependence of elastic modulus on the average droplet size for highly concentrated emulsions.

force for drop deformation is the shear stress, and such deformation is resisted by the interfacial tension, as determined by the Laplace pressure. Thus, the morphology of a drop is determined by the ratio of stress to the Laplace pressure; that is, the capillary number Ca given by the following expression:

$$Ca = \frac{\eta_o \dot{\gamma}}{\sigma/R} \tag{6.19}$$

where η_o is the viscosity of the medium, $\dot{\gamma}$ is the shear rate, σ is the interfacial tension, and R is the droplet radius.

The degree of anisotropy D of a deformed drop is based on the classical Taylor model for the viscosity of dilute emulsions [27]:

$$D = \frac{16 + 19\lambda}{16(\lambda + 1)} Ca \tag{6.20}$$

where λ is the ratio of viscosity of the disperse phase and disperse medium.

For a moderately concentrated emulsion, the dynamic interaction between the drops and D must be taken into account; this is given by the following expression [28]:

$$D = \left[\frac{16 + 19\lambda}{16(\lambda + 1)}\right]\left[1 + \frac{5(2 + 5\lambda)}{4(\lambda + 1)}\phi\right] Ca \tag{6.21}$$

One successful method for obtaining experimental results at various emulsion volume fractions is based on modification of the capillary number, whereby the viscosity of the medium η_o is replaced by the "mean field" viscosity–that is, the viscosity of the emulsion as a whole η_{em}:

$$Ca_{\mathrm{m}} = \frac{\eta_{\mathrm{em}} \dot{\gamma}}{\sigma/R} \tag{6.22}$$

A plot of D versus Ca_{m} is shown in Figure 6.24 for emulsions with different volume fractions. All results fall on the same line, thus confirming the validity of Equation 6.22.

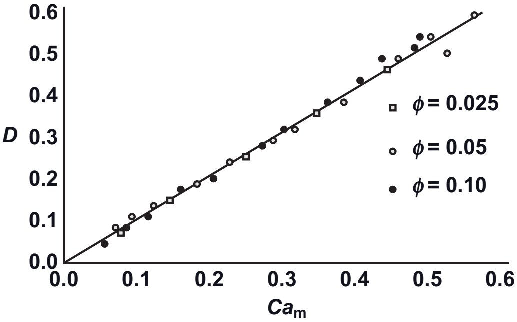

Figure 6.24 Variation of D with Ca_m for emulsions with various volume fractions.

The connection between the shape of the droplet and the whole complex behavior of emulsions was established in a series of publications [29–34] for various flow geometries. The final results were obtained in an analytical form. The shear stress in steady flow is expressed as a function of shear rate and capillary number.

The shear stress τ is related to Ca, the ratio of viscosities of the disperse phase and medium λ, and the volume fraction ϕ of the oil by the following expression:

$$\tau = \frac{2KCaf_1f_2^2}{3(Ca^2 + f_1^2)} \tag{6.23}$$

where f_1 and f_2 are given by the following expressions:

$$f_1 = \frac{40(\lambda+1)}{(3+2\lambda)(16+9\lambda)} \tag{6.24}$$

$$f_2 = \frac{5}{3+2\lambda} \tag{6.25}$$

The factor K represents the influence of volume fraction on the viscosity:

$$K = \left(\frac{6\sigma}{5R}\right)\frac{(\lambda+1)(3+\lambda)\phi}{5(\lambda+1)-5(2+5\lambda)\phi} \tag{6.26}$$

The problem of calculating the droplet deformation in a flow of viscous liquid was rigorously formulated by Maffettone and Minale [35]. This deformation consists of the transition from spherical to ellipsoidal shape, and the exact solution to the problem was provided by Wetzel and Tucker [36] (without taking into account the interfacial tension), and later by Jackson and Tuker [37], who proposed a complete solution which included the influence of all factors affecting the shape of a drop. A comparison between the theoretical prediction of the dependence of D on Ca and the experimental results [37] is shown in Figure 6.25.

The deformation of drops in flow from spherical to ellipsoidal shape influences the viscosity of the emulsion [38], which can be confirmed by measurement of the viscosity of an emulsion (water in viscous alkyd resin) at various shear rates.

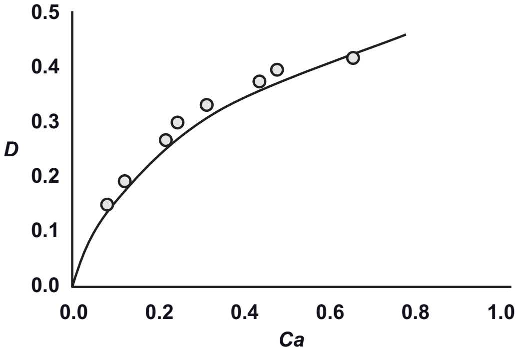

Figure 6.25 Comparison of theoretical prediction of dependence of droplet deformation on capillary number in viscous liquid flow ($\lambda = 3.6$) (solid line) with experimental results (circles).

In the low-shear rate regime (where no deformation occurs) the viscosity–volume fraction curve is very close to that of a suspension. However, in the high-shear rate regime, where deformation of the drops occurs as a result of the low viscosity ratio λ, a non-Newtonian flow is observed and the volume fraction dependence of viscosity is given by the following empirical equation:

$$\eta = \eta_o(1-\phi) \tag{6.27}$$

Equation 6.27 shows that the viscosity of the emulsion in the high-shear rate regime is lower than that of the medium.

The above problem of calculating the deformation of a drop in a flow is considered without taking into account inertia – that is, at very low Reynolds number (*Re*). Estimations have shown that the increase in *Re* enhances the impact of inertia, which in turn leads to a stronger deformation of the drop and consequently to the growth of stresses in the interfacial layer [39]. It also influences the stability of the drop which is determined by surface stresses.

The possibility of drop break-up is determined by the balance of the outer stress created by the flow of liquid around the drop (given by the product of the viscosity and shear rate $\eta_o\dot{\gamma}$), and the Laplace pressure (σ/R). Thus, the determining factor for drop stability is a critical value for the capillary number Ca^*, which depends on the ratio of the viscosities of disperse droplets and medium λ. The value of Ca^* decreases with increase of λ in the domain $\lambda < 1$. Hinch and Arcivos [40] expressed the variation of Ca^* with λ (at low values) by,

$$Ca^* = 0.054\lambda^{-2/3} \tag{6.28}$$

Complete results were obtained by Grace [41], who examined both simple shear as well as the 2-D extension in the full range of λ-values, as illustrated in Figure 6.26. The data in Figure 6.26 demonstrate two interesting results: (i) a minimum in Ca^* of 0.4 when $\lambda = 1$ (i.e., when the viscosities of the disperse phase and medium are equal); and (ii) an absence of drop-break-up in laminar flow when $\lambda > 4$ (i.e., drops of high viscosity).

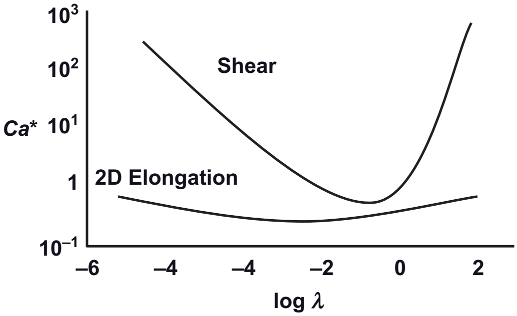

Figure 6.26 Dependence of Ca^* on λ in simple shear and two-dimensional extensional flow.

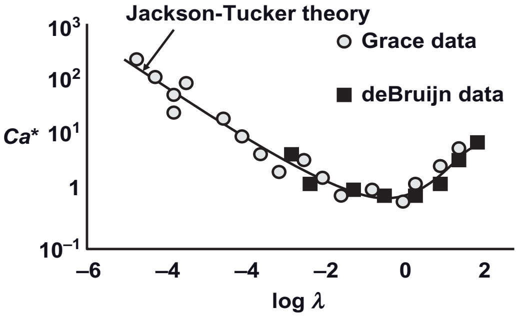

Figure 6.27 Correlation of theoretical dependence of Ca^* on λ (solid line) with experimental data (circles and squares) in laminar simple shear.

The results of systematic investigation of single droplet break-up are shown in Figure 6.27. These experimental data are in reasonable agreement with the theoretical predictions of Jackson and Tucker [37], with the break-up conditions being defined as the limit of their deformation (as discussed above). It is assumed that, when a deformation results in some steady state of a drop, then this rate of deformation is less than that corresponding to the critical value Ca^*. The calculations show that droplet deformation becomes continuous without limit, which means that the drop will break when $Ca > Ca^*$.

The critical conditions for droplet break-up in a viscoelastic medium are different from those in a purely viscous liquid. Notably, the surface stresses at the interface may vary, and represent a function of the Reynolds number and the Weissenberg number (the ratio of the characteristic time of outer action and inner relaxation). The use of numerical modeling has shown that the capillary number increases as the Weissenberg number is increased; that is, when the viscoelasticity of the medium is enhanced [42].

Although the above discussions refer to the case of single drops, in concentrated emulsions (practical systems) it is necessary to include certain modifications so as

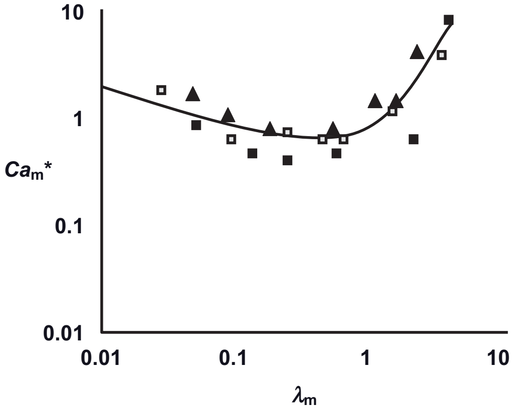

Figure 6.28 Condition of break-up for silicone oil-in-water emulsions at different oil volume fractions (0–0.7).

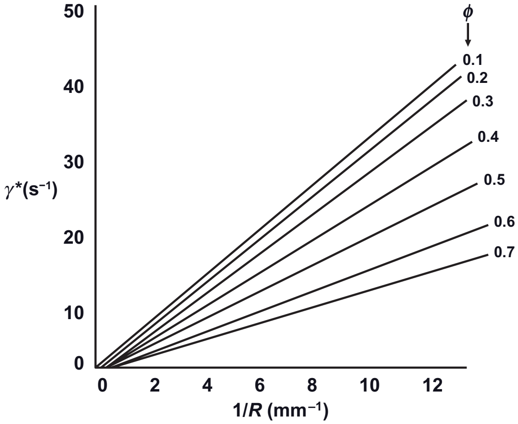

Figure 6.29 Dependence of the critical shear rate corresponding to break-up on droplet size for emulsions at different volume fractions.

to take into account the droplet–droplet interactions. One convenient method for this is to modify the definition of Ca^* and λ by substituting the viscosity of the medium with that of the emulsion (mean field approximation). In this way, the modified viscosity ratio λ_m is given as:

$$\lambda_m = \frac{\eta_{dr}}{\eta_{em}} \tag{6.29}$$

The results of experimental studies discussed in terms of the function $Ca_m^*(\lambda_m)$ are shown in Figure 6.28 for emulsions with a wide volume fraction range (up to $\phi = 0.7$). The influence of volume fraction can be clearly seen in Figure 6.29, which

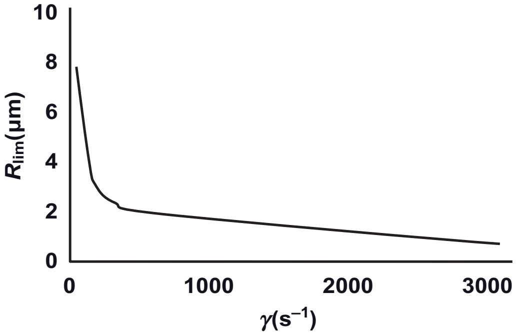

Figure 6.30 Dependence of drop size (as a result of laminar shearing) on shear rate for silicone oil-in-water emulsions ($\phi = 0.7$).

shows plots of the critical shear rate of break-up as a function of reciprocal radius. In this case, the higher the value of ϕ, the lower the shear rate required for break-up of the drops, a situation which is consistent with the increase of stress with increasing ϕ.

The drop break-up at a given shear rate can continue up to a limiting value R_{lim} because the capillary number decreases with the decrease of radius, such that it finally becomes less than the critical value Ca^*. This is illustrated in Figure 6.30, which shows the dependence of R_{lim} on shear rate. In this case, a parabolic relationship is obtained that is represented by the following scaling law [43]:

$$R_{\text{lim}} = C\frac{\sigma}{\eta\dot{\gamma}} \tag{6.30}$$

Here, the factor C is of the order of 1, and reflects the critical value of the capillary number.

It is essential that all theoretical models must be conducted, and experimental results obtained, under the conditions of laminar flow. The transition to a higher Reynolds number (>2000) – that is, under a turbulent regime – will greatly complicate the break-up of droplets in emulsions. The basic problem is the presence of wide fluctuations in the local velocities and stresses, which in turn greatly complicates the theoretical analysis when compared to the case of laminar flow.

Generally speaking, there are two regimes for turbulent flow – namely, "turbulent inertial" (TI) and "turbulent viscous" (TV). The difference between these is related to the ratio of the characteristic sizes of the liquid droplets and the turbulent vortex [44]. The minimum droplet size in the TI regime depends on the ratio of the dynamic fluctuation (break-up of a droplet) and surface tension, whereas for the TV regime the break-up of droplets occurs under shear stresses across the continuous medium.

Vankova *et al.* [45] have shown that the maximum size of a droplet in the TI regime, $d_{\text{TI,max}}$ is given by the following expression:

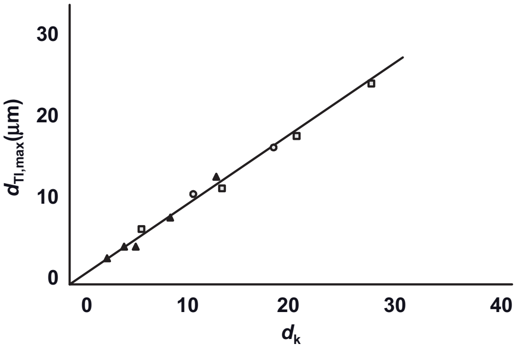

Figure 6.31 Dependence of the maximum droplet diameter $d_{TI,max}$ in turbulent inertial regime on the determining factors, d_k predicted by Equation 6.31 for emulsions with different emulsifiers.

$$d_{TI,max} = A_1(\varepsilon^{-2/5}\sigma^{3/5}\rho_c^{-3/5}) = A_1 d_k \tag{6.31}$$

where A_1 is a factor that is of the order of 1, ε is the intensity of energy dissipation characterizing the dynamic situation in a flow, and ρ_c is the density of the continuous phase. The term in brackets designated as d_k is a characteristic length.

The maximum size of a drop in the TV regime, $d_{TV,max}$, is determined by the viscous shear stresses:

$$d_{TV,max} = A_2(\varepsilon^{-1}\eta_o^{-1/2}\rho_c^{-1/2}\sigma) \tag{6.32}$$

where the constant $A_2 \approx 4$ and η_o is the viscosity of the medium.

Equation 6.32 is only valid for low-viscosity drops. For emulsions with more viscous drops dispersed in a medium of arbitrary viscosity, $d_{TV,max}$ is given by the following general expression [46–50]:

$$d_{TV,max} = A_3\left(1 + A_4\frac{\eta_{dr}\varepsilon^{1/3}d_{TV,max}^{1/3}}{\sigma}\right)^{3/5} d_k \tag{6.33}$$

where A_3 and A_4 are constants, and η_{dr} is the viscosity of the dispersed liquid drops.

The results of experimental investigations of the dependence of droplet size on the determining factors for the TI regime confirm the validity of Equation 6.31 with $A_1 = 0.86$. This is shown in Figure 6.31 for hexadecane-in-water emulsions using different emulsifiers, where $d_{TI,max}$ is plotted versus d_k. A comparison of experimental results with theory for the TV regime is shown in Figure 6.32 for a large number of emulsions, again confirming the validity of Equation 6.33.

Although, the above analysis is focused on the final equilibrium state of the droplets, the kinetics of the break-up process is also of great interest. This kinetic process was considered by Vankova *et al.* [51], who introduced a single additional constant k_{dr} that depends on the droplet diameter, d:

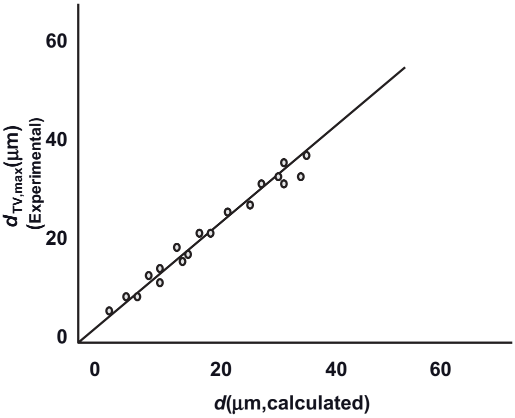

Figure 6.32 Comparison of experimental and theoretical dependence of the maximum droplet diameter $d_{TI,max}$ in turbulent viscous regime on the calculated d predicted by equation for different emulsions.

$$k_{dr}(d) = B_1 \frac{\varepsilon^{1/3}}{d^{2/3}} \exp\left[-B_2\left(\frac{d_k}{d}\right)^{5/3}\left(1 + B_3 \frac{\eta_{dr}\varepsilon^{1/3}d^{1/3}}{\sigma}\right)\right] \tag{6.34}$$

where B_1, B_2 and B_3 are fitting constants.

The experiments carried out on different emulsions confirmed the validity of Equation 6.34, and allowed Vankova *et al.* [51] to calculate the values of the constants in Equation 6.34.

It should be mentioned that the break-up of drops in the flow of emulsions leads to the formation of a large number of droplets with different sizes. The emulsion should be characterized by its maximum size as well as its size distribution. In most cases, the size distribution is represented by a Gaussian function, although the real droplet size distribution depends on the viscosity of the droplets [52].

References

1 Criddle, D.W. (1960) The viscosity and viscoelasticity of interfaces, in *Rheology*, vol. **3** (ed. F.R. Eirich), Academic Press, New York, Chapter 11, pp. 429–442.

2 Edwards, D.A., Brenner, H., and Wasan, D.T. (1991) *Interfacial Transport Processes and Rheology*, Butterworth-Heinemann, Boston, London.

3 Prince, A., Arcuri, C., and van den Tempel, M. (1967) *J. Colloid Interface Sci.*, **24**, 811.

4 Biswas, B. and Haydon, D.A. (1963) *Proc. Roy. Soc.*, **A271**, 296; Biswas, B. and Haydon, D.A. (1963) *Proc. Roy. Soc.*, **A271**, 317; Biswas, B. and Haydon, D.A. (1962) *Kolloid Z.*, **185**, 31; Biswas, B. and Haydon, D.A. (1962) *Kolloid Z.*, **186**, 57.

5 Einstein, A. (1906) *Ann. Physik.*, **19**, 289; Einstein, A. (1911) *Ann. Physik.*, **34**, 591.

6 Bachelor, G.K. (1977) *J. Fluid Mech.*, **83**, 97.

7 Krieger, I.M. and Dougherty, T.J. (1959) *Trans. Soc. Rheol.*, **3**, 137.

8 Krieger, I.M. (1972) *Adv. Colloid Interface Sci.*, **3**, 111.

9 Pal, R. (2000) *J. Colloid Interface Sci.*, **225**, 359.

10 Phan-Thien, N. and Pharm, D.C. (1997) *J. Non-Newtonian Fluid Mech.*, **72**, 305.

11 Pal, R. (2001) *J. Rheol.*, **45**, 509.

12 Mason, T.G., Bibette, J., and Weitz, D.A. (1996) *J. Colloid Interface Sci.*, **179**, 439.

13 Derkach, S.R. (2009) *Adv. Colloid Interface Sci.*, **151**, 1.

14 Tadros, T.F. (1991) Rheological properties of emulsion systems, in *Emulsions – A Fundamental and Practical Approach*, vol. **363** (ed. J. Sjoblom), NATO ASI Series, Kluwer Academic Publishers, London, pp. 173–188.

15 Saiki, Y., Horn, R.G., and Prestidge, C.A. (2008) *J. Colloid Interface Sci.*, **320**, 569.

16 Tadros, T.F. (1994) *Colloids Surf.*, **A91**, 215.

17 Princen, H.M. (1986) *Langmuir*, **2**, 519.

18 Lacasse, M.D., Grest, C.S., Levine, D., Mason, T.G., and Weitz, D.A. (1996) *Phys. Rev. Letters*, **76**, 3448.

19 Mason, T.G., Lacasse, M.D., Grest, C.S., Levine, D., Bibette, J., and Weitz, D.A. (1997) *Phys. Rev. E*, **56**, 3150.

20 Mason, T.G. (1999) *Curr. Opin. Colloid Interface Sci.*, **4**, 231.

21 Babak, V.C. and Stebe, M.J. (2002) *J. Dispersion Sci. Technol.*, **23**, 1.

22 Princen, H.M. and Kiss, A.D. (1986) *J. Colloid Interface Sci.*, **112**, 427.

23 Ponton, A., Clement, P., and Grossiord, J.L. (2001) *J. Rheol.*, **45**, 521.

24 Zao, G. and Chen, S.B. (2007) *J. Colloid Interface Sci.*, **316**, 858.

25 Masalova, I. (2007) *Colloid J.*, **69**, 185.

26 Pal, R. (1996) *AICHE J.*, **42**, 3181.

27 Taylor, G.I. (1934) *Proc. Roy. Soc. A*, **146**, 501.

28 Choi, C.J. and Schowalter, W.R. (1975) *Phys. Fluids*, **18**, 420.

29 Palierne, J.F. (1990) *Rheol. Acta*, **29**, 204.

30 Doi, M. and Ohta, T. (1991) *J. Chem. Phys.*, **95**, 1242.

31 Bousmina, M. (1999) *Rheol. Acta*, **38**, 73.

32 Grmela, M., Bousmina, M., and Palierne, J.F. (2000) *Rheol. Acta*, **40**, 560.

33 Bousmina, M., Grmela, M., and Palierne, J.F. (2002) *Rheol. Acta*, **46**, 1381.

34 Bousmina, M., Grmela, M., and Zhou, C. (2002) *J. Rheol.*, **46**, 1401.

35 Maffettone, P.L. and Minale, M. (1998) *J. Non-Newtonian Fluid Mech.*, **78**, 227.

36 Wetzel, E.D. and Tucker, C.L. (2001) *J. Fluid Mech.*, **426**, 199.

37 Jackson, N.E. and Tucker, C.L. (2003) *J. Rheol.*, **47**, 659.

38 Torza, S., Cox, R.G., and Mason, S.G. (1972) *J. Colloid Interface Sci.*, **38**, 395.

39 Li, X. and Sarker, K. (2005) *J. Rheol.*, **49**, 1377.

40 Hinch, T.J. and Arcivos, A. (1980) *J. Fluid Mech.*, **98**, 305.

41 Grace, H.P. (1982) *Chem. Eng. Commun.*, **14**, 225.

42 Renardly, Y. (2008) *Rheol. Acta*, **47**, 89.

43 Mason, T.G. and Bibette, J. (1996) *J. Phys. Rev. Lett.*, **77**, 3481.

44 Heinze, J.O. (1955) *AICHE*, **1**, 289.

45 Vankova, N., Tcholakova, S., Denkov, N.D., Ivanov, I.B., Vulchev, V.D., and Danner, T. (2007) *J. Colloid Interface Sci.*, **312**, 363.

46 Podgorska, W. (2006) *Chem. Eng. Sci.*, **61**, 2986.

47 Calabrese, R.V., Chang, T.P.K., and Dang, P.T. (1986) *AICHE J*, **32**, 657.

48 Wang, C.Y. and Calabrese, R.V. (1986) *AICHE J*, **32**, 677.

49 Razzaque, M.M., Afacan, A., Lu, S., Nandakumar, K., Jacob, H., Masliyah, J.H., and Sanders, R.S. (2003) *Int. J. Multiphase Flow*, **29**, 1451.

50 Eastwood, C.D., Armi, L., and Lasheras, J.C. (2004) *J. Fluid Mech.*, **502**, 309.

51 Vankova, N., Tcholakova, S., Denkov, N.D., and Danner, T. (2007) *J. Colloid Interface Sci.*, **313**, 612.

52 Tcholakova, S., Vankova, N., Denkov, N.D., and Danner, T. (2007) *J. Colloid Interface Sci.*, **310**, 570.

7

Rheology Modifiers, Thickeners, and Gels

7.1

Introduction

In any formulation (personal care, cosmetic, paint, printing ink, pharmaceutical or agrochemical), there is a need to modify the rheology of the system so as to achieve: (i) a long-term physical stability (an absence of creaming or sedimentation and separation); and (ii) an ease of application:

- For most formulations, a shear thinning system is required to achieve a good spreadability and, in the case of personal care products, a good "skin feel."
- For paints, a good coating is required, and also a lack of "sag."
- For pharmaceuticals, an ease of flow is required for injectables, and an ease of spreading for topical applications.
- For agrochemical formulations, there must be an ease of flow from the container, and an ease of dispersion on dilution.

7.2

Classification of Thickeners and Gels

Rheology modifiers can be classified into several categories:

- Gels produced as a result of repulsive interaction, for example, expanded double layers.
- Self-structured systems, whereby a weak flocculation is induced so as to produce a "gel" by the particles or droplets. This requires control of the particle size and shape, the volume fraction of the dispersion, and the depth of the secondary minimum.
- Thickeners consisting of high-molecular-weight polymers or finely divided particulate systems that interact in the continuous phase, forming a "three-dimensional" (3-D) structure.
- Crosslinked polymers (chemical gels).

Rheology of Dispersions: Principles and Applications. Tharwat F. Tadros

ISBN: 978-3-527-32003-5

- Self-assembled structures, such as associative thickeners.
- Liquid crystalline structures of the hexagonal, cubic, or lamellar phases.

7.3
Definition of a "Gel"

In all of the above systems, essentially a "gel" – a "semi-solid" consisting of a "network" in which the solvent is "entrapped" – is produced. A gel may be classified as a "liquid-in-solid" dispersion, and demonstrates not only certain solid-like properties but also liquid-like properties; that is, it is a *viscoelastic system*. Depending on the gel strength, the system may behave as either a viscoelastic solid or a viscoelastic liquid, depending on the stress applied on the gel. For "strong" gels (such as those produced by chemical crosslinking), the system may behave as a viscoelastic solid up to high stresses, and the gel might also show a significant yield value. For "weaker" gels, such as those produced by associative thickeners, the system may show a viscoelastic, liquid-like behavior at lower applied stresses when compared to chemical gels.

7.4
Rheological Behavior of a "Gel"

7.4.1
Stress Relaxation (after Sudden Application of Strain)

One of the most useful ways to describe a gel is to consider the relaxation time of the system (as discussed in Chapter 4). When considering a "gel" where the components are in some form of 3-D structure, in order to deform the gel instantly a stress is required, with energy being stored in the system (a high-energy structure). Subsequently, in order to maintain the new shape (i.e., a constant deformation), the stress required will become smaller as the components of the "gel" undergo a degree of diffusion that results in the gradual creation of a lower-energy structure (this is termed structural or stress relaxation). In the long term, however, the deformation will become permanent with a complete relaxation of the structure (new low-energy structure) and viscous flow will occur [1, 2].

The above behavior is shown schematically in Figure 7.1, where the stress (after a sudden application of strain) is plotted as a function of time. This representation is for a viscoelastic liquid (the Maxwell element represented by a spring and dashpot in series), with complete relaxation of the springs at infinite time (see Chapter 4). In other words, the stress approaches zero at infinite time.

The above exponential decay of the stress can be represented by the following equation:

$$\sigma(t) = \sigma_o \exp\left(-\frac{t}{\tau}\right) \tag{7.1}$$

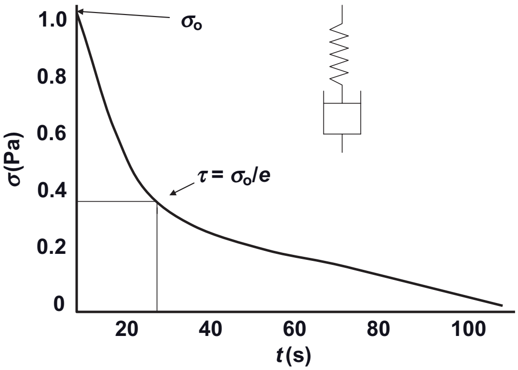

Figure 7.1 Stress relaxation after sudden application of strain for a viscoelastic liquid.

where τ is the stress relaxation time.

If the stress is divided by the strain, then the modulus G is obtained:

$$G(t) = G_o \exp\left(\frac{t}{\tau}\right) \tag{7.2}$$

where G_o is the instantaneous modulus (the spring constant).

Many crosslinked gels behave like viscoelastic solids (Kelvin model), with another spring in parallel having an elasticity G_e. The modulus does not decay to zero.

The relaxation modulus is given by:

$$G(t) = G_o \exp\left(\frac{t}{\tau}\right) + G_e \tag{7.3}$$

Figure 7.2 shows the variation of $G(t)$ with time for a viscoelastic solid.

A useful way to distinguish between the various gels is to consider the Deborah number, D_e:

$$D_e = \frac{\tau}{t_e} \tag{7.4}$$

For a gel that shows "solid-like" behavior (3-D structure"), D_e is large when compared to a gel that behaves as a viscoelastic liquid.

7.4.2
Constant Stress (Creep) Measurements

In this case, a constant stress σ is applied and the strain (deformation) γ or compliance J ($= \gamma/\sigma$; Pa^{-1}) is followed as a function of time. A gel that consists of a strong 3-D structure (e.g., crosslinked) behaves as a viscoelastic solid, as illustrated in Figure 7.3. This behavior may occur up to high applied stresses; in other words, the critical stress above which significant deformation occurs can be quite high.

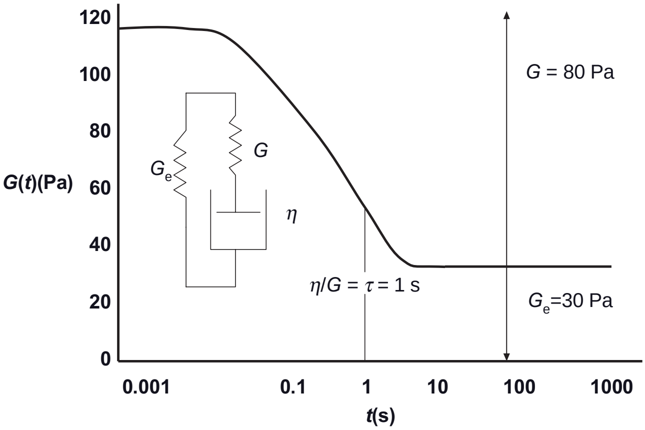

Figure 7.2 Variation of $G(t)$ with t for a viscoelastic solid.

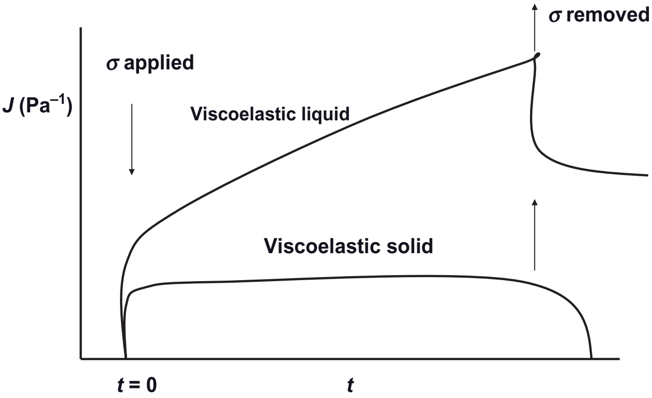

Figure 7.3 Viscoelastic solid and viscoelastic liquid response for gels.

A weaker gel (produced for example from high-molecular-weight polymers that are physically attached) behaves as a viscoelastic liquid, as shown in Figure 7.3. In this case, the viscoelastic solid behavior only occurs at much lower stresses than are observed with the crosslinked gels.

7.4.3
Dynamic (Oscillatory) Measurements

A sinusoidal strain (or stress) with amplitude γ_o and frequency ω (rad s^{-1}) is applied to the system, and the resulting stress (or strain) with amplitude σ_o is simultaneously measured [1, 2]; this is illustrated in Figure 7.4.

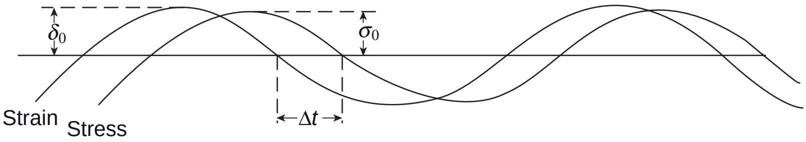

Δt = time shift for sine waves of stress and strain
$\Delta t\ \omega = \delta$ phase angle shift
ω = frequency in rad s^{-1}
$\omega = 2\pi\upsilon$

Perfectly elastic solid	$\delta = 0$
Perfectly viscous liquid	$\delta = 90°$
Viscoelastic system	$0 < \delta < 90°$

Figure 7.4 Sine waves for strain and stress.

For any gel $\delta < 90°$, and the smaller the value of δ the stronger the gel. From the amplitudes of stress and strain (σ_o and γ_o) and the phase angle shift δ, it is possible to obtain the following viscoelastic parameters:

$$|G^*| = \frac{\sigma_o}{\gamma_o} \tag{7.5}$$

$$\text{Storage (elastic) modulus } G' = |G^*|\cos\delta \tag{7.6}$$

$$\text{Loss (viscous) modulus } G'' = |G^*|\sin\delta \tag{7.7}$$

$$\text{Tan}\,\delta = \frac{G''}{G'} \tag{7.8}$$

For gels, tan $\delta < 1$, and the smaller the value, the stronger the gel.

7.5
Classification of Gels

Gels may be conveniently classified into two main categories: (i) gels based on macromolecules (polymer gels); and (ii) gels based on solid particulate materials. Numerous examples of gels based on polymers may be identified, including gels produced by the overlap or "entanglement" of polymer chains (physical gels), gels produced by the association of polymer chains (the so-called associative thickeners), and gels produced by the physical or chemical crosslinking of polymer chains (sometimes referred to as "microgels"). The most common particulate gels are those based on "swelling" clays (both, aqueous and nonaqueous) and finely divided oxides (e.g., silica gels).

Apart from the above two main classes, gels can also be produced from surfactant liquid crystalline phases, such as hexagonal, cubic, or lamellar structures. These gels may be produced not only from single surfactant molecules, usually at high concentrations (>30%), but also by using mixtures of surfactants and other amphiphiles such as long-chain alcohols (e.g., mixtures of alcohol ethoxylates with cetyl, stearyl, or ceto-stearyl alcohol). Gels may also be produced from ionic surfactants by the addition of other ingredients, such as salts and/or long-chain alcohols.

7.5.1
Polymer Gels

7.5.1.1 Physical Gels Obtained by Chain Overlap

Flexible polymer that produce random coils in solution can produce "gels" at a critical concentration C^*, referred to as the polymer coil "overlap" concentration [3]. This picture can be realized by considering the coil dimensions in solution: if a polymer chain is represented by a random walk in three dimensions, then two main parameters may be defined: (i) the root mean square end-to-end length $<r^2>^{1/2}$;and (ii) the root mean square radius of gyration $<s^2>^{1/2}$ (sometimes denoted by R_G). These two parameters are related by:

$$\langle r^2 \rangle^{1/2} = 6^{1/2} \langle s^2 \rangle^{1/2} \tag{7.9}$$

The viscosity of a polymer solution increases gradually with any increase in its concentration and, at a critical concentration, C^*, the polymer will coil with a radius of gyration R_G and a hydrodynamic radius R_h (R_h is higher than R_G due to solvation of the polymer chains) begin to overlap, and this results in a rapid increase in viscosity. This is illustrated in Figure 7.5, which shows the variation of $\log \eta$ with $\log C$.

In the first part of the curve, $\eta \propto C$, whereas in the second part (above C^*) $\eta \propto C^{3.4}$. A schematic representation of polymer coil overlap is shown in Figure 7.6, which shows the effect of gradually increasing the polymer concentration. The polymer concentration above C^* is referred to as the semi-dilute range [3].

C^* is related to R_G and to the polymer molecular weight, M by:

$$C^* = \left(\frac{4}{3}\right) \pi R_G^3 \left(\frac{N_{av}}{M}\right) \approx 1 \tag{7.10}$$

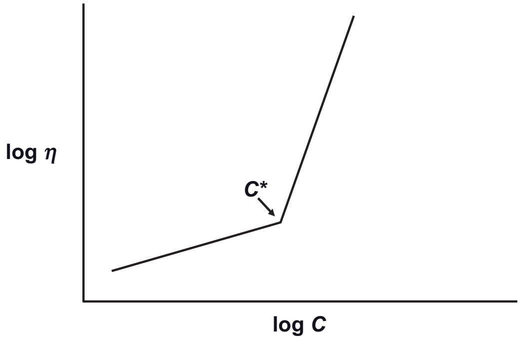

Figure 7.5 Variation of $\log \eta$ with $\log C$.

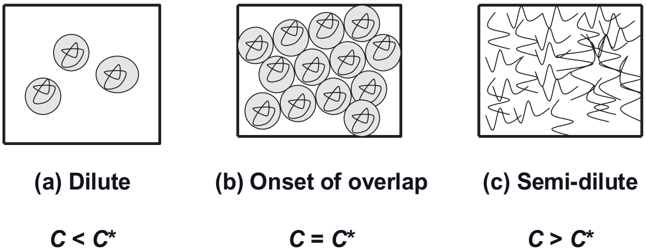

Figure 7.6 Cross-over between dilute and semi-dilute solutions.

where N_{av} is Avogadro's number. As M increases, C^* becomes progressively lower, showing that, in order to produce physical gels at low concentrations by a simple polymer coil overlap, it is necessary to use high-molecular-weight polymers.

Another method which allows the polymer concentration at which chain overlap occurs to be reduced, is to use polymers that form extended chains. An example of this is xanthan gum, which produces a conformation in the form of a helical structure with a large axial ratio. These polymers produce much higher intrinsic viscosities, and demonstrate both rotational and translational diffusion. However, although the relaxation time for the polymer chain is much higher than that of a corresponding polymer with the same molecular weight, it produces a random coil conformation.

The above polymers interact at very low concentrations, and the overlap concentration can be very low (<0.01%). These polysaccharides are used in many formulations to produce physical gels at very low concentrations.

7.5.1.2 Gels Produced by Associative Thickeners

Associative thickeners are hydrophobically modified polymer molecules whereby alkyl chains (C_{12}–C_{16}) are either randomly grafted onto a hydrophilic polymer molecule such as hydroxyethyl cellulose (HEC), or simply grafted at both ends of the hydrophilic chain. An example of a hydrophobically modified HEC is Natrosol plus (Hercules), which contains three to four C_{16} grafted randomly onto HEC. An alternative example of a polymer containing two alkyl chains at both ends of the molecule is HEUR (Rohm and Haas); this is composed of polyethylene oxide (PEO) that has been capped at both ends with a linear C_{18} hydrocarbon chain.

The above hydrophobically modified polymers form gels when dissolved in water. Moreover, gel formation can occur at relatively lower polymer concentrations when compared to the unmodified molecule.

The most likely explanation of gel formation is due to a hydrophobic bonding (association) between the alkyl chains in the molecule, and which effectively causes an apparent increase in the molecular weight. These associative structures are similar to micelles, except that the aggregation numbers are much smaller [4].

Figure 7.7 shows the variation of viscosity (measured using a Brookfield viscometer at 30 rpm as a function of the alkyl content (C_8, C_{12}, and C_{16}) for a hydrophobically modified HEC (HMHEC). In this case, the viscosity reached a maximum at

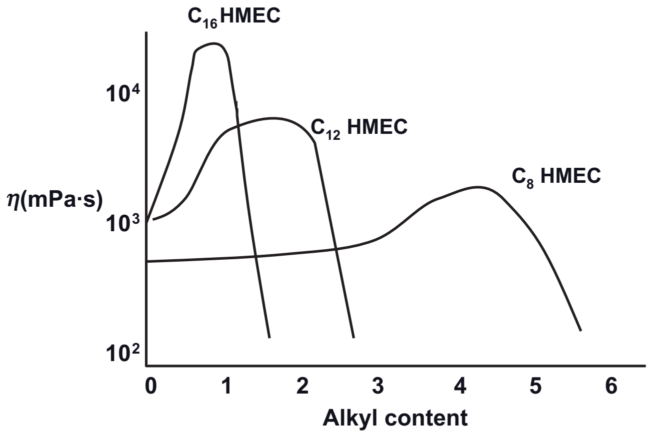

Figure 7.7 Variation of viscosity of 1% hydrophobically modified hydroxyethyl cellulose (HMHEC) versus alkyl group content of the polymer.

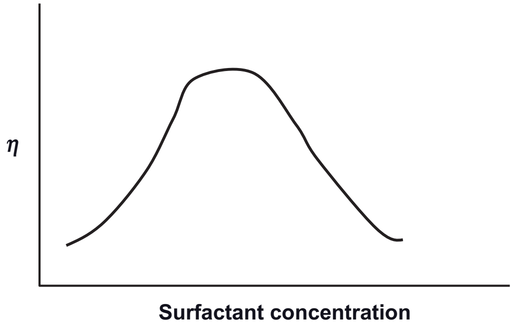

Figure 7.8 Schematic plot of viscosity of hydrophobically modified polymer with surfactant concentration.

a given alkyl group content that decreased with an increase in alkyl chain length. The viscosity maximum also increased with an increase in alkyl chain length.

Associative thickeners also demonstrate an interaction with surfactant micelles that are present in the formulation. The viscosity of the associative thickeners shows a maximum at a given surfactant concentration that depends on the nature of the surfactant; this is shown schematically in Figure 7.8. Here, the increase in viscosity is attributed to the hydrophobic interaction between the alkyl chains on the backbone of the polymer with the surfactant micelles. A schematic image of the interaction between HM polymers and surfactant micelles is shown in Figure 7.9. In this case, at higher surfactant concentration, the "bridges" between the HM polymer molecules and the micelles are broken (free micelles) and η decreases.

The viscosity of hydrophobically modified polymers shows a rapid increase a critical concentration, which may be defined as the critical aggregation concentra-

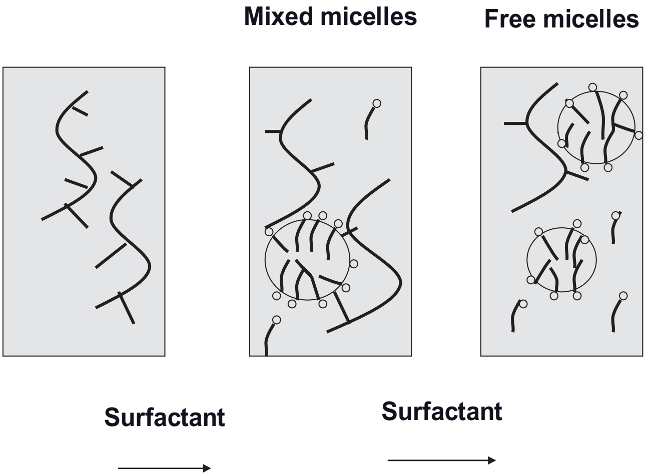

Figure 7.9 Schematic representation of the interaction of polymers with surfactants.

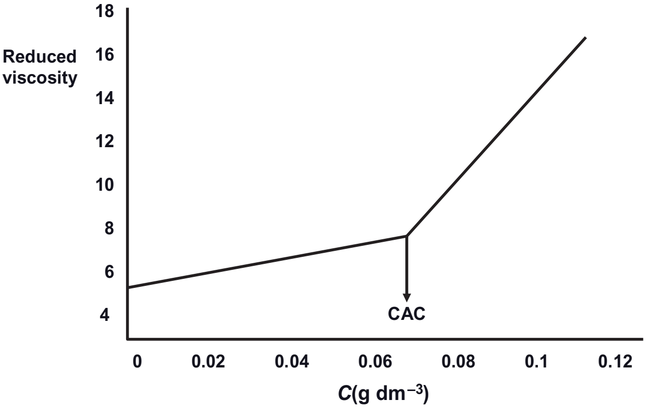

Figure 7.10 Variation of reduced viscosity with hydrophobically modified hydroxyethyl cellulose (HMHEC) concentration.

tion (CAC), as illustrated in Figure 7.10 for HMHEC (WSP-D45 from Hercules). Here, the assumption is made that the CAC is equal to the coil overlap concentration, C^*. From a knowledge of C^* and the intrinsic viscosity $[\eta]$, it is then possible to determine the number of chains in each aggregate. For the above example, $[\eta] = 4.7$ and $C^*[\eta] = 1$, giving an aggregation number of ~4.

At C^*, the polymer solution shows non-Newtonian flow (shear thinning behavior), and also a high viscosity at low shear rates. This is illustrated graphically in Figure 7.11, which shows the variation of apparent viscosity with shear rate (using a constant stress rheometer). Below ~0.1 s^{-1}, a plateau viscosity value $\eta(0)$ (referred to as residual or zero shear viscosity) is reached (~200 Pa·s). With an increase in

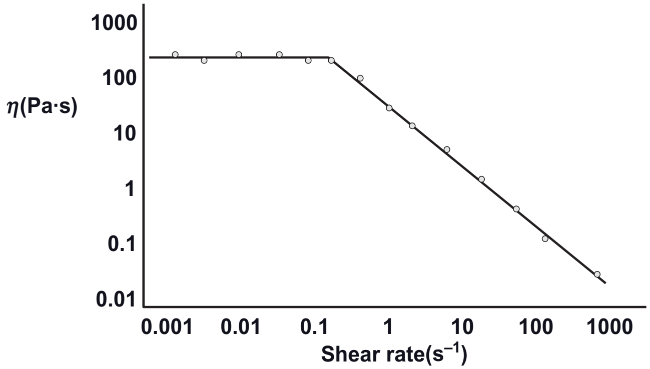

Figure 7.11 Variation of viscosity with shear rate for HMHEC WSP-47 at 0.75 g 100 cm^{-3}.

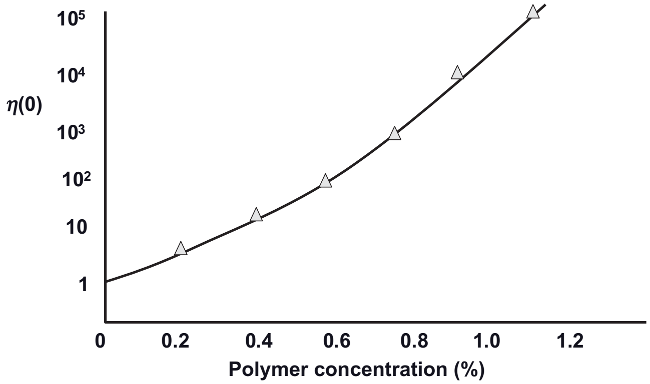

Figure 7.12 Variation of $\eta(0)$ with polymer concentration.

the polymer concentration above C^*, the zero shear viscosity increases in line with the increased polymer concentration; this situation is illustrated in Figure 7.12.

The above hydrophobically modified polymers are viscoelastic; this is illustrated in Figure 7.13 for a solution 5.25% of C_{18} end-capped PEO with M = 35 000, which shows the variation of the storage modulus G' and loss modulus G'' with frequency ω (rad s^{-1}). In this case, G' increases with an increase in frequency and ultimately reaches a plateau value at high frequency. G'' (which is higher than G' in the low-frequency regime) increases with an increase in frequency, reaches a maximum at a characteristic frequency ω^* (at which $G' = G''$), and then decreases to a near-zero value in the high-frequency regime.

The above variation of G' and G'' with ω is typical for a system that shows Maxwell behavior.

From the crossover point ω^* (at which $G' = G''$), it is possible to obtain the relaxation time τ of the polymer in solution:

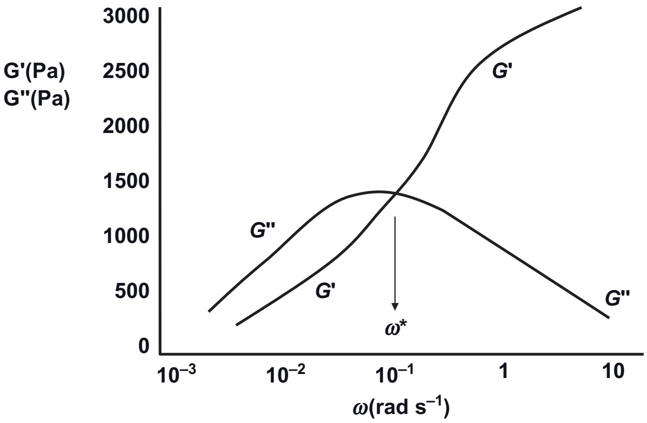

Figure 7.13 Variation of G' and G'' with frequency for 5.24 hydrophobically modified polyethylene oxide (HMPEO).

$$\tau = \frac{1}{\omega^*} \tag{7.11}$$

For the above polymer, $\tau = 8\,\text{s}$.

The above gels (which sometimes are referred to as "rheology modifiers") are used in many formulations to produce the correct consistency, and also to reduce the sedimentation or creaming of suspensions and emulsions. These hydrophobically modified polymers can also interact with hydrophobic particles in a suspension, so as to form several other associative structures.

The high-frequency modulus (sometimes referred to as the "network modulus") can be used to obtain the number of "links" in the gel network structure. By using the theory of rubber elasticity, the network modulus G_N is related to the number of elastically effective links N and a factor A that depends on the junction functionality [1, 2]:

$$G_N = ANkT \tag{7.12}$$

where k is the Boltzmann constant and T is the absolute temperature.

For an end-capped PEO (i.e., HEUR), the junctions should be multifunctional ($A = 1$), whilst for tetra-functional junctions, $A = 1/2$.

7.5.1.3 **Crosslinked Gels (Chemical Gels)**

Many commercially available gels are produced by using crosslinking agents to create what are sometimes referred to as "microgels". The microgel particles are dispersed in the liquid and undergo solvent swelling that may also be enhanced by certain chemical modifications, for example, pH adjustment in aqueous systems.

A typical example of crosslinked gels is that based on polyacrylic acid, which is available commercially under the trade name "Carbopol" (B.F. Goodrich). In this case, the microgel particles are dispersed in aqueous solution and, on neutralization with NaOH or ethanolamine, swell as a result of the ionization of the polyacrylic acid chains. Such ionization occurs when the pH is increased above ~5, such that the ionized chains form extended double layers to create gels at low microgel concentrations (mostly <1% of the microgel particles).

One other example of a microgel is that based on *N*-isopropyl acrylamide (polyNIPAM) crosslinked with *N*,*N*″-methylene bisacrylamide. These microgel particles are swollen by temperature changes. Typically, at temperatures above 35 °C, the crosslinked polymer is in a collapsed state, but when the temperature is reduced the polymer swells as it absorbs water, such that its volume may be increased by several order of magnitude. These polymer gels are often referred to as "smart" colloids, and are widely used in controlled release formulations.

7.5.2
Particulate Gels

Two main interactions can cause gel formation with particulate materials:

- **Long-range repulsions between the particles:** An example is the use of extended electrical double layers or steric repulsion resulting from the presence of adsorbed or grafted surfactant or polymer chains.
- **Van der Waals attractions between particles:** This process, termed flocculation, can lead to the production of 3-D gel networks in the continuous phase.

All of the above-described systems produce non-Newtonian systems that show a "yield value" and high viscosity at low shear stresses or shear rates.

Several examples may be quoted to illustrate the above particulate gels:

- **Swellable clays:** An example of this is sodium montmorillonite (often referred to as bentonite) at low electrolyte concentrations. These produce gels as a result of the formation of extended double layers. At moderate electrolyte concentrations, the clay particles may form association structures as a result of face-to-edge flocculation (see below). These clays can be modified by interaction with alkyl ammonium salts (cationic surfactants) to produce hydrophobically modified clays that may be referred to as "organo-clays" or "bentones"; these can be dispersed in nonaqueous media and swollen by the addition of polar solvents.
- **Finely divided oxides:** An example is silica, which can produce gels by aggregation of the particles so as to form 3-D gel structures. In many cases, the particulate solids are combined with high-molecular-weight polymers to enhance gel formation, for example, as a result of "bridging" or "depletion flocculation."

7.5.2.1 Aqueous Clay Gels

Gel formation using swellable clays such as sodium montmorillonite can be appreciated from the structure of the clay mineral and interparticle interaction in aqueous solutions. These clay minerals are formed from very thin plates (1 nm

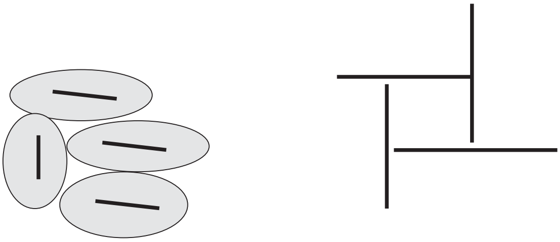

(a) Gels produced by double layer overlap

(b) Gels produced by edge-to-face association

Figure 7.14 Schematic representation of gel formation in aqueous clay dispersions.

thickness) that in turn are formed from two layers of tetrahedral silica and one octahedral alumina sheet (located between the two silica layers). The charge in the clay mineral is produced by a process referred to as "isomorphic substitution," whereby atoms with a high valency are substituted with ions of a lower valency (e.g., S^{4+} is replaced by Al^{3+}). This produces a negative charge on the surface of the platelet that is compensated by Na^+ ions. The edges of the clay platelets contain an oxide-like material (e.g., Al–OH) which can acquire a positive charge at $pH < 7$ (the isoelectric point of Al–OH is pH ~7–9).

Various interactions between clay particles in aqueous solution can be produced, depending on the pH and electrolyte concentration [5]. At very low electrolyte concentrations the double layers are extended and gels produced when the double layers begin to overlap. However, at intermediate electrolyte concentrations the double layers at the faces and edges are compressed, such that interaction may take place by edge-to-face association (thus creating T-junctions, referred to as a "house of card structure"). This also leads to the production of a gel in aqueous solution.

The above two types of interaction are shown schematically in Figure 7.14.

Evidence for the above structures may be obtained using rheological measurements. Figure 7.15 shows the variation of yield value σ_β (for a 3.22% clay dispersion) as a function of electrolyte concentration. When $C = 0$, the double layers are extended and gel formation occurs due to a double layer overlap (Figure 7.14a). The first addition of NaCl causes a compression of the double layers, which in turn causes the yield value to decrease very rapidly. At intermediate NaCl concentrations, gel formation occurs as a result of face-to-edge association (house of card structure), and the yield value increases very rapidly with an increase in NaCl concentration. If the NaCl concentration is increased further, face-to-face association may occur and the yield value will be decreased (i.e., the gel is destroyed).

7.5.2.2 **Organo-Clays (Bentones)**

These are produced by exchanging the Na^+ ions with alkyl ammonium ions, such as dodecyl or cetyltrimethyl ammonium ions. When, in some cases, dialkyl ammonium ions are used, the clay particle surface becomes covered with

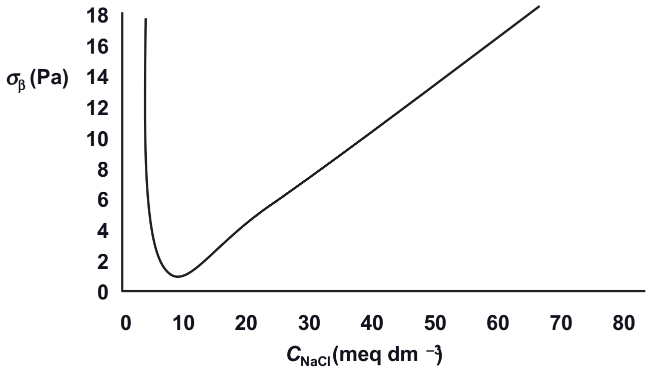

Figure 7.15 Variation of yield value with NaCl concentration for 3.22% sodium montmorillonite dispersions.

hydrophobic alkyl groups so that it can be dispersed in organic solvents, such as hydrocarbon or silicone oils. However, this exchange is not carried out completely, and a few hydrophilic groups are left on the surface. The dispersed organo-clays are then activated by the addition of a polar solvent such as propylene carbonate, alcohols, or glycols.

The gel is produced by hydrogen bonding between the polar groups on the surface of the clay and the polar solvent which has been added. Currently, several types of organo-clay are available commercially, depending on the application and the type of solvent in which a gel is required. In some cases, organo-clays may be supplied in a preactivated form.

Organo-clays may also be applied to "thicken" personal care products, such as foundations, non-aqueous creams, nail polishes and lipsticks. In this case, the procedures used to disperse the organo-clay particles and effect their subsequent activation are crucial and require good process control.

7.5.2.3 **Oxide Gels**

The most commonly used oxide gels are based on silica, and can be produced in a wide variety of forms, the most common being referred to as "fumed" and "precipitated" silicas. Fumed silicas (e.g., Aerosil 200) are produced by the reaction of silicon tetrachloride with steam. The surface contains siloxane bonds and isolated silanol groups (referred to as "vicinal" groups), and the precipitated silicas are produced from sodium silicate by acidification. The surface of a precipitated silica is more densely populated with silanol groups than that of a fumed silica, and contains geminal OH groups (two of which are attached to the same Si atom). Both, fumed and precipitated silicas can produce gels in either aqueous or non-aqueous systems. Gelation results from the aggregation of silica particles, producing 3-D gel networks with a yield value.

In aqueous media, the gel strength depends on the pH and the electrolyte concentration [6]. To illustrate this, Figure 7.16 shows the variation of viscosity and

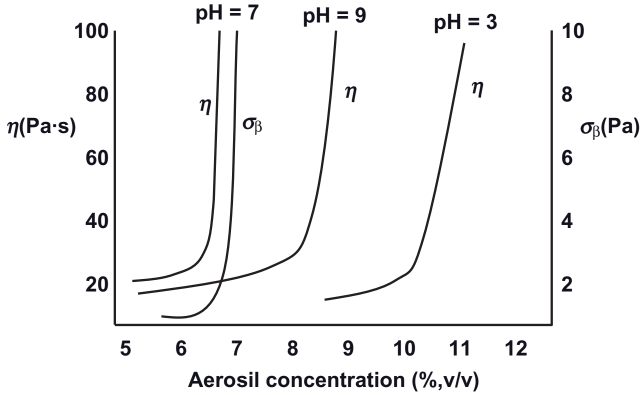

Figure 7.16 Variation of viscosity η and yield value σ_β with Aerosil 200 concentration at three pH values.

yield value with Aerosil silica (which has been dispersed by sonication) concentrations at three different pH values. In each case, the viscosity and yield value shows a rapid increase above a certain silica concentration, that is dependent on the pH of the system.

At pH 3 (close to the isoelectric point of silica) the particles are aggregated (to form flocs), and the increase in viscosity occurs at a relatively high silica concentration (>11%, v/v). At pH 7, the silica becomes negatively charged and the double layers stabilize the silica particles against aggregation. In this case, the particles remain as small units and the viscosity and yield value increases sharply above a silica concentration of 7% (v/v). At pH 9, some aggregation occurs as a result of the electrolyte being released when the pH is adjusted; in this case, the viscosity increases at a higher silica concentration (>9%, v/v) when compared to the results obtained at pH 7.

The above results clearly indicate the importance of pH and electrolyte concentration in the gelation of silica, with optimum gel formation seeming to occur at neutral pH.

Currently, silica gels are used in many personal care applications, in particular to control the rheology of tooth paste. The hydrophilic silica (Aerosil 200) can also be applied to gel formation in nonaqueous media; in this case, gel formation results from hydrogen bond formation between the particles, producing 3-D structures in the nonaqueous medium.

7.5.2.4 **Gels Produced Using Particulate Solids and High-Molecular-Weight Polymers**

In many cases, particulate materials are combined with high-molecular-weight polymers to produce 3-D structures by association of the polymer with the particles. Several mechanisms have been suggested for gel formation in these mixtures, including bridging by the polymer chains and depletion-flocculation.

The above mixtures provide more robust gel structures that, in many cases, have a smaller temperature dependence when compared to the individual components. The optimum composition of these particulate–polymer mixtures can be determined using rheological measurements.

By measuring the yield value as a function of polymer concentration at a fixed particulate concentration, it is possible to obtain the optimum polymer concentration required. In most cases, the yield value reaches a maximum at a given ratio of particulate solid to polymer. This trend may be due to bridging flocculation, which reaches an optimum at a given surface coverage of the particles (usually at 0.25–0.5 surface coverage).

All of the above-mentioned gels produce thixotropy – that is, the reversible decrease of viscosity on the application of shear (at constant shear rate), and a recovery of viscosity on standing. Such thixotropic behavior finds application in many systems in personal care, such as creams, toothpastes and foundations.

One of the most effective techniques for studying thixotropy is to follow the change of modulus with time, following the application of shear. For this, after subjecting the dispersion to a constant shear rate, oscillatory measurements are carried out at low strains and high frequency, after which the increase in modulus with time (which is exponential) can be used to characterize the recovery of the gel.

7.6
Rheology Modifiers Based on Surfactant Systems

In dilute solutions, surfactants tend to form spherical micelles with aggregation numbers in the range of 50 to 100 units. Whilst these micellar solutions are isotropic and have a low viscosity, at much higher surfactant concentrations (>30%, depending on the surfactant nature) they produce liquid crystalline phases of the hexagonal (H_1) and lamellar (L_α) phases, both of which are anisotropic with much higher viscosities [7, 8]. Schematic representations of the hexagonal and lamellar phases are shown in Figures 7.17 and 7.18, respectively.

Whilst those liquid crystalline phases which are viscoelastic can be used as rheology modifiers, for practical applications (e.g., in shampoos) such a very high surfactant concentration would be undesirable. One way to increase the viscosity of a surfactant solution at lower concentrations would be to add an electrolyte that would cause the micelles to change from a spherical to a cylindrical shape. The micelles could then grow in length to become worm-like in nature and, above a critical surfactant volume fraction ϕ^*, would begin to overlap to form a "gel" (as shown in Figure 7.19).

An alternative method for producing gels in emulsions is to use mixtures of surfactants. Indeed, with the correct choice of surfactant type (e.g., their hydrophilic–lipophilic balance, HLB), it is possible to produce lamellar liquid crystalline structures that can "wrap" around the oil droplets and extend in solution so as to form gel networks. These structures – which sometimes are

Figure 7.17 Schematic representation of hexagonal phase.

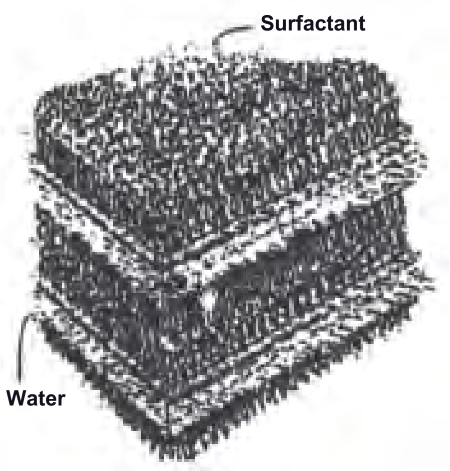

Figure 7.18 Schematic representation of lamellar phase.

referred to as “oleosomes” – are shown schematically in Figure 7.20. Alternatively, the liquid crystalline structures may produce a 3-D gel network such that the oil droplets become entrapped in the “holes” of the network. Such structures, which may be referred to as “hydrosomes,” are illustrated schematically in Figure 7.21.

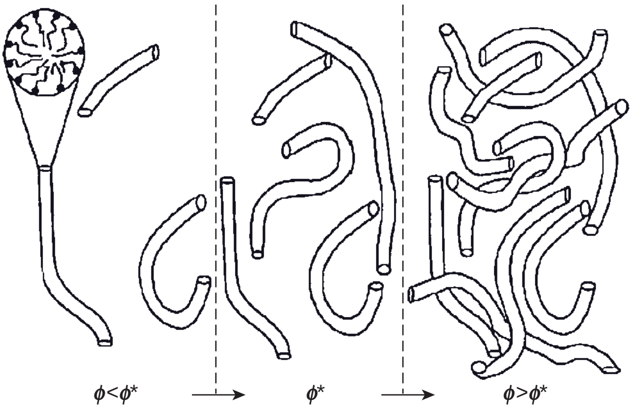

Figure 7.19 Overlap of thread-like micelles.

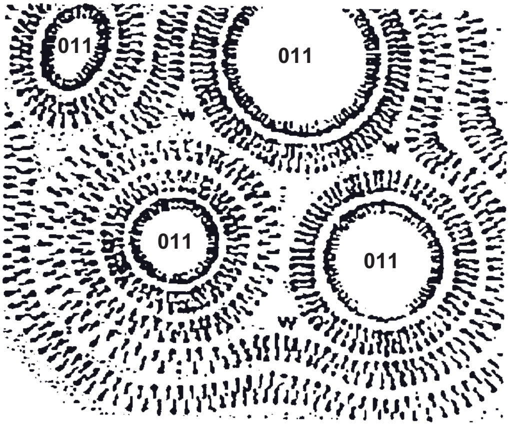

Figure 7.20 Schematic representation of "oleosomes."

The above-described surfactant systems are used in many personal care and cosmetic formulations. In addition to providing the optimum consistency for application (e.g., good skin-feel), they are also effective in stabilizing emulsions against creaming or sedimentation, flocculation, and coalescence.

Liquid crystalline structures may also influence the delivery of active ingredients of both lipophilic and hydrophilic types. Moreover, as lamellar liquid crystals are able to mimic the skin structure (notably the stratum corneum), they can offer a prolonged potential for hydration.

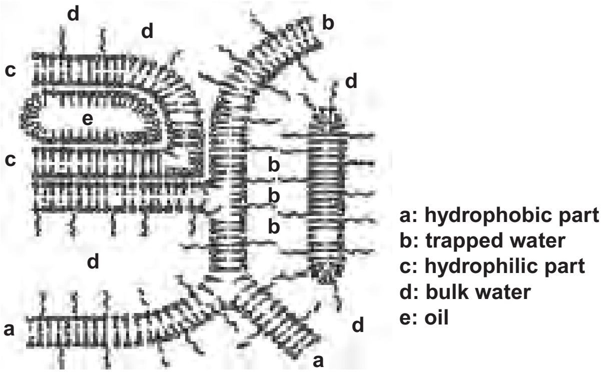

Figure 7.21 Schematic representation of "hydrosomes."

References

1 Ferry, J.D. (1980) *Viscoelastic Properties of Polymers*, John Wiley & Sons, Inc., New York.

2 Goodwin, J.W. and Hughes, R.W. (2000) *Rheology for Chemists*, Royal Society of Chemistry Publication, Cambridge.

3 de Gennes, P.G. (1979) *Scaling Concepts in Polymer Physics*, Cornell University Press, Ithaca, London.

4 Goddard, E.D. (1999) *Polymer/Surfactant Interaction*, Chapters 4 and 5 (eds E.D. Goddard and J.V. Gruber), Marcel Dekker, New York, pp. 113–215.

5 Van Olphen, H. (1961) *Clay Colloid Chemistry*, John Wiley & Sons, Inc., New York.

6 Heath, D. and Tadros, T.F. (1983) *J. Colloid Interface Sci.*, **93**, 307, 320.

7 Holmberg, K., Jonsson, B., Kronberg, B., and Lindman, B. (2003) *Surfactants and Polymers in Solution*, John Wiley & Sons, Ltd, Chichester.

8 Tadros, T.F. (2005) *Applied Surfactants*, Wiley-VCH Verlag GmbH, Germany.

8
Use of Rheological Measurements for Assessment and Prediction of the Long-Term Physical Stability of Formulations (Creaming and Sedimentation)

8.1
Introduction

Most formulations undergo creaming or sedimentation as a result of the density difference between the disperse phase particles and the medium [1]. This situation is particularly the case with most practical systems that contain particles with radii R that are large (>1 μm), whereby the Brownian diffusion is not sufficient to overcome the gravity force; that is:

$$kT << (4/3)\pi R^3 \Delta\rho g L$$

where k is the Boltzmann constant, T is the absolute temperature, R is the particle radius, $\Delta\rho$ is the density difference between the disperse phase and the medium, g is the acceleration due to gravity, and L is the height of the container.

It is perhaps useful to consider the process of sedimentation and how this is affected by the volume fraction of the suspension.

8.2
Sedimentation of Suspensions

As discussed above, most suspensions undergo separation on standing as a result of the density difference between the particles and the medium, unless the particles are small enough for Brownian motion to overcome gravity. This is illustrated in Figure 8.1 for three cases of suspensions. The first case is that of *submicron particles*, where the Brownian diffusion is higher than the gravity force and hence no sedimentation occurs. The second case is that of coarse particles ($R > 1\,\mu$m) with a uniform size.

The most practical situation is that represented by (C), whereby a concentration gradient of the particles occurs across the container. The concentration of particles C can be related to that before any settling C_o by the following equation,

$$C = C_o \exp\left(-\frac{mgh}{kT}\right) \tag{8.1}$$

Rheology of Dispersions: Principles and Applications. Tharwat F. Tadros

ISBN: 978-3-527-32003-5

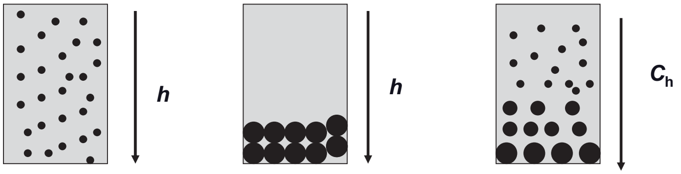

(a) $kT > (4/3)\pi R^3 \Delta\rho g h$

(b) $kT < (4/3)\pi R^3 \Delta\rho g h$

$C_h = C_o \exp(-mgh/kT)$
C_o = conc. at $t = 0$
C_h = conc. at time t and height h
$m = (4/3)\pi R^3 \Delta\rho$

Figure 8.1 Schematic representation of the sedimentation of suspensions.

where m is the mass of the particles that is given by $(4/3)\pi R^3 \Delta\rho$ (where R is the particle radius and $\Delta\rho$ is the density difference between the particle and medium), g is the acceleration due to gravity, and h is the height of the container.

For a very dilute suspension of rigid noninteracting particles, the rate of sedimentation v_o can be calculated by application of Stokes' law, whereby the hydrodynamic force is balanced by the gravitational force:

$$\text{Hydrodynamic force} = 6\pi\eta R v_o \tag{8.2}$$

$$\text{Gravity force} = (4/3)\pi R^3 \Delta\rho g \tag{8.3}$$

$$v_o = \frac{2}{9}\frac{R^2 \Delta\rho g}{\eta} \tag{8.4}$$

where η is the viscosity of the medium (water).

In this case, v_o was calculated for three particle sizes (0.1, 1, and 10 μm) for a suspension with density difference $\Delta\rho = 0.2$. The values of v_o were 4.4×10^{-9}, 4.4×10^{-7}, and $4.4 \times 10^{-5}\,\text{ms}^{-1}$, respectively, and the times required for complete sedimentation in a 0.1 m container were 250 days, 60 h, 40 min, respectively.

For moderately concentrated suspensions, $0.2 > \phi > 0.01$, the sedimentation is reduced as a result of hydrodynamic interaction between the particles, which no longer sediment independently of each other [2]. The sedimentation velocity, v, can be related to the Stokes' velocity v_o by the following equation:

$$v = v_o(1 - 6.55\phi) \tag{8.5}$$

This means that for a suspension with $\phi = 0.1$, $v = 0.345 v_o$; that is, the rate is reduced by a factor of ~3.

For more concentrated suspensions ($\phi > 0.2$), the sedimentation velocity becomes a complex function of ϕ. At $\phi > 0.4$, the hindered settling regime is usually entered, whereby all the particles sediment at the same rate, independent of their size.

A schematic representation for the variation of v with ϕ is shown in Figure 8.2, which also shows the variation of relative viscosity with ϕ. It can be seen that v

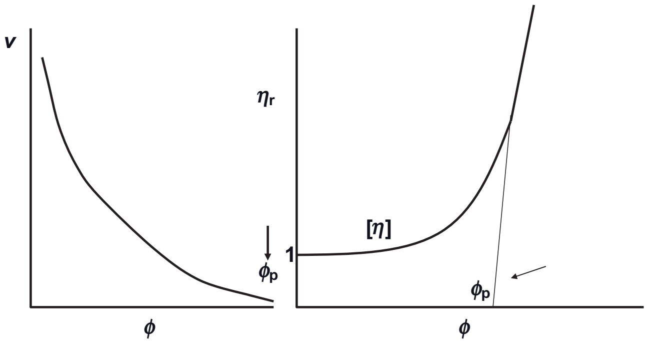

Figure 8.2 Variation of ν and η_r with ϕ.

decreases exponentially with increase in ϕ, and ultimately approaches zero when ϕ approaches a critical value ϕ_p (the maximum packing fraction).

The relative viscosity shows a gradual increase with increase in ϕ, and when $\phi = \phi_p$, the relative viscosity approaches infinity.

The maximum packing fraction ϕ_p can be easily calculated for monodisperse rigid spheres. For hexagonal packing $\phi_p = 0.74$, whereas for random packing $\phi_p = 0.64$. The maximum packing fraction increases with polydisperse suspensions. For example, for a bimodal particle size distribution (with a ratio of ~10 : 1), $\phi_p > 0.8$.

8.2.1
Accelerated Tests and Their Limitations

Several tests have been designed to accelerate the process of sedimentation or creaming, the most commonly used methods being based on increasing the temperature or subjecting the suspension or emulsion to high *g*-forces (using a high-speed centrifuge).

With increasing temperature, the viscosity of the system usually decreases, and hence sedimentation or creaming is accelerated. The assumption is usually made that, if a suspension or emulsion does not show any sedimentation, creaming or separation at 50 °C for perhaps one month, then the system will show no separation at ambient temperatures for more than one year.

However, the above method is only valid if the formulation viscosity η follows the Arrhenius equation, which predicts a linear increase in ln η with $(1/T)$, where T is the absolute temperature. Most practical formulations do not follow such a plot, due to the possible phase changes or flocculation that may occur at high temperatures. With many surfactant systems, such phase changes may result in the formation of liquid crystalline phases that have a higher viscosity at high temperatures; hence no separation will result at high temperatures (although it could occur under ambient conditions).

8.2.2
Application of a High-Gravity (*g*) Force

If carefully applied, this technique may offer a better accelerated method, and has been applied particularly to emulsions. The assumption is also made here that, by increasing the *g*-force, the rate of sedimentation or creaming would be significantly increased, and that this could be applied to predict the process from measurement over short time periods.

In a centrifuge, the gravitational force is given by:

$$g = \omega^2 x \tag{8.6}$$

where x is the mean distance of the centrifuge tube from the axis of rotation, and ω is the angular velocity ($\omega = 2\pi\nu$, where ν is the number of revolutions per second). It should be noted that, if the centrifuge tube is not small compared to x, then the applied centrifugal field cannot be considered to be uniform over the length of the tube.

The modern analytical ultracentrifuge allows the separation of emulsions to be followed in quantitative manner. With typical oil-in-water (O/W) emulsions, three layers are generally observed: (i) a clear aqueous phase; (ii) an opaque phase consisting of distorted polyhedral oil droplets; and (iii) a clear separated oil phase, resulting from a coalescence of the polyhedra.

The degree of emulsion stability may be taken as the volume of the opaque phase remaining after time t. Alternatively, the volume of oil separated at infinite time may be used as an index of stability. A simple expression may be used to treat the data in a quantitative manner:

$$\frac{t}{V} = \frac{1}{bV_\infty} + \frac{1}{V_\infty} \tag{8.7}$$

where V is the volume of oil separated at time t, V_∞ is the extrapolated volume at infinite time, and b is a constant.

A plot of t/V versus t should give a straight line from which b and V_∞ may be calculated; these two parameters may be taken as indices for emulsion stability.

A more rigorous procedure to study emulsion stability using the ultracentrifuge is to observe the system at various speeds of rotation. At relatively low centrifuge speeds, the expected opaque cream layer can be observed, but at sufficiently high centrifuge speeds it is possible to observe a coalesced oil layer and a cream layer that are separated by an extra layer of deformed oil droplets. This deformed layer resembles a “foam,” in that it consists of oil droplets separated by thin aqueous films.

For certain emulsions it has been found that, by increasing the centrifuge speed, the “foam”/cream layer boundary does not move. Hence, under conditions where there is an equilibrium between the “foam”/cream layer, it may be concluded that there is no barrier to be overcome when forming the foam layer from the cream layer. This, in turn, implies that in the foam layer the aqueous film separating two oil droplets becomes thinned to a “black” film under the action of the van der

Waals forces. The boundary between the foam layer and the coalesced layer is associated with a force (or pressure) barrier.

It is also possible to determine the minimum centrifuge speed necessary to produce a visible amount of coalesced oil after, say 30 min, of centrifugation. This centrifuge speed may then be used to calculate the "critical pressure" that needs to be applied so as to induce coalescence.

8.2.3
Rheological Techniques for the Prediction of Sedimentation or Creaming

Sedimentation or creaming can be prevented by the addition of "thickeners" that form a "3-D elastic" network in the continuous phase. If the viscosity of the elastic network – at shear stresses (or shear rates) comparable to those exerted by the particles or droplets – exceeds a certain value, then creaming or sedimentation is completely eliminated.

The shear stress, σ_p, exerted by a particle (force/area) can be simply calculated as:

$$\sigma_p = \frac{(4/3)\pi R^3 \Delta\rho g}{4\pi R^2} = \frac{\Delta\rho R g}{3} \tag{8.8}$$

For a 10 μm radius particle with a density difference Δρ of 0.2 g cm^{-3},the stress is equal to:

$$\sigma_p = \frac{0.2\times 10^3 \times 10\times 10^{-6} \times 9.8}{3} \approx 6\times 10^{-3}\ \text{Pa} \tag{8.9}$$

For smaller particles, smaller stresses are exerted.

Thus, in order to predict creaming or sedimentation, it is necessary to measure the viscosity at very low stresses (or shear rates). Such measurements can be carried out using a constant-stress rheometer (e.g., Carrimed, Bohlin, Rheometrics, Haake, or Physica).

Normally, a good correlation is obtained between the rate of creaming or sedimentation v and the residual viscosity $\eta(0)$; this is illustrated in Figure 8.3. Above a certain value of $\eta(0)$, v becomes equal to 0. Clearly, to minimize creaming or

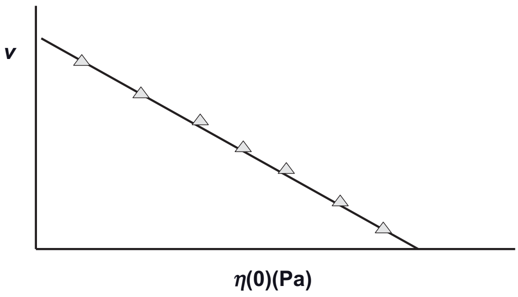

Figure 8.3 Sedimentation rate versus $\eta(0)$.

sedimentation it is necessary to increase $\eta(0)$; an acceptable level for the high shear viscosity η_∞ must be achieved, depending on the application. In some cases, a high $\eta(0)$ may be accompanied by a high η_∞ (which may not be acceptable for application, for example if spreading of a dispersion on the skin is required). If this is the case, the formulation chemist should seek an alternative thickener.

8.2.4
Separation of Formulation: Syneresis

Another problem encountered with many dispersions is that of *syneresis*; that is, the appearance of a clear liquid film at the bottom (if creaming is the case) or the top (if sedimentation is the case) of the container. Syneresis occurs with most "flocculated" and/or "structured" dispersions (i.e., those containing a thickener in the continuous phase).

Syneresis may be predicted from measurement of the yield value (using steady-state measurements of shear stress as a function of shear rate) as a function of time, or by using oscillatory techniques, whereby the storage and loss modulus are measured as a function of strain amplitude and frequency of oscillation.

The oscillatory measurements are perhaps more useful since, in order to prevent separation, the bulk modulus of the system should balance the gravitational forces given by $h\rho\Delta g$ (where h is the height of the disperse phase, $\Delta\rho$ is the density difference, and g is acceleration due to gravity).

The bulk modulus is related to the storage modulus G'. A more useful predictive test is to calculate the cohesive energy density of the structure E_c that is given by the following equation (see also Chapter 4):

$$E_c = \int_0^{\gamma_{cr}} G'\gamma d\gamma = \frac{1}{2}G'\gamma_{cr}^2 \tag{8.10}$$

The separation of a formulation decreases with increase in E_c. This is illustrated in Figure 8.4, which shows graphically the reduction in percentage separation with an increase in E_c. The value of E_c required to complete block any separation depends on the particle or droplet size distribution, the density difference between

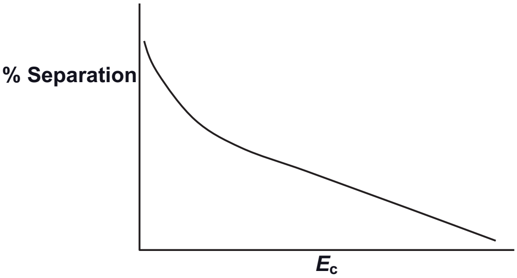

Figure 8.4 Schematic representation of the variation of percentage separation with E_c.

the particle or droplet and the medium, and also on the volume fraction ϕ of the dispersion.

8.2.5
Examples of Correlation of Sedimentation or Creaming with Residual (Zero-Shear) Viscosity

8.2.5.1 Model Suspensions of Aqueous Polystyrene Latex

The sedimentation rate is a complex function of the volume fraction ϕ. This was tested using polystyrene latex suspensions with radius $R = 1.55\,\mu\text{m}$ in $10^{-3}\,\text{mol}\,\text{dm}^{-3}$ NaCl. It might be possible to correlate the change in the rate of sedimentation with increasing φ with the viscosity of the suspension, as predicted by the Dougherty–Krieger equation [3]:

$$\frac{v}{v_o} \propto \frac{\eta_o}{\eta} \tag{8.11}$$

$$\frac{v}{v_o} = \alpha \frac{\eta_o}{\eta} \tag{8.12}$$

where α is a constant.

$$\frac{v}{v_o} = \left[1 - \left(\frac{\phi}{\phi_p}\right)\right]^{-[\eta]\phi_p} \tag{8.13}$$

where ϕ_p is the maximum packing fraction and $[\eta]$ is the intrinsic viscosity.

Equation 8.13 was tested for polystyrene dispersions, as illustrated in Figure 8.5

8.2.5.2 Sedimentation in Non-Newtonian Liquids

In order to reduce sedimentation, the normal approach is to add a high-molecular-weight material, for such as hydroxyethylcellulose or xanthan gum (e.g., Kelzan, Keltrol or Rhodopol). However, above a critical concentration, C^*, such polymer

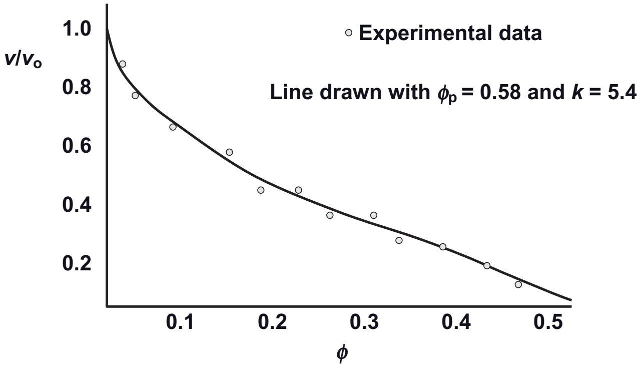

Figure 8.5 Variation of sedimentation rate with volume fraction for polystyrene dispersions.

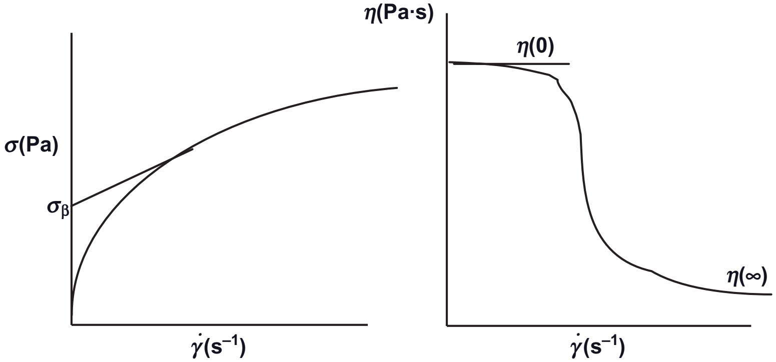

Figure 8.6 Flow behavior of “thickeners.”

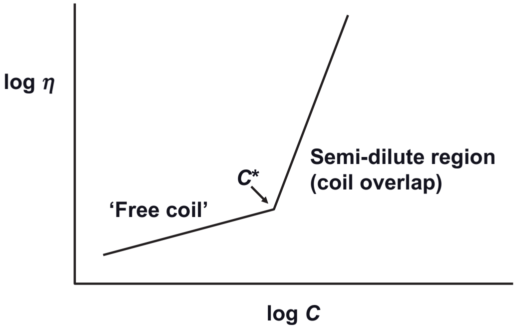

Figure 8.7 Variation of log η with log C.

solutions demonstrate non-Newtonian flow in aqueous solution. This is illustrated in Figure 8.6, which illustrates graphically the variation of shear stress and viscosity with shear rate. Figure 8.7 demonstrates the variation of log η with log C to illustrate the onset of free coil overlap.

Before the overlap, $\eta \propto C$, whereas after the overlap $\eta \propto C^{3.4}$. Two limiting Newtonian viscosities are identified here: (i) residual (zero-shear) viscosity $\eta(0)$; and (ii) Newtonian high-shear rate viscosity η_∞. Notably, $\eta(0)$ may be several orders of magnitude (10^3–10^5) higher than η_∞, and such a high $\eta(0)$ can significantly reduce either creaming or sedimentation.

8.2.5.3 Role of Thickeners

As mentioned above, thickeners reduce creaming or sedimentation by increasing the residual viscosity $\eta(0)$, which must be measured at stresses comparable to those exerted by the droplets or particles (mostly <0.1 Pa). At such low stresses, $\eta(0)$ is increased very rapidly in line with any increase in the “thickener” concentration. However, this rapid increase is not observed at high stresses, which illustrates the need for measurements to be made at low stresses (using constant stress

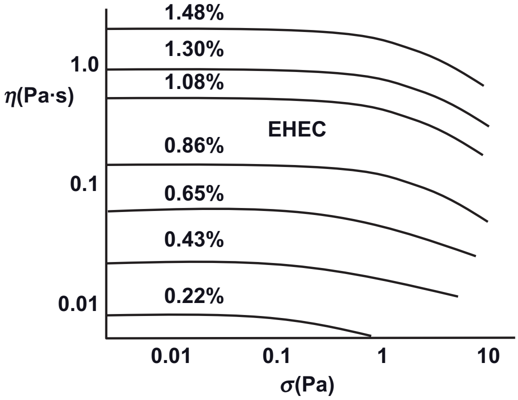

Figure 8.8 Constant-stress (creep) measurements for polystyrene latex dispersions as a function of ethylhydroxyethylcellulose (EHEC) concentration.

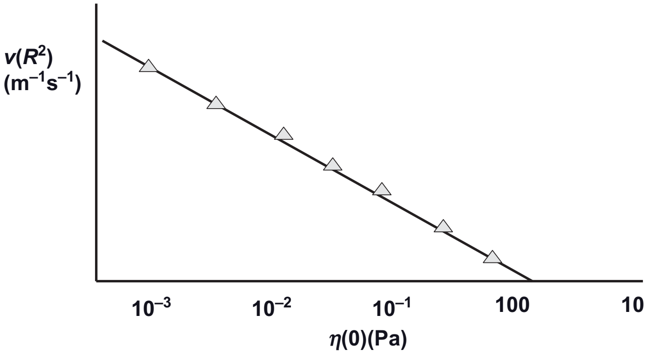

Figure 8.9 Sedimentation rate versus $\eta(0)$.

or creep measurements). As an illustration, Figure 8.8 shows the variation of η with applied stress σ for ethylhydroxyethylcellulose (EHEC), a thickener that is applied in some formulations.

From Figure 8.8, it can be seen that the limiting residual viscosity increases rapidly with any increase in EHEC concentration. A plot of sedimentation rate for 1.55 μm polystyrene (PS) latex particles versus $\eta(0)$ is shown in Figure 8.9, which demonstrates an excellent correlation. In this case, a value of $\eta(0) \geq 10\,\text{Pa·s}$ is sufficient for reducing the rate of sedimentation to 0.

8.2.6
Prediction of Emulsion Creaming

For the above purpose, some model emulsions were prepared using mixtures of oils and commercial surfactants. The oil phase of the emulsion consisted of 10 parts Arlamol HD (isohexadecane; UNIQEMA, ICI), two parts of Estol 3603 (caprylic/capric triglyceride; UNIQEMA), one part of sunflower oil (Florasen 90, *Helanthus annus*; Florateck), and one part of avocado oil (*Persea gratissima*; Mosselman).

Two emulsifier systems were used to prepare the O/W emulsions:

- The first emulsifier was Synperonic PEF 127, an A–B–A block copolymer of poly(ethylene oxide) (PEO; the A chains, which contain about 100 EO units each) and poly(propylene oxide) (PPO; the B chain, which contains about 55 PO units) (all supplied by UNIQEMA).
- The second emulsifier system was Arlatone V-100 (supplied by UNIQEMA), a nonionic emulsifier systems made from a blend of Steareth-100 (stearyl alcohol with 100 EO units), Steareth-2 (stearyl alcohol with 2 EO units), glyceryl stearate citrate, sucrose, and a mixture of two polysaccharides, namely mannan and xanthan gum (Keltrol F; Kelco). In some emulsions, xanthan gum was used as a thickener.

All emulsions contained a preservative (Nipaguard BPX).

The rate of creaming and cream volume was measured using graduated cylinders. The creaming rate was assessed by comparing the cream volume V_c with that of the maximum value V_∞ obtained when the emulsion was stored at 55 °C. The time $t_{0.3}$ taken to reach a value of $V_c/V_\infty = 0.3$ (i.e., 30% of the maximum rate) was calculated [4].

All rheological measurements were carried out using a Physica UDS 200 (Universal Dynamic Spectrometer). A cone and plate geometry was used with a cone angle of 2°. The emulsions were also investigated using optical microscopy and image analysis.

Figure 8.10 shows the results for creaming rates obtained at various temperatures, using a 20/80 (v/v,%) O/W emulsion stabilized with Synperonic PEF 127. Clearly, $t_{0.3}$ was shown to decrease in line with an increase of temperature.

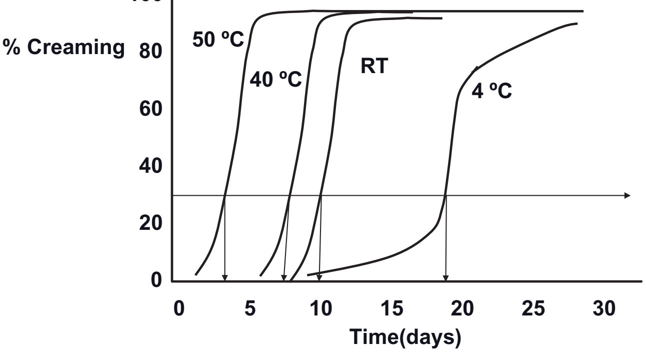

Figure 8.10 Percentage creaming versus time at various temperatures.

8.2.6.1 Creep Measurements for Prediction of Creaming

The most useful method to predict creaming is to use constant-stress (creep) measurements [5, 6], from which it is possible to obtain the residual (zero-shear) viscosity $\eta(0)$.

Results were obtained for 20/80 (v/v,%) emulsions as a function of Arlatone V-100 concentration. The results, obtained after several periods of storage (one day, one week, two weeks, and one month), are shown in Figure 8.11. In this case, $\eta(0)$ showed a large decrease after one day, which may have been due to equilibration of the structure. However, the results obtained after one week, two weeks and one month were much close to each other, there being a significant increase in $\eta(0)$ when the Arlatone V 100 concentration was increased above 0.8%. The creaming rate of the emulsion also showed a sharp decrease above 0.8% Arlatone V 100, indicating a correlation between $\eta(0)$ and the creaming rate.

8.2.6.2 Oscillatory Measurements for Prediction of Creaming

One very useful method for predicting creaming is to measure the cohesive energy density, as given by Equation 8.10. As an illustration, Figure 8.12 shows the variation of cohesive energy density E_c with Arlatone V 100 concentration. The results

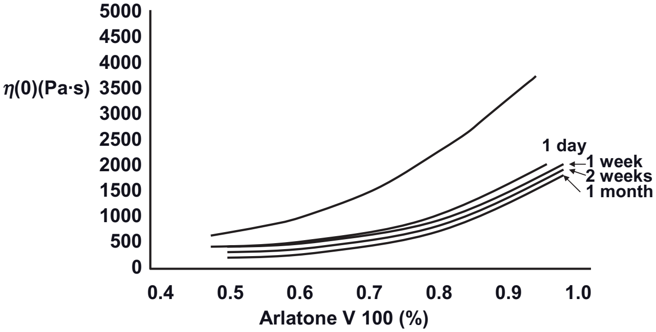

Figure 8.11 Variation of residual viscosity with Arlatone V 100 concentration at various storage times.

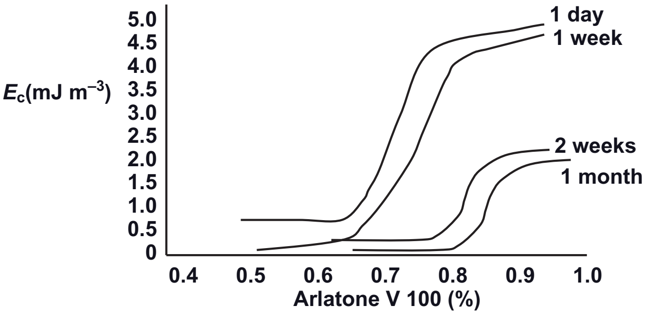

Figure 8.12 Variation of E_c with percentage Arlatone V 100 in the emulsion.

showed, clearly, a rapid increase in E_c above 0.8% Arlatone V 100, but E_c appeared to show decreased values after a two-week storage. This may have been due to a small increase in droplet size (as a result of some coalescence), which in turn resulted in a reduction of the cohesive energy density. Yet, this small increase in droplet size was not detected microscopically as the change was very small.

8.3
Assessment and Prediction of Flocculation Using Rheological Techniques

8.3.1
Introduction

Steady-state rheological investigations may be used to investigate the state of flocculation of a dispersion. Weakly flocculated dispersions usually demonstrate thixotropy, the change in which with applied time may be used as an indication of the strength of this weak flocculation.

Unfortunately, the above-described methods are only qualitative in nature, and the results obtained cannot be used on a quantitative basis. This is due to the possible breakdown of the structure when transferring the formulation to the rheometer, and also during the uncontrolled shear experiment. Superior techniques for studying the flocculation of a formulation include constant-stress (creep) or oscillatory measurements. Indeed, by carefully transferring the sample to the rheometer (with minimum shear), the structure of the flocculated system may be maintained.

8.3.2
Wall Slip

One very important point that must be considered for any rheological measurement is the possibility of “slip” during the measurements. This is especially the case with highly concentrated dispersions, where the flocculated system may form a “plug” in the gap of the platens, leaving a thin liquid film at the walls of the concentric cylinder or cone-and-plate geometry. This behavior is caused by a degree of syneresis of the formulation in the gap of the concentric cylinder or cone and plate. In order to reduce slip, it is necessary to use roughened walls for the platens, or a vane rheometer may be used.

8.3.3
Steady-State Shear Stress–Shear Rate Measurements

Currently, this is by far the most common method used to investigate flocculation in many industrial laboratories. Basically, the dispersion is stored at various temperatures, and the yield value σ_β and plastic viscosity η_{pl} are measured at various time intervals. Any flocculation in the formulation should be accompanied by an increase in σ_β and η_{pl}.

One rapid technique used to study the effect of temperature changes on the flocculation of a formulation involves carrying out temperature sweep experiments, running the samples from say 5° to 50 °C. The trend in the variation of σ_β and η_{pl} with temperature can quickly provide an indication of the temperature range at which a dispersion will remain stable (during that temperature range, both σ_β and η_{pl} will remain constant).

8.3.4
Influence of Ostwald Ripening and Coalescence

If Ostwald ripening and/or coalescence occur simultaneously, σ_β and η_{pl} may be changed, in complex manner, with the storage time. Ostwald ripening and/or coalescence may result in a shift of the particle size distribution to higher diameters, and this has the effect of reducing both σ_β and η_{pl}. If flocculation were to occur simultaneously, causing increases in both of these rheological parameters, then the net effect may be either an increase or decrease of the rheological parameters.

However, as the above trend depends on the extent of flocculation relative to the Ostwald ripening and/or coalescence, the ability to follow σ_β and η_{pl} with storage time will require a previous knowledge of Ostwald ripening and/or coalescence. Hence, only in the absence of these latter breakdown processes can rheological measurements be used to assess flocculation.

8.3.5
Constant-Stress (Creep) Experiments

Basically, a constant stress σ is applied to the system, and the compliance J (Pa^{-1}) is plotted as a function of time (see Chapter 4). These experiments are repeated several times, during which the stress is increased in small increments from the smallest possible value that can be applied by the instrument, so as to produce a set of creep curves at the various applied stresses. From the slope of the linear portion of the creep curve (when the system has reached steady state), the viscosity at each applied stress, η_σ, is calculated. Subsequently, a plot of η_σ versus σ allows measurement of the limiting (or zero-shear) viscosity $\eta(0)$ and the critical stress σ_{cr} (which may be identified with the "true" yield stress of the system; see Chapter 4). The values of $\eta(0)$ and σ_{cr} may be used to assess the flocculation of the dispersion on storage.

If flocculation occurs on storage (without any Ostwald ripening or coalescence), then the values of $\eta(0)$ and σ_{cr} may show a gradual increase with increase of storage time. As discussed in Section 8.3.3, the trend becomes complicated if Ostwald ripening and/or coalescence occur simultaneously, as both have the effect of reducing $\eta(0)$ and σ_{cr}.

The above-described measurements should be supplemented by particle size distribution measurements of the diluted dispersion (making sure that no flocs are present after dilution) in order to assess the extent of Ostwald ripening and/or coalescence. Another complication may arise from the nature of the flocculation since, if the latter occurs in an irregular manner (producing strong and tight flocs), then $\eta(0)$ may increase while σ_{cr} may show some decrease, thus complicating the analysis of the results. Despite these complications, constant-stress measurements may provide valuable information on the state of the dispersion on storage.

Unfortunately, performing creep experiments and ensuring that a steady state is reached can be very time-consuming. Normally, a stress sweep experiment will be carried out whereby the stress is gradually increased (within a predetermined time period so as to ensure that the steady state will soon be reached) and plots of η_{σ} versus σ can be established.

The above experiments are carried out at a variety of storage times (perhaps every two weeks) and temperatures. Subsequently, from the change of $\eta(0)$ and σ_{cr} with storage time and temperature, information may be obtained regarding the degree and rate of flocculation of the system. Clearly, an interpretation of the rheological data obtained requires an expert knowledge of rheology, in addition to measurements of the particle size distribution as a function of time.

One major problem when performing these types experiment is that of *sample preparation*. Typically, when a flocculated dispersion is removed from the container, care must be taken not to cause any disturbance to that structure (a minimum shear should be applied when transferring the formulation to the rheometer). It is also advisable to use separate containers when assessing the flocculation; normally, a relatively large sample would be prepared and then transferred to several separate containers. Each of these samples would then be used separately at a given storage time and temperature. Care must be taken when transferring the sample to the rheometer; if any separation does occur in the formulation, the sample can be gently mixed by placing it on a roller. It is advisable to use as minimum shear as possible when transferring the sample from the container to the rheometer (preferably, the transfer is achieved using a "spoon," or simply by pouring from the container). Moreover, the experiment should be carried out without an initial pre-shear.

8.3.6
Dynamic (Oscillatory) Measurements

In oscillatory measurements, two sets of experiments are typically carried out, namely strain and oscillatory sweep measurements.

8.3.6.1 Strain Sweep Measurements

In this case, the oscillation is fixed (say at 1 Hz) and the viscoelastic parameters are measured as a function of strain amplitude (see Chapter 4). G^*, G' and G'' remain virtually constant up to a critical strain value, γ_{cr}; this region is the *linear viscoelastic region*. Above γ_{cr}, however, G^* and G' begin to fall, whereas G'' begins to increase; this is the *nonlinear viscoelastic region*.

The value of γ_{cr} may be identified with the minimum strain above which the "structure" of the dispersion starts to break down (e.g., the breakdown of flocs into smaller units and/or breakdown of a "structuring" agent).

From γ_{cr} and G', it is possible to obtain the cohesive energy E_c (Jm^{-3}) of the flocculated structure, using Equation 8.5. E_c may be used in a quantitative manner as a measure of the extent and strength of the flocculated structure in a dispersion; notably, the higher the value of E_c, the more flocculated is the structure.

Clearly, E_c depends not only on the volume fraction of the dispersion but also on the particle size distribution (which determines the number of contact points in a floc). Therefore, in order to make a quantitative comparison between various systems, it must be ensured that the volume fraction of the disperse particles is the same, and that the dispersions have very similar particle size distributions. E_c is also dependent on the strength of the flocculated structure – that is, the energy of attraction between the droplets – which in turn depends on whether flocculation is occurring in the primary or secondary minimum. Flocculation in the primary minimum is associated with a large attractive energy, and this leads to higher values of E_c when compared to values obtained for secondary minimum flocculation (weak flocculation). For a weakly flocculated dispersion, such as the case with secondary minimum flocculation of an electrostatically stabilized system, the deeper the secondary minimum the higher will be the value of E_c (at any given volume fraction and particle size distribution of the dispersion).

With a sterically stabilized dispersion, weak flocculation can also occur when the thickness of the adsorbed layer is decreased. Again, the value of E_c can be used as a measure of the flocculation – the higher the value of E_c, the stronger the flocculation. If an incipient flocculation occurs (on reducing the solvency of the medium for the change to worse than θ-condition), then a much deeper minimum will be observed, and this will be accompanied by a much larger increase in E_c.

In order to apply the above analysis, it is necessary to have available an independent method for assessing the nature of the flocculation. Rheology is a bulk property that can provide information on the interparticle interaction (whether repulsive or attractive), and before applying it in a quantitative manner it is important to know the nature of these interaction forces. However, rheology can be used in a qualitative manner to follow the change of the formulation on storage.

Providing that the system does not undergo any Ostwald ripening and/or coalescence, the change of the moduli with time – and, in particular, the change of the linear viscoelastic region – may be used as an indication of flocculation. Strong flocculation is usually accompanied by a rapid increase in G', and this may be accompanied by a decrease in the critical strain above which the "structure" breaks down. This may be used as an indication of formation of "irregular" and tight flocs which become sensitive to the applied strain. The floc structure will entrap a large amount of the continuous phase, and this leads to an apparent increase in the volume fraction of the dispersion, and hence to an increase in G'.

8.3.6.2 **Oscillatory Sweep Measurements**

In this case, the strain amplitude is kept constant in the linear viscoelastic region (normally, a point is taken far from γ_{cr} but not too low – that is, in the mid-point of the linear viscoelastic region), and measurements are carried out as a function of frequency. Both, G^* and G' increase with increase in frequency and ultimately, above a certain frequency, will reach a limiting value and show little dependence on frequency. G'' is higher than G' in the low-frequency regime; it also increases with an increase in frequency such that, at a certain characteristic frequency ω^* (that depends on the system), it becomes equal to G' (this is usually referred to as the "crossover point"). Subsequently, G'' reaches a maximum and then shows a reduction with further increase in frequency.

From ω^*, it is possible to calculate the relaxation time τ of the system:

$$\tau = \frac{1}{\omega^*} \tag{8.14}$$

The relaxation time may be used as a guide for the state of the dispersion. For a colloidally stable dispersion (at a given particle size distribution), τ increases with increase of the volume fraction of the disperse phase, ϕ. In other words, the crossover point shifts to lower frequency with an increase in ϕ. For a given dispersion, τ increases with increase in flocculation, provided that the particle size distribution remains the same (i.e., there is no Ostwald ripening and/or coalescence).

The value of G' also increases with an increase in flocculation, as aggregation of the particles usually results in liquid entrapment, such that the effective volume fraction of the dispersion shows an apparent increase. With flocculation, the net attraction between the particles also increases, and this results in an increase in G'. The latter is determined by the number of contacts between the particles and the strength of each contact (which is determined by the attractive energy).

It should be mentioned that, in practice, it may not be possible to obtain the full curve, due to the frequency limit of the instrument; measurements made at low frequency are also time-consuming, and usually only part of the frequency dependence of G' and G'' is obtained. In most cases, the system is more elastic than viscous.

Most disperse systems used in practice are weakly flocculated, and also contain "thickeners" or "structuring" agents to reduce creaming or sedimentation. Such agents also help in acquiring the correct rheological characteristics for application, for example in hand creams and lotions. The exact values of G' and G'' required depends on the system and its application. In most cases, a compromise must be made between acquiring the correct rheological characteristics for application and the optimum rheological parameters for long-term physical stability. The application of rheological measurements to achieve these conditions requires a great deal of skill and understanding of the factors that affect rheology.

8.3.7
Examples of Application of Rheology for Assessment and Prediction of Flocculation

8.3.7.1 Flocculation and Restabilization of Clays Using Cationic Surfactants

Hunter and Nicol [7] studied the flocculation and restabilization of kaolinite suspensions using rheology and zeta-potential measurements. Figure 8.13 shows plots of the yield value σ_β and electrophoretic mobility as a function of cetyl tri-

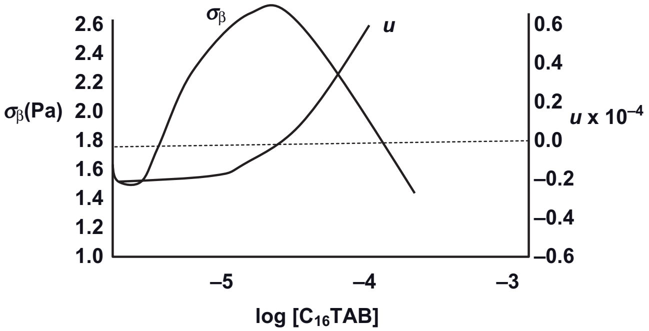

Figure 8.13 Variation of yield value σ_β and electrophoretic mobility u with C_{16}TAB concentration.

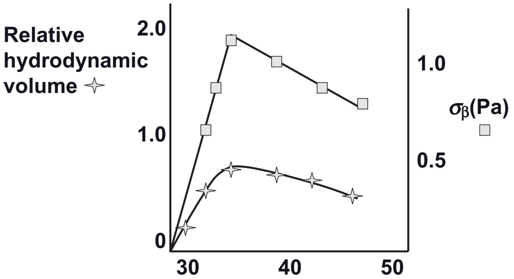

Figure 8.14 Variation of σ_β and hydrodynamic volume with temperature.

methyl ammonium bromide (CTAB) concentration at pH 9. In this case, σ_β increases with the increase in CTAB concentration, reaching a maximum at the point where the mobility reaches zero – at the isoelectric point (p*I*) of the clay – and then decreases with further increases in CTAB concentration. This trend can be explained on the basis of flocculation and restabilization of the clay suspension.

The initial addition of CTAB causes a reduction in the negative surface charge of the clay (due to the adsorption of CTA^+ at the negative sites of the clay), and this is accompanied by a reduction in the negative mobility of the clay. When complete neutralization of the clay particles has occurred (at the p*I*), maximum flocculation of the clay suspension occurs, accompanied by a maximum in σ_β. On further increasing the CTAB concentration, a further adsorption of CTA^+ occurs that results in charge reversal and restabilization of the clay suspension. This is accompanied by a reduction in σ_β.

8.3.7.2 Flocculation of Sterically Stabilized Dispersions

Neville and Hunter [8] studied the flocculation of a poly(methylmethacrylate) (PMMA) latex stabilized with PEO. Flocculation was induced by the addition of an electrolyte and/or an increase in temperature. The variation of σ_β with increased temperature at a constant electrolyte concentration is shown in Figure 8.14. It can

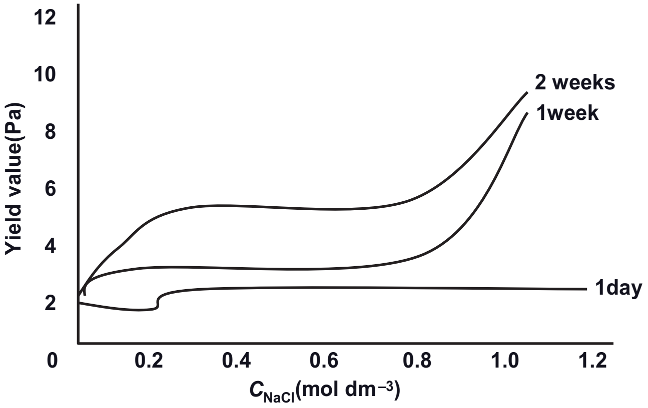

Figure 8.15 Variation of yield value with NaCl concentration.

be seen that σ_β increases with an increase of temperature, to reach a maximum at the critical flocculation temperature (CFT), but then decreases with any further increase in temperature. The initial increase in σ_β is due to flocculation of the latex with increased temperature; this is due to a reduction of the solvency of the PEO chains with the increase in temperature. The reduction in σ_β after the CFT is due to a reduction in the hydrodynamic volume of the dispersion.

8.3.7.3 **Flocculation of Sterically Stabilized Emulsions**

Emulsions were prepared using an A–B–A block copolymer of PEO–PPO–PEO (Synperonic F127), with flocculation being induced by the addition of NaCl. The variation of the yield value (calculated using the Herschel–Bulkley model) as a function of NaCl concentration at various storage times is shown in Figure 8.15. In the absence of NaCl, the yield value did not change with storage time over a period of one month, indicating an absence of flocculation. However, in the presence of NaCl the yield value was increased with increase in storage time. Notably, this increase was highly significant when the NaCl concentration was increased above 0.8 mol dm^{-3} NaCl.

The above increase in yield value indicated that flocculation of the emulsion had occurred, and this was confirmed using optical microscopy. The smaller increase in yield value below 0.8 mol dm^{-3} NaCl was indicative of a weak flocculation, and this could be confirmed by redispersion of the emulsion with gentle shaking. Yet, above 0.8 mol dm^{-3} NaCl, the flocculation was strong and irreversible. In this case, the solvency of the medium for the PEO chains becomes poor, and resulted in incipient flocculation.

Further evidence of flocculation was also obtained from dynamic (oscillatory) measurements. Figure 8.16 shows the variation of G' with NaCl concentration at various storage times. Below 0.8 mol dm^{-3} NaCl, G' showed a modest increase with storage time over a two-week period, indicating a weak flocculation. However, above 0.8 mol dm^{-3} NaCl, G' showed a rapid increase in line with storage time,

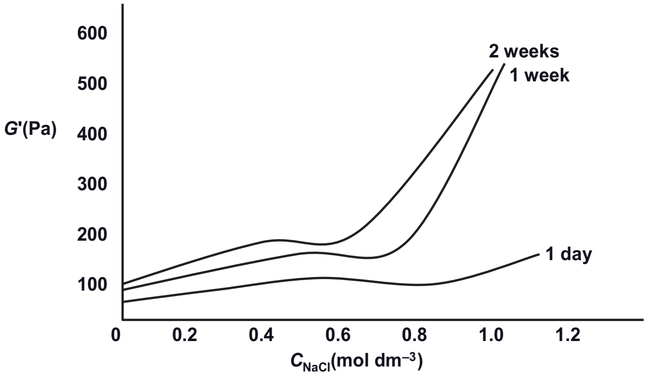

Figure 8.16 Variation of G' with NaCl concentration.

indicating a strong flocculation. This strong (incipient) flocculation was considered due to the reduction of solvency of PEO chains (worse than θ-solvent), which resulted in a strong attraction between the droplets, making them difficult to redisperse.

8.4
Assessment and Prediction of Emulsion Coalescence Using Rheological Techniques

8.4.1
Introduction

The driving force of emulsion coalescence is the thinning and disruption of the liquid film between the droplets [9, 10]. When two emulsion droplets come into contact – for example, in a cream layer or a floc, or even during Brownian collision – the liquid film between them undergoes some fluctuation in thickness. in this case, the thinnest part of the film will have the highest van der Waals attractions, and this is the region where coalescence starts. Alternatively, the surfaces of the emulsion droplets may undergo fluctuation so as to produce waves that may grow in amplitude; the strongest van der Waals attractions occur at the apices of these fluctuations, and coalescence occurs by further growth of the fluctuation. It is possible to define a critical film thickness below which coalescence will occur.

8.4.2
Rate of Coalescence

The rate of coalescence is determined by the rate at which the film thins; this process usually follows a first-order kinetics:

$$N = N_o \exp(-Kt) \tag{8.15}$$

where N is the number of droplets after time t, N_o is the number at zero time, and K is the rate constant of coalescence.

Alternatively, the average droplet diameter d can be measured as a function of time:

$$d = d_o \exp(Kt) \tag{8.16}$$

Provided that the emulsion does not undergo any flocculation, the coalescence rate can be simply measured by following the number of droplets or average diameter as a function of time. A given volume of the emulsion is carefully diluted into the Isotone solution of the Coulter counter, and the number of droplets is measured; the average droplet diameter can be obtained using laser diffraction methods (e.g., using the Master Sizer). By following this procedure at various time periods, it is possible to determine the coalescence rate constant, K.

For this, $\log N$ or $\log d$ is usually plotted versus t, and the slope of the line in the initial period gives the rate of coalescence K. Clearly, the higher the value of K the higher the coalescence of the emulsion. An accelerated test may be used by subjecting the system to higher temperatures; usually, the rate of coalescence increases with an increase of temperature (though this is not always the case). Care must be taken during the dilution procedure, particularly if the oil is significantly soluble (e.g., >10 ppm) in the Isotone solution or in the tank of the Master Sizer. In this case, the solution should be saturated with the oil before diluting the concentrated emulsion for droplet counting or sizing.

8.4.3
Rheological Techniques

8.4.3.1 Viscosity Measurements

In the absence of any flocculation, the coalescence of an emulsion results in a reduction of its viscosity. At any given volume fraction of oil, an increase in droplet size will result in a reduction in viscosity; this is particularly the case with concentrated emulsions [10–13]. Thus, by following the decrease in emulsion viscosity with time, it is possible to obtain information on the emulsion's coalescence. However, care must be taken when applying simple viscosity measurements, particularly if flocculation occurs simultaneously (as this results in an increase in the viscosity). It is possible (at least, in principle) to predict the extent of viscosity reduction on storage, if the results of a droplet size analysis (or droplet number) as a function of time are combined with the reduction in viscosity during the first few weeks.

Freshly prepared emulsions with various droplet sizes are prepared by controlling the speed of the stirrer used for emulsification. The emulsifier concentration in these experiments should be kept constant, and care taken to avoid the presence of excess emulsifier in the continuous phase. The viscosity of these freshly prepared emulsions can then be plotted against the average droplet diameter, so as to produce a "master curve" that relates the emulsion viscosity to the average droplet size. The viscosity is shown to decrease monotonically with the increase in average droplet size.

By using the Coulter counter or Master Sizer, it is possible to determine the rate of coalescence by plotting the log of the average droplet diameter versus time in the first few weeks. This allows a prediction to be made of the average droplet diameter over a longer period (e.g., 6–12 months); the predicted droplet diameter is then used to obtain the viscosity achieved on storage, by using the master curve of viscosity versus the average drop size.

The above procedure is quite useful for setting the limit of viscosity that may be reached on storage as a result of coalescence. With many creams, the viscosity of the system is not allowed to drop below an acceptable limit (which is important for application). The limit that may be reached after a one-year storage period may be predicted from the viscosity and rate constant measurements over the first few weeks.

8.4.3.2 **Measurement of Yield Value as a Function of Time**

Since the yield value σ_β of an emulsion depends on the number of contacts between the droplets, any coalescence should be accompanied by a reduction in the yield value. However, this trend is only observed if no flocculation occurs (this causes an increase in σ_β).

The above change was recently measured using O/W emulsions that had been stabilized with an A–B–A block copolymer of PEO (A) and PPO (B) (Synperonic NPE 127; UNIQEMA). Subsequently, 60 : 40 O/W emulsions were prepared using 0.5, 1.0, 1.5, 2.0, 3, 4, and 5% emulsifier; the variation in droplet size with time at various Synperonic PEF 127 concentrations is shown in Figure 8.17. At an emulsifier concentration >2% there was no change of droplet size with time, indicating an absence of coalescence. However, below an emulsifier concentration of 2% the droplet size increased with time, indicating the presence of coalescence.

8.4.3.3 **Measurement of Storage Modulus G′ as a Function of Time**

This is perhaps the most sensitive method for predicting coalescence. G' provides a measure of the contact points of the emulsion droplets, as well as their strength. Provided that no flocculation occurs (which would result in an increase in G'), any reduction in G' on storage indicates the presence of coalescence.

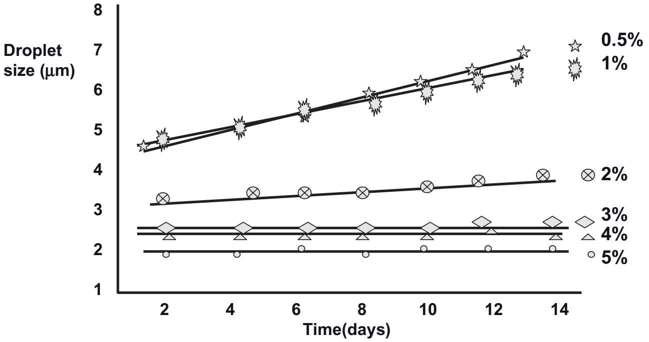

Figure 8.17 Variation of droplet size with time at various Synperonic PEF 127 concentrations.

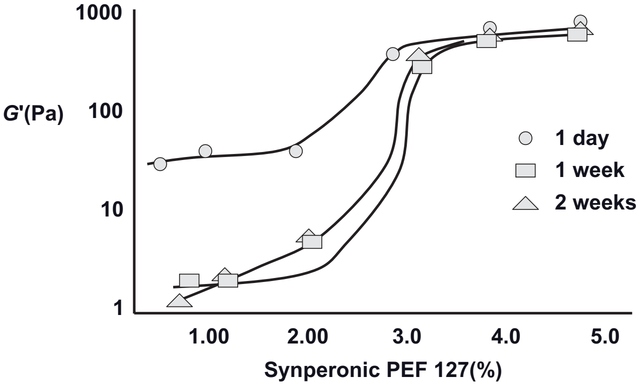

Figure 8.18 Variation of G' with Synperonic PEF 127 concentration at various storage times.

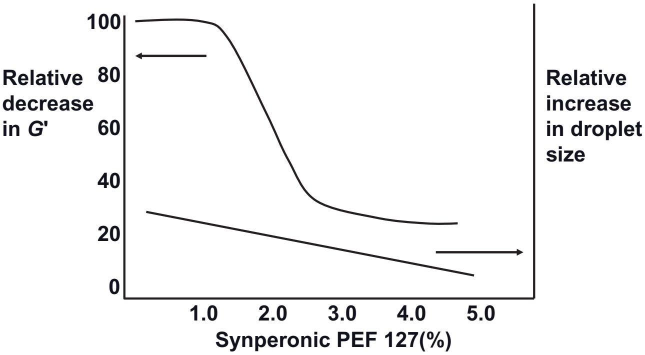

Figure 8.19 Correlation of relative decrease in G' with relative increase in droplet size.

The above trend was confirmed using the emulsions described above. Those emulsions containing less than 3% Synperonic PEF 127 showed a rapid reduction in G' when compared to those containing >3%, which showed virtually no change in G' over a two-week period (see Figure 8.18).

8.4.4
Correlation between Elastic Modulus and Coalescence

The correlation between the emulsion elastic modulus and coalescence rate can be easily represented if the relative decrease in G' is calculated after two weeks:

$$\text{Relative decrease of } G' = \left(\frac{(G_{\text{initial}} - G_{\text{after2weeks}})}{G_{\text{initial}}} \right) \times 100 \tag{8.17}$$

The variation of the relative decrease in G' and relative increase in droplet size in relation to the Synperonic PEF127 concentration is shown in Figure 8.19. In this

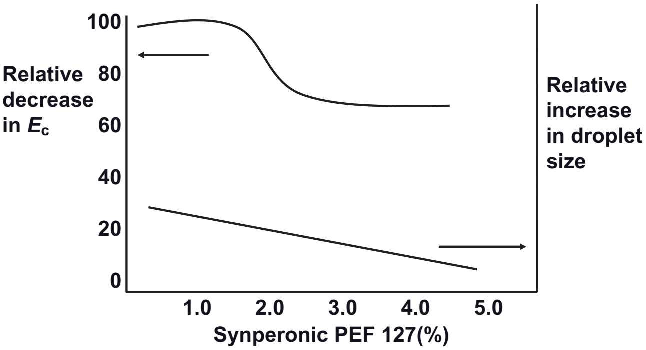

Figure 8.20 Correlation of relative decrease in E_c with relative increase in droplet size.

case, the correlation between the relative decrease in G' and relative increase in droplet size due to coalescence, was very clear.

8.4.5
Cohesive Energy E_c

The cohesive energy E_c is the most sensitive parameter for the assessment of coalescence:

$$E_c = (1/2)G'\gamma_{cr}^2 \tag{8.18}$$

where γ_{cr} is the critical strain above which the linear response (where G' is independent on the applied strain) changes to a nonlinear response. Any coalescence will result in a decrease of the number of contact point, and cause a reduction in E_c.

When using the above-described emulsions, E_c was found to decrease with an increase of droplet size (as a result of coalescence). At and above 3% Synperonic PE 127, E_c remained virtually unchanged, indicating an absence of coalescence. The variation in the relative decrease of E_c with a relative increase in droplet size is shown in Figure 8.20, where the correlation is clearly seen.

References

1 Tadros, T.F. (1987) *Solid/Liquid Dispersions*, Academic Press, London.

2 Bachelor, G.K. (1972) *J. Fluid Mech.*, **52**, 245; Bachelor, G.K. (1976) *J. Fluid Mech.*, **79**, 1.

3 Buscall, R., Goodwin, J.W., Ottewill, R.H., and Tadros, T.F. (1982) *J. Colloid Interface Sci.*, **85**, 78.

4 Salager, J.L. (2000) *Pharmaceutical Emulsions and Suspensions*, Marcel Dekker, New York.

5 Ferry, J.D. (1960) *Viscoelastic Properties of Polymers*, John Wiley & Sons, Inc., New York.

6 Goodwin, J.W. and Hughes, R. (2000) *Rheology for Chemists*, Royal Society of Chemistry Publications, Cambridge.

7 Hunter, R.J. and Nicol, S.K. (1968) *J. Colloid Interface Sci.*, **28**, 250.

8 Neville, P.C. and Hunter, R.J. (1974) *J. Colloid Interface Sci.*, **49**, 204.

9 Tadros, T.F. and Vincent, B. (1983) *Encyclopedia of Emulsion Technology*, vol. **1** (ed. P. Becher), Marcel Dekker, New York, Chapter 3.

10 Tadros, T.F. (1994) *Colloids Surf. A*, **91**, 39.

11 Tadros, T. (2004) *Adv. Colloid Interface Sci.*, **227**, 108–109.

12 Tadros, T.F. (1996) *Adv. Colloid Interface Sci.*, **68**, 91.

13 Tadros, T.F. (1992) Rheological Properties of Emulsion Systems, in *Emulsions – A Fundamental and Practical Approach*, vol. **363** (ed. J. Sjoblom), NATO ASI Series, Kluwer Academic Publishers, Series C, pp. 173–188.

Index

Rheology of Dispersions: Principles and Applications. Tharwat F. Tadros

ISBN: 978-3-527-32003-5